ISSN 1590-8844
Vol. 16 No 01
2015

International Journal of Mechanics and Control

Editor: Andrea Manuello Bertetto

LIBRERIA EDITRICE UNIVERSITARIA
LEVROTTO & BELLA
TORINO

Official Torino Italy Court Registration
n.5390, 5th May 2000

Deposito presso il Tribunale di Torino
numero 5390 del 5 maggio 2000
Direttore responsabile:
Andrea Manuello Bertetto

International Journal of Mechanics and Control

The Journal is addressed to scientists and engineers who work in the fields of mechanics (mechanics, machines, systems, control, structures). It is edited in Turin (Northern Italy) by Levrotto&Bella Co., with an international board of editors. It will have not advertising.

Turin has a great and long tradition in mechanics and automation of mechanical systems. The journal would will to satisfy the needs of young research workers of having their work published on a qualified paper in a short time, and of the public need to read the results of researches as fast as possible.

Interested parties will be University Departments, Private or Public Research Centres, Innovative Industries.

Aims and scope

The *International Journal of Mechanics and Control* publishes as rapidly as possible manuscripts of high standards. It aims at providing a fast means of exchange of ideas among workers in Mechanics, at offering an effective method of bringing new results quickly to the public and at establishing an informal vehicle for the discussion of ideas that may still in the formative stages.

Language: English

International Journal of Mechanics and Control will publish both scientific and applied contributions. The scope of the journal includes theoretical and computational methods, their applications and experimental procedures used to validate the theoretical foundations. The research reported in the journal will address the issues of new formulations, solution, algorithms, computational efficiency, analytical and computational kinematics synthesis, system dynamics, structures, flexibility effects, control, optimisation, real-time simulation, reliability and durability. Fields such as vehicle dynamics, aerospace technology, robotics and mechatronics, machine dynamics, crashworthiness, biomechanics, computer graphics, or system identification are also covered by the journal.

Please address contributions to

Prof. Guido Belforte
Prof. Andrea Manuello Bertetto
PhD Eng. Elvio Bonisoli

Dept. of Mechanics
Technical University - Politecnico di Torino
C.so Duca degli Abruzzi, 24.
10129 - Torino - Italy - E.C.

www.jomac.it
e_mail: jomac@polito.it

Subscription information

Subscription order must be sent to
the publisher:

Libreria Editrice Universitaria
Levrotto&Bella
C.so Luigi Einaudi 57/c – 10129 Torino – Italy

www.levrotto-bella.net
e_mail: info@levrotto-bella.net
ph.: +39 011 4275423
mob.: +39 328 5369063
fax: +39 011 4275425

ISSN 1590-8844
International Journal of Mechanics and Control, Vol. 16, No. 01, 2015

Preface for the special issue of the JoMaC dedicated to the 23rd edition of the Workshop on Robotics in Alpe-Adria-Danube Region, RAAD 2014

Since the year 1992 RAAD Workshop, now RAAD Conference, are yet traditional meetings of professionals working in research, application and education covering all major research areas related to robotics. In these events take part academicians, research professionals and students not only from Alpe-Adria-Danube region countries, but they became a well-established forum providing the opportunity to present and to exchange knowledge and experiences among researchers and institutions within all European countries and within world-wide robotic community too. Every year are evaluated and awarded the best papers in three fields: significant theoretical contribution, most innovative or interesting application and best student papers. This is the important feature of this conference motivating especially young researchers and PhD students to present their works.

Last year, the RAAD 2014 was organized in collaboration of Institute of Informatics SAS and Slovak University of Technology in Bratislava under supervision of the Slovak committee for cybernetics and informatics, and under sponsorships of two professional world communities IFToMM and IEEE. It took place in September 2-5, 2014, in the Smolenice castle - the Congress Centre of the Slovak Academy of Sciences (www.raad2014.org). There were orally presented 52 papers and 7 posters by authors from 16 countries. Plenary lectures showed the research achievements in mobile and industrial robotics, attended by exposition. Presented papers reflect actual trends, objectives in robotic research and achievements have been reached in labs / institutions of participants.

Štefan Havlík

Chair of the RAAD2014 conference

ISSN 1590-8844
International Journal of Mechanics and Control, Vol. 16, No. 01, 2015

OPTIMAL DESIGN OF A NEW SPHERICAL PARALLEL MANIPULATOR USED AS MASTER DEVICE

Houssem Saafi Med Amine Laribi Marc Arsicault Said Zeghloul

Dept.of GMSC, Pprime Institute

CNRS - University of Poitiers - ENSMA - UPR 3346, France

ABSTRACT

This paper deals with the optimization of a New Spherical Parallel Manipulator (N_SPM). The N_SPM is obtained by changing the kinematic of one leg of a classic spherical parallel manipulator. This change is carried out to reduce the presence of the singularity in the useful area of the workspace. The mobility of the N_SPM is similar to the classic one. First, the less-singular working mode of the N_SPM was identified then an optimization of the dexterity is made to eliminate the singularity from the useful workspace. Finally, the optimal N_SPM is presented.

Keywords: Spherical Parallel Manipulator; Optimization; Workspace; Dexterity; Genetic Algorithm.

1 INTRODUCTION

In the recent years, parallel manipulators still widely popular. They are used in many domains such as industry [1], research [2] and medicine [3]. The main advantages of parallel manipulators are their high stiffness, their high accuracy and their load capability.

The spherical parallel manipulators (SPMs) are a class of parallel manipulator that gives three degrees of freedom of rotations. They are composed of three identical legs with three revolute joints. The main application of the SPMs is orienting device such as minimally invasive surgery master device [4, 5] and camera orienting device [6, 7].

Parallel manipulators performances depend on their geometric parameters. An optimization process is needed to choose the optimal geometry for each specific application. In [4], a SPM is optimized for a MIS application. The self-rotation was not considered in the optimization process. This generates the presence of singularity in the SPM workspace for some values of the self-rotation.

In this paper we try to solve the problem of the singularity. A kinematic modification of the SPM was carried out to reduce the presence of the singularity. The New SPM (N_SPM) is then optimized to eliminate the singularity from the prescribed workspace and to improve the dexterity distribution.

The paper is organized as follows. In section 2, an evaluation of the classic SPM is shown. In Section 3, the new structure of the SPM is presented. A comparative study was made in section 4 to choose the less-singular assembly mode of the N_SPM. Section 5 discusses an optimization of the N_SPM. Finally, Section 6 summarizes this paper.

Contact author: Said Zeghloul

said.zeghloul@univ-poitiers.fr.

2 EVALEATION OF THE CALSSIC SPM

The SPM (Fig. 1) was developed as a part of a tele-operation system to control a surgical robot. The target application is the minimally invasive surgery (MIS). In a previous work [4], the workspace of the MIS was studied to identify its size.

The SPM has three identical legs, each leg is made of two links and three revolute joints, see Fig. 2. All axes of the revolute joints are intersecting in one common point, called CoR (Centre of Rotation). Each link is characterized by the angle between its two revolute joints, as shown in Fig. 3.

This angle is constant and it represents the dimension of the link. The angle, α, characterizes the first link size and the angle, β, the second link size. The angle, γ, defines the orientation of the axis z of the platform with respect to the last joint axis. The actuated joint axes are located along an orthogonal frame.

Figure 1 Master device of a tele-operation system.

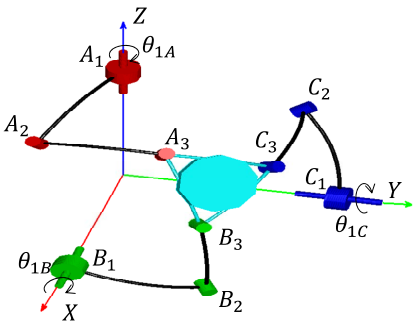

Figure 2 Spherical parallel manipulator kinematic.

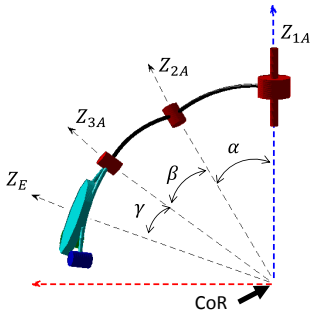

Figure 3 Kinematic of the leg A.

The orientation of the SPM is described by the Euler angles (ψ, θ, φ). The workspace of the SPM can be identified by its inverse model. The inverse model is solved using equation (1) for leg K (K=A, B and C).

$$Z_{2K}Z_{3K} = \cos(\beta) \tag{1}$$

With

$$\begin{cases} Z_{2K} = R_Z(\theta_{1K})R_X(\alpha)Z \\ Z_{3K} = R_Z(\psi)R_X(\theta)R_Z(\varphi)R_X(\gamma)Z \end{cases} \tag{2}$$

After substitution, the equation (1) leads to the following three scalar equations:

$$A_j \cos(\theta_{1K}) + B_j \sin(\theta_{1K}) = C_j; j \in \{1,2,3\} \tag{3}$$

Where A_j, B_j and C_j are coefficients that depend on the parameters (α, β, γ) and the variation of the platform given by the Euler angles (ψ, θ, φ).

Equation 3 has a solution if and only if the following constraints CD_j are respected:

$$CD_j(\alpha,\beta,\gamma,\psi,\theta,\varphi): \frac{C_j^2}{A_j^2 + B_j^2} \le 1 \tag{4}$$

These three conditions are used to identify the workspace size of the spherical parallel manipulator (SPM) and called as the orientation power function, which indicates if the arm j is able to reach the given orientation or not. The Jacobian matrix of the SPM can be written by differentiating Equation 1:

$$\dot{Z}_{2K}Z_{3K} + Z_{2K}\dot{Z}_{3K} = 0 \tag{5}$$

where,

$$\begin{cases} \dot{Z}_{2K} = \dot{\theta}_{1K}Z_{1K} \times Z_{2K} \\ \dot{Z}_{3K} = \omega \times Z_{3K} \end{cases} \tag{6}$$

with, × is the cross product and ω is the angular velocity of the end-effector.

$$\omega = \begin{bmatrix} \dot{\theta}\cos(\psi) + \dot{\varphi}\sin(\theta)\sin(\psi) \\ \dot{\theta}\sin(\psi) - \dot{\varphi}\sin(\theta)\cos(\psi) \\ \dot{\psi} + \cos(\theta) \end{bmatrix} \tag{7}$$

Equation 4 becomes:

$$\dot{\theta}_{1K}(Z_{1K} \times Z_{2K}) \cdot Z_{3K} = \omega \cdot Z_{2K} \times Z_{3K} \tag{8}$$

Indeed, we can write equation (9) in matrix form as:

$$A \cdot \omega = B \cdot \dot{\theta} \tag{9}$$

$$\omega = J \cdot \dot{\theta} \tag{10}$$

where, $\dot{\theta} = \left[\dot{\theta}_{1A}, \dot{\theta}_{1B}, \dot{\theta}_{1C}\right]^T$ is the vector of actuated joint velocities and J is the Jacobian matrix of the SPM defined as follows:

$$J = A^{-1}B \tag{11}$$

Matrix A is a 3x3 matrix and it is defined as follows:

$$A = \left[Z_{3A} \times Z_{2A} \quad Z_{3B} \times Z_{2B} \quad Z_{3C} \times Z_{2C}\right]^T \tag{12}$$

Matrix B is a diagonal 3x3 matrix and it is defined as follows:

$$\begin{aligned} B = diag[&Z_{1A}(Z_{2A} \times Z_{3A}); Z_{1B}(Z_{2B} \times Z_{3B}); \\ &...Z_{1C}(Z_{2C} \times Z_{3C})] \end{aligned} \tag{13}$$

Dexterity is a measure reflecting the error amplification due to the kinematic and statistic transformations between the joints and Cartesian space. The dexterity, $\eta(J)$, is

measured using the inverse of the condition number, *κ(J)*, of the Jacobian matrix [8], see Eq. 14.

$$\eta(J)=\frac{1}{\kappa(J)} \qquad \text{With } \kappa(J)=\|J\|\cdot\|J^{-1}\| \tag{14}$$

In previous work [4], the SPM was optimized in order to have a compact structure with a maximum of dexterity. The resulting structure is defined by the following vector of optimal design parameters:

$$I_{SPM}=[\alpha,\beta,\gamma]^T=[39.4°,34.1°,18.2°]^T$$

However a simplifying assumption was considered in this SPM optimization procedure, only a constant value for the self-rotation, $\varphi=\pi/10$, is considered. For other values of φ, the kinematic behaviour of the robot is deteriorated. Fig. 4 presents the dexterity distribution of the SPM for $\varphi=50°$ and shows the presence of the singularity inside the workspace (the singular are in dark red).

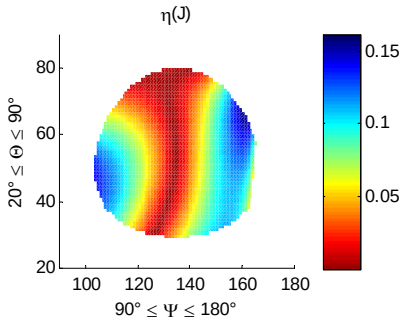

Figure 4 The dexterity distribution of the SPM over the useful workspace for φ=50° (singular area in dark red).

3 SOLVING THE SINGULARITY PROBLEM

In a previous work [9], a solution avoiding the singularity problem was proposed. This solution is based on the use of a redundant actuator without changing the design of the SPM. It was proved that the use of the redundant actuator eliminates the presence of singularity inside the workspace. However, this solution increases the weight of the end-effector. Consequently, it's not well suitable. In this present work, we propose a solution with a design change. The kinematic of only one leg is replaced. The new structure of the SPM is presented in Fig. 5.

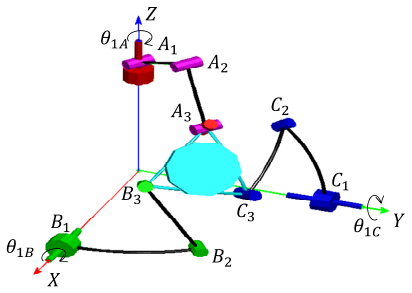

Figure 5 Kinematic structure of the new SPM.

The legs B and C are not changed and described by the same geometric parameters, [α, β, γ], as the classic SPM. The RRR kinematic structure of leg A was replaced by URU structure as illustrated in Fig 6 (R for Revolute joint and U for Universal joint). The links of the new leg have the same length, L.

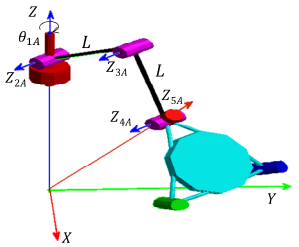

Figure 6 New kinematic of the leg A.

In order to obtain the Jacobian matrix of the new SPM, we should express the relationship between the angular velocity of the platform ω and the actuated joint velocities, $\dot{\theta}_{1A}$, $\dot{\theta}_{1B}$ and $\dot{\theta}_{1C}$.

For the legs B and C, the equation (8) is applicable. For the new leg A, we can write

$$\omega=\dot{\theta}_{1A}Z_{1A}+\dot{\theta}_{2A}Z_{2A}+\dot{\theta}_{3A}Z_{3A}+\dot{\theta}_{4A}Z_{4A}+\dot{\theta}_{5A}Z_{5A} \tag{15}$$

The reciprocal screw is used to eliminate all passive joint velocities $\dot{\theta}_{2A}$, $\dot{\theta}_{3A}$, $\dot{\theta}_{4A}$ and $\dot{\theta}_{5A}$ from equation (15) and defined as follows:

$$\$^r_{1A}=Z_{4A}\times Z_{5A} \tag{16}$$

This vector is perpendicular in all configurations to the vectors Z_{2A}, Z_{3A}, Z_{4A} and Z_{5A}. We multiply equation (16) by the reciprocal screw:

$$\$^r_{1A}\cdot\omega=\$^r_{1A}\cdot\dot{\theta}_{1A}Z_{1A} \tag{17}$$

$$Z_{4A}\times Z_{5A}\cdot\omega=\dot{\theta}_{1A}\cdot Z_{1A}\cdot(Z_{4A}\times Z_{5A}) \tag{18}$$

The matrices *A* and *B* become:

$$A=\begin{bmatrix}Z_{4A}\times Z_{5A} & Z_{3B}\times Z_{2B} & Z_{3C}\times Z_{2C}\end{bmatrix}^T \tag{19}$$

$$B=diag[Z_{1A}(Z_{4A}\times Z_{5A});Z_{1B}(Z_{2B}\times Z_{3B});\ldots Z_{1C}(Z_{2C}\times Z_{3C})] \tag{20}$$

4 THE LESS SINGULAR WORKING MODE OF N_SPM

If we consider the new leg, the new SPM has eight solutions (Working Modes (W.Ms)) to the inverse kinematic model. The new leg has no effect on the kinematic behavior of the N_SPM. So we consider only four working modes presented in Fig. 7. Each one of these working modes has a different behavior inside the useful workspace. The aim of this section is to identify the most suitable working mode in term of kinematic behavior. An equivalent study was made for the classic SPM in [10].

In this section, we consider that the dimensions of legs B and C are identical to those of the classic SPM (see Section II). An optimization problem will be performed in the next section in order to identify the optimal dimensions.

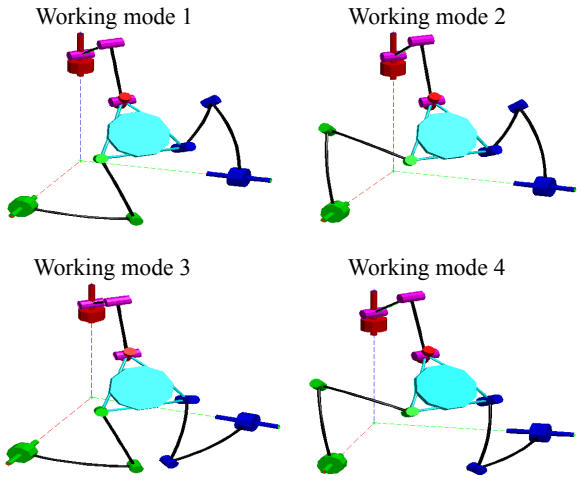

Figure 7 Working modes of the N_SPM.

For the considered parallel structure, the change of working mode is possible only through a serial singularity, when one of the two spherical legs B or C is extended or folded on in itself. This is possible only in the border of the workspace.

Figures 8, 9 and 10 show the dexterity distribution and the singularity location in the useful workspace for φ=0°, φ=50° and φ=-50° respectively.

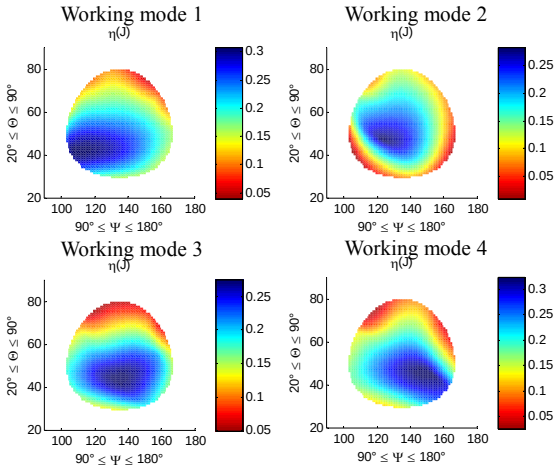

Figure 8 The dexterity distribution for the all W.Ms (φ=0°).

The singular configurations for all working modes are located on the borders of the workspace for φ=0°. However, we note that the W.Ms 1 and 4 do not present a maximum of the dexterity at the center of the workspace, unlike the W.Ms 2 and 3.

For φ=50°, the W.M. 4 presents the most suitable distribution of the dexterity. There is no singular configurations inside the workspace.

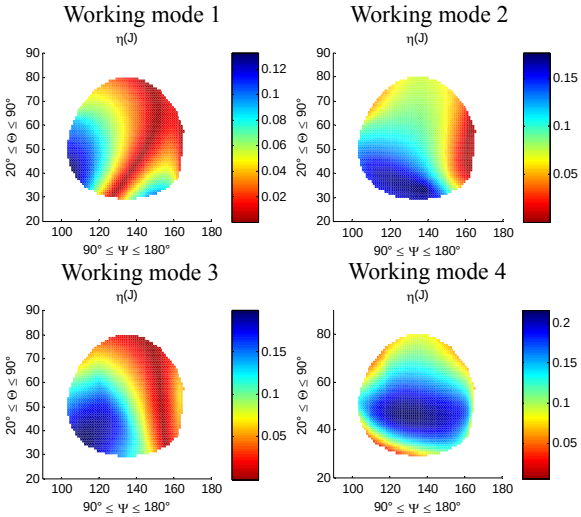

Figure 9 The dexterity distribution for the all W.Ms (φ=50°).

For φ=-50°, only W.M. 1 doesn't contain any singular configuration in the workspace. Working mode 2 contains a small singularity area in the left border of the workspace. Figures 8, 9 and 10 show that the W.M. 2 is the less singular working mode. In order to prove this observation, we propose to calculate the minimum distance, rmin, between the singularity location and the useful workspace center $O_0(\psi_0, \theta_0)$ (see Fig. 11).

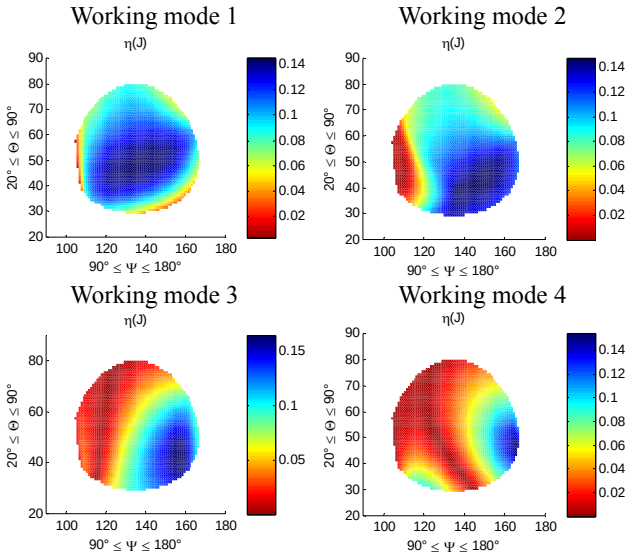

Figure 10 The dexterity distribution for the all W.Ms (φ=-50°).

This distance is calculated as follows:

$$r_{\min} = \min(r_i) = \min(\sqrt{(\psi_0 - \psi_i)^2 + (\theta_0 - \theta_i)^2} \quad (21)$$

The N_SPM is considered in singular configuration if the dexterity value is less than 0.02.

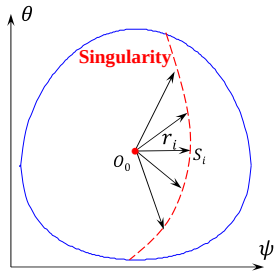

Figure 11 Minimum distance identification between the singularity and the useful workspace center, O_0.

Fig. 12 shows the evolution of r_{min} with respect to the self-rotation of the plateform. We can observe that the singularity locations are close to the border of the workspace for all considered self-rotation values. Therefore the assembly mode 2 is the less-singular assembly mode. This mode is then chosen.

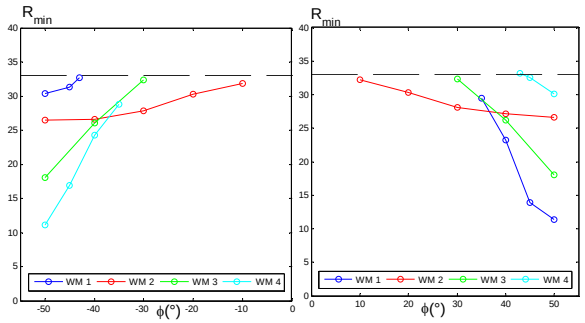

Figure 12 R_min evolution with respect to the self-rotation of the platform.

The symmetry of the architecture presented by the working mode 2 (see Fig. 7) has leads to a symmetric kinematic behavior. Due to this symmetry, the following study will focus only on values of the self-rotation between 0° and 50°.

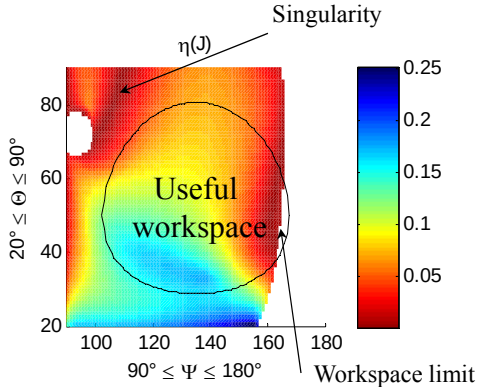

Figure 13 The dexterity destribution for the W.M. 2 (φ=50°).

In addition of the presence of the singularity for φ=-50° and φ=50°, the workspace size does not fit the needed workspace, see Fig. 13. To solve this problem, we propose to optimize the parameters of the N_SPM in order improve the workspace size and to eliminate the presence of singularity.

4 OPTIMIZATION OF THE N_SPM

In this section, the dexterity was considered as a criterion to determine the link dimensions of the optimal new SPM. The link dimensions are defined by the design vector I=[α,β,γ]. The performance is evaluated over a workspace free of singularity, which is specified as a cone with an apex angle equal to 26°. This represents the dimensional characteristic of the prescribed workspace.

Since the singularities are located at the border of the workspace, only the workspace boundary is considered in order to simplify the optimization process. The workspace border is discretized by 100 points as illustrated on Fig. 14.

The proposed approach is based on the minimization of an objective function F(I) subjected to two constraints. The first constraint concerns the workspace and aims to guarantee that the N_SPM workspace fits the prescribed one for the self-rotation φ between 0° and 50°. The second constraint concerns the Jacobian matrix conditioning to guarantee dexterous workspace (free of singularity) for φ between 0° and 50°.

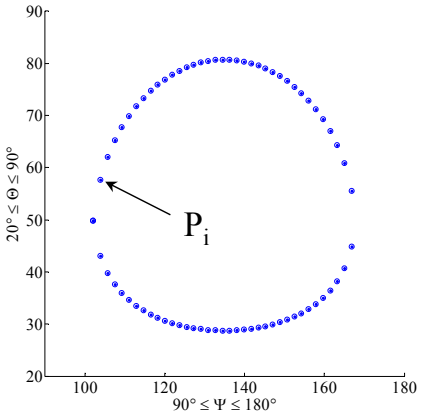

Figure 14 Prescribed workspace border in (θ, ψ) plane and discretized on N=100 points.

The optimization problem can be then formulated as follows:

minimize: $F(I) = \sum_{i}^{N} \kappa(I, P_i, \varphi = 0°) + \sum_{i}^{N} \kappa(I, P_i, \varphi = 50°)$

subject to:

1- $CD_j(\alpha, \beta, \gamma, \psi, \theta, \varphi) : \dfrac{C_j^2}{A_j^2 + B_j^2} \le 1$

2- $\kappa(I, P_i) < \kappa_{\max}$

3- $x_{lb} \le x \le x_{up}; \quad x \in \{\alpha, \beta, \gamma\}$

where *F(I)* is the objective function defined as a sum of the condition number value for all points *Pi* for φ=0° and φ=50°, x_{lb} and x_{up}, are the lower and upper bounds of the variables *x* given in Table 1 respectively, and κ_{max} represents the maximum permissible value for the condition number which is considered equal to 25 in the optimization process.

Table I - The lower and upper bounds of the design variables *x*

	α[deg]	β[deg]	γ[deg]
x_{lb}	35	30	16
x_{up}	50	45	20

A genetic algorithm (GA) is used to solve the optimization problem, because of its robustness and simplicity. Initially the algorithm generates 500 sets of different design parameters as the first parent generation. Then the three standard genetic operations (reproduction, crossover, and mutation) are performed to produce a new generation. Such procedures are repeated until the maximum number of generations is achieved, or the required accuracy is satisfied.
The optimal design vector of the resulted structure is given in table 2. Fig. 15 shows the Optimal N_SPM.

Table II - OPTIMAL SOLUTION.

Design vector	Variables			κ_{max}
	α[deg]	β[deg]	γ[deg]	
I_{nSPM}	49.5	39.1	16.1	25

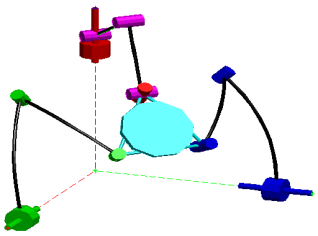

Figure 15 Optimal N_SPM.

The dimension of the new kinematic leg is defined by the parameter *L* calculated using the following equation:

$$L = R\frac{\sin(\theta_{2A}^{MAX})}{2} \tag{22}$$

where, R is the SPM radius, $\theta_{2A}^{MAX} = \theta^{MAX} + \delta - \gamma$ the maximum angle between Z_{1A} and Z_{5A} and δ is the security angle chosen to be equal to 2° in order to avoid the serial singularity of the leg A.
The dexterity distributions for the resulted structure for φ=0°, φ=50° and φ=-50° are shown in Fig. 16.

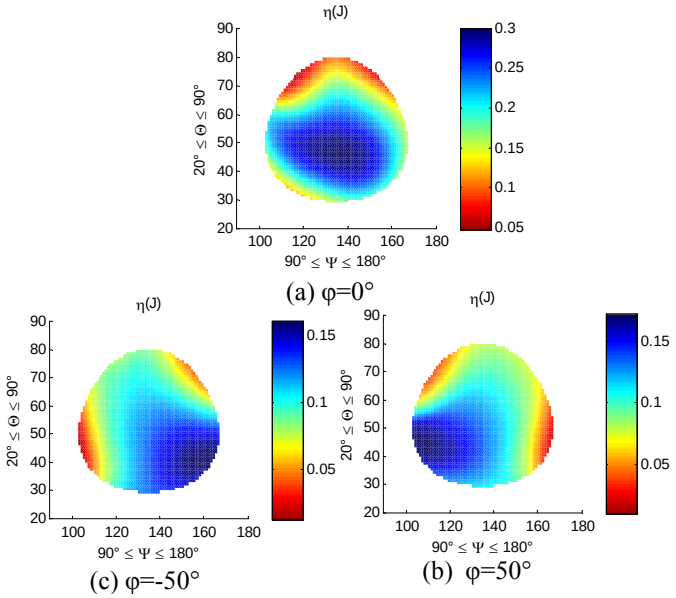

Figure 16 Dexterity distribution for the optimal N_SPM.

We can observe first, that the robot workspace fits the prescribed workspace for φ between -50° and 50°, which means that the robot is able to reach all the orientations needed to achieve the surgical task. Second, the obtained workspace is free-singular for φ between -50° and 50°.

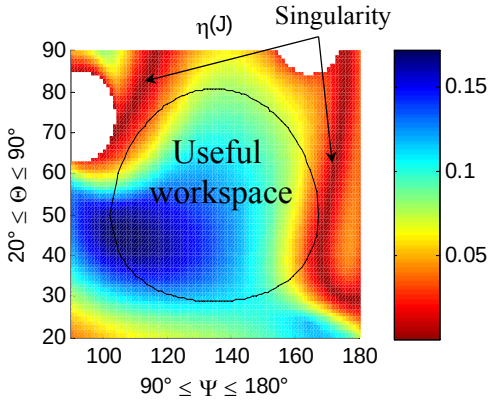

Figure 17 Dexterity distribution for the optimal N_SPM for the whole workspace(φ=50°).

Fig. 17 shows the singularity area of the optimal N_SPM for φ=50°. We can observe that the singularity is outside the useful workspace.
Fig. 18 shows a 3d printed prototype of the optimal N_SPM. This prototype was made to validate the functioning of the N_SPM. It is made of ABS and its size is about the third of the size of the master device presented in Fig. 1.

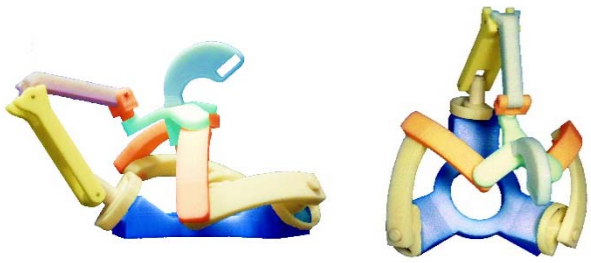

Figure 18 Prototype of the optimal SPM.

6 CONCLUSION

An optimization of a new spherical parallel manipulator (N_SPM) was presented in this work. The objective of this optimization is to obtain a new SPM with a workspace overlaying the prescribed workspace without presence of the singularity. First, the singularity problem of the classic SPM was shown. Second, a new architecture of the spherical parallel manipulator was presented. Then, the less-singular assembly mode of the new SPM was identified and selected. Finally, an optimization based on the dexterity and subject to the workspace size and the presence of singularity is made to improve the kinematic behaviour of the N_SPM.

ACKNOWLEDGMENT

This research is supported by the Poitou-Charentes region 2007-2013 (program project 10 Images and interactivities), in partnership with the European Union (FEDER/ERDF, European Regional Development Fund) and by ROBOTEX, the French national network of robotics platforms (N° ANR-10-EQPX-44-01).

REFERENCES

[1] S. M. Wang and K. F. Ehmann, “Error Model and Accuracy Analysis of a Six-Dof Stewart Platform,” ASME Journal of Manufacturing Science and Engineering, Vol. 124, No. 2, 2002, pp. 286-295. doi: 10.1115/1.1445148

[2] J. Wang, C. Wu and X. J. Liu, “Performance Evaluation of Parallel Manipulators: Motion/Force Transmissibility and Its Index,” Mechanism and Machine Theory, Vol. 45, No. 10, 2010, pp. 1462-1476.

[3] Saafi, H.; Laribi, M.A.; Zeghloul, S.; Ibrahim, M.Y., “Development of a spherical parallel manipulator as a haptic device for a tele-operation system: Application to robotic surgery,” Industrial Electronics Society, IECON 2013 - 39th Annual Conference of the IEEE, vol., no., pp. 4097-4102, 10-13 Nov. 2013.

[4] A. Chaker, A. Mlika, M. A. Laribi, L. Romdhane and S. Zeghoul, “Synthesis of a Spherical Parallel Manipulator for a Dexterous Medical Task”, Front. Mech. Eng. 2012, Volume 7, Number 2, pp. 150-162, doi: 10.1007/s11465-012-0325-4.

[5] A. Ma, S. Payandeh, Analysis and experimentation of a 4-dof haptic device, in: Haptic interfaces for virtual environment and teleoperator systems, 2008, pp. 351-356. doi: 10.1109/HAPTICS.2008.4479970.

[6] L. Birglen, C. Gosselin, N. Pouliot, B. Monsarrat, T. Laliberte, Shade, a new 3-dof haptic device, Robotics and Automation, IEEE Transactions on 18 (2) (2002), pp. 166–175. doi: 10.1109/TRA.2002.999645.

[7] C. Gosselin, E. St.Pierre, M. Gagne, On the development of the agile eye, Robotics Automation Magazine, IEEE 3(4), 1996, pp. 29–37. doi: 10.1109/100.556480.

[8] C. Gosselin, J. Angeles, “A Global Performance Index for the Kinematic Optimisation of Robotic Manipulators”, ASME Journal of Mechanical Design, vol.113, n° 3, pp. 220-226, 1991.

[9] Saafi, H.; Laribi, M.A.; Zeghloul, S.; “Redundantly actuated 3-RRR spherical parallel manipulator used as a haptic device: improving dexterity and eliminating singularity”, 22nd international conference on robotics in Alpe-Adria-Danube region, Portoroz, Slovenia, 11-13 September 2013.

[10] Saafi, H.; Laribi, M.A.; Zeghloul, S.; “Less-Singular Assembly-Mode for 3-RRR Spherical Parallel Manipulator”, 3rd IFToMM International Symposium on Robotics and Mechatronics, 2-4 October 2013, Singapore.

ISSN 1590-8844
International Journal of Mechanics and Control, Vol. 16, No. 01, 2015

AN UNDERACTUATED MECHANICAL HAND: THEORETICAL STUDIES AND PROTOTYPING

Vincenzo Niola Francesco Penta Cesare Rossi Sergio Savino

Department of Industrial Engineering, University of Naples "Federico II", Naples, Italy

ABSTRACT

In the present paper a model of an underactuated tendon driven mechanical hand is proposed. The aim of the activity was to study the possibility of realization of a mechanical hand five fingers, the movement of which is realized by the use of one only actuator. The mechanism is conceived as an hand prosthesis. The main particularity of the device essentially consist in that it is based on an adaptive scheme. In this way it is possible to obtain that the three phalanxes of each of the fingers adapt their rotation to the grasped object shape. This will be obtained by non-extendible tendons. So each finger will grasp the object surface independently on the configuration of the finger itself and independently on the configuration of the other fingers.

Keywords: Mechanical hand; Hand Prostesis; Underactuated mechanism.

1 INTRODUCTION

In the last decades, many devices for human prostheses were developed improving the life quality of a number of people.

It is well-known that human hand is one of the most complex and multi-functional organ; even if the thumb capability to rotate is neglected, the hand still has 15 d.o.f. or even 17 if some movements of the thumb are considered. The great progress in actuator miniaturization and in the control systems made it possible to design multi-finger and multi-phalanx grasping tools operated by several actuators; nevertheless, both the mechanical parts and the control are very complex, hence the cost is very high while the reliability is rather low. For these reasons underactuated multi-finger grasping devices moved by a single actuator were proposed. So, several multi-finger systems working likewise the human hand or human prostheses have been developed. Despite the progress in micro motors developing, in the grasping devices that use fingers, if the system's dimensions are comparable to those of an human hand, it is rather difficult to operate each of the finger phalanxes by a (micro)motor, so the fingers are moved by tendons.

Contact author: Cesare Rossi [1]
[1]Email: cesare.rossi@unina.it

In Fig. 1 some examples are shown. In Fig. 1,a is reported a scheme [1] of a five finger hand moved by a single actuator; the auto-adaptabilily of the fingers to the shape of the grasped object is obtained by means of "sliding pulleys". In fig. 1,b is shown a study [2] in which the synergy concept was developed, based on the anatomic links of the human hand between muscle and tendons mostly as far as the coordination of the fingers is concerned (eigenpostures); this was obtained, essentially, by means of some pulleys fitted on the same shaft but having different diameters, as shown in figure 1,c. It must be told that the early prototypes reached the desired finger positions not very accurately; the behaviour of the device was then improved by means of further mechanical and control complexity, using a further actuator and a gear system.

In Fig.1,d is shown a model [3] widely inspired to the human body; most of the phalanxes joints have variable stiffness, allowing higher efforts and better adaptability. Since the hand is designed to be a part of a mechanical arm, the motors are located in the arm. The fingers are operated in antagonistic way by two motors for each d.o.f. and 38 motors, fitted in the forearm, were used; hence the device is not underactuated.

In Fig.1,e is reported a first prototype (see e.g. [4]) developed at the Scuola Superiore Sant'Anna (Pisa, Italy) having 16 d.o.f., operated by 4 motors, which was further developed in subsequent research activities, (see e.g [5,6,7,8]). Another Italian research team, born from the collaboration between the University of Pisa and the

Research Center "E.Piaggio", rather recently, developed the hand shown in fig 1,f, (see e.g. [9]). The device is operated by one actuator only, the joints are based on the Hillberry joint and the tendon are elastic.
In Fig.1,g the Multifunctional Hand Prosthesis is reported [10]. Fluid operated actuator are used, fed by a pump fitted in the metacarpal together with micro-valves controlled by a micro-controller.

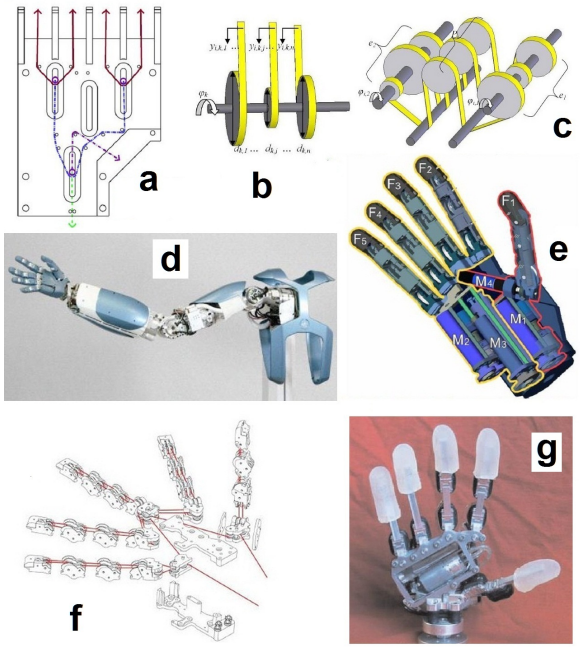

Figure 1 Examples of mechanical hands.

In Fig.2,a and b are reported the “Larm hand” and the kinematic scheme of one finger of a grasping device developed at the University of Cassino (Italy) [11,12,13,14], that essentially consists in a four finger underactuated hand.
In Fig.2,c is reported the Southampton Remedi Hand [15]; it has 6 d.o.f. with 6 small motors; 4 of them move the fingers and 2 move the thumb.
The above mentioned ones are perhaps among the most representative examples of mechanical hands. As for the underactuated designs, it must be sayd that they essentially belong to 2 types schematically shown in Fig.2,d. The soft synergy is essentially based on the presence of elastic tendons while the adaptive synergies is essentially based on differential mechanism. During the grasping, both the systems permit the fingers to adapt themselves to objects having a complicated shape (i.e. different sections in correspondence of each of the fingers), but the adaptive synergies with “rigid” tendons, permit, also, to grip the object exerting practically the same gripping force.
As for the tendon operated fingers, different solutions can be adopted as it was reported in [16]; essentially possible solutions range from a tendon for each of the phalanxes to a single tendon for the three phalanxes; the joints between the latter can be represented by simple hinges or more complex kinematic systems or even by simple elastic links.

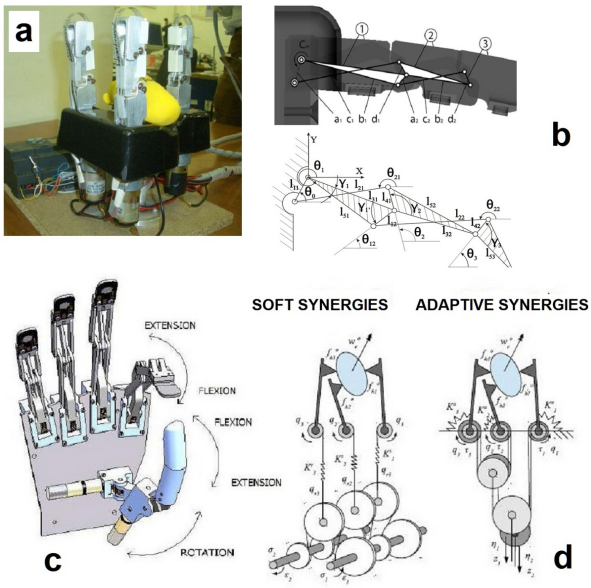

Figure 2 Examples of mechanical hands.

From the above reported, it seems interesting to study the possibility of designing a rather simple and cheap hand, based on adaptive synergies underactuated by means of a single actuator.

2 DESCRIPTION OF THE HAND

2.1 THE FINGER

Most of the choices adopted during the design phase of the device were based on the predictions of a hand model derived from the under-actuated finger mechanism presented in [18]. This mechanism is also shown in figure 3.

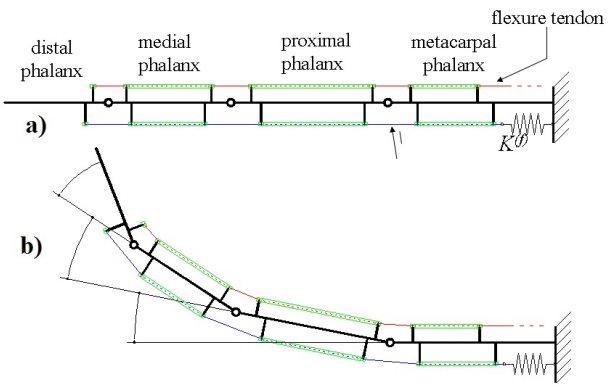

Figure 3 Scheme of the underactuated finger

It is a plane system having only three degrees of freedom, since it is composed of four rigid links connected together by three hinges free of friction. Of these four links, one is fixed and is indicated with the term metacarpal, the remaining three are movable and function as proximal, medial and distal phalanxes, respectively.

The finger is equipped with a flexural and an extensor tendon, both having an end fixed to the distal phalanx. The other end of the flexural tendon is mechanically linked to the differential mechanism, which transfers the hand actuator load (see sect. 2.2). The extensor tendon is instead elastically constrained to the metacarpus by a helical spring. All the phalanxes, furthermore, are provided with a couple of cylindrical guides along which the tendons can freely slide when the finger deforms. We assume that both the tendons are inextensible, free of thickness and have zero bending stiffness.

In the following, each finger of the hand device will be identified by a natural number *f*, with *f=1, 2, …, 5* and where *1* stands for the Thumb, *2* for the Index finger, …, *5* for the little finger, and a quantity pertaining to the finger *f* will be labeled by the superscript *f*.

As lagrangian coordinates of a finger we choose the absolute rotation $\varphi_1^{(f)}$ of its proximal phalanx, the relative rotation $\varphi_2^{(f)}$ between the proximal and the medial phalanx and, finally, the relative rotation $\varphi_3^{(f)}$ between the medial and the distal phalanx (fig. 3,b)).

Hence, denoting with $\boldsymbol{\varphi}^{(f)} = \left[\varphi_1^{(f)}, \varphi_2^{(f)}, \varphi_3^{(f)}\right]$ the column vector of the coordinates of the finger *f*, a hand configuration is univocally defined by the components of the column vector

$$\boldsymbol{\varphi} = \begin{bmatrix} \boldsymbol{\varphi}^{(1)} \\ \boldsymbol{\varphi}^{(2)} \\ \cdots \\ \boldsymbol{\varphi}^{(5)} \end{bmatrix}.$$

In the present study the initial or reference configuration of the hand is the one with all the fingers totally extended (see fig. 3,a)), that is with all the rotations $\varphi_i^{(f)} = 0$.

For sake of simplicity, the hinges of a finger are numbered consistently with the adopted notation for the lagrangian coordinates: $i^{(f)}$ will denote the hinge where the rotation $\varphi_i^{(f)}$ occurs. Moreover, a movable phalanx is also identified by the same number of the hinge that is on its right side in the reference configuration.

In fig. 4,b) an enlarged view of the deformed configurations assumed by the extensor and flexure tendons close to the hinge $i^{(f)}$ is sketched.

Denoting respectively with $d_i^{(f)}$ and $s_i^{(f)}$ the fixed distances from the hinge centre of the points P_i and Q_i and with $\overline{d}_i^{(f)}$ and $\overline{s}_i^{(f)}$ those respectively of the points R_i and S_i, by the Carnot theorem, the following expressions for the lengths $\overline{P_iQ_i} = z_i^{(f)}$ and $\overline{R_iS_i} = l_i^{(f)}$ are obtained:

$$z_i^{(f)} = \sqrt{d_i^{(f)2} + s_i^{(f)2} - 2 \cdot d_i^{(f)} s_i^{(f)} \cos\left(\Phi_i^{(f)} - \varphi_i^{(f)}\right)}$$

$$l_i^{(f)} = \sqrt{\overline{d}_i^{(f)2} + \overline{s}_i^{(f)2} - 2 \cdot \overline{d}_i^{(f)} \overline{s}_i^{(f)} \cos\left(\overline{\Phi}_i^{(f)} + \varphi_i^{(f)}\right)},$$

where $\Phi_i^{(f)}$ and $\overline{\Phi}_i^{(f)}$ are the angles defined in fig. 4,a).

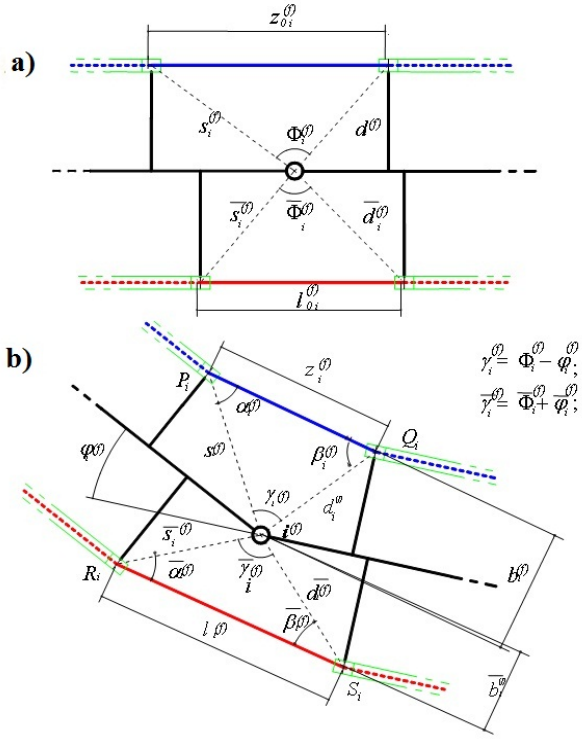

Figure 4 Inital (a) and deformed (b) configurations of the flexure and extensor tendons.

When the finger *f*, starting from the reference configuration, reaches the configuration $\boldsymbol{\varphi}^{(f)}$, the flexure tendon free paths $\overline{P_iQ_i}$ experience the shortenings

$$\Delta z_i^{(f)} = z_{0i}^{(f)} - z_i^{(f)},$$

with *i=1,…,3* and $z_{0i}^{(f)}$ initial value of $z_i^{(f)}$ (fig. 4,a)). Therefore, the end of the flexure tendon that is connected to the differential mechanism performs the displacement

$$u^{(f)} = \sum_{i=1}^{3} \Delta z_i^{(f)}.$$

Similarly, the free paths $\overline{R_iS_i}$ of the extensor tendon experience the length changes

$$\Delta l_i^{(f)} = l_i^{(f)} - l_{0i}^{(f)},$$

with $l_{0i}^{(f)}$ initial value of $l_i^{(f)}$. Therefore, the corresponding elongation of the spring connected to this tendon is:

$$\Delta l^{(f)} = \sum_{i=1}^{3} \Delta l_i^{(f)}.$$

In Fig 5 a simulation of the finger made by means of the multi -body code WM 2D™ is shown. In the figure the

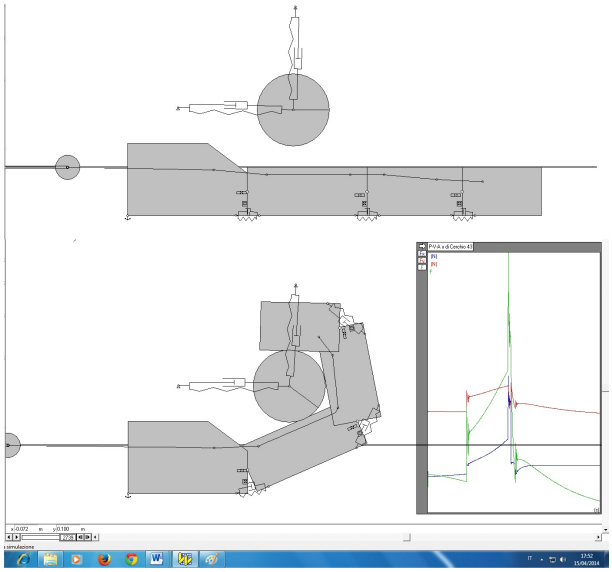

Figure 5 WM 2D™ model and simulations

grasping of an object is simulated; the object consists in a circle hold by two orthogonal elastic constraints. This simulates the self-adaptability of the underactuated finger to an object that moves or changes its shape during the grasping. From Fig.5 it is possible to observe that each of the three phalanxes correctly adapts its rotation to the object shape and to the object position respect to the finger itself. Moreover, in the same figure, the force in each of the elastic constraint (computed by the multi-body code) is also plotted; in this way the resultant of the grasping force can be also computed.

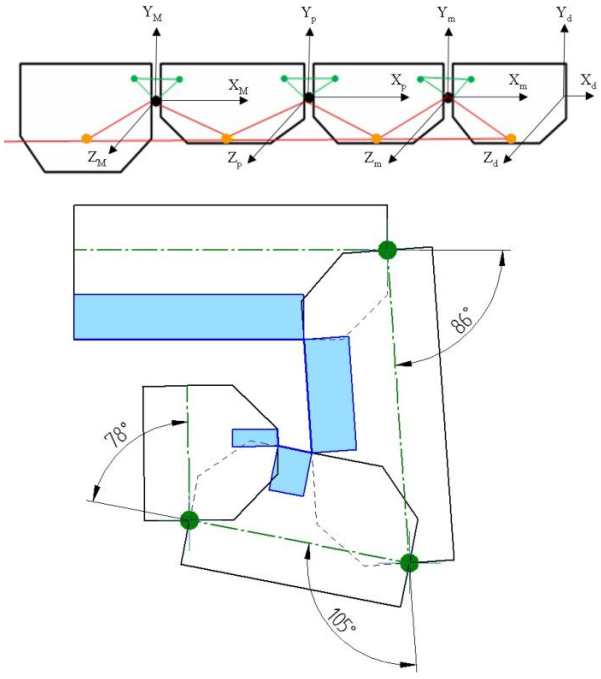

Figure 6 D-H representation and optimum computed domain of the tendon's guides.

Investigations were carried on in order to determine both the kinematic and the dynamic behavior of the underactuated finger [17, 18, 19, 20].
In particular, in fig. 6 the "Denavit and Hartemberg" representation of the finger model is represented together with the computed domain along the x and y axes of the tendon's guides.

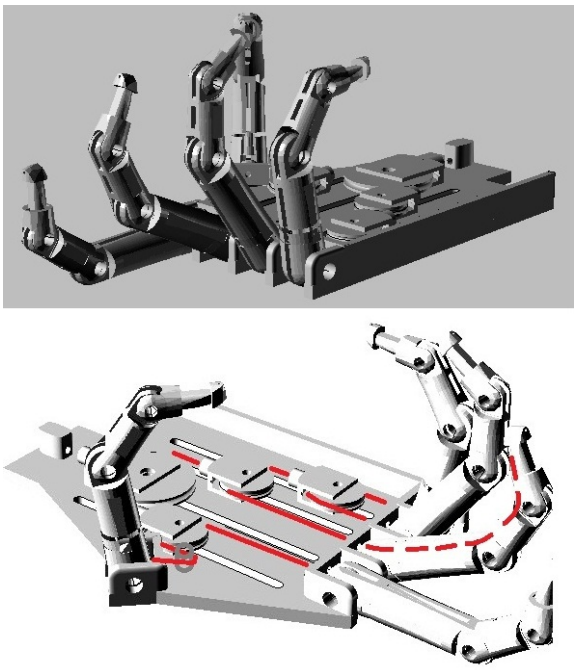

Figure 7 CAD design of the proposed device

2.1 THE HAND
In Fig. 7 CAD drawings of the first prototype of the hand are shown.
The hand was designed by using simple elements that guarantee the cheapness and simplicity of operation. In particular, the hand is composed by five fingers, each made of three phalanxes hinged to each other by pins, which represent the different articulations of a human finger. The finger is closed by means of an inelastic tie-rod as shown in Fig. 7.In the lower part of the figure one of the tendons inside the finger is represented with a dotted line; the tendons mechanism are also shown. Hence the working principle of the hand mechanism is evident.
In fig. 8 the scheme of the pulley system that permits the self-adapting of the fingers to the object shape during the grasping is shown together with the distribution of the force between the fingers of the hand. The repartition of the actuating force F allows to reach a configuration in which for each finger the force is:

F/4 on thumb;
F/4 on index;
F/4 on middle finger;
F/8 on ring finger;
F/8 on little finger.

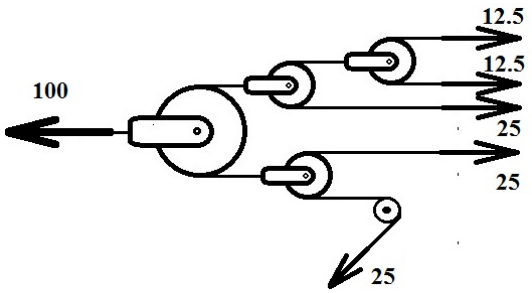

Figure 8 Pulleys system

The tendons, made of inelastic tie rod, passing through distribution pulleys system, distributes the gripping tension between the fingers. Thus permitting the fingers to adjust themselves to the grasped object size and shape.
The rotation of the pulleys, in fact, will occur at any contact of each phalanx with the gripped object. Once each phalanx enters into contact with the gripping object, the finger is aligned in such a way to tighten the object and ensure its grip. Thanks to the larger pulleys installed on the palm of the hand, the force is distributed also to the other fingers; the set will move up until each phalanx is in contact with the object to be taken, achieving the gripping.

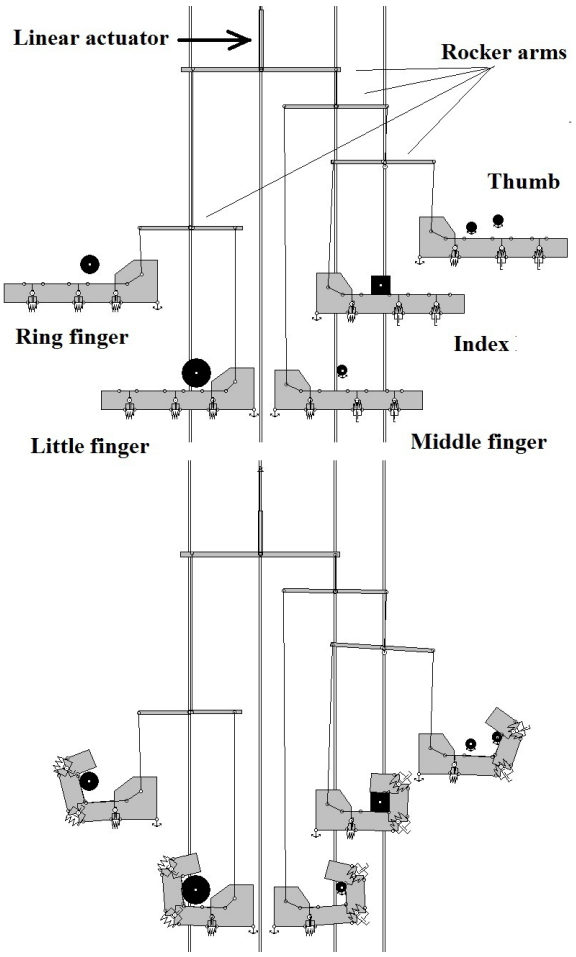

Figure 9 WM 2D™ model and simulations

The design of the hand was first studied by means of the multi-body code WM 2D™ again. In Fig. 9 the five finger model is shown. The model is essentially made by five fingers; each of them is almost equal to the one shown in Fig.3. The tendons are linked to the common linear actuator by means of rocker arm; each of the latter represents one of the pulleys of the pulley system. Since the rocker arms rotations are very little, the tendons kinematics does not differ significantly from the one of the pulley system.
In the upper part of Fig. 8 the hand is represented open, while in the lower part an object is grasped. The latter is represented in the simulation by means of the black fixed bodies; these represent the sections of the object in correspondence of each of the fingers. How it is possible to observe, in the shown simulation, the object section are very different in shape and position respect to the finger.
In the lower part of Fig. 9 the grasping is shown. How it can be observed, each of the fingers adapts its phalanxes rotation to the shape of the section the object presents to each of the fingers. This behavior is permitted because once a finger stops having touched the object, the rotation of a pulley (or of the rocker arm in the simulation) does not increase the tendon push but permits to the other tendons to move until the contact is reached by the other fingers. In other words, the pulley system permits that each of the non-extendible tendons is pulled always with the same amount of the actuator's force but its displacement is self-adapted to the phalanxes rotation required to grasp that section of the object.How it is possible to observe, despite the dynamical effects during the transient, the repartition of the forces is the one we had expected.
In fig. 10 an example of the simulation results is reported; the stress in the tendons during the grasping shown in fig.9. From the upper part of the figure the curves represent the thumb, the index, the middle and the ring finger, respectively. The curves have all the same magnification and are equally spaced along the vertical.

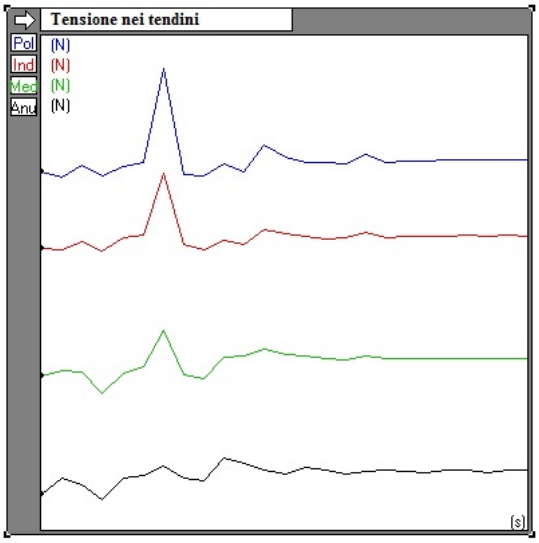

Figure 10 Example of the simulation results

2.1.1 Analisys of the grasping

We have analysed the hand behaviour during the grasping of an object fixed in the space. The analysis was conducted under the simplifying assumption that each finger initially touches the object with the proximal phalanx, then with the medial and finally with the distal one. Therefore, being the object fixed, when the phalanx $i^{(f)}$ is in contact with the object, only changes of the finger coordinates $\varphi_j^{(f)}$, with $j > i$, can occur (fig. 11).

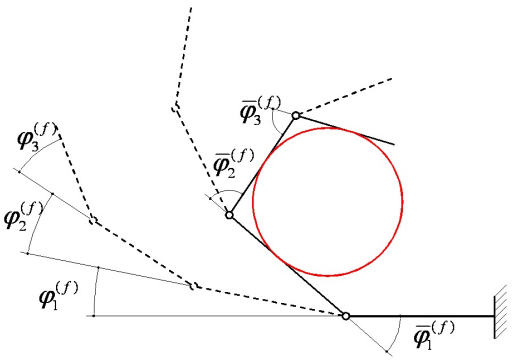

Figure 11 Deformed configurations of a finger during the grasping operation of an object.

If the hand actuator operates under displacement control during the grasping of the object, the hand equilibrium configurations $\boldsymbol{\varphi}$ have to satisfy both the stationary condition of the elastic strain energy E,

$$dE = d\left(\frac{1}{2}\sum_{f=1}^{5} K^{(f)}\Delta l^{(f)2}\right) =$$

$$= \sum_{f=1}^{5}\sum_{i=1}^{3} K^{(f)}\Delta l^{(f)} \cdot \frac{\partial \Delta l^{(f)}}{\partial \varphi_i^{(f)}} \cdot d\varphi_i^{(f)} = 0 \qquad \forall d\varphi_i^{(f)},$$

where $K^{(f)}$ is the stiffness of the spring connected to the extensor tendon of the finger f, the following constraint equation:

$$g(\boldsymbol{\varphi}) = u(\boldsymbol{\varphi}) - \bar{u} = 0$$

with $\bar{u}$ prescribed value for the displacement $u(\boldsymbol{\varphi})$ of the hand actuator, and the following contact conditions for the phalanxes touching the object:

$$\varphi_i^{(f)} - \bar{\varphi}_i^{(f)} = 0,$$

being $\bar{\varphi}_i^{(f)}$ the contact value of the coordinate $\varphi_i^{(f)}$, fig. 11.

According to the Lagrange multipliers method, the hand equilibrium problem is equivalent to searching for the stationary condition of the function:

$$\bar{E}_c = E(\boldsymbol{\varphi}) - \lambda \cdot g(\boldsymbol{\varphi}) - \sum_{(i,f)\in C} \mu_i^{(f)} \cdot \left(\varphi_i^{(f)} - \bar{\varphi}_i^{(f)}\right),$$

where the summation is extended to the set C of couples of index (i, f) identifying d.o.f.'s that are contact constrained. λ and $\mu_i^{(f)}$ are unknown Lagrange multipliers having respectively the meaning of load applied by the hand actuator to the differential mechanism and reaction moment with respect to the hinge i_f of the actions exerted by the object on the phalanxes j_f, with $j \geq i$.

The hand equilibrium equations, that are obtained by equating to zero the partial derivatives of the function $\bar{E}_c$, are non linear and have been solved numerically by the Newton-Raphson method following a small step incremental approach.

Some model predictions of the hand behaviour during both the free flexion of the fingers and the grasping of an object are synthetically presented in this section. The adopted values of the contact angles $\bar{\varphi}_i^{(f)}$ are listed in table I.

Table I - Contact angles $\bar{\varphi}_i^{(f)}$ (in degrees)

Finger	f	$\bar{\varphi}_1^{(f)}$	$\bar{\varphi}_2^{(f)}$	$\bar{\varphi}_3^{(f)}$
thumb	1	40°	68°	78°
index	2	35°	65°	70°
middle fin.	3	42°	70°	90°
ring finger	4	55°	81°	90°
little finger	5	70°	80°	90°

The numerical simulations have been carried out with an increment Δu of the actuator displacement u equal to 0.0125 mm. This value has been determined by trial and error and has proven be suitable to generate very small contact penetrations in each calculation step and to allow the Newton-Raphson algorithm to converge with very few iterations. Furthermore, checks for contact detection were carried out both at the beginning and at the end of each calculation step in order to detect changes of the contact conditions that may cause large penetrations in the subsequent step.

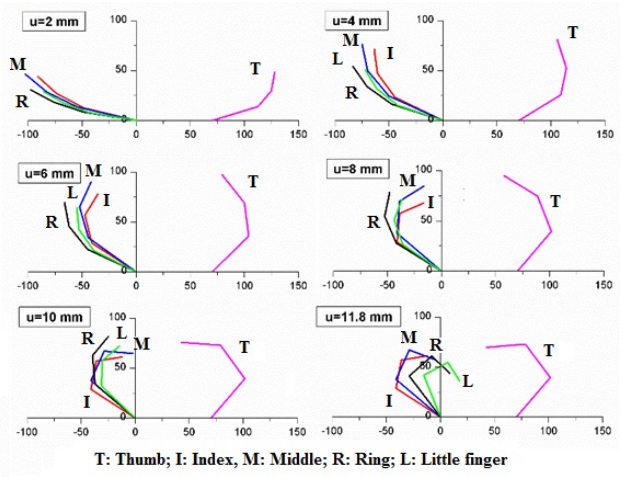

Figure 12 Deformed configurations of the fingers during the grasping of an object.

In fig. 12 and fig. 13,a) are respectively shown the deformed configurations of the fingers for several values of the actuator displacement u and the diagram of the flexural tendons ends displacements $u_i^{(f)}$ as function of the actuator force λ. Inspection of these figures indicates that the geometry adopted for the fingers joints is such that, during the grasping operation, the relative rotations between phalanxes are always of the same sign, that is S-shaped configurations of the fingers does not occur. Furthermore, the displacements $u^{(f)}$ of each finger are continuous and increasing functions of the actuator force, since in the hand equilibrium paths are absent both snapping and buckling phenomena.

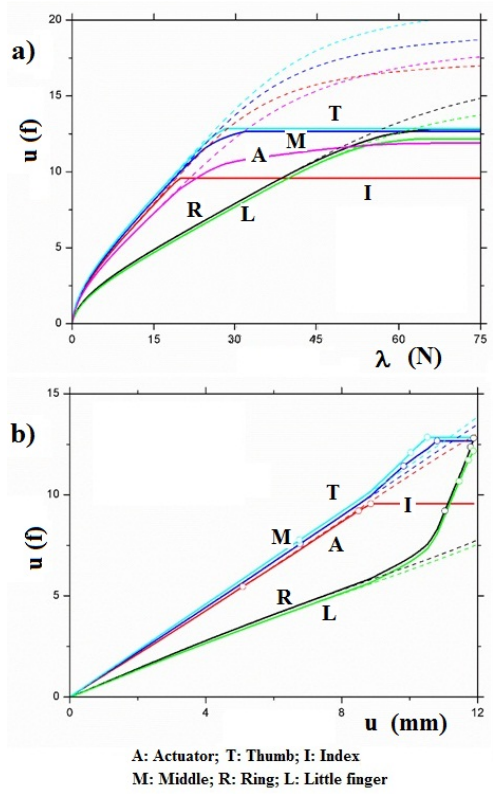

Figure 13 Diagram of the displacements $u^{(f)}$ of the flexural tendons ends as function of the actuator load λ, a), and of the actuator displacement u, b) (dash lines, free flexion of the fingers; solid lines, grasping action).

In the diagram of fig. 13,b) the displacements $u^{(f)}$ are plotted versus the actuator displacement u. Finger-object contact events are also marked by dot symbols along each curve.
By comparison with curves of fig. 13,a) and observing that the tractions in flexural tendons are proportional to the actuator force, the effects of the pulleys system of the differential mechanism are easily noted: the fingers stiffness changes due to contact events are totally compensated by the rotations of the pulley, without jumps in the tendon traction values. Thus, during the grasping operation, the values of the displacement increments imposed to the flexure tendons are continuously self-adapted to the actual finger contact conditions.

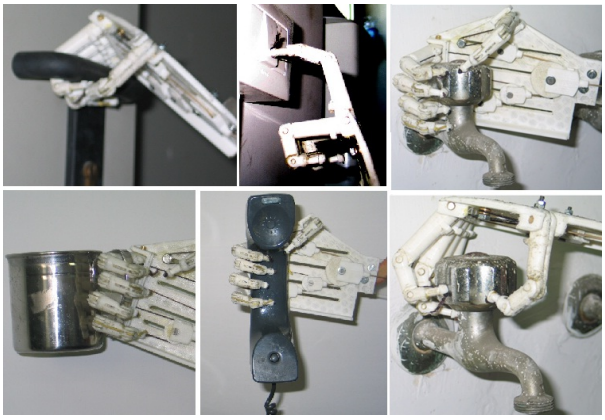

Figure 14 Examples of grasping of the first prototype

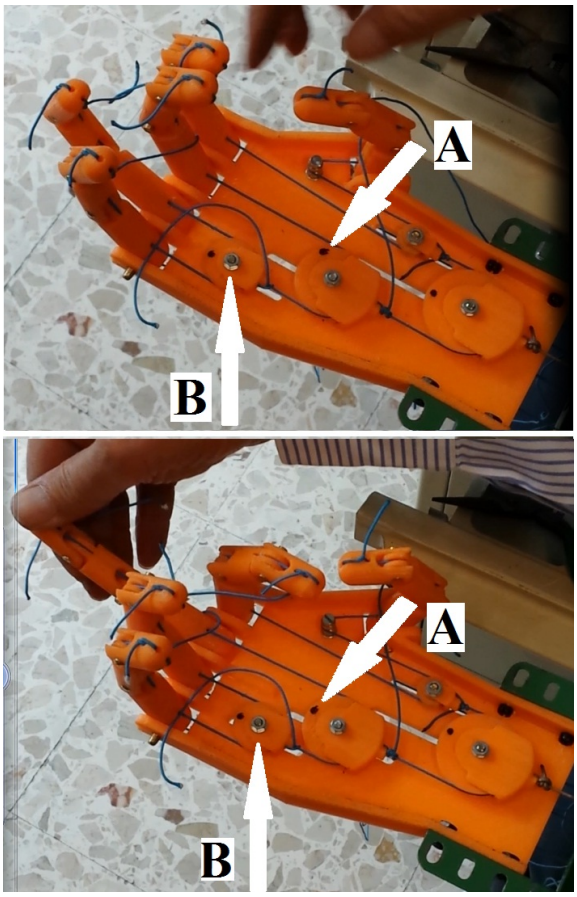

Figure 15 The second prototype.

3 THE PROTOTYPE

Two prototypes were built. In the first one the extension tendons were represented by simple rubber elastic bands.
In Fig. 14 examples of grasping of the first prototype are reported.

The second prototype was fitted with unextendible tendons, each connecter to a spring. In the figures 15 and 16 pictures of the second prototype are shown.
In Fig. 15 is shown how the three phalanxes of each of the fingers adapt their rotation: in both the figure the actuator was in the same position while the human hand forces a finger to move. By comparing the two images, it can be observed that when the middle finger is stretched, all the other fingers move; in particular, in this case, this movement is mainly permitted by the rotation of the pulley indicated by the arrow A (see the little mark on the pulley) and the translation of the pulley indicated by the arrow B.
In figure 16 the grasping of a rather complex object is shown. The object used for the reported grasping test is made by three different cylinders having rather different diamenters.
In the upper part of Fig. 16 the hand with the fingers completely released is shown while in the lower part the fingers are completely clamped on the object. How it is possible to observe, all the phalanxes automatically rotate in order to fall onto contact with the object surface, ensuring a satisfactory and stable grasping.
Both the prototypes wwere almost completely made by a 3D printer in polyactide (PLA), a thermoplastic aliphatic polyester, starting from the CAD drawings

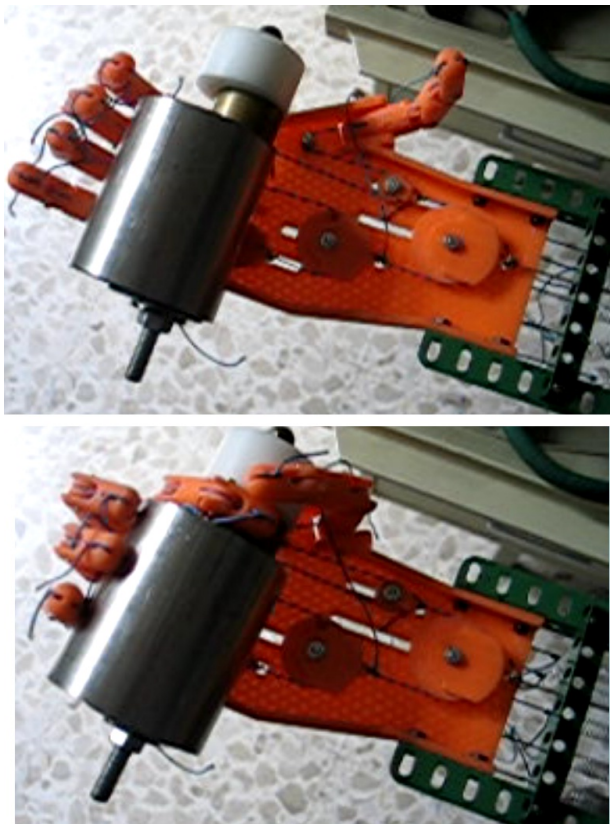

Figure 16 Grasping

4 CONCLUSIONS

Studies on kinematics and dynamics of an underactuated mechanical hand (presented in previous papers) permitted to design and built a first prototype that was the mail goal of this contribution; it has shown very encouraging results.
In conclusion the pulley system satisfactory works and shows a satisfactory auto-adaptability of the so actuated fingers, hence permitting to replicate several functions of a human hand.

REFERENCES

[1] Gosselin C., Pelletier F., Laliberte T. (2008) An Anthropomorphic Underactuated Robotic Hand with 15 Dofs and a Single Actuator. 2008 IEEE Int. Conf. on Robotics and Automation Pasadena, CA, USA, May 19-23, 2008.

[2] Brown C.Y., Asada H.H. (2007) Inter-Finger Coordination and Postural Synergies in Robot Hands via Mechanical Implementation of Principal Components Analysis. 2007 IEEE/RSJ Int. Conf. on Intelligent Robots and Systems San Diego, CA, USA, Oct 29 - Nov 2, 2007.

[3] Grebenstein M., Chalon M., Hirzinger G., and Siegwart R. (2010) Antagonistically Driven Finger Design for the Anthropomorphic DLR Hand Arm System. IEEE-RAS International Conference on Humanoid Robots Nashville, TN, USA, December 6-8, 2010.

[4] Controzzi M., Cipriani C. and Carrozza M.C. (2008) Mechatronic Design of aTransradial Cybernetic Hand. IROS February 22, 2008.

[5] Cipriani C., Controzzi M., Carrozza M. C., (2011) The Smart Hand Transradial Prosthesis, Journal Of Neuro-engineering And Rehabilitation, 2011, n. 8.

[6] Roccella S., Carrozza M.C., Cappiello G., Dario P., Cabibihan J.J., Zecca M., Miwa H., Itoh K., Matsumoto M., Takanishi A., Design, fabrication and preliminary results of a Novel anthropomorphic hand for humanoid robotics: RCH- 1, Proceedings of 2004 IEEE/RSJ International Conference on Intelligent Robots and Systems, Sendai, Japan, September 28 - October 2, 2004.

[7] S. Roccella, M.C. Carrozza, G. Cappiello, J.J. Cabibihan, C. Laschi, P. Dario, H. Takanobu, M. Matsumoto, H. Miwa, K. Itoh, A. Takanishi, Design and Development of Five-Fingered Hands for a Humanoid Emotion Expression Robot, International Journal Of Humanoid Robotics, 2007, n. 4, pp. 181-206.

[8] S. Roccella, E. Cattin, N. Vitiello, F. Giovacchini, A. Chiri, F. Vecchi, M.C. Carrozza, Design of a hand exoskeleton (handexos) for the rehabilitation of the hand, Gerontechnology; N. 7(2), 2008, pp. 197-197.

[9] M.G.Catalano, G.Grioli, A.Serio, E.Farnioli, C.Piazza, A.Bicchi (2012) Adaptive Synergies for a Humanoid Robot Hand. Proc. of IEEE-RAS

International Conference on Humanoid Robots Osaka, Japan, Nov. 29th - Dec. 1st, 2012.

[10] C.Pylatiuk, S.Mounier, A.Kargov, S.Schulz, G.Bretthauer (2004) Progress in the Development of a Multifunctional Hand Prosthesis. Proc. of the 26th Annual International Conf. of the IEEE EMBS San Francisco, CA, USA, September 1-5, 2004.

[11] Carbone G. and Ceccarelli M. (2008) 'Experimental Tests on Feasible Operation of a Finger Mechanism in the LARM Hand ', Mechanics Based Design of Structures and Machines, 36:1, pp. 1 – 13, doi: 10.1080/15397730701729445

[12] Wu Li Cheng, Carbone G., and Ceccarelli M. (2009) 'Designing an underactuated mechanism for a 1 active DOF finger operation' Mechanism and Machine Theory 44, 2009, pp. 336–348.

[13] Carbone G., Ceccarelli M. (2008) 'Design of LARM Hand: Problems and Solutions' Journal of Control Engineering and Applied Informatics, Vol.10, n.2, pp. 39-46.

[14] Yao S., Ceccarelli M., Carbone G., Zhan Q. and Lu Z. (2011) 'Analysis and optimal design of an underactuated finger mechanism for LARM hand' Front. Mech. Eng. 2011, 6(3), pp. 332–343, doi: 10.1007/s11465-011-0229-8

[15] D.P.J. Cotton, A. Cranny, P.H. Chappell, N.M. White, S.P. Beeby, Control Strategies For A Multiple Degree Of Freedom Prosthetic Hand. Electronic Systems Design Group, School of Electronics and Computer Science, University of Southampton, 2006.

[16] F. Lotti, G. Vassura (2012) Sviluppo Di Soluzioni Innovative Per La Struttura Meccanica Di Dita Articolate Per Mani Robotiche. Associazione Italiana per l'Analisi delle Sollecitazioni (AIAS) XXXI Convegno Nazionale, 18-21 September 2002, Parma.

[17] Fiore P., Niola V., Pisani G., Rossi C., Savino S., Troncone S., "A model of a robotic hand based on a tendon driven mechanism", Proc. of 22th Internation Workshop on Robotics in Alpe-Adria-Danube Region, Portorož, Slovenia, September 11-13, 2013.

[18] Rossi C., Savino S., "Mechanical Model of a Single Tendon Finger", Proc. of ICNAAM 2013: 11th International Conference of Numerical Analysis and Applied Mathematics, Rhodes, Greece, Sep 21-27, 2013.

[19] Rossi C., Savino S, "An underactuated multi-finger grasping device", International Journal of Advanced Robotic Systems, Vol. 11(1), 17 February 2014, Article number 20.

[20] Rossi C., Savino S., Niola V., Troncone S., "A Study of a Robotic Hand with Tendon Driven Fingers", Robotica. ISSN: 0263-5747, doi: 10.1017/S02635 74714001179.

[21] F. Penta, C. Rossi, S. Savino, An Underactuated Finger for a Robotic Hand, International Journal of Mechanics and Control, Vol. 15(2), 2014, ISSN: 1590-8844.

ISSN 1590-8844
International Journal of Mechanics and Control, Vol. 16, No. 01, 2015

SIMULATION AND CONSTRUCTION OF A MEMS CSFH BASED MICROGRIPPER

Nicola P. Belfiore* Giovanni B. Broggiato* Matteo Verotti* Marco Balucani** Rocco Crescenzi**
Alvise Bagolini*** Pierluigi Bellutti*** Maurizio Boscardin***

* Department of Mechanical and Aerospace Engineering, Sapienza University of Rome, Italy

** Department of Information Engineering, Electronic and Telecommunications, Sapienza University of Rome, Italy

*** Fondazione Bruno Kessler (FBK), Micro Nano Facility (MNF), Italy

ABSTRACT

This paper describes the design, simulation, construction process and experimental analysis of a microgripper, which makes use of a new concept hinge, called CSFH (Conjugate Surfaces Flexure Hinge). The new hinge combines a curved cantilever beam, as flexible element, and a pair of conjugate surfaces, whose contacts depend on load conditions. CSFHs improve accuracy and guarantee that minimum stress conditions hold within the flexible beam. This microgripper is designed for Deep Reactive-Ion Etching (DRIE) construction process and comb-drive actuation. Theoretical basis and Finite Element Analysis (FEA) simulations have been employed in order to predict the feasibility of the device under construction. Finally, some experimental evidence of the construction process has been provided.

Keywords: Microgripper, MEMS, Conjugate surfaces flexure hinge, DRIE

1 INTRODUCTION

Micro-grippers have been increasingly employed in many applications during the last decades thanks to the continuous improvements in MEMS-based Technologies.
In 1995, a piezoelectric milligripper [1] for in vivo tissue manipulation has been optimized in order to obtain a maximum gripping force. In the same paper, a cochlear electrode implant has been suggested, also, in order to stimulate the auditory nerve and, so, restore hearing to the profoundly deaf. Then, a micro needle has been proposed for skin painlessly puncturing and drugs delivery. Finally, a microbiological assay device has been presented to quantify yeast cells metabolic growth rate. In the same year, multicomponent force-displacement sensing techniques, which are particularly useful at the micro scale, have been discussed [2].

Contact author: Nicola P. Belfiore[1]

[1] Dept. Mechanical and Aerospace Engineering, Sapienza University of Rome. Via Eudossiana 18, 00184 Rome, Italy.
E-mail: belfiore@dima.uniroma1.it

In 2001, specially designed micro-grippers [3] with force-feedback have been presented for the handling of pieces with sizes from 10 μm up to 2 mm. The mechanisms have been built by using wire electro-discharge-machining of spring steel. In 2002, SU-8 photoepoxy [4] has been adopted in order to build micro valves and micro-grippers with good aspect ratio, equipped with beams and hinges with in-plane compliance. In the same work, the elastic properties of the material has been measured by employing a tactile force sensor.
In 2004, a transparent electrostatic gripper [5] has been used to build a miniature assembly cell for MEMS assembly and packaging. Thanks to the gripping force and stage positioning accuracy, insertion operation of 500 μm wide parts in 550 μm wide slots etched in silicon wafers were possible. In 2006, a multi-objective optimization [6] has been suggested in order to improve the design of micro-grippers by taking into account performance metrics and design constraints. Lumped spring and pseudo-rigid-body model approximations have been used in the optimization process. In 2007, out-of-plane piezoelectric micro-grippers have been presented [7]. Thanks to the electromechanical and gripping characteristics and to micro cantilevers

actuation, these gripper accurately handled 100 μm diameter metallic ball without any adhesion problems between two jaws of gripper and the ball. In 2008, a precision manipulator and a micro gripper have been presented for micro assembling [8]. The PRR 3 DoF manipulator, which has been actuated by modular revolute and prismatic actuators, was equipped with a micro-gripper MEMS-Technology based end-effector, whose jaws displacement was up to about 143 μm. A real gripping test has been also conducted to evaluate the robotic system. In the same year, a MEMS based piezoresistive sensor has been designed, for micro-force measurement and a resolution within the micronewton range could be achieved, by means of surface and bulk micromachining technology on single crystal silicon wafer [9]. Boron diffusion process, combined with Deep Reactive Ionic Etching (DRIE), has been used to form side direction force sensors. In 2009, a four arms structure MEMS gripper integrated sidewall piezoresistive force sensor has been designed [10,11]. Vertical sidewall surface piezoresistor etching technique has been used to form the side direction force sensors. An electrostatically driven microactuator has been also designed to provide the force to operate the other two movable arms. In the same year, a versatile MEMS gripper has been designed and fabricated, with the MetalMUMPs process, for two-dimensional manipulation [12]. This has been accomplished by a multiple DoF electrothermal actuator which can achieve independent in-plane and out-of-plane motions. A novel electro-thermal 100 μm device layer micro-gripper has been presented also in Ref. [13], where 1-D steady state heat equations have been used in order to model the thermal behaviour of a general 5 lineshape microbeam's actuator. Another MEMS micro-gripper [14] has been integrated with a plunging mechanism in order to impact the micro object and gain sufficient momentum to overcome adhesion forces. This device was able to achieve 100 % successful release rate on 200 trials, with an accuracy of 0.70±0.46 μm in the the manipulation of 7.5 − 10.9 μm borosilicate glass spheres under an optical microscope. In 2010, a three DoF meso/micromanipulation system has been developed and tested for handling microobjects [15], for example, biological cells and microbeads.

In the same year, Havlik suggested a method for minimizing compliance errors and a calibration procedure for multi DoF positioning or multi-component sensing devices based on compliant mechanisms [16]. Furthermore, some design problems of compliant mechanisms for particular devices were discussed and an optimization procedure was applied for designing compliant joints [17]. In 2011, an electrothermally driven MEMS gripper has been designed, fabricated and characterized [18, 19]. The system uses a new metallic V-shape actuator and a set of modified Guckel U-shape actuators. In 2012, a new MEMS-Technology based micro-gripper has been developed to serve as micromanipulation robotic system [20]. The *pseudo-rigid body mechanism* has been used to model the manipulator and to estimate the grip force. Results have been verified by simulations and experiments. In the same year, a novel monolithic nano-micro-gripper structure has been simulated (motion and control) for biologic cells manipulation [21]. In 2013, an electrostatic comb-drives actuated MEMS micro-gripper, with an integrated electrothermal force sensors, has been presented for biomedical and micro industrial applications [22, 23]. This structure has been fabricated in a Silicon On Insulator (SOI) MEMS foundry (MEMSCAP).

In 2014, an electrothermal actuator with two DoF and independent in-plane and out-of-plane motions has been presented [24]. The structure has been fabricated with the Metal MUMPs, which offers silicon nitride, polysilicon, and nickel as the major structural materials. Thanks to this method, new micro-grippers with 2-D manipulation can be constructed with two actuators, each of which serves as the gripper arm. Another micro-gripper with two grade displacement amplification has been designed, simulated and fabricated, based on flexible hinges, and actuated by piezoelectric ceramics [25].

The Authors of the present investigation have been also involved in the development of grippers and micro-grippers and MEMS-Technology based devices.

In 1997, an atlas of 64 linkage-type grippers has been presented [26]. For each mechanism, the graph representation and one of the possible functional schematic have been provided. The adopted enumeration methodology has been based on Graph Theory and an extension of the concept of isomorphism to the class of actuated mechanisms has been recalled. In 2000, some issues related to some peculiar characteristics of plane kinematic chains have been introduced [27, 28], while some years later some problems related to the tribological behaviour of mechanical components have been analyzed [29–31]. In 2010, the development of a 3 DoF plane micro platform with remote system of actuation has been presented [32]. MEMS Technology has been used to develop this system which has been built and simulated through FEA. The whole device overall size was less than 4mm. In 2011, a new multibody system code, based on Lagrange Multiplier method of dynamic analysis, has been applied to the *pseudo-rigid body model* of a micro-compliant mechanisms for studying the static and dynamic analysis [33]. In 2012, the performance of compliant parallel micromanipulators [34] has been evaluated in terms of the *MA*, mechanical advantage, and *k(J)*, kinematic condition number (see also Refs. [35–37] for index characterization). This evaluation has been done on the pseudo-rigid body equivalent mechanism, by means of a new and fast method for direct kinematic analysis of parallel manipulators. In 2013, a plane parallel micromanipulator has been presented for general purposes in-plane micropositioning and a numerical procedure has been used in order to optimize some kinetostatic performance indices [38]. The approach has been based on a refined simplification of the direct kinematic problem and

it is applied to the pseudo-rigid body equivalent model of the original compliant mechanism. Genetic Algorithms have been used for the global optimization of these parameters.

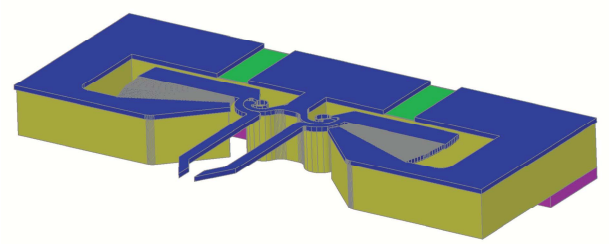

Figure 1 Pictorial view of the gripper as it was mounted on the chip.

Finally, an early version of a MEMS-Technology based micro-gripper, which is based on a new flexural hinge, has been designed for cell manipulation after FEA-assisted simulations and improvements [39].
At the beginning of 2014, a new method of functional synthesis of a new class of MEMS has been disclosed [40]. The design approach is based on CSFHs and on the accurate detection of the pseudo-rigid-body equivalent mechanism, which allows the application of several classic algorithms well known in kinematic synthesis (see for example Ref. [41, 42]). In the same year, the Authors made an attempt to offer a contribution to the experimental analysis of tribological issues in MEMS [43] and, so, a new concept design of a microtribometer for testing silicon-silicon sliding in-MEMS devices has been presented. A dedicated MEMS has been designed, whose only purpose is recreating silicon-silicon sliding under prescribed loads and, then, assessing friction and wear.
In the present paper, a new comb-driven actuated silicon micro-gripper, depicted in Fig. 1, will be presented and in the following paragraphs its design, physical construction, and experimental analysis will be discussed.

2 GRIPPER DESIGN AND SIMULATION

The adopted design method is based mainly on the choice of embedding so-called CSFHs, Conjugate Surfaces Flexure Hinges [44], within the gripper layout. The main advantage of adopting this kind of hinges consists in the possibility of being manufactured by means of planar technology processes. Although the CSFH hinge can be built at any scale, the new component is believed to give its best at the microscale, where most of MEMS-Technology based processes perform successfully on silicon wafers. The CSFH is composed of two main parts: *a)* a flexible curved beam and *b)* a portion of revolute joint conjugate surfaces. Fig. 2 shows one of the possible configurations for a CSFH. The two bodies A and B are joined by means of a thin curved beam, which, on the action of external torques and forces, deflects much more than the pseudo-rigid bodies A and B, whose thickness makes their deformation negligible with respect to the curved beam deflection On the other hand, bodies A and B make up a kinematic pair with circular conjugate profiles, as the Figure displays, which are the so-called kinematic elements of the pair A and B.

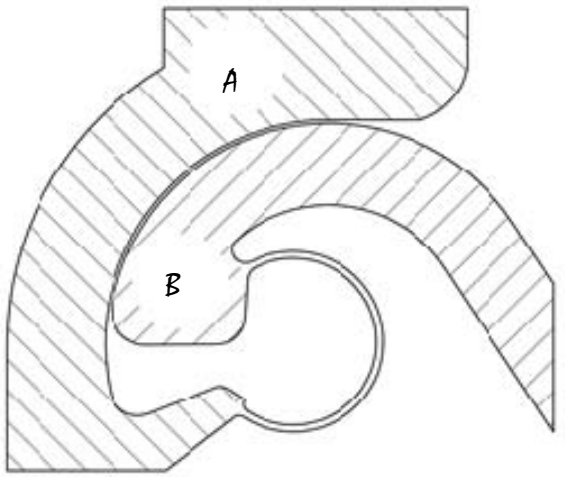

Figure 2 Schematic representation of the CSFH hinge connecting parts A and B.

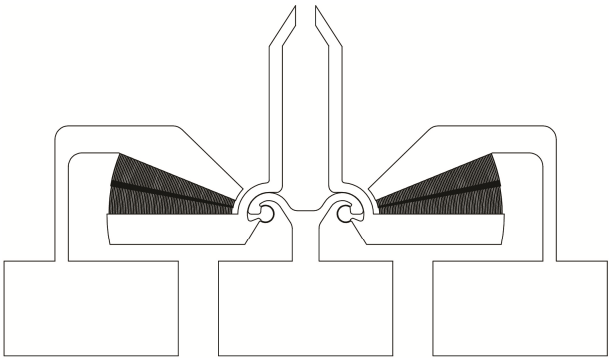

Figure 3 Front view of the gripper device.

According to the original idea [45], the curved beam elastic weights center is positioned in correspondence of the center of the conjugate profiles.

2.1 DESIGN

Since MEMS-Technology based silicon devices are, essentially, compliant mechanisms the method based on the pseudo-rigid body equivalent mechanism can be adopted [46–48]. However, the gripper presented in this paper has two hinges only, and so the kinematic structure is rather elementary. In fact, the pseudo-rigid equivalent mechanism consists in two links connected, independently, to the frame link. Fig. 3 shows how the two claws are allowed to rotate about rotation centers which keep stationary during motion. Although the topological structure is very simple for the proposed case, its actual design and dimensioning is not trivial at all. For this reason it is necessary to use both theoretical and numerical tools in order to predict the forces and torques and to simulate the gripper motion during

operation. A theoretical approach for simulation of CSFH-equipped compliant mechanisms has been recently suggested [49].

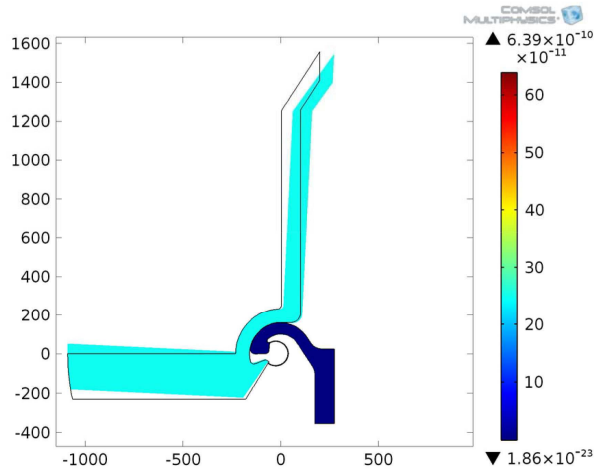

Figure 4 Results of preliminary simulation: single jaw.

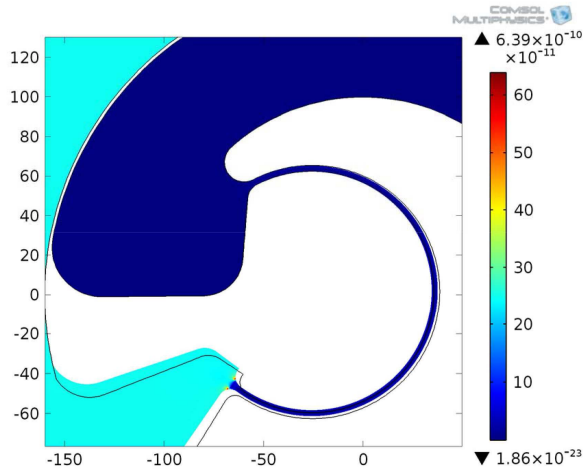

Figure 5 Results of preliminary simulation: curved beam.

This method has been proposed for the inverse kinetostatic analysis of compliant four-bar linkages with flexible circular joints and pseudo-rigid bodies. The theory of curved beams has been applied to the flexible parts and a novel closed form symbolic expression has been presented for the compliance matrix, which maps the generalized forces and relative displacements for the free section of the curved beam with respect to the framed one. The theory of planar displacement matrices has been applied in order to solve the static balance of the whole system. The method has been applied at the microscale.
The following paragraph will describe how Finite Element Analysis can be used in order to simulate the gripper under development.

2.2 PRELIMINARY SIMULATION

A preliminary simulation was performed in Comsol Multiphysics, by imposing a prescribed rotation of the movable comb drive with respect to the center of the conjugate surfaces. In first approximation, an isotropic material was considered (with E = 160 GPa and μ = 0.28), and a rotation angle equal to 2.75 ◦. Figures 4 and 5 show the whole simplified gripper and the flexure hinge, respectively.

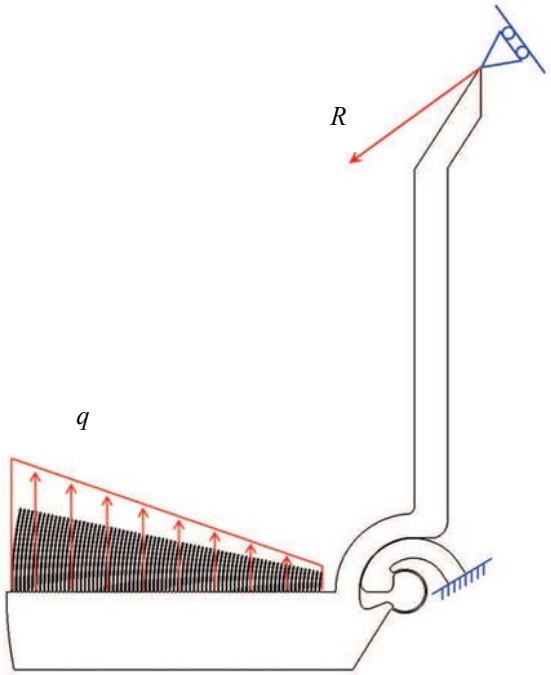

Figure 6: Static simulation under the action of a reaction force *R* and a linearly distributed load *q*

2.3 MICRO-GRIPPER STRUCTURAL MODEL

In order to study the micro-gripper mechanical behaviour a Finite Element model has been built. It takes into account a single grip jaw loaded on the comb drive arm by distributed load and constrained on the gripper tip to tighten flat or cuneiform bodies which react with differently oriented forces (see Fig. 6).
The aim of the analysis has been to evaluate the movements of the hinge centre and of the actuator fingers to identify the load conditions that imply the closure of gap between hinge conjugate surfaces or that involve the risk of contact between the two combs. Besides, in all the studied load conditions, the stress state of curved beam has been monitored to detect possible critical loads and to get hints for a future topological optimization.
Two-dimensional plane-strain elements have been used to model the flexural beam and the gripper jaw. Figures 7 and 8 show the mesh details (the CSFH and the flexible beam, respectively) generated with the commercial software ANSYS. All the analyses have been run by large displacement solver, simulating both the phase when the jaws approach each other (where the comb-drive works just

against the beam elastic reaction) and the phase when their clenching against a rigid body that has been modelled as a roller constraint. In addition, the roller sliding plane has been oriented from zero to 75° to generate an oblique reaction force on the gripper tip, as already mentioned.

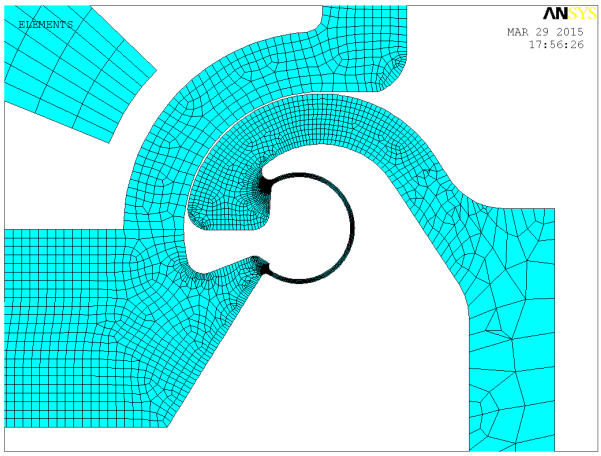

Figure 7 Finite-element mesh: CSFH.

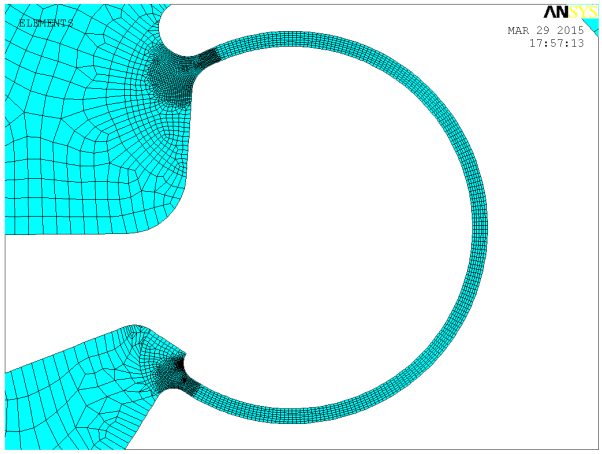

Figure 8 Finite-element mesh: flexible beam.

The comb-drive has been actuated applying a linear variable negative pressure on the mobile arm up to reach a torque moment equal to 0.6 µNm.
The diagrams shown in Fig. 9 confirm that, during free closure, the jaw motion is a pure rotation around hinge centre. In fact, when the complete closure is reached, for

- gripper tip travel: 75 µm,
- jaw rotation: 2.75°,
- applied torque: 0.0125 µNm and
- estimated actuation voltage: 40 V,

the off-centre displacement is less that 0.015 µm along *X* direction, and about 0.065 µm along *Y* direction (Y component of displacement is larger because of off axis action of comb force). Also, during this phase, finger gap deviation from initial value is at most 0.004 µm.
Critical tightening condition may be identified looking at Fig. 10, where the minimum gap between hinge conjugate surfaces and between comb fingers are plotted as a function of applied torque. It can be noticed that only hinge gap depends on reaction force direction, and that quite high external load are required to cause hinge gap closure.
Instead, independently from tip reaction orientation, excessive actuation torque (larger than 0.45 µNm) may cause dangerous contacts among comb fingers.

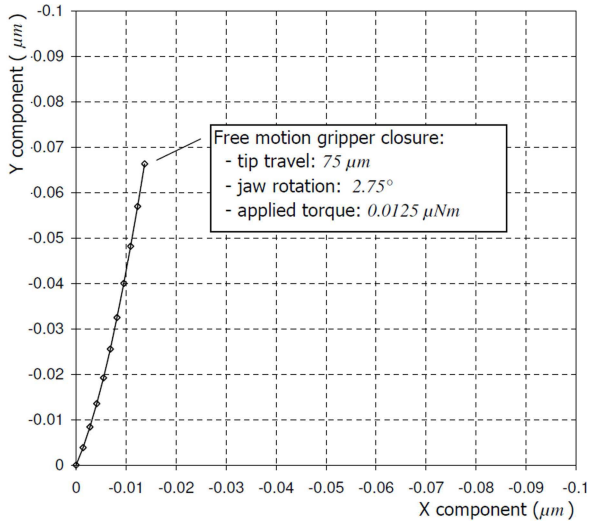

Figure 9 Off-center displacements along *X* and *Y* axes.

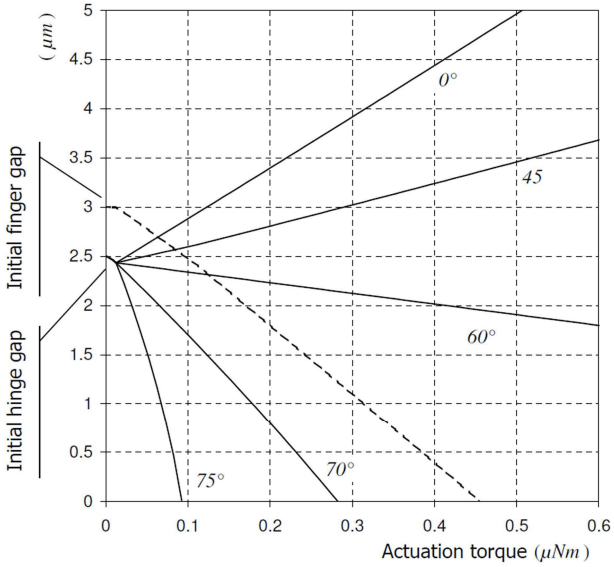

Figure 10 Finger contact avoidance design chart, for different directions of *R*.

3 COMB DRIVES ANALYSIS

With reference to Fig. 11, the capacitance associated to each comb finger is composed of two terms, one resulting from the finger gaps, g, and one resulting from the distance between the finger free-end section and the side wall surface of the opposite comb system, depending on the angle a. In most practical cases, the latter is sufficiently small to be neglected [50].

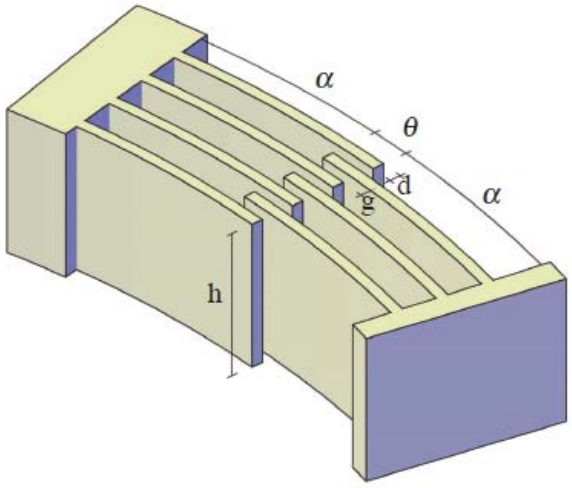

Figure 11 Comb-drive actuator geometric parameters.

Table I - Geometric parameters of the comb drive actuator

Geometric parameter	model 1	model 2
Thickness of the device layer (h)	40 μm	40 μm
Finger width (d)	3 μm	2 μm
Finger gap (g)	3 μm	2 μm
Number of fingers	77	100
Finger angle (α+θ)	12°	12°
Finger initial overlap (θ)	2°	2°

The total capacitance C_T can then be calculated as [51]:

$$C_T = \varepsilon_0 h\theta\left[\sum_{i=1}^{n-1}(\ln A)^{-1} + \sum_{i=0}^{n-1}(\ln B)^{-1}\right], \quad (1)$$

where

$$A = \frac{r_0 + 2i(d+g)}{r_0 + 2i(d+g) - g},$$

$$B = \frac{r_0 + (2i+1)(d+g)}{r_0 + 2i(d+g) + d}.$$

In the previous equation, ε_0 is the vacuum permittivity, h is the thickness of the device layer, θ is the overlap angle, n is the number of fingers in the comb, r_0 is the radius of the first finger, and d is the finger width.

The corresponding electrostatic torque can be determined by [50]:

$$\tau = \frac{1}{2}\left(\frac{\partial C_T}{\partial \theta}\right)V^2, \quad (2)$$

where V is the applied voltage. Substituting (1) in (2), we obtain

$$\tau = \frac{1}{2}\varepsilon_0 h V^2\left[\sum_{i=1}^{n-1}(\ln A)^{-1} + \sum_{i=0}^{n-1}(\ln B)^{-1}\right]. \quad (3)$$

In the present investigation, two different models are considered, characterized by different finger width, gap, and total number. Table 1 lists the values of the geometric parameters for each model. The torque values for different applied voltage values are shown in Fig. 12.

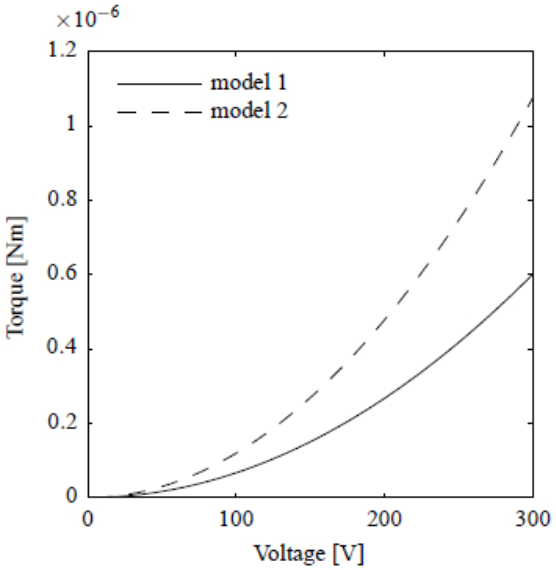

Figure 12 Applied voltage and resultant torque for the comb actuators.

4 MICRO-GRIPPER CONSTRUCTION METHOD

In the present section, the construction processes followed in order to obtain the compliant micro-mechanism are presented. The aim of this study is to obtain a device with suspended parts and other clamped zones. The device is a monolithic silicon based object composed of (see Figure 13):

- pads, used for the electrical polarization and clamped to an external platform with the electrical connections;
- comb-drives, used to carry out the claws, suspended and free to move on the plane of the device;
- claws, which are the device external parts and need both structural strength and flexibility.

All the moving parts are connected to the device suspended mainframe and consequently to the pads.

In order to obtain this structure a SOI (Silicon on Insulator) wafer has been used with device thickness of 40 μm, buried SiO_2 thickness of 3 μm and a handle thickness of 400 μm. This kind of substrate suites very well our purposes as it's possible to obtain suspended structures by etching, separately, the device and the handle silicon layers and, then, removing the oxide film. In this way the upper silicon parts are not in contact with the bottom parts.

The process sequence is based on DRIE (Deep Reactive Ion Etching), as the thickness of silicon to be etched is 40 μm for the device layer and 400 μm for the handle layer. Furthermore, vertical sidewalls are necessary for hinge bending.

The corresponding technological steps will be briefly resumed for the sake of completeness.

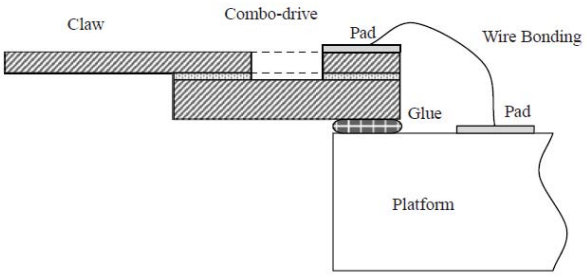

Figure 13 Device scheme.

With reference to Figures 14 and 15, the adopted process can be summarized as follows for both sides:

1. One layer of aluminum is deposited on the device layer surface by magnetron sputter deposition.
2. A photoresist layer is deposited on the aluminum layer by spin coating;
3. the mask is positioned between the wafer and the UV source in order to perform the exposure;
4. The mask geometry is transferred on the sample by photoresist developing;
5. Final geometry after photoresist developing;
6. the unprotected aluminum layer is etched by a solution of phosphoric acid (H3PO4,80%), nitric acid (HNO3,5%) and deionized water (DI,10%) and the geometry is transferred on aluminum;
7. Deep Reactive Ion Etching is applied on a SOI wafer;
8. Final 3D geometry after DRIE;
9. Etching of exposed silicon dioxide and separation of floating parts.

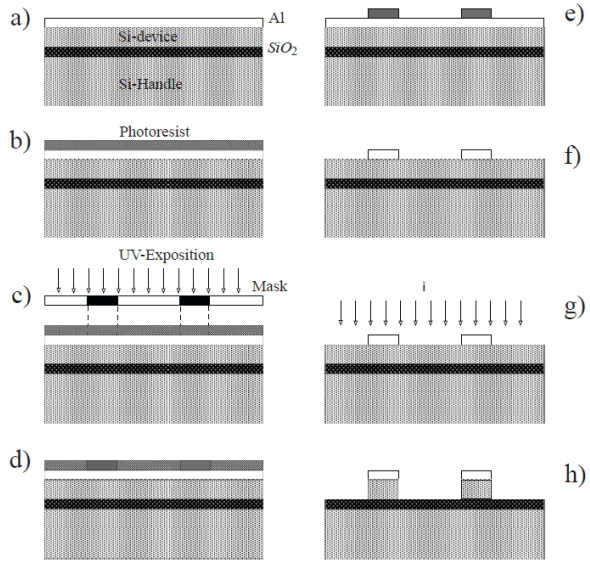

Figure 14 The process phases adopted for the Device Layer Etching.

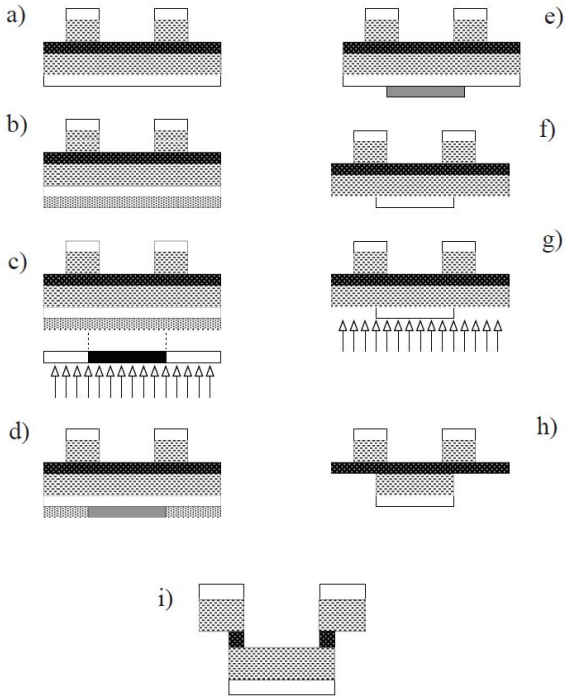

Figure 15 The process phases adopted for the Handle Layer Etching.

4.1 EXPERIMENTAL RESULTS OF THE DEVICE LAYER ETCHING PHASE

In this section the part of the construction process represented in Fig. 14, from a) to h), is briefly illustrated. Fig. 16 shows an image of the top layer (device layer) obtained by means of a scanning electron microscope (SEM). The device geometry can be recognized. However, there are, in the Figure, also some separation lines, which can be recognized, that are extraneous to the device geometry, which have been etched in order to extract the sacrificial floating plates easily. Thanks to this image it is possible to observe that

- the device geometry is replicated with a acceptable accuracy;
- the curved lines are also well replicated, which is a critical issue for the proposed device;
- the aspect ratio is quite feasible for the application;
- comb drives are also constructed with a fair accuracy.

A preliminary test on the wafer has been performed by analyzing the morphology of the front layer after D-RIE process. Fig. 17 shows the actual feasibility of the comb drive construction process. The teeth have an acceptable shape and are separated by an acceptable gap. Fig. 18 presents a detailed view of the whole flexure hinge: the flexible curved beam, the adjacent links and even a view of the conjugate cylindrical surfaces. Finally, Fig. 19 shows the CSFH and the electrostatic comb drive of the device after the final step of the construction process: separation of the floating parts by etching of silicon dioxide.

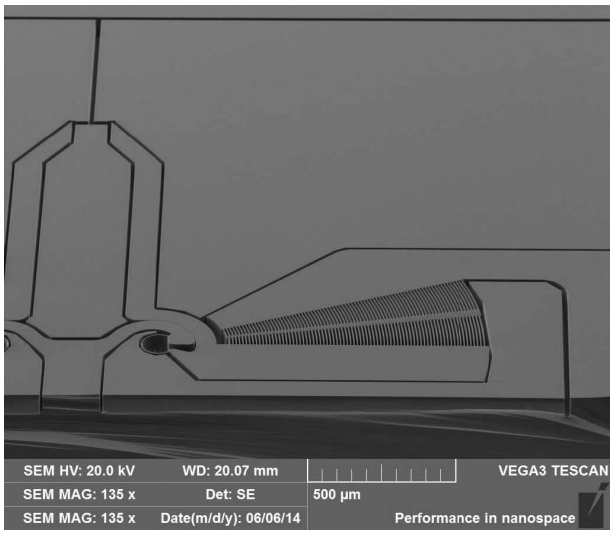

Figure 16 Etched wafer frontside: the sample is 30 degrees tilted and a section of it is visible in the lower portion of the image (FBK MNF Micro Nano Facility).

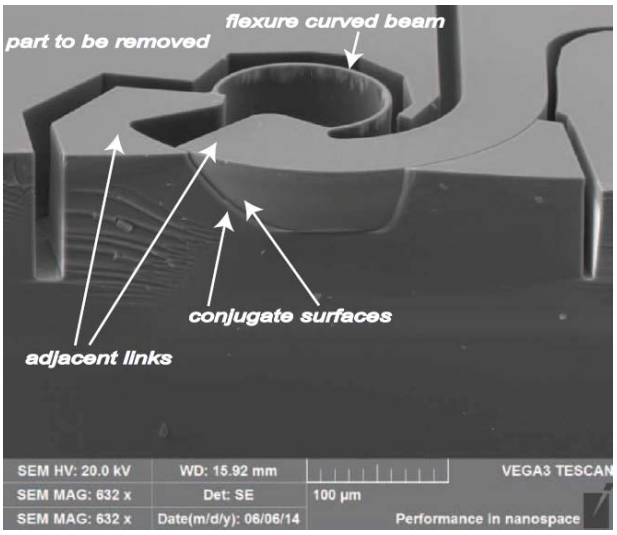

Figure 18 The flexure hinge and a pair of adjacent links before reaching the SiO2 layer (FBK MNF Micro Nano Facility).

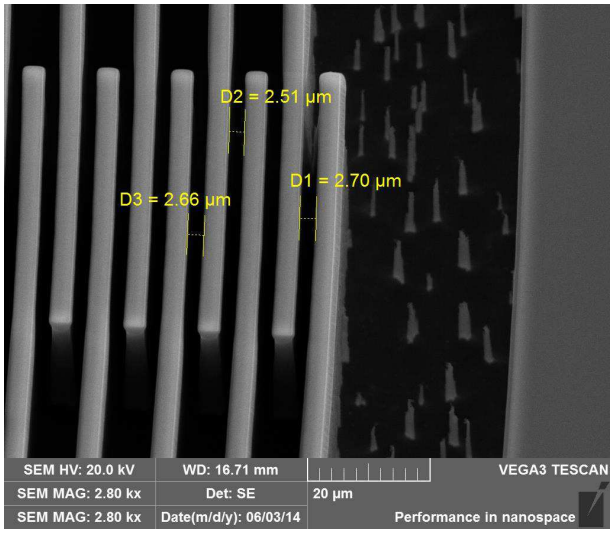

Figure 17 The teeth of the constructed comb drive (FBK MNF Micro Nano Facility).

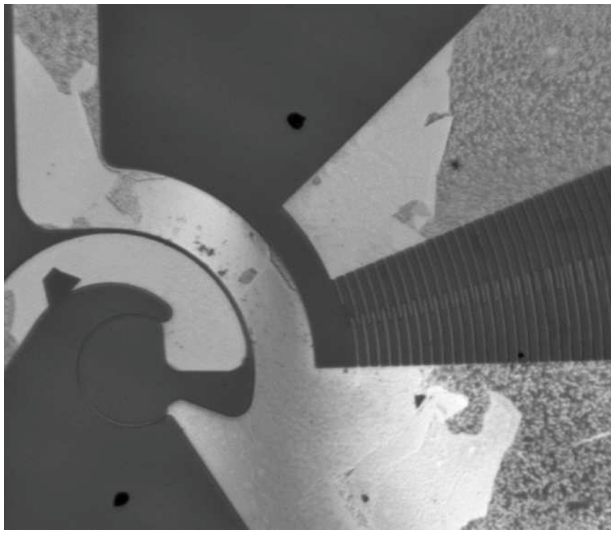

Figure 19 Device detail after the final step of the construction process: CSFH and electrostatic comb drive

5 CONCLUSION

This paper has shown how a new silicon micro gripper for micro manipulation can be designed, simulated and constructed. Although the overall size does not exceed 3×3 mm, with the smallest subpart thickness equal to about 3 µm, the experimental tests, after the top layer etching stage, showed a satisfying accuracy in geometry, also in curved lines replication. This characteristic is a crucial aspect for the proposed device because it gives an experimental proof that, generally speaking, silicon micro devices based on Conjugate Surfaces Flexure Hinges (CSFHs) can be constructed without problems.

REFERENCES

[1] Pisano A.P. Biomedical applications of MEMS: A look at grippers, cochlear implants, micro needles and microchemical assay devices. In *ASME DSC*, vol. 57-2, p.949, 1995.

[2] Havlik S. Modeling, analysis and optimal design of multi-component force/displacement sensors. In *Proc.on the First ECPD Int. Conf. on Advanced Robotics and Intelligent Automation*, pp. 283–289, Sept. 6-8, Athens, Greece,1995.

[3] Petrovic D., Popovic G., Chatzitheodoridis E., Del Medico O., Almansa A., Detter H. and Brenner W. Mechanical gripper system for handling and assembly

in MEMS. In *SPIE 2001*, vol. 4557, pp. 151–156, 2001.

[4] Seidemann V., Batefisch S. and Battgenbach S. Fabrication and investigation of in-plane compliant SU8 structures for MEMS and their application to micro valves and micro grippers. *Sensors and Actuators, A: Physical*, vol. 97-98, pp. 457–461, 2002.

[5] Enikov E. and Minkov L. Micro-assembly and packaging of MEMS using optically transparent electrostatic gripper. In *ASME MED*, vol. 15, pp. 511–518, 2004.

[6] Kang B. and Wen J. Design of compliant MEMS grippers for micro-assembly tasks. In *IEEE ICIRS*, pp. 760–765, 2006.

[7] Jeon C.S., Park J.S., Lee S.Y. and Moon C.W. Fabrication and characteristics of out-of-plane piezoelectric micro grippers using MEMS processes. *Thin Solid Films*, vol. 515, no. 12, pp. 4901–4904, 2007.

[8] Kim B., Park J.S., Moon C., Jeong G.M. and Ahn H.S. A precision robot system with modular actuators and MEMS micro gripper for micro system assembly. *Journal of Mechanical Science and Technology*, vol. 22, no. 1, pp. 70–76, 2008.

[9] Chen T., Chen L., Sun L., Wang J. and Li X. A sidewall piezoresistive force sensor used in a MEMS gripper. *Intelligent Robotics and Applications*, Springer Berlin Heidelberg, 2008.

[10] Chen T., Chen L., Liu B., Wang J. and Li X. Design of a four-arm structure MEMS gripper integrated with sidewall force sensor. In *NEMS 2009*, pp. 75–79, 2009.

[11] Chen T., Chen L., Sun L. and Li X. Design and fabrication of a four-arm-structure MEMS gripper. *IEEE Transactions on Industrial Electronics*, vol. 56, no. 4, pp. 996–1004, 2009.

[12] Chen D.S., Yin C.Y., Lai R.J. and Tsai J.C. A multiple degrees of freedom electrothermal actuator for a versatile MEMS gripper. In *IEEE MEMS 2009*, pp. 1035–1038, 2009.

[13] Mayyas M. and Stephanou H. Electrothermoelastic modeling of MEMS gripper. *Microsystem Technologies*, vol. 15, no. 4, pp. 637–646, 2009.

[14] Chen B., Zhang Y. and Sun Y. Novel MEMS grippers capable of both grasping and active release of micro objects. In *TRANSDUCERS 2009*, pp. 2389–2392, 2009.

[15] Vijayasai A., Sivakumar G., Mulsow M., Lacouture S., Holness A. and Dallas T. Haptic controlled three-axis MEMS gripper system. *Review of Scientific Instruments*, vol. 81, no. 10, 2010.

[16] Havlik S. Improving accuracy of compliant robotic (micro) devices. In *Proc. 19th International Workshop on Robotics in Alpe-Adria-Danube Region, RAAD 2010*, pp. 385–389, 2010.

[17] Hricko J., Havlik S. and Hart'ansky R. Optimization in designing compliant robotic micro-devices. In *Proc. 19th International Workshop on Robotics in Alpe-Adria-Danube Region*, pp. 397–402, 2010.

[18] Khazaai J., Qu H., Shillor M. and Smith L. An electrothermal MEMS gripper with large tip opening and holding force: Design and characterization. *Sensors and Transducers*, vol. 13, pp. 31–43, 2011.

[19] Khazaai J., Qu H., Shillor M., Smith L. and Cheok K. Design and fabrication of a metallic MEMS gripper using electro-thermal V-shape and modified U-shape actuators. In *NSTI-Nanotech 2011*, vol. 2, pp. 353–356, 2011.

[20] Kim B.S., Park J.S., Hun Kang B. and Moon C. Fabrication and property analysis of a MEMS microgripper for robotic micro-manipulation. *Robotics and Computer-Integrated Manufacturing*, vol. 28, no. 1, pp. 50–56, 2012.

[21] Abbasi A. and Ahmadian M. Force controlled manipulation of biological cells using a monolithic mems based nano-micro gripper. In *ASME IMECE*, vol. 2, pp.193–201, 2012.

[22] Piriyanont B. and Moheimani S. Design, modeling, and characterization of a MEMS micro-gripper with an integrated electrothermal force sensor. In *AIM 2013*, pp. 348–353, 2013.

[23] Piriyanont B., Moheimani S. and Bazaei A. Design and control of a MEMS micro-gripper with integrated electro-thermal force sensor. In *AUCC 2013*, pp. 479–484, 2013.

[24] Chen D.S., Yeh P.F., Chen Y.F., Tsai C.W., Yin C.Y., Lai R.J. and Tsai J.C. An electrothermal actuator with two degrees of freedom serving as the arm of a MEMS gripper. *IEEE Transactions on Industrial Electronics*, vol. 61, no. 10, pp. 5465–5471, 2014.

[25] Hao Y., Dong F., Zhang J. and Bao L. Study on microgripper based on MEMS mechanism assembly. *Zhongguo Jixie Gongcheng/China Mechanical Engineering*, vol. 25, no. 5, pp. 596–601, 2014.

[26] Belfiore N.P. and Pennestrì E. An atlas of linkage type robotic grippers. *Mechanism and Machine Theory*, vol. 32, no. 7, pp. 811–833, 1997.

[27] Belfiore N.P. Distributed databases for the development of mechanisms topology. *Mechanism and Machine Theory*, vol. 35, no. 12, pp. 1727–1744, 2000.

[28] Belfiore N.P. Brief note on the concept of planarity for kinematic chains. *Mechanism and Machine Theory*, vol. 35, no. 12, pp. 1745–1750, 2000.

[29] Belfiore N.P., Faralli M., Presta M., Moretti M., Ianniello F., Scaccia M. and Consorti L. On a test bench for studying lubrication in a spherical bearing:

Simulations and experimental validation. *Tribo Test*, vol. 12, no. 4, pp. 287–308, 2006.

[30] Belfiore N.P., Ianniello F., Natali S., Casadei F. and Stocchi D. The development of a feasible method for the tribological characterization of gear teeth surface treatments. *Tribology International*, vol. 39, no. 8, pp. 789–795, 2006.

[31] Belfiore N.P., Ianniello F., Stocchi D., Casadei F., Bazzoni D., Finzi A., Carrara S., González J., Llanos J.,Heikkila I., Peñalba F. and Gómez X. A hybrid approach to the development of a multilayer neural network for wear and fatigue prediction in metal forming. *Tribology International*, vol. 40, no. 10-12, pp. 1705–1717, 2007.

[32] Balucani M., Belfiore N., Crescenzi R. and Verotti M. The development of a MEMS/NEMS-based 3 D.o.F. compliant micro robot. *International Journal of Mechanics and Control*, vol. 12, no. 1, pp. 3–10, 2011.

[33] Balucani M., Belfiore N.P., Crescenzi R., Genua M. and Verotti M. Developing and modeling a plane 3 D.o.F. compliant micromanipulator by means of a dedicated mbs code. In *Technical Proceedings of the 2011 NSTI Nanotechnology Conference and Expo, NSTI-Nanotech 2011*, vol. 2, pp. 659–662. 2011.

[34] Belfiore N., Balucani M., Crescenzi R. and Verotti M. Performance analysis of compliant mems parallel robots through pseudo-rigid-body model synthesis. In *ASME 2012 11th Biennial Conference on Engineering Systems Design and Analysis, ESDA 2012*, vol. 3, pp. 329–334. 2012.

[35] Belfiore N., Verotti M. and Consorti L. Comparative analysis of isotropy indices in RR and RRP arms. *International Journal of Mechanics and Control*, vol. 11, no. 1, pp. 3–12, 2010.

[36] Belfiore N., Di Giamberardino P., Rudas I. and Verotti M. Isotropy in any RR planar dyad under active joint stiffness regulation. *International Journal of Mechanics and Control*, vol. 12, no. 1, pp. 75–81, 2011.

[37] Belfiore N.P., Verotti M., Di Giamberardino P. And Rudas I.J. Active joint stiffness regulation to achieve isotropic compliance in the Euclidean space. *Journal of Mechanisms and Robotics*, vol. 4, no. 4, pp. 041010 1–11, 2012.

[38] Belfiore N.P., EmamiMeibodi M., Verotti M., Crescenzi R. and adn P. Nenzi M.B. Kinetostatic optimization of a MEMS-based compliant 3 DOF plane parallel platform. In *IEEE 9th International Conference on Computational Cybernetics, ICCC*, Tihany, Hungary, 2013.

[39] Belfiore N.P., Verotti M., Crescenzi R. and Balucani M. Design, optimization and construction of MEMS - Based micro grippers for cell manipulation. In *IEEE International Conference on System Science and Engineering, ICSSE,* Budapest, Hungary, 2013.

[40] Belfiore N.P. Functional synthesis of a new class of micro electro-mechanical systems. *Advances in Soft Computing, Intelligent Robotics and Control*, vol. 8 of *Topics in Intelligent Engineering and Informatics*, pp. 81–93. Springer International Publishing, 2014.

[41] Pennestrì E. and Belfiore N.P. Modular third-order analysis of planar linkages with applications. In *American Society of Mechanical Engineers, Design Engineering Division (Publication) DE*, vol. 70-1, pp. 99– 103. 1994.

[42] Pennestrì E. and Belfiore N.P. On the numerical computation of generalized Burmester points. *Meccanica*, vol. 30, no. 2, pp. 147–153, 1995.

[43] Belfiore N.P., Prosperi G. and Crescenzi R. A simple application of conjugate profile theory to the development of a silicon micro tribometer. In *Proc. ASME 2014 12th Biennial Conf. on Eng. Systems Design and Analysis*. Copenhagen, Denmark, 2014.

[44] Verotti M., Crescenzi R., Balucani M. and Belfiore N.P. MEMS-Based Conjugate Surfaces Flexure Hinge. *Journal of Mechanical Design, Transactions of the ASME*, vol. 137, no. 1, pp. 012301–012301, 2015.

[45] Belfiore N.P., Scaccia M., Ianniello F. and Presta M. Selective compliance hinge World Intellectual Property Organization, WO/2009/034551, Int. Appl. No. PCT/IB2008/053697, Publ. Date March, 19th, 2009, US Patent Application No. 12/677975, 2011.

[46] Midha A., Norton T.W. and Howell L.L. On the nomenclature, classification and abstractions of compliant mechanisms. *Journal of Mechanical Design*, vol. 116, pp. 270–279, 1994.

[47] Howell L.L., Midha A. and Norton T.W. Evaluation of equivalent spring stiffness for use in a pseudo rigid-body model of large-deflection compliant mechanisms. *Journal of Mechanical Design, Trans. ASME*, vol. 118, pp. 126–131, 1996.

[48] Howell L.L. *Compliant Mechanisms*. John Wiley & Sons, 2001.

[49] Belfiore N.P. and Simeone P. Inverse kinetostatic analysis of compliant four-bar linkages. *Mechanism and Machine Theory*, vol. 69, pp. 350 – 372, 2013.

[50] Chang H., Zhao H., Ye F., Yuan G., Xie J., KraftM. And Yuan W. A rotary comb-actuated microgripper with a large displacement range. *Microsystem Technologies*, vol. 20, no. 1, pp. 119–126, 2014.

[51] Andrew Yeh J., Huang J.Y., Chen C.N. and Hui C.Y. Design of an electrostatic rotary comb actuator. *Journal of Micro/Nanolithography, MEMS, and MOEMS*, vol. 5, no. 2, pp. 023008–023008–13, 2006.

ISSN 1590-8844
International Journal of Mechanics and Control, Vol. 16, No. 01, 2015

CONVERSION OF PEAUCELLIER–LIPKIN STRAIGHT-LINE MECHANISM TO COMPACT COMPLIANT DEVICE

Jaroslav Hricko

Institute of Informatics, Slovak Academy of Sciences, Banská Bystrica, Slovakia

ABSTRACT

Structures of straight-line mechanisms are very often used in building of smart precise robotic devices, to which requirements based on high accuracy and precision with manipulation of micro- and nano- scale objects are put. In this case only compact compliant devices can be used. The parasitic deformations in movement of compliant mechanisms must be minimized, when exact straight-line output motion is required. This put higher requirements to complexity of such devices design. This paper deals with design procedures (conversion) for device based on compact compliant mechanical structure, where kinematical structure of Peaucellier–Lipkin straight-line mechanism was used. Design problems of transformation between straight-line mechanisms and flexure structures are discussed.

Keywords: compact compliant devices; precise positioning; Peaucellier–Lipkin mechanism; mechanisms design; modelling and simulation;

1 INTRODUCTION

The modularity of robotic devices is current trend in design of robotic devices [1, 2], but in the case of small robotic devices based on compact compliant mechanical structures [3, 4, 5] is this approach impossible. Such devices are usually build from one piece of material and output motion is produced by elastic deformation of material. In comparison with classic constructions of robot mechanisms such devices have one disadvantage and this is restricted movement of whole mechanisms, but this is the advantage of such devices too, in relationship to positioning accuracy. Compliant mechanisms can be divided in two groups: structures with concentrated (lumped) and distributed flexibility. In the first group of mechanisms the rigid parts/arms are connected by flexible joints. The second group, beside rigid parts, includes flexible joints and flexible arms too. In this paper the mechanisms with elastic joints only will be discussed.

Contact author: Jaroslav Hricko[1]

[1] Institute of Informatics, Slovak Academy of Sciences, Ďumbierska 1, 974 01 Banská Bystrica, Slovakia
Email: hricko@savbb.sk

The reason of choice of compliant mechanisms with elastic joints is similarity between design of classic construction of mechanisms and such devices [6, 7]. Main focus will be oriented on the plane mechanisms problems solution.
The design of compact compliant mechanical structure based on Peaucellier-Lipkin straight-line mechanism is the main aim of the paper. Design of precise positioning device with minimized parasitic deformations and with straight-line output motion enables utilization of not so complex control system. In other words, because the mechanisms produce straight-line output motion with minimized parasitic deformations we shouldn't use the control system which needn't solve tasks connected with compensations of undesired motions. Other advantage of chosen approach is based on the fact, that usually only one actuator for control of one moving axis is used. In the case of flexure devices it is not attainable to use one actuator to one joint as it is in the classical kinematical structures.

2 STRAIGHT-LINE MECHANISMS

Mechanisms which are designed to produce a straight-line motion are known as straight line motion mechanisms [8]. Such mechanisms very often convert rotary motion to straight-line motion. A mechanism with sliding pair is the most common type of such devices, but sliding pair is

bulky and subjected to comparatively rapid wear so a mechanism is constrained by the use of turning pair, or as combination of both types of kinematics pairs. According to [8] straight-line mechanisms are divided into three categories:

- Exact straight-line motion mechanism
- Approximate straight-line motion mechanism
- Straight-line copying mechanism

Extract straight-line motion mechanism follows a mathematical relation which holds true for all positions of input link such that output link follows straight-line [8]. The most known such devices are Peaucellier–Lipkin linkage, Hart mechanism and Scott Russell linkage. Only last mentioned device is composite from combination of sliding and turning pairs, other mechanisms are built only from turning pairs.

Some mechanisms describe an approximate straight-line motion; usually a four bar chain or its modified variant. To this category belong: Watt mechanism, Tchebicheff's mechanism (some resources talk about Chebyshev linkage), Grasshopper mechanism and Roberts's mechanism.

In design of precise micro-robotic devices are often utilized the straight-line kinematic structures. However complexity of such structures could not enable using of all structures in compliant mechanical devices. Therefore only kinematics of Hoeken lineage, Scott-Russell straight-line mechanisms and Watt mechanism are utilized in design process of small robotic mechanism.

2.1 MICRO-GRIPPERS UTILIZED STRAIGHT-LINE STRUCTURES

When is talked about gripping of small object is one important requirement connected by moving of gripper fingers. Many tasks require that movement of finger of gripper will be moving parallelly with all gripper's fingers [9, 10], in case of planar devices it mean movement of two fingers. But parallel movement of some fingers is possible to gain only by utilization of straight-line structure in structure of whole gripper. The design of griper with straight-line jaw motion of fingers (see Figure 1) may be desired for micromechanical tension/compression tests, and for gripping soft objects such as cells, gels, and assemblies of nanostructures such as carbon nano-tubes. This gripper utilizes Hoekens linkage with connected parallelogram for removing rotation of output point in respect to global coordinate system [10]. Similar approach for design of robot end-effector is presented on [11], where a modified Scott Russell straight-line mechanism was utilized.

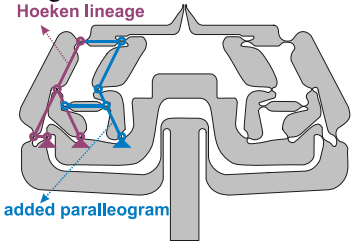

Figure 1 Structure of compliant micro-gripper with utilized Hoeken lineage for parallelly moving of fingers [10]

2.2 PRECISION POSITIONING MICRO-STAGES

An example of nano-manipulation mechanisms based on Scott-Russell straight-line mechanism is developed on [12] (see Figure 2 a)). Such mechanism has only one moving axis for manipulation tasks. The flexure-based Scott–Russell mechanism is monolithically constructed to provide high positioning accuracy and long-term repeatability what is obtained by piezoelectric actuator.

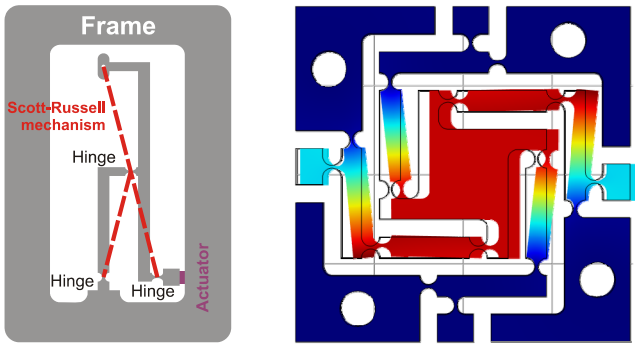

a) b)

Figure 2 a) Nano-manipulation mechanisms based on Scott-Russell straight-line mechanism [12]; b) Design of our XY micro stage with minimized parasitic deformations based on Watt mechanism

In the design of linear motion stage with two motion axes is very important minimize cross-displacement effect caused by properties of flexure joint, because replacement of revolute joint with flexure joint is not ideal and flexural joint create undesired movement in other axis. Our design of precise motion stage based on minimal cross-displacement effects and flexure-based Watt mechanisms is delineated on the Figure 2. b).

3 PROBLEMS IN DESIGN PROCESS OF SMALL ROBOTIC DEVICES WITH STRAIGHT-LINE STRUCTURES

The design of compliant mechanisms with lumped compliance is based on similarity with design process of classical mechanical devices [6, 7]. Between both designs procedures are small differences, and the main difference is transformation of classical kinematical pairs to compliant kinematical pairs. Two basic transformations of classical kinematical pairs with compliant element are shown on the Figure 3. For instance, transformation of turning pair is usually based on application of flexure joint, which is the connection of two relatively rigid parts with flexure element which is usually place with notches. Shape of notches defines (express) the properties of this main building element of compact compliant mechanism [3, 5]. One example, circular flexure joint has relatively linear working characteristic, but in other site maximal deformation is small, but for instance, the right-circular joint could produce larger output deformation but moving the rotation of centre is bigger. Transformation of sliding

pair to compliant device is much more complicated, because in compliant mechanisms don't exist directly substitution. Such mechanisms are compounded from some flexure joints to parallelogram. But movement of parallelogram is on circle and not straight-line. This is one reason too, why it is necessary to use structures of straight-line mechanisms in compliant devices for producing of exact linear motion.

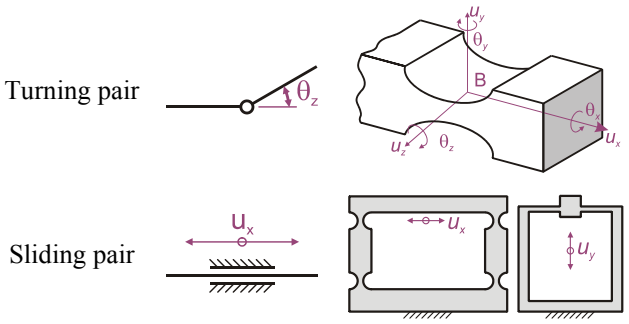

Figure 3 Basic transformations of classical kinematical pairs with compliant element

Because compliant structures work on elastic deformation of material, the expression between deflection of structure (for instance of basic build block flexure hinge) and actuated force/torque is expressed as

$$\begin{pmatrix} u_x \\ u_y \\ u_z \\ \theta_x \\ \theta_y \\ \theta_z \end{pmatrix} = \begin{pmatrix} C_{xFx} & 0 & 0 & 0 & 0 & 0 \\ 0 & C_{yFy} & 0 & 0 & 0 & C_{yMz} \\ 0 & 0 & C_{zFz} & 0 & C_{zMy} & 0 \\ 0 & 0 & 0 & C_{\theta xMx} & 0 & 0 \\ 0 & 0 & C_{\theta yFz} & 0 & C_{\theta yMy} & 0 \\ 0 & C_{\theta zMz} & 0 & 0 & 0 & C_{\theta zMz} \end{pmatrix} \bullet \begin{pmatrix} F_x \\ F_y \\ F_z \\ M_x \\ M_y \\ M_z \end{pmatrix} \quad (1)$$

where, on the principle of reciprocity

$$C_{yMz} = C_{\theta zFy}$$
$$C_{zMy} = C_{\theta yFz} \quad (2)$$

where u_i and θi are arisen deformations, matrix components C_{iLi} represents compliances, where first part of sub-index express direction of deformation (movement or rotation) and second part of sub-index express acting load (force/torque). The vector composed from F_i and M_i express common load acting to the compliant device.

Because motion of compliant mechanisms is produced by elastic deformation of used material, the replacement by flexure joint in the case of turning pair is not equal. Maximal rotation of flexure joint is depended on dimensions itself joint and mechanical properties of used material. Maximal arisen stress in the flexure joint is expressed by (3) and this value must be smaller as allowed stress (Yield strength) of used material.

$$\sigma_{\max} = K_{ta}\frac{F_x}{wt} + K_{tb}\frac{6\left(l_F F_y + M_z\right)}{wt^2} \quad (3)$$

where K_{ta} and K_{tb} are theoretical stress concentration factors, where K_{ta} is connected with axial load, and K_{tb} is connected with bending. Parameters w (joint width) and t (thickness – thinnest place of the flexure joint) are construction parameters and l_F is distance between joint and actuation place of force F_y. Theoretical stress concentration factors are given on the base of experimental measurements or by approximate theoretical calculation. For instance, the theoretical stress concentration factors for circular flexure hinge are

$$K_{ta} = 3.065 - 3.472\left(\frac{2r}{2r+t}\right) + 1.009\left(\frac{2r}{2r+t}\right)^2 + 0.405\left(\frac{2r}{2r+t}\right)^3 \quad (4)$$

$$K_{tb} = 3.065 - 6.637\left(\frac{2r}{2r+t}\right) + 8.229\left(\frac{2r}{2r+t}\right)^2 - 3.636\left(\frac{2r}{2r+t}\right)^3 \quad (5)$$

Other problems connected with design of compliant devices with structure of straight-line mechanisms are gained according to kinematical analysis. Using MATLAB SimMechanics toolbox kinematic analysis from chosen lineages was made. The analysed straight-line mechanisms are chosen with respect to relatively easy structure and/or according to basic research indicated in the introduction, where are described some applications of small robotic devices utilized straight-line kinematical structure in structure of whole compliant device.

Table I - Results from the kinematic analysis of some SLM

SLM	Output motion			Joints rot. /[°]	
	u_{out} /[m]	u_{err} /[m]	θ_{out} /[°]	min.	max.
Peaucellier–Lipkin	0.045	1.80e-9a	-	29.68	76.59
Scott Russell	0.0447	7.94e-09	180	180	180
Hoekens	0.0444	9.75e-05	58.5	26.58	209.25
Watt	0.0132	2.41e-04	18.3	52.36	55.13
Chebyshev	0.02	4.88e-05	180	53.13	126.75
Roberts	0.0456	8.96e-04	74.98	69.66	141.43

In the Table I. are presented some results from the kinematic analysis of chosen straight-line mechanisms (SLM). Table is divided to two different parts (output motion and joints rotation). The first group is connected with motion of output point of the mechanisms. Variable u_{out} express maximal movement similar to straight-line motion. Variable u_{err} express amplitude between ideal straight-line motion and real motion of analyzed device (see Figure 4). Last variable θ_{out} express the value of rotation between stable (global) coordinate system and coordinate system located on the output point. For the first analysed device is not defined value of rotation of local coordinate system located at output point of lineage to global coordinate system because, in this case the output point is revolute joint. One conclusion from data analysis is that extract straight-line motion mechanisms produce better straight-line motion as approximate devices, where

waviness is around hundred micrometers compared to units of nanometres.

Second group of values in the Table I are connected with rotation of revolute joints of analysed device in process of producing output straight-line motion. According to values of angles it is clear, that classical kinematic structures of straight-line mechanisms utilize revolute joint as much as it is possible, but in the case of compliant structures the rotation of flexure joint is limited by material properties, by dimensions and by form (shape) of notch.

Other problem of such devices is rotation of output point towards to global coordinate system (θ_{out}). This problem is in the case of compact compliant mechanisms design solved by two main approaches:

- adding a sliding pair,
- adding parallel mechanism.

In the case of adding a sliding pair to minimize rotation of output point is approach based on, adding to output point of device one revolute joint and connect it with moving part of sliding pair. This approach is for instance presented on [13], were some straight-line mechanisms (see mechanisms labelled as S1, S3, S12, S36 and others) utilize sliding pair for produce straight-line motion.

Other approach is based on utilization of equal parallel mechanisms, where again at output point of device is added revolute joint, and both joints (original and from added device) are connected by relatively rigid element [14]. In case that both mechanisms are actuated synchronous, or in this same place by one actuator, then it is not possible to gain crossing. Similar approach was utilized in the case of described micro-gripper (see Figure 1) where whole Hoeken lineage was not added to the structure, but only parallelogram.

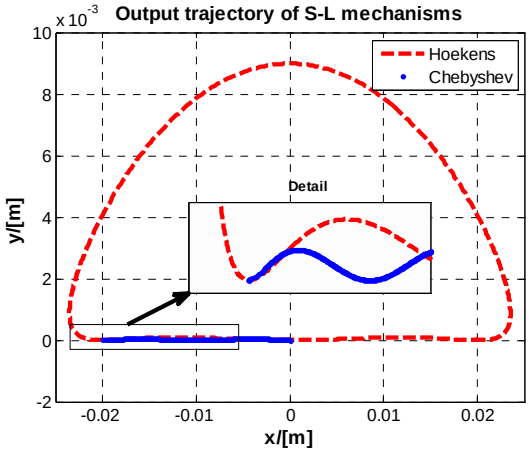

Figure 4 Output trajectory and detail of some analyzed straight-line mechanisms

4 COMPLIANT PEAUCELLIER–LIPKIN MECHANISM

The Peaucellier-Lipkin mechanism was the first planar straight-line mechanisms capable transforming rotary motion into perfect straight-line motion [15]. The main reason, why it is necessary to transform such devices intro compliant mechanism is, that many straight-line structures utilized in compliant devices belong into group of approximate straight-line mechanisms (see Figure 1 and 2). What mean, that with transformation to the compliant device we could not get ideal straight-line output motion, but only their approximate equivalent. But in the case of the compliant devices, with the parasitic deformations we must calculate to the output motion, what mean, that output motion of compliant device, is combination of error gained from parasitic deflections and error arise from approximate straight-line device. In the case of Peaucellier-Lipkin mechanism, the error u_{err} (see Table I) is very small and therefore whole error of output trajectory from compliant device is combination of parasitic deformations and changing of the structure (see below).

The mechanism consists of isosceles four bar chain *OCBD* (Figure 5). Additional links *AC* and *AD* from, a rhombus *ACBD*. *A* is constrained to move on a circular path by the radius bar O_1A which is equal to the length of the fixed link OO_1 [16].

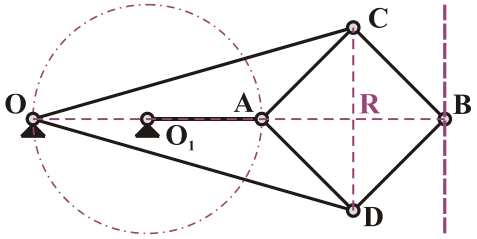

Figure 5 The Peaucellier-Lipkin straight-line mechanism

From the geometry of the figure, it follows that

$$AC = CB = BD = DA$$
$$OC = OD; \quad OO_1 = O_1A \tag{6}$$

It may be proved that the product $OA \times OB$ remains constant, when the link O_1A rotates. Join *CD* to bisect *AB* at *R*. Now from right angled triangles *ORC* and *BRC*, we have

$$OC^2 = OR^2 + RC^2 \tag{7}$$
$$BC^2 = RB^2 + RC^2 \tag{8}$$

Subtracting (8) from (7)

$$\begin{aligned} OC^2 - BC^2 &= OR^2 - RB^2 \\ &= (OR + RB)(OR - RB) \\ &= OB \times OA \end{aligned} \tag{9}$$

Since *OC* and *BC* are of constant length, therefore the product $OB \times OA$ remains constant. Hence the point *B* traces a straight path perpendicular to the diameter *OP*.

4.1 KINEMATICAL ANALYSIS

As was mentioned, during design of compliant mechanisms with lumped compliance it is necessary to transform kinematic structure of designed device to flexure structure. However, the kinematical structure of Peaucellier-Lipkin mechanism use revolute joints, which connect three different rigid bodies (see Figure 5. points A, C, D), but as is clear from the Figure 3., flexure joint can connect only two relatively rigid bodies with elastic element. Therefore the kinematical analysis of some modifications such device was made for gaining structure which is build from revolute joint which connect only two rigid parts. Other

problem is, that we will use designed mechanism as one building part of other devices, for instance precise positioning micro-stage, therefore it is necessary to design such device, where straight-line output motion will not be produced by a point but minimal one edge. All kinematical analysis was made in MATLAB SimMechanics toolbox.

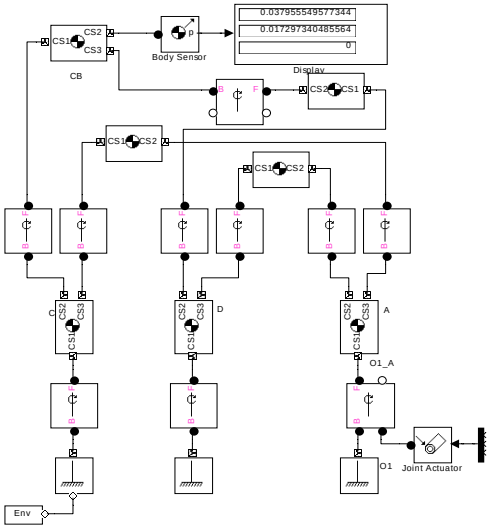

a)

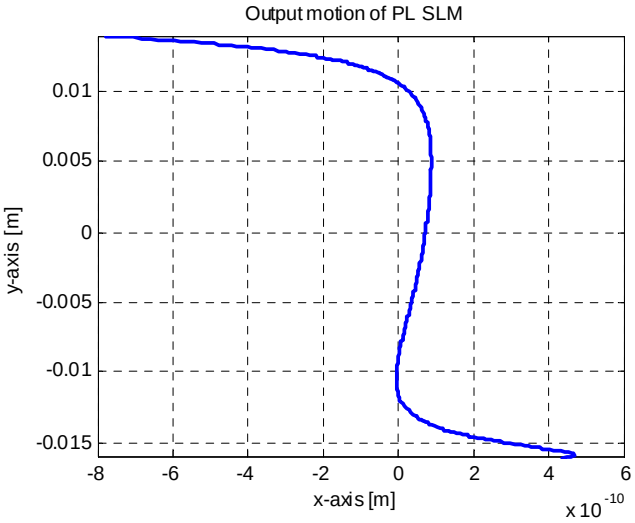

b)

Figure 6 a) Kinematic model of Peaucellier-Lipkin straight line mechanism in MATLAB SimMechanic toolbox, b) trajectory of output point of analyzed PL SLM

Kinematic analysis of some modifications of Peaucellier-Lipkin mechanism was analysed. All modifications were made with respect to the pole of planar displacement, which is that point which does not move under an arbitrary planar operator. It is unique, unless the planar operator is a pure translation. An operator can be related to a different frame by pre- and post-multiplying by the coordinate transformation to the different frame and its inverse respectively. When related to the pole, the equivalent operator is a pure rotation [17].

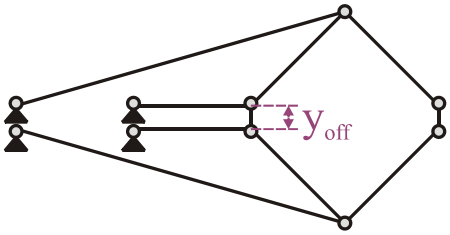

a)

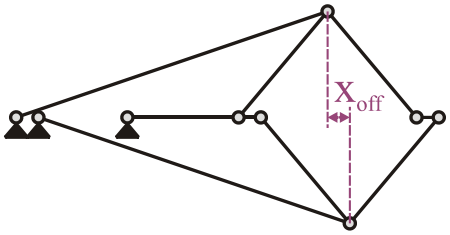

b)

Figure 7 Approaches how to transform joint in the point A, a) horizontal, b) vertical

Two approaches were analysed in the case of transformation of joint located at the point *A*. First one is based on horizontal movement and dividing of such joint (see Figure 7a)) and second approach was based on vertical movement and dividing of joint located on the point *A* (see Figure 7b)).

According to comparison of output movement of both structures the first approach based on horizontal movement of joints was completely removed from the further analysis.

In the case of transformation of the joint located on the point *C* or *D*, more approaches had been studied. The link *OC* (*OD*) can be connected to the link *AC* or *BC*, and in both cases minimum of three types of connections are possible. On the Figure 8 are shown all analysed modifications of joint *C*.

The results from the kinematic analysis of the modifications of Peaucellier-Lipkin mechanism are presented on the Table II.

Table II - Results from the kinematic analysis of modified Peaucellier-Lipkin mechanism

Modification	u_{err} / [m]	θ_{out} /[°]
mod_01a	47.04e-5	
mod_01b	7.00e-05	9.86
mod_02a	1.46e-04	11.38
mod_02b	4.63e-04	9.86
mod_03a	1.58e-03	2.232
mod_03b	1.44e-03	3.3
mod_03c	1.52e-04	8.84
mod_04a	2.24e-04	9.86
mod_04b	3.79e-04	9.86
mod_04c	1.17e-04	9.86

Considering to results from kinematic analysis of modified Peaucellier-Lipkin mechanism only two modifications (mod_02a and mod_04c) will be analysed below. The reason of choice is that such devices have smallest error in relationship to ideal straight-line motion, in other site, rotation of output edge is higher as in modification 3b and 3c, but the error in such modification is relatively high. In the Table II are modifications called mod_01a and mod_01b, such modifications are shown on the Figure 7, but in the case of mod_01a was added parallelogram to the link *CB*.

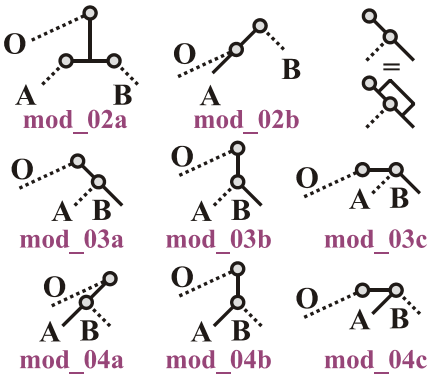

Figure 8 Analysed modifications of joint located in the point C

4.2 FEM ANALYSIS

For chosen kinematic structures of modified Peaucellier-Lipkin mechanism was designed compliant structures. The Comsol Multiphysics software was used as tool for design verifying and as tool replaced experimental results. In the Figure 9 are drawn compliant structures of analysed devices.

Input parameters were: material Polyamide PA2200 with Young's modulus *1.65GPa* and with Yield strength *48MPa*. The width of structures was *40mm* and height around *20mm*; thickness of both structures was *1mm*. Dimensions of flexure joint; radius 0.525mm, and joint thickness 0.175mm. Because we want to know relatively real results of mechanisms behaviour nonlinear solver was applied, in the case of linear solver the results were relatively good, when the error u_{err} was around between 5e-9 to 3.08e-7 (see Figure 9c) and 9d)), but as it is clear from the kinematic analysis (see Table II.) such values was expected in different range of values.

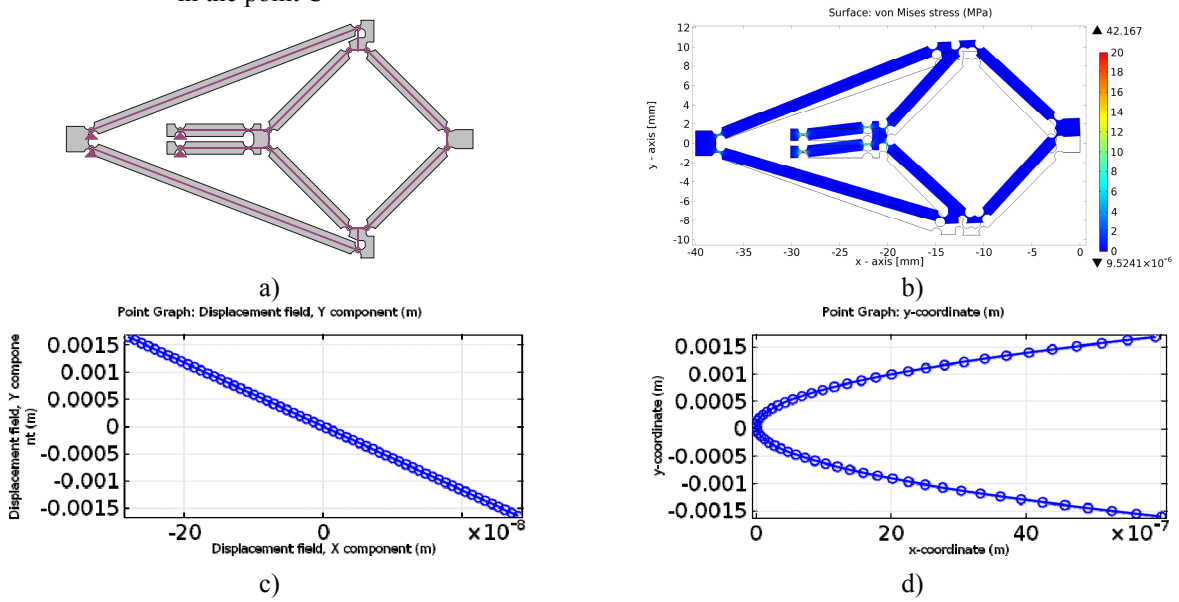

Figure 9 Compliant structures of modified Peaucellier-Lipkin mechanism a) mod_02a; b) Stress and deformation of compliant Peaucellier-Lipkin mechanism (modification mod_04c), Trajectory of output point of compliant PL SLM from FEM analysis c) linear solver, d) non-linear solver

In the Figure 9 b) it is shown how the compliant structure (mod_04c) is deformed and where the maximal stress is arisen. As is clear from this figure, the stress is concentrated in the flexure joint of small parallelogram; the reason of this is that on small parallelogram load is acted.

The Figure 10 showed the results from the FEM analysis of chosen compliant structures of modified Peaucellier-Lipkin mechanisms. On the figure the output trajectories are shown, last trajectory is from the FEM analysis of parallelogram, with equal dimensions. According to results it is clear that our design of compliant straight-line mechanisms has better properties as application of the parallelogram. On the other site our structure is more complex as easy parallelograms structure.

The numerical values of results from FEM analysis are:

- Mod_02a: u_{err}=15.5µm, θ_{out}=4.415°
- Mod_04c: u_{err}=5.92µm, θ_{out}=4.608°
- Parallelogram: u_{err}=37.9µm, θ_{out}=0.027°

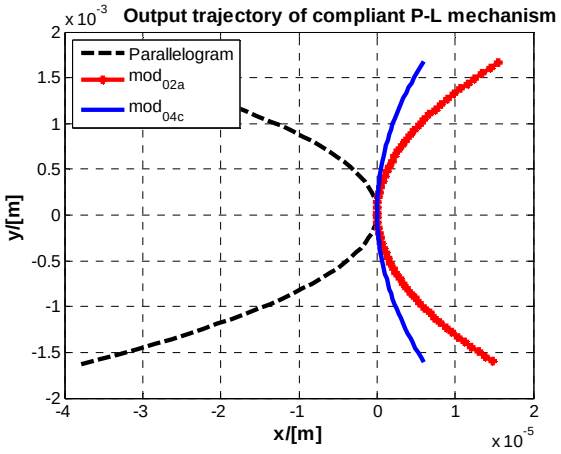

Figure 10 Output trajectories of modified compliant Peaucellier-Lipkin mechanisms compared with parallelogram

5 CONCLUSION

Structures of straight-line mechanisms are very often used in building of smart precise robotic devices, to which requirements based on high accuracy and precision with manipulation of micro- and nano- scale objects are put. The paper deals with problems in design process of one specific straight-line mechanism worked on principle of compact compliant mechanical structure. It was shown that theory about the pole of planar displacement could be utilized for transformation of revolute joint which connected more than two rigid bodies to group of joints which connect only two rigid bodies, what is necessary condition to design of compliant structure. The kinematic analysis of some modified Peaucellier-Lipkin straight-line mechanisms was made in MATLAB SimMechanics toolbox and after results evaluation only two modifications had been transformed to the compact compliant structure. The FEM analysis is confirmed rightness of both mechanisms design. The movement of the designed compliant straight-line mechanism is six-times better and closer to the straight-line motion as it is in the case of the parallelogram. In other site, the problem of rotation of output point/edge in values around plus/minus 2.3 degrees is not acceptable now.

In the future work the combination of advantages of designed straight-line mechanism and parallelogram should be done. The simple parallelograms structure and precision of compliant straight-line mechanism motion could be one way how to design compliant multi-axis positioning micro-stage whit small requirements to the control system, and with minimized parasitic deformations.

ACKNOWLEDGMENT

This paper presents the research work supported by the national scientific grant agency VEGA under project No.: 2/0048/13 “(Micro) Electro-mechanisms for robotics and extremely work spaces (environments).”

REFERENCES

[1] Hajduk, M., Semjon, J., Vagaš M., Design of the welding fixture for the robotic station for spot welding based on the modular concept, *Acta Mechanica Slovaca*. Vol. 13, no. 4, 2009, p. 30-36, ISSN 1335-2393

[2] Vagaš, M., Hajduk, M., Semjon, J., Páchniková, L., Jánoš, R., The view to the current state of robotics, *Advanced Materials Research*. Vol. 463-464, 2012, p. 1711-1714. - ISSN 1022-6680

[3] Lobontiu, N., *Compliant Mechanisms: Design of Flexure Hinges*, CRC Press, 2003, ISBN 0849313678

[4] Howell, L. L., *Compliant Mechanisms*, Wiley-IEEE, 2001, ISBN 047138478X, 459 p.

[5] Smith, T.S., *Flexures: elements of elastic mechanisms.* Gordon and Breach Science Publishers, 448 s., 2000, ISBN 90-5699-261-9

[6] We-Shing, H., *A Study on the Design and Analysis of micrograpper for Microassembly*, thesis. National Sun Yat-Sen University, 131 p, 2003, http://etd.lib.nsysu.edu.tw/ETD-db/ETD-search/view_etd?URN=etd-0710103-144403

[7] Havlík, Š., Hricko, J., Mechanisms of precise positioning devices – design study, *atp journal plus*, 2013, no. 1, p. 6-13. ISSN 1336-5010 (in slovak)

[8] Sharma, C. S., Purohit, K., *Theory of mechanisms and machines*, PHI Learning Pvt. Ltd., 2006, ISBN: 978-8120329010

[9] Vagaš, M., Varga, J., Design of modular gripper for industrial robot, *Applied Mechanics and Materials* Vol. 436, 2013, pp 351-357

[10] Beroz, J., Awtar, S., Bedewy, M., Sameh, T., Hart, A. J., *Compliant Microgripper with Parallel Straight-line Jaw Trajectory for Nanostructure Manipulation,* Proceedings of 26th American Society of Precision Engineering Annual Meeting, Denver, CO

[11] Liao, Y. G., Design and Analysis of a Robot End-Effector for Straight-Line Pick-and-Place Motion, *Journal of Applied Science & Engineering Technology*, vol 4, 2011, ISSN 1933-0421

[12] Tian, Y., Shirinzadeh, B., Zhang, D., Alici, G. Development and dynamic modelling of a flexure-based Scott–Russell mechanism for nano-manipulation, *Mechanical Systems and Signal Processing*, vol. 23, 2009, p. 957–978

[13] Information on http://kmoddl.library.cornell.edu/model.php?cat=S

[14] Pei, X., Yu, J., Zong, G., Bi, S., Design of Compliant Straight-line Mechanisms Using Flexural Joints, *Chinese journal of mechanical engineering*, Vol. 27, No. 1, 2014, p. 146 – 153

[15] blogspot.com, *Peaucellier–Lipkin and Sarrus Straight-line Mechanism*, http://mechanical-design-

handbook.blogspot.sk/2011/02/peaucellierlipki n-and-sarrus-straight.html, 2011

[16] Khurmi, R. S., Gupta, J. K., *Theory of Machines*, Eurasia Publishing House, 2008, ISBN 9788121925242

[17] Hollerbach, J. M., *Planar Transformations and Displacements*, University of Utah, http://www.bioen.utah.edu/faculty/BAMW/Be6900.html, 2000

ISSN 1590-8844
International Journal of Mechanics and Control, Vol. 16, No. 01, 2015

SEPARATE ADJUSTMENT OF TORQUE AND STIFFNESS FOR PNEUMATIC ROBOT ACTUATORS WITH ANTAGONISTIC ROTARY ELASTIC CHAMBERS

David Baiden*, ~ Oleg Ivlev*, ~

* Friedrich-Wilhelm-Bessel-Institute (FWBI) Research Company, Germany

~ Institute of Automation (IAT), University of Bremen, Germany

ABSTRACT

In modern applications robots share the workspace with humans for service tasks or they are even attached to the human body to provide assistance in movement training. A possible approach to realize "human-like" interaction is to adapt the robot compliance/stiffness appropriately, depending on the manipulation task and/or the capabilities of the individual person. This can for instance be accomplished with stiff actuators and evasive robot motions using force sensors (active compliance) or alternatively with inherent (passive) compliant actuators and an invariant position reference. With respect to safety, fluidic soft-actuators similar to pneumatic muscles are beneficial due to light-weight and adjustable passive compliance. However, even common position or force control for pneumatic muscles still remains challenging due to non-linear dependency on actuator displacement, air pressure as well as friction effects. This article presents an approach for separate torque and stiffness adjustment of direct acting soft-actuators with pneumatic *rotary elastic chambers* (REC) in antagonistic arrangement, which are usable for human-robot-interaction (HRI) applications.

Keywords: Pneumatic soft-actuators, antagonistic, stiffness, control

1 IMPORTANCE OF COMPLIANCE FOR HUMAN-ROBOT-INTERACTION

Robot application has expanded in recent years from conventional industrial pick and place scenarios to more safety critical tasks, where the demand is to operate in rehabilitation, service and medical surgery. In many applications physical contact between robot and human or even the attachment of a robotic exoskeleton to human limbs is intended. Therefore it is necessary to design robotic systems that exhibit compliant behaviour and are able to adapt to human movement patterns. The development of safe and dependable robots especially suitable for HRI should consider at least three important aspects: i) mechanical design, ii) actuation principle and iii) control architecture.

The first mandatory step is to minimize the robot mass. In many respects a lightweight construction with reduced moving masses is beneficial. Besides the case of an impact with end-effector based robots, the wearer of an exoskeleton would have to carry the entire weight of the robot, if there are no means of gravity compensation. But mass reduction is limited, since it depends on torque requirements as for instance the payload of the robot.

The next step in the design process is to introduce compliance, i.e. spring-like behaviour into the actuation system. In contrast to a stiff actuator, a compliant drive will not remain at the specified position. It will rather allow position deviations which depend on the interaction forces, imitating a more natural human-like behaviour. Compliance for a stiff actuator can be implemented by means of feed-back control, using sensors to measure interaction forces.

Contact author: David Baiden[1,2]

[1]Friedrich-Wilhelm-Bessel-Institute (FWBI)
Research Company
[2]Institute of Automation (IAT), University of Bremen
Otto-Hahn-Allee, 28359 Bremen, Germany
Email: baiden@fwbi-bremen.de

ISSN 1590-8844
International Journal of Mechanics and Control, Vol. 16, No. 01, 2015

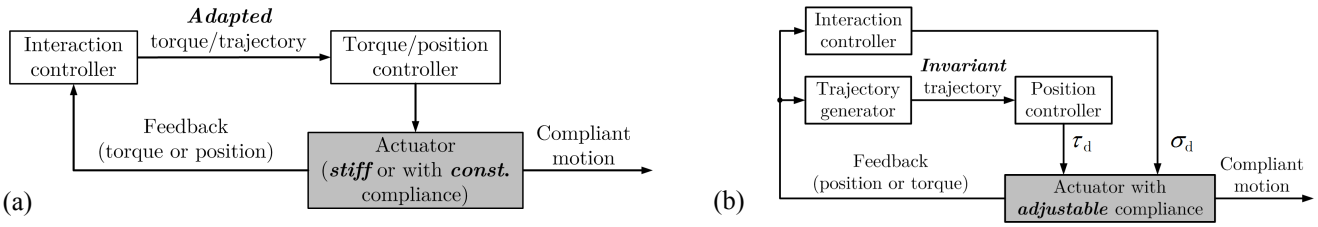

Figure 1 Realization examples to obtain compliant motion: (a) for stiff or constantly compliant actuators back-drivability and "human-like" interaction is imitated by torque or trajectory adaption; (b) with a fixed position reference the interaction controller creates back-drivability by direct actuator compliance adjustments.

This is denoted as *active compliance* and allows realizing back-drivability [1]. It is furthermore even possible to adjust compliance for the task requirement, but such an active system is not able to store energy and additional low controller bandwidth prevents to absorb high-frequency impacts. From this perspective the integration of a mechanical compliant element i.e. a spring, is specified as *passive compliance* and increases the safety level considerably.

It should be emphasised again, that inherent safety only results from naturally low impedance due to passive mechanical elements. However, the drawbacks are bandwidth restrictions that result in performance limitations. These relationships compel to compromise between safety and performance [2]. The desirable approach would be a combination between passive and active compliance, exploiting the benefits of inherent safety with adaptable compliance.

Control architecture is finally related to higher control layers, e.g. interaction controller and safety observer, whereas the latter is beyond the scope of this article. Interaction control should specify how a robot interacts with a human [3]. A frequently established fundament for "human-like" physical interaction control is based on impedance or stiffness (inverse of compliance) adaption [4]. With regard to the manipulation task and/or the capabilities of the individual person, the interaction controller should decide the level of adaption based on performance measures, which can be position errors or interaction forces [5, 6]. For *stiff* or *constantly compliant* actuators, this can be realized by evasive motions due to torque or trajectory adaption (Fig. 1 (a)). An alternative approach, which is followed here, is to use an invariant position reference and adjust the stiffness of the actuator, to allow position deviations (Fig. 1 (b)).

This paper presents an approach to independently adjust torque and stiffness of pneumatic soft-actuators with direct acting *rotary elastic chambers* (REC actuators) [7]. The purpose is to combine passive and active adjustable stiffness and integrate these modular soft-actuators into robots for safe physical HRI in orthopaedic and neurologic rehabilitation.

2 THE DIRECT ACTING ROTARY PNEUMATIC SOFT-ACTUATORS

The REC actuators are constructed of two fluid chambers in an antagonistic arrangement, similar to the principle of human muscles (Fig. 2). They are designed as direct acting rotary drives without gear and exhibit several distinctive properties like compactness and lightweight, paired with passive compliance [7]. Hydraulic or pneumatic operation is generally possible, if power supply and valve systems are appropriately adapted, such that oil, water or pressurized air is usable as fluid.

Air-pressured REC actuators convert pneumatic power into mechanical power and belong to the class of pneumatic muscles. If one chamber is inflated, i.e. the agonist, the internal air pressure increases and exerts a force to extend the chamber. The mechanical construction transfers this unidirectional expansion into a rotation and a torque is generated. In order to obtain turning into the opposite direction, the other chamber, i.e. the antagonist has to be charged. According to Fig. 2, the joint torque is the difference of the single chamber torques

$$\tau = \tau_2 - \tau_1. \quad (1)$$

Analysis and experiments in this paper are based on the patented pneumatic version, the *sREC* (DE 10 2011 081 727 A1) with skewed chambers (Fig. 3). However, control of this type of actuators is challenging due to non-linear behaviour and undesired effects like friction and hysteresis. For motion control two

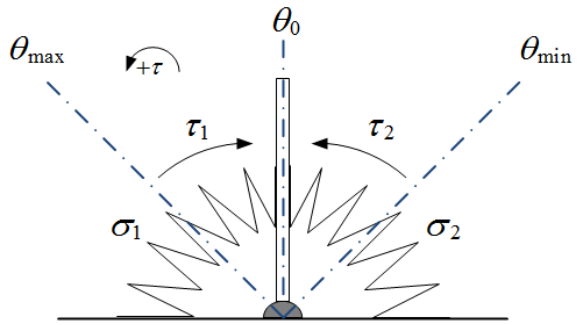

Figure 2 Working scheme of a fluidic soft-actuator with *rotary elastic chambers* (REC).

ISSN 1590-8844
International Journal of Mechanics and Control, Vol. 16, No. 01, 2015

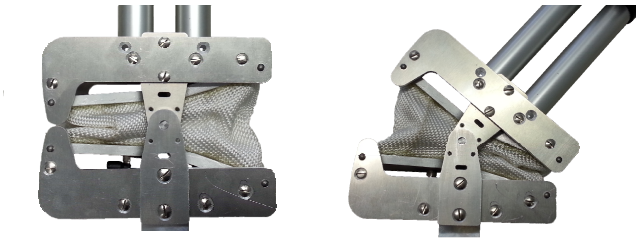

Figure 3 *sREC* actuator with skewed chambers (construction with unsymmetrical working range from 0 to approx. 45°).

valves and two pressure sensors are necessary to activate each chamber of a REC soft-actuator independently.

2.1 TORQUE MAP

In contrast to other approaches, where torque characteristics of actuators are mostly theoretically modelled with mathematical formulas based on physical relationships [8], the REC actuators are modelled experimentally. This procedure requires possessing plant and experimental setup in advance, but it is especially beneficial, if the internal structure of the system is unknown. Furthermore, quite precise models can be obtained with comparatively little effort in a short time.

The measurement routine is automated with a specifically developed test-rig shown in Fig. 4 [9]. Static torque values of one *single chamber* are captured in a specific sequence. Therefore an integrated electrical motor moves the actuator to predefined equally spaced angular positions across the whole operating range. At each position the pressure is varied with pressure proportional valves between 0–6 bar. The parameters are initial and final values of angle and pressure and in addition, angle and pressure resolutions $\delta\theta$ and δp, i.e. the step widths, are specified. The measurement starts according to Fig. 5 at the initial joint angle θ_1 with the initial pressure $p_{i,1}$, where each quantity can be either the minimum or maximum value and i indicates the number of the chamber. At the first position the pressure is stepwise incremented corresponding to $p_{i,k+1} = p_{i,k} + \delta p$ for $k = 1 \ldots n$. Before commanding the motor to move the actuator to the next angle $\theta_{j+1} = \theta_j + \delta\theta$, the chamber is exhausted. Then the process is repeated for $j = 1 \ldots m$, until the final angle is reached. Torque captures are only done in steady state, after

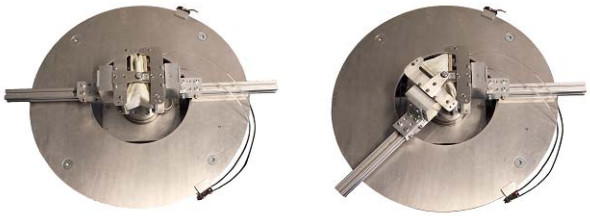

Figure 4 REC actuator mounted on the automated test-rig for torque characteristic measurements.
The generated torque is measured at different angle-pressure combinations.

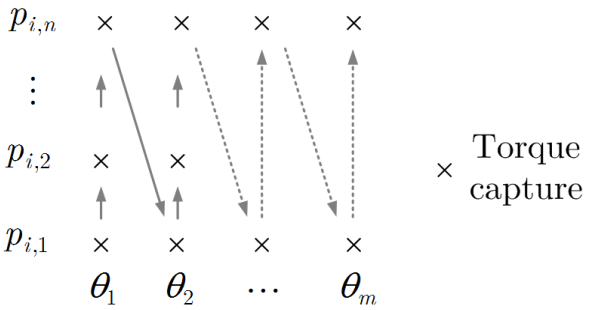

Figure 5 Sequence of static torque captures for one single chamber: the pressure is step-wise changed (increased or decreased) at a constant position.
After venting, the actuator is placed to the next constant position where the process is repeated.

torque and pressure values remain within a selectable tolerance band for at least 5 sec. During this time span the motor brake is activated and the pressure proportional valve has attained the specified set point. Quite good results have been obtained with resolutions for pressure $\delta p = 1$ bar and angle $\delta\theta = 2.5°$.

After data processing two static torque maps are obtained and stored in a look-up table. They reproduce the torque as non-linear function of pressure and angular position in form of

$$\tau_i = f(p_i, \theta) \tag{1}$$

where τ_i indicates the torque of one single chamber, p_i is the internal air pressure and θ is the joint angle.

Even though the opposite chamber is not actuated during measurement in the antagonistic setup, the stiffness influence of the material is still included. In order to account for friction effects, the average of two measurements with first increasing and then decreasing angle has been used.

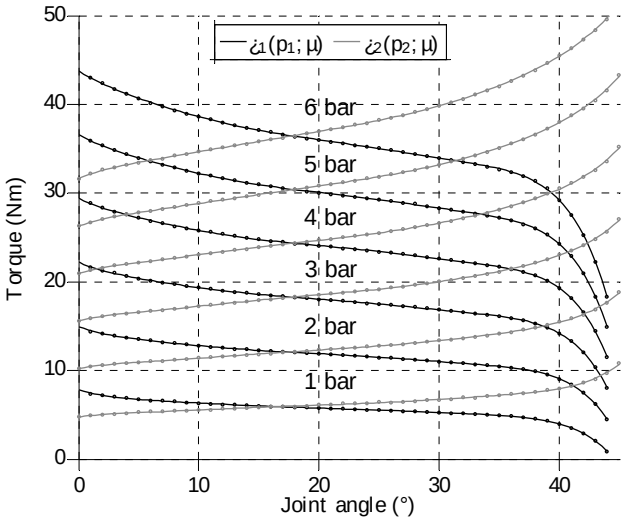

Figure 6 Averaged torque characteristic from two measurements with increasing and decreasing angle stored in data maps.

3 INDEPENDENT TORQUE AND STIFFNESS CONTROL

Stiffness control of actuators enables to adapt interaction forces of rehabilitation robots and is important with respect to human-like behaviour. In literature several approaches can be found, focusing mainly on position and stiffness control for linear pneumatic artificial muscles (PAM) or pneumatic cylinders. In this paper an approach for independent torque and stiffness adjustment of a rotary soft-actuator is presented, considering the individual torque characteristics of both pneumatic chambers.

3.1 EFFECTS OF THE DELTA-PRESSURE PRINCIPLE

In previous approaches that were mainly related to position control of the REC actuators, the motion control problem has been considered by applying the frequently used *delta-pressure* principle, as for example described in [10, 11]. This allows partitioning the single output of a position controller into two desired chamber pressures. Stiffness can be increased by adding the same offset pressure to both antagonistically arranged chambers, such that an additional torque is generated by each side

$$\begin{aligned} p_1 &= \Delta p + p_0 \\ p_2 &= -\Delta p + p_0 \end{aligned} \tag{2}$$

where p_1, p_2 are the resulting internal chamber pressures, Δp is the output of the position controller, i.e. a differential pressure and p_0 is the initial offset pressure. In this way the total pressure in each chamber is composed of one component, which should be solely responsible for motion (Δp) and another one, which only should have influence on stiffness (p_0), providing an adjustable compliant behaviour. With the choice $|\Delta p| \le p_0 \le p_s - |\Delta p|$, the resulting chamber pressures are limited to $0 \le p_{(1,2)} \le p_s$, where p_s ist the supply pressure. Fig. 7 illustrates the simultaneous change of the two chamber pressures depending on the Δp-variable for several different constant offsets. The offset pressure should be selected, such that the adjustment ranges for the chamber pressures lay within usable bounds and both chambers participate simultaneously. In other words, a too low offset pressure value may lead to one-sided actuation by one chamber only, if a high controller output occurs. Likewise a too high value leads to desired values above the supply pressure. For equal internal pressures each chamber of a *symmetrically constructed* REC actuator only generates the same torque at the centre position, namely the natural equilibrium at θ_0. Unequal chamber pressures, caused by arbitrary numbers of combinations between Δp and p_0 result in other torque balances at new equilibrium positions different from the natural equilibrium. The delta-pressure approach is appealing due to its simplicity, but there are several noteworthy limitations with respect to HRI control, as explained subsequently:

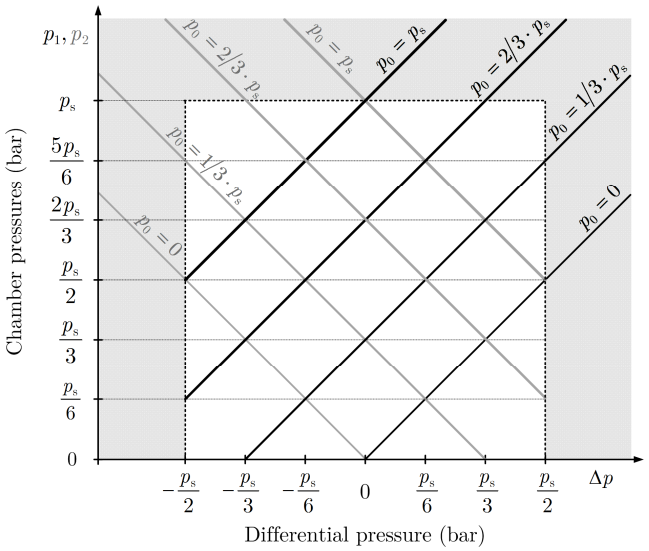

Figure 7 Resulting chamber pressures obtained by the delta-pressure principle with respect to the supply p_s.

- *Nominal value*: it is not possible to specify a particular nominal stiffness value in terms of the SI unit Nm/rad. The angle depending spring-like properties are not modelled and thus the resulting behaviour is not predictable.
- *Manual deflection*: another issue resulting from the same reason is recognizable by a manual deflection from any arbitrary equilibrium position, as indicated by Fig. 8. Assuming constant values for Δp and p_0, a displacement, which is a linear change in angle, leads to a generation of non-linear restoring torques, meaning non-constant or *variable stiffness*.
- *Position deviation*: if at the natural equilibrium position the initial pressure p_0 and thus both chambers pressures are equally increased, the position remains constant. At any other equilibrium an increase of the p_0-value promotes a deviation from the current position due to diverse single torques that do not compensate each other. Thus the actuator tends to move back to its natural equilibrium. This effect is not only relevant for open loop accuracy, but also affects a closed-loop position controller and requires *controller parameter adjustment* for any other p_0-value.

Even though the delta-pressure principle enables to adjust compliance around a set point, adding a constant offset pressure for both chambers without incorporating the non-linear relation between pressure, angle and torque, revealed by the torque characteristic (Fig. 6) does not result in comprehensible defined spring-like properties. While the delta-pressure principle may be applicable in combination with a robust position controller, it cannot be utilized, when the inverted torque characteristics are applied for plant linearization and to enable torque control. The inverted relation directly dictates the total necessary chamber pressures

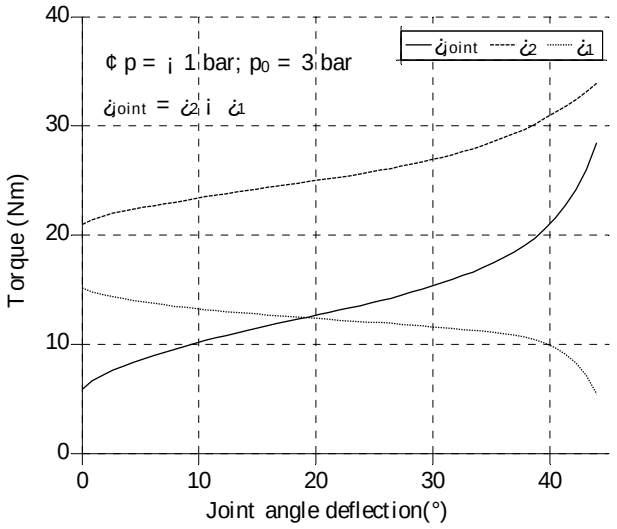

Figure 8 Manual deflection across the whole operating range at constant chamber pressures (Δp = -1 bar, p_0 = 3 bar): a linear change in angle leads to a generation of different non-linear restoring torques that do not compensate.

$$\boldsymbol{p}_{\mathrm{d}} = f^{-1}(\tau,\theta) = [p_{1\mathrm{d}} \quad p_{2\mathrm{d}}]^{\mathrm{T}} \tag{3}$$

without any possibility to adjust the stiffness behaviour. Any additional offset pressure would distort the torque balance and subsequently cause a drift from the equilibrium position as well.

3.2 OTHER APPROACHES

Force and stiffness control for pneumatic cylinders has been demonstrated by Shen and Goldfarb [12] and similarly by Taheri *et al.* [13]. Due to sliding-mode controller design in the first case and back-stepping sliding-mode technique with valve dynamics incorporation in the latter case, impressive performance of the controllers was demonstrated with bandwidths of up to 4 Hz for sinusoidal torque and stiffness tracking. In [14] a sequential position and compliance control concept for enhanced safety of a 2 DOF pneumatic manipulator is presented. The actuator model is based on the commonly used representation by mass, spring and damping parameters. Because muscles are assumed to be identical, their angle dependency is expected to compensate. Ariga *et al.* implemented an equilibrium-point position and stiffness control for a set of antagonistic PAMs [15]. Two variables, representing the relation between the two muscle pressures and the difference of them respectively, allow adjusting position and stiffness intuitively. Due to the more linear PAM characteristics muscle forces are approximated linear with respect to contraction length and pressure. Another mechanical equilibrium model based on a geometrical approach is proposed by Nakamura *et al.* in order to compensate instantaneous load changes during position control [16]. Model and physical actuator show well correspondence, but the model establishment is quite sophisticated and furthermore torque feedback is required.

3.3 PARAMETRIC TORQUE CHARACTERISTIC

For torque-only model-based control, data maps can be utilized for plant linearization. However, in order to establish a linear relation between joint torque, joint stiffness and the two chamber pressures, neither the delta-pressure approach is suitable, nor data-based torque maps can be applied directly. Instead, parametric models are established that are identified based on the same measurement, which was initially used to create the torque maps. The parametric model for each torque characteristic can be approximated sufficiently accurate with linear pressure dependency and nonlinear angle dependency by an *individual polynomial* of type

$$\tau_i = \alpha_i(\theta)\, p_i + \beta_i(\theta) \tag{4}$$

where i $\in$ [1,2] indicates the chamber number. The term $\alpha_i(\theta)$ represents pressure and angle proportional constants, while $\beta i(\theta)$ describes angle related coefficients only. They both describe the slopes and the intercepts of the approximated curves as polynomials

$$\alpha_i(\theta) = \sum_{j=0}^{4} a_{ij}\theta^j \tag{5}$$

$$\beta_i(\theta) = \sum_{j=0}^{5} b_{ij}\theta^j \tag{6}$$

where j is the index number. Substituting Eq. (5) and (6) into (4) results in the following expression

$$\begin{aligned}\tau_i = {} & b_{i5}\theta^5 + a_{i4}\theta^4 p_i + b_{i4}\theta^4 + a_{i3}\theta^3 p_i + b_{i3}\theta^3 \\ & + a_{i2}\theta^2 p_i + b_{i2}\theta^2 + a_{i1}\theta p_i + b_{i1}\theta \\ & + a_{i0} p_i + b_{i0}\end{aligned} \tag{7}$$

where the parameter bi0 can be understand as a global offset. By applying the least squares method, model parameters are estimated and fitted to the data sets of the torque maps. The obtained parametric torque characteristics of both chambers are plotted according to Fig. 9 for pressure values $p_i \in [1, 2, \ldots, 6]$, revealing similar but not symmetrical trend.

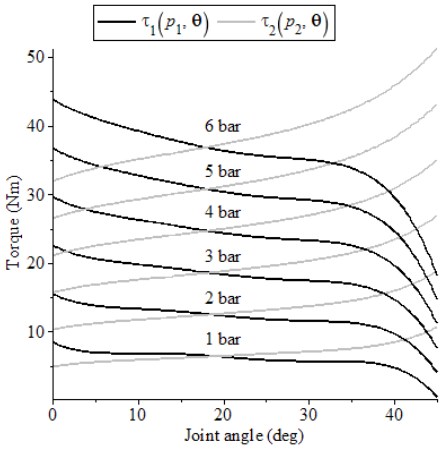

Figure 9 Approximated averaged torque characteristics of both chambers represented by individually fitted polynomials.

3.4 MODEL WITH INDEPENDENT TORQUE AND STIFFNESS INTERFACES

The parametric torque characteristics are used to model the joint torque, which is given by the difference of the single chamber torques

$$\begin{aligned}\tau &= \tau_2 - \tau_1 \\ &= \alpha_2(\theta)\, p_2 + \beta_2(\theta) - (\alpha_1(\theta)\, p_1 + \beta_1(\theta))\end{aligned} \tag{8}$$

while the joint stiffness is defined as the derivative of the joint torque with respect to the joint angle and must equal the sum of the single stiffness functions

$$\sigma = \frac{\partial \tau(p_2, p_1, \theta)}{\partial \theta} = \sigma_2 + \sigma_1 \tag{9}$$

where for $i \in [1, 2]$ each chamber stiffness is represented by

$$\begin{aligned}\sigma_i &= (4a_{i4}\theta^3 + 3a_{i3}\theta^2 + 2a_{i2}\theta + a_{i1})\, p_i \\ &\quad + (5b_{i5}\theta^4 + 4b_{i4}\theta^3 + 3b_{i3}\theta^2 + 2b_{i2}\theta + b_{i1}) \\ &= \Gamma_i(\theta)\, p_i + \Omega_i(\theta).\end{aligned} \tag{10}$$

For simplification Eqs. (7)–(10) are merged into a matrix equation

$$\begin{bmatrix}\tau \\ \sigma\end{bmatrix} = \mathbf{E}\begin{bmatrix}p_1 \\ p_2\end{bmatrix} + \boldsymbol{r} \tag{11}$$

where

$$\begin{aligned}\mathbf{E}_{(2x2)} &= \begin{bmatrix}-\alpha_1(\theta) & \alpha_2(\theta) \\ \Gamma_1(\theta) & \Gamma_2(\theta)\end{bmatrix}, \\ \boldsymbol{r}_{(2x1)} &= \begin{bmatrix}\beta_2(\theta) - \beta_1(\theta) \\ \Omega_2(\theta) + \Omega_1(\theta)\end{bmatrix}\end{aligned} \tag{12}$$

for $\det(\mathbf{E}) \neq 0$, rearranging of Eq. (11) leads to

$$\begin{bmatrix}p_1 \\ p_2\end{bmatrix} = \mathbf{E}^{-1}\left(\begin{bmatrix}\tau_d \\ \sigma_d\end{bmatrix} - \boldsymbol{r}\right). \tag{13}$$

The obtained system in Eq. (13) represents the REC actuator compliance model where the input values are desired torque τ_d and desired stiffness σ_d and the outputs are the two required pressure values. These are passed to the subsequent pressure controller as desired values $\boldsymbol{p}_d = [p_{1d}\ p_{2d}]^T$ according to Fig. 10, representing the implemented structure for real-time control. The pressure-valve subsystem is exchangeable for using either of-the-shelf pressure proportional valves or mass-flow proportional valves with specific pressure controllers that consider the dynamics of the pneumatic subsystem.

For the proposed approach it is important that the torque-pressure relationship is preferably linear with respect to pressure, such that the variable p can be incorporated into the polynomials with first order and thus Eq. (11) can easily be solved. Furthermore the order of the joint angle θ should be chosen relatively high, to preserve accuracy in the stiffness calculation after torque derivation.

3.5 SIMULATION ANALYSIS

Preceding simulation is conducted to investigate the expectable behaviour and understand the specific properties of the REC actuator. The modelled joint stiffness by Eq. (9) is plotted in Fig. 11 for several equal and distinctive pressure combinations in both chambers, revealing strong nonlinearity. As mentioned before, each polynomial contains the influence of the opposite chamber. The quite stiff chamber material already provides a spring-like behaviour at zero pressure, therefore a minimum value 0.4 bar is required to compensate the *passive stiffness*. Due to the fact, that the pneumatic chambers cannot contract, it is only possible to control stiffness actively by varying pressure upwards, beginning from this level.

The next aspect of interest is the required pressure range. The graph in Fig. 12 contains both chamber pressures vs. joint angle for two contrasting examples a) low torque with high stiffness: $\tau_d = 1$ Nm, $\sigma_d = 0.4$ Nm/deg and conversely b) high torque with low stiffness $\tau_d = 15$ Nm, $\sigma_d = 0.2$ Nm/deg. Comparing again with Fig. 11, it is obvious that joint stiffness at the edges of the operating range is passively high and in these areas less pressure is necessary. By trend, for high stiffness values both pressures are increased, while for high torque values (either positive or negative) one pressure value is increased and the other one is reduced.

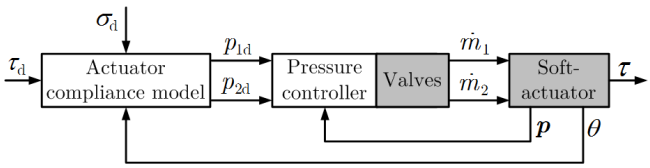

Figure 10 Control structure for independent torque and stiffness adjustment.

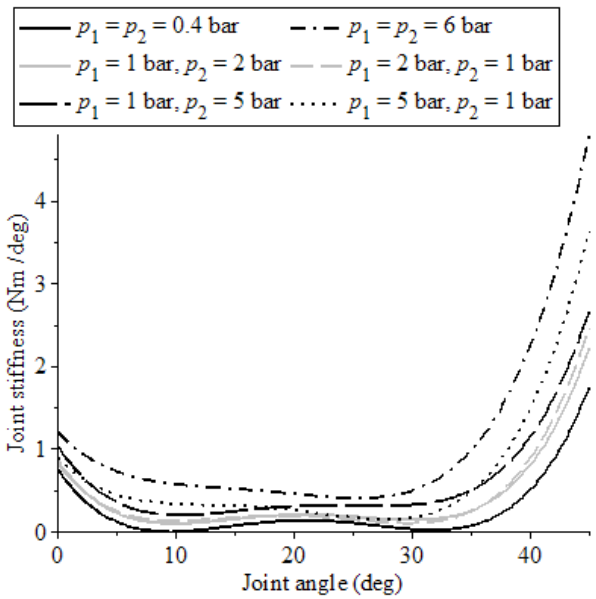

Figure 11 Simulated joint stiffness at different pressure combinations.

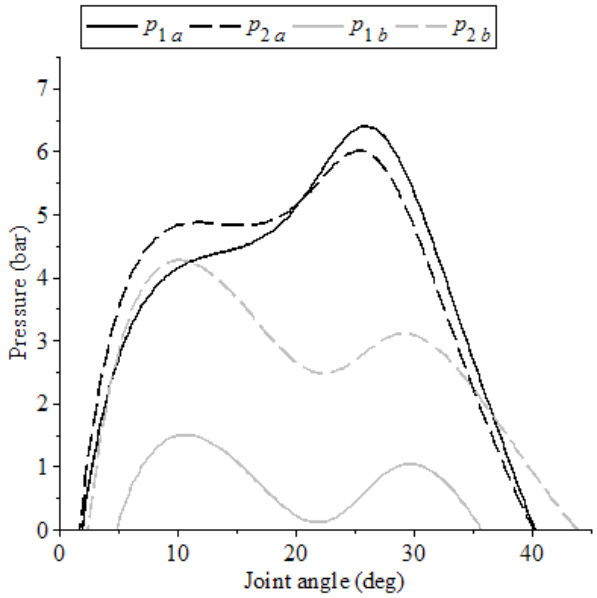

Figure 12 Simulation of required pressures for two example combinations of desired values: low torque with high stiffness (black lines) and high torque with low stiffness (grey lines).

In contrast to the previous torque-only control, the stiffness option reduces the maximal achievable joint torque. Based on these observations it can be concluded, that large torque commands lead to one-sided actuation which is in general similar to the toque-only approach, however with reduced accuracy. Furthermore because torque and stiffness are coupled by pressure, assuming a supply range between 0–6 bar, the desired values need to be chosen carefully in order to remain within valid pressure limits.

4 EXPERIMENTAL RESULTS

The control structure according to Fig. 10 was implemented on a real-time signal processor board (*dSPACE, DS1102*) and model verification has been conducted by using the previously introduced test-rig (Fig. 4). For pressure control the integrated pressure proportional valves (*FESTO, VPPM-6L-L-1-G18-0L10H*) were utilized. The generated actuator torque and pressures were monitored with the integrated torque and pressure sensors (*HBM, TB1A* and *Sensortechnics, CTE 700 GU0*). Motor commanding and data capturing have been done manually. Three kinds of experiments have been carried out to illustrate the controller reaction during steady position, for unbounded conditions and furthermore to involve external interaction. To exclude gravity effects the actuator was horizontally orientated.

4.1 TORQUE AND STIFFNESS TRACKING AT CONSTANT POSITION

In the initial series of experiments the actuator was connected to the lever of the test-rig to fix it at any arbitrary constant position. At joint angle $\theta = 35°$, first a constant desired torque $\tau_d = -15$ Nm in combination with a sinusoidal stiffness $\sigma_d = 0.4 \pm 15$ Nm/deg at frequency $f_\sigma = 0.3$ Hz was adjusted (Fig. 13 (a)). Despite pressure variation of $p_1 = 4.45 \pm 0.95$ bar and $p_2 = 1.4 \pm 0.8$ bar respectively, torque could be maintained nearly constant. Due to torque control, stiffness could not be measured directly by deflection experiments, but stiffness changes are noticeable in concurrent pressure adaption. Next, at the same angular position the shapes of the input trajectories were changed to sinusoidal torque $\tau_d = -15 \pm 5$ Nm, $f_\sigma = 0.2$ Hz and constant stiffness $\sigma_d = 0.5$ Nm/deg. Fig. 13 (b) shows that despite

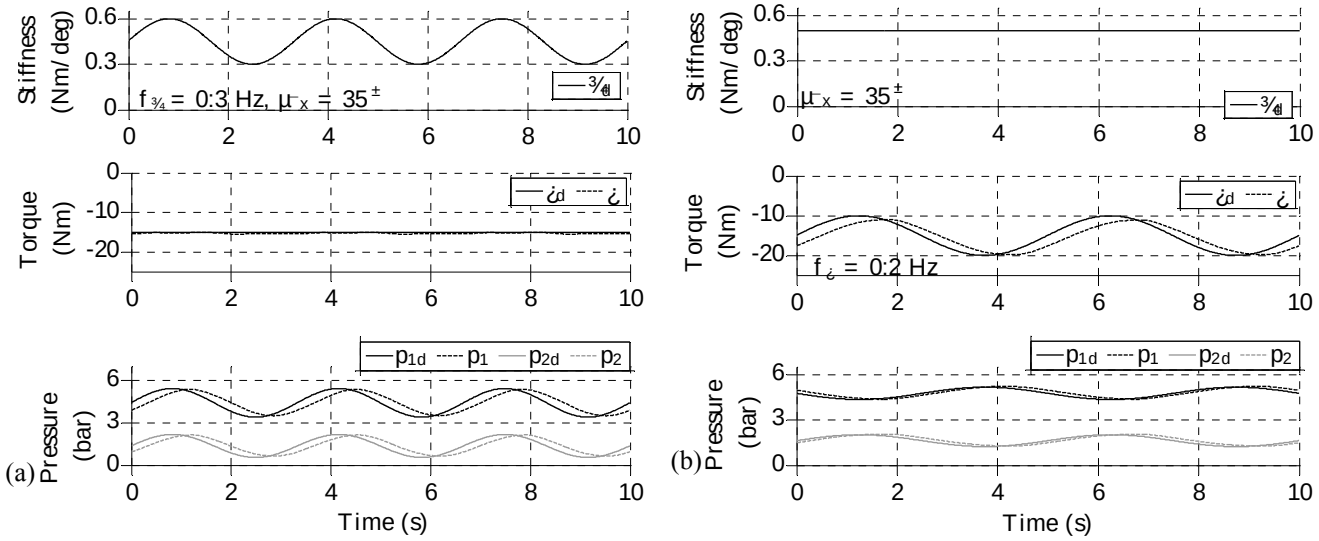

Figure 13 Experiments at constant position: (a) desired sinusoidal stiffness: $\sigma_d = 0.4 \pm 15$ Nm/deg, $f_\sigma = 0.3$ Hz and desired const. torque $\tau_d = -15$ Nm; (b) desired const. stiffness: $\sigma_d = 0.5$ Nm/deg and desired sinusoidal torque: $\tau_d = -15 \pm 5$ Nm, $f_\sigma = 0.2$ Hz.

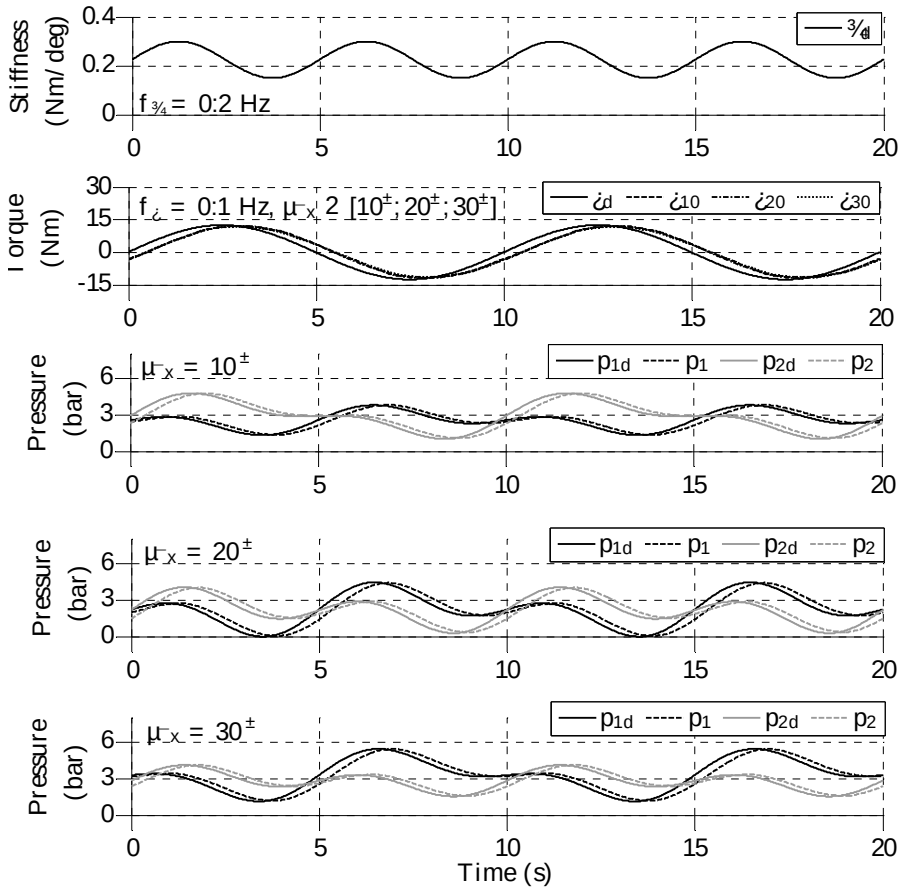

Figure 14 Superposition of desired sinusoidal torque and stiffness profiles at three different fixed angles.

smaller pressure variations $p_1 = 4.75 \pm 0.45$ bar and $p_2 = 1.65 \pm 0.35$ bar, torque is tracked with delay. Finally desired values for torque and stiffness have been set simultaneously with $f_\sigma = 0.2$ Hz and $f_\tau = 0.1$ Hz at $\theta_{fix} = \in [10°, 20°, 30°]$ confirming the concept with similar results (Fig. 14).

4.2 STIFFNESS TRACKING UNDER UNCONSTRAINED CONDITION

In this experimental setup the actuator was detached from the motor to be unrestricted and the joint angle was measured with the actuator's integrated magnetic sensor (*AMS, PRAS 21*). Since toque is not measurable in this test, the desired torque was set to zero while stiffness was stepwise increased by $\Delta\sigma_d = 0.05$ Nm/deg and the focus was put on pressure and position deviations. Ideally the actuator should find its natural equilibrium and remain at this position for every adjusted stiffness value. As expected, both chamber pressures were simultaneously increased in accord with stiffness commands (Fig. 15), but this trial also exposed deficiencies in pressure control. Small position deviations of $\Delta\theta = \pm 1.8°$ could be observed that are attribute to model inaccuracies.

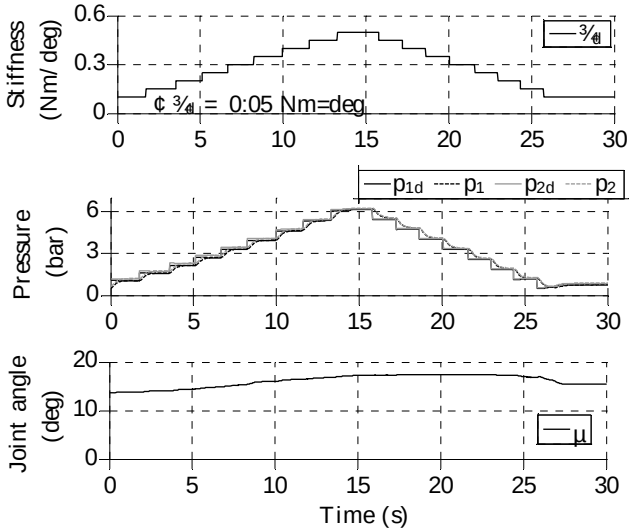

Figure 15 Step-wise change of desired stiffness with $\Delta\sigma_d = 0.05$ Nm/deg.

4.3 EMULATED HUMAN-ROBOT-INTERACTION

For the intended application in rehabilitation devices with physical contact to persons and adaptable HRI, the control response to external influences under dynamic conditions should be investigated. Therefore the REC was attached to the test-rig lever again and deflected by the motor in the sequence $\theta_d = 5{-}35{-}5°$ with an angular velocity of $\dot{\theta}_d = 2$ deg/s. The desired torque was set to $\tau_d = 5$ Nm, while the desired stiffness was specified to $\sigma_d = 0.15$ Nm/deg. Pressure values were tracked well in this test, however the maximal torque error of $\Delta\tau = 2$ Nm seems to be subject to uncompensated hysteresis effects due to the use of averaged torque characteristics.

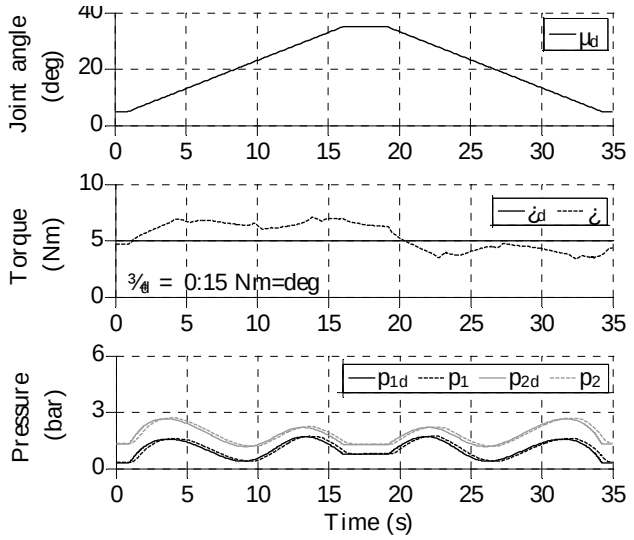

Figure 16 Torque and stiffness control under dynamic conditions with $\tau_d = 5$ Nm, $\sigma_d = 0.15$ Nm/deg, position sequence $\theta_d = 5{-}35{-}5°$ and angular velocity $\dot{\theta}_d = 2$ deg/s.

5 CONCLUSION AND FUTURE WORKS

First the importance of compliant actuation was discussed and rationales to develop pneumatic actuators with adjustable stiffness were exposed. Furthermore the limitations of the frequently applied delta-pressure principle have been explained in this paper.

Beginning from an experimental data-based model of the pneumatic REC actuators, torque and stiffness relationships have been derived and approximated by polynomials. The new model offers independent torque and stiffness interfaces for subsequent higher control layers, e.g. human-robot-interaction controllers. An explicit torque input might be advantageous, if the robot controller is based on torque control, which also enables to compensate for inaccuracies in a kinematic robot chain, especially when compensation of robot gravity is incorporated.

The presented model is able to cope with high torque-angle non-linearity and is basically applicable to all types of pneumatic muscles. Torque tracking performance could certainly be improved by utilizing mass flow proportional valves and applying the same model-based pressure controller considering pressure dynamics, as already done in parallel ongoing research work. The approach requires the torque characteristic to be preferably linear with respect to pressure, in order to solve the approximated polynomials easily. Thus it is worthwhile to consider this aspect in future actuator chamber design. Similar to the previous torque-only control, there is neither torque nor stiffness feedback in the open loop structure. The choice of desired torque and stiffness combinations must be valid for keeping necessary pressure values within limited ranges. This is subject for future work as well as torque-angle hysteresis compensation.

6 ACKNOWLEDGEMENTS

This work was developed under the grant 13EZ1121A within the joint research project KoBSAR-II, supported by the German Federal Ministry of Education and Research (BMBF).

REFERENCES

[1] Zinn M., Roth B., Khatib O., and Salisbury J. K., A new actuation approach for human friendly robot design. *The international journal of robotics research*, vol. 23, no. 4–5, pp. 379–398, 2004.

[2] Bicchi A. and Tonietti G., Fast and "soft-arm" tactics [robot arm design]. *Robotics Automation Magazine, IEEE*, vol. 11, no. 2, pp. 22–33, June 2004.

[3] Marchal-Crespo L. and Reinkensmeyer D. J., Review of control strategies for robotic movement training after neurologic injury. *Journal of neuroengineering and rehabilitation*, 6(1), 20, 2009.

[4] Reinkensmeyer D. J., Kahn L. E., Averbuch M., McKenna-Cole A., Schmit B. D. and Rymer W. Z., Understanding and treating arm movement impairment after chronic brain injury: progress with the ARM guide. *Journal of rehabilitation research and development*, 37(6), pp. 653–662, 2000.

[5] Krebs H. I., Palazzolo J. J., Dipietro L., Ferraro M., Krol J., Rannekleiv K., Volpe B. T. and Hogan N., Rehabilitation robotics: Performance-based progressive robot-assisted therapy. *Autonomous Robots*, 15(1), pp. 7–20, 2003.

[6] Riener R., Lunenburger L., Jezernik S., Anderschitz, M. Colombo G. and Dietz V., Patient-cooperative strategies for robot-aided treadmill training: first experimental results. *Neural Systems and Rehabilitation Engineering, IEEE Transactions on*, 13(3), pp. 380–394, 2005.

[7] Ivlev O., Soft fluidic actuators of rotary type for safe physical human-machine interaction. In *Rehabilitation Robotics, 2009. ICORR 2009. IEEE International Conference on*, pp. 1–5, June 2009.

[8] Kelasidi E., Andrikopoulos G., Nikolakopoulos G., and Manesis S., A survey on pneumatic muscle actua-

tors modelling. In *Industrial Electronics (ISIE), 2011 IEEE International Symposium* on, pp. 1263–1269, June 2011.

[9] Rehr J. and Ivlev O., Automated torque testing machine for fluidic rotary soft-actuators. *tm-Technisches Messen*, vol. 78, no. 10, pp. 431–438, 2011.

[10] Daerden F., Lefeber D., Verrelst B. and Van Ham R., Pleated pneumatic artificial muscles: actuators for automation and robotics. In *Advanced Intelligent Mechatronics, 2001. Proceedings. 2001 IEEE/ASME International Conference on* (Vol. 2, pp. 738–743). IEEE.

[11] Tsagarakis, N. G. and Caldwell, D. G., Development and control of a 'soft-actuated' exoskeleton for use in physiotherapy and training. *Autonomous Robots*, 15(1), pp. 21–33, 2003.

[12] Shen X. and Goldfarb M., Simultaneous force and stiffness control of a pneumatic actuator. *Journal of Dynamic Systems Measurement and Control-transactions of The Asme*, vol. 129, no. 4, pp. 425–434, 2007.

[13] Taheri B., Case D., and Richer E., Design of robust nonlinear force and stiffness controller for pneumatic actuators. In *Decision and Control (CDC), 2012 IEEE 51st Annual Conference on*, pp. 1192–1198, Dec 2012.

[14] Choi T.-Y., Choi B.-S., and Seo K.-H., Position and compliance control of a pneumatic muscle actuated manipulator for enhanced safety. *Control Systems Technology, IEEE Transactions on*, vol. 19, no. 4, pp. 832–842, July 2011.

[15] Ariga Y., Pham H., Uemura M., Hirai H., and Miyazaki F., Novel equilibrium-point control of agonist-antagonist system with pneumatic artificial muscles. In *Robotics and Automation (ICRA), 2012 IEEE International Conference on*, pp. 1470–1475, May 2012.

[16] Nakamura T., Tanaka D., and Maeda H., Joint stiffness and position control of an artificial muscle manipulator for instantaneous loads using a mechanical equilibrium model. *Advanced Robotics*, vol. 25, no. 3–4, pp. 387–406, 2011.

ISSN 1590-8844
International Journal of Mechanics and Control, Vol. 16, No. 01, 2015

SAFETY AND LOGISTICS PERFORMANCE EVALUATION OF A RFID SYSTEM IN A BLOOD TRANSFUSION CENTRE

Gianluca Borelli * Pier Francesco Orrù ** Francesco Zedda**

* AOB Azienda Ospedaliera Brotzu, Piazza Ricchi,1 09100 Cagliari (Italy)

** Università degli Studi di Cagliari, via Marengo 2, 09100 Cagliari (Italy)

ABSTRACT

This papers aims to describe the development framework of a Transfusion Medicine RFId application, which was designed in order to enhance patient safety and in order to improve blood inventory management processes.
In the first part of the study, a reverse engineering of present processes (As-Is) was performed through two analysis tools : Flow Charts and Activity Forms. In the second part of the study, an RFId-based processes re-engineering has been designed in order to reduce criticalities and to improve Transfusion Medicine service performance. Then a Return on Safety (ROS) assessment was performed through a RFId-enabled processes FMECA and through Key Performance Indexes (KPI) design. ROS assessment showed a clinical risk reduction in every blood chain process.

Keywords: RFID, Blood supply chain, clinical risk

1 INTRODUCTION

Clinical Risk reduction, safety and quality improving of Italian Healthcare system services, is nowadays a priority and Transfusion medicine is one of the most interesting intervention areas. Due to high complexity of transfusion process, characterized by various checks, analysis and handlings of blood assets, probability of human errors is still the most dangerous. Infectious exposure and mistransfusion (mismatch between patient and assigned haemocomponent blood group) are the most serious transfusion risks.
Recent international studies reveal that pre analytical and clinical errors, which include incorrect ABO bedside testing and mistaken or missing patient identity check, represents about 80% of total adverse events [1].
Particularly "Acute Hemolytic Reaction", due to mistransfusion, has deadly consequences in about 10% of cases [2].

Contact author: Pier Francesco Orrù[1]

[1] Address: Università degli Studi di Cagliari
via Marengo 2, 09100 Cagliari (Italy)
E-mail: pforru@unica.it

Statistical data of ABO-incompatible RBC transfusions incidence are relevant in different countries (rarely data are collected with standard procedures): Germany 1:36000; USA (New York) 1:38000; France 1:135207 (including autologous blood); Ireland 1:71428 [1].
Viral transmission has been reduced since the early '90, thanks to the introduction of compulsory tests based on sierology and Nucleic Acid Amplification Technique (NAT) [1]. Estimates of the risk per unit of blood in the post-NAT era are approximately 1:1,900,000 for HIV and 1:1,600,000 for HCV [3].
This study aims to devise a method to enhance patient safety, by reducing error rate of mistransfusion and viral transmissions, to improve blood inventory management processes through an RFID-based process reengineering and also to estimate the potential clinical risk reduction [4] [5].
This study is the experience developed at Blood Transfusion Centre (BTC) of Brotzu Hospital (AOB) in Cagliari (Sardinia Island, Italy). Brotzu Hospital Blood Transfusion Centre operates in all standard transfusion processes: blood and platelet letting, therapeutic aphaeresis, blood-components separation, typing, analysis and assignment. About 50,000 blood units are treated every year, 60% of which are imported from other Italy regions in order to cover high Sardinian demand.

2 REVERSE ENGINEERING

In the first part of the study, a reverse engineering of present processes was performed, in order to define information and material flows and to analyze infrastructure and technology present status. Visits in Hospital Unit wards and in the Labs during working hours were scheduled and operators answered to analyst's questions about procedures. This analysis step involved BTC and two Operative Units where transfusions are often performed: Transplant Unit and Brain Surgery Unit. In the first one, all processes are performed in a standard traditional way, while the second one was studied because it is the only Operative Unit where both paper and digital blood request forms are sent to BTC. Only ward patient bedside transfusion were considered for the study; intra-operative transfusions were disregarded.

Two main analysis tools were used: Flow Charts and Activity Forms. Flow chart is an algorithm graphical language. It allows to describe all process operations as a scheme. More than 20 Flow charts were designed, including both deep analysis charts and overall macro-process analysis charts.

A specific form, was filled for each activity in order to focus on the main pieces of information and to highlight inputs outputs and involved resources.

Due to the high number of processes to analyse and to their high level of complexity, they have been conceptually split into two sub-systems. The first one, called "Transfusion Loop", includes macro-processes from patient admission to blood component transfusion; the second one includes donation, blood components separation, validation and storage stages. Analysis and synthesis phases were independently performed for each sub-system; nevertheless they are mutually complementary [4] [5].

Patient safety depends on Blood Chain data tracing methods, so they were deeply analysed and reported on activity forms. Blood components traceability is nowadays ensured by only hand-filled paper books. One-dimensional barcode is the only employed technology and it supports at present only BTC-inside processes. Barcode technology is indispensable for automatic clinical and laboratory blood-test systems, while it is not able to achieve a complete process automation because of restricted technical potentialities.

As for patients, they are not tracked with any automatic system, nevertheless operating staff reach high level of patients direct knowledge because large unit wards have no more than 30 beds.

2 FMECA

Criticalities and process error sources were put in evidence through a process FMECA (Failure Modes Effects and Criticalities Analysis). Since 2001 the Joint Commission on Accreditation of Healthcare Organizations (JCAHO) requires the incorporation of prospective process analysis methods as FMEA into organizational patient safety plans. FMEA approach is "bottom up": potential error modes were considered for each activity, causes were searched and potential consequences related to efficiency and effectiveness (patient safety) were evaluated [6]. While this step (FMEA) provided only a qualitative failure modes analysis (risk estimation), FMECA provided a criticality evaluation of each failure mode (risk evaluation). The failure modes analysis passed from qualitative to quantitative analysis through the assignment of three numerical parameters related to Detection Possibility (D), Severity (S) and error Frequency (F) and consequently by defining a Risk Priority Index (RPI):

$$RPI = D * S * F \tag{1}$$

Standard linear scales ranging from 1 to 10 were used for each parameter evaluation. Severity parameter's scale is based on the patient's injuries: S=1-2 means no injury while S= 9-10 is used when patient suffers a permanent injury. Frequency parameter's scale is based on failure modes likelihood, while detection possibility index is related to the chances of finding out the error and fixing all related problems before they lead to consequences.

Risk Priority index also allowed to classify errors. Extracted data were processed by creating a bar chart set and by performing an ABC analysis. ABC thresholds were set as different among the processes. They were calculated on the basis of the RPI data, in order to find out three zones (A, B, C) with a quite homogeneous RPI range and to focus on a "A zone" with a quite similar number of criticalities in every macro-process. Processes carried out inside BTC are characterised by an high number of checks, so they resulted safer than those carried out inside Unit wards, so, for instance A zone limit for the Request reception and blood assignation macro-process was set to RPI= 60, while for blood request macro-process was set to RPI=100.

2.1 "TRANSFUSION LOOP" FMECA

FMECA and ABC analysis put in evidence that critical Activities are carried out inside Unit Wards, confirming literature data. Particularly patient recognition and pilot test tubes labeling activities have an high RPI value (RPI=144).

Brain Surgery processes were analyzed in order to point out criticalities in activities that were modified due to the digital blood-request form introduction. This study step pointed out that an high number of criticalities within the early stages of Transfusion Loop were removed. Brain surgery Unit is actually the most suitable pilot Unit for RFID project development.

2.2 FROM DONATION TO STORAGE PROCESS FMECA

FMECA pointed out that critical activities are related to patient recognition and manual operations, such as:

- Test tubes and blood bags labelling (RPI=144; RPI=135);
- Copying donation data from Paper register to management software's Data Base (RPI=84);

- Infected (or unsuitable for transfusion) blood units registration and elimination (RPI=108).

Human errors were the most dangerous, while low RPI values were measured for adverse events related to instrumentation problems because of their very low Frequency parameter value.

3 RFID APPLICATION

In the second part of the study, an RFID technology application has been designed, in order to reduce criticalities. According to As-is analysis, necessary technical integrations were studied and network infrastructure modifications were suggested in order to maximize RFId Technology impact on process efficiency and effectiveness.

Use of passive Tags integrated in barcode labels, wristbands and cards has been hypothesized. Two types of tags have been considered: HF tags emitting signals at 13.56 MHz frequency, and UHF tags emitting signals at 865-868 MHz frequency. Readers are both mobile and tunnel type. Mobile readers are based on PDA computers equipped with HF or UHF aerial. These devices enable BTC staff to perform Tag reading and writing through simple approach with the Reader. Tunnel readers broadcast an electromagnetic field allowing three dimensional Tag scanning. Thanks to the use of anti-collision protocols, up to 50 HF Tags or up to UHF 1000 tags concurrently can be read and recorded in BTC management software.

3.1 HF vs UHF

For these two types of technologies, pros and cons were analyzed, regarding unit costs, functionality and electromagnetic compatibility. Due to their unit cost, both HF and UHF Passive Tags (totally energy supply free) can be embedded into disposable RFID labels, so that To Be model was studied independently from the frequency that will be chosen for the application.

13,56 MHz HF frequency is world-wide compatibly allocated [7] and exposure tests to 13.56 MHz radio energy on RBCs and whole blood–derived platelets have recently revealed no biologic damage [8]. In addition, HF system is not affected by proximity of liquids during Tag reading phase [4]. For these reasons, use of ISO/IEC 18000-3 mode 1 13.56 MHz RFID tags has been recently accepted by the United States FDA as supplemental data carriers on blood products [9]. In HF systems, reading potentialities at medium-long range are limited, but this does not penalize the system performances.

UHF tags are the most used RFId tags for asset tracking in the world [7] because of their low unit cost. Mid UHF frequency is not homogeneously allocated in all world regions for RFId applications [7]. Nevertheless BTC imports Blood bags from Europe only, so European Standard EN 302 208 RFID could be used for project development.

As for UHF technology evaluation, two experimental results are necessary. The first one is the biological damage absence in blood components due to UHF energy exposure. The second one is relative to the minimum system performance evaluation for single/multiple reading and writing tasks in proximity of biological liquids.

3.2 EM COMPATIBILITY ANALYSIS

Despite both system are classified as Short Range Device (SRD) in order to respect non interference principles, EM compatibility analysis to hospital instrumentation is going to be performed [7].

Experimental tests will be realized in a semi-anechoic room, in order to evaluate both read/write performances, and immunity/emission electromagnetic characteristics of the system. EM analysis will be performed on the basis of a EM noise model of hospital environment, in order to create a “electromagnetic shared test environment” similar to the real one. Reliability test of the system will be finally performed. This study step will lead to a system improvement before pilot plant installation inside Hospital Operative Units.

3.3 ECONOMIC ASSESSMENT

Due to the difference of the two technologies tag costs, the research team is nowadays developing an economic evaluation (Return on Investment, ROI) of both technologies in order to quantify the economic advantages of using UHF, instead of the classic HF Technology.

This analysis involves the two technologies and several development scenarios, for example RFID application to “Transfusion loop” only processes or to all blood chain processes, RBC tracking only or all blood components tracking, using disposable or reusable tags. In the economic analysis cash flows will be computed, considering separately plant and operating costs and all economic revenues (missing disbursements). Economic assessment for technology choice should consider the only revenues due to productivity increasing (cycle time reduction) and quality increasing (reduction of wastes) in order to compute classic evaluation financial indicators (Net Present Value NPV, Pay Back Period PBP, etc.) for every technology and applicative scenario. This kind of analysis will help to the decision between UHF and HF and it will provide information about minimum targets to be achieved on the base of project dimension. As a matter of fact by varying some parameters like number of tags, economic analysis will provide the range of waste reduction which has to be reach in order to obtain reasonable values of the main economical evaluation parameters (NPV, PBP). These values will be measured during pilot test plant experimentation stage, and they will be compared so that an economic assessment will be performed before the project extension to all Hospital Operative Units, by projecting data from pilot plant to a larger context.

Then the analysis should be implemented performing an economic conversion of non-economic benefits derived from RFID-processes using, related to safety enhancement, including for example reduction of lawsuits, image return ecc.

4 RFID-ENABLED PROCESS DESIGN

RFID technology application brings to processes re-engineering (To Be model).
According to Hammer and Champy [10] Business Process Re-engineering is the fundamental rethinking and radical redesign of business processes to achieve dramatic improvements in critical, contemporary measures of performance, such as cost, quality, service, and speed.
TO BE model aims to change especially critical activities according to FMECA analysis, while re-engineered processes do not vary as a function of the chosen tag frequency band (HF or UHF).
The synthesis stage was divided in two different parts, called "1st Level Step" and "2nd Level Step". Each one regarded a specific process re-engineering technique application, based on RFId technology introduction. The first one regarded "Transfusion Loop" processes [5] while the second one regarded all processes from Blood Donation to final storage [4]. The two applications were studied in order to ensure their mutual compatibility, so that their implementation would be a new system model for whole Blood Chain process management.

4.1 FIRST LEVEL APPLICATION STEP

Procedures modifications and technical integrations were studied in order to increase transfusion process efficiency and effectiveness. The most important measure suggested deals with the patient recognition through an optical reading of Healthcare ID Card.
Then processes were re-engineered, and a PDA-based RFId system was included in the study. Patients have a Tag Embedded ID wristband which stores their personal data, and all assets have an RFId tag which store personal data of patient they are assigned to. Data cross match tests would be performed between wristband and pilot test tube tags during ABO bedside test stage, and between and allocation ticket and wristband tags before blood transfusion. If test returned a negative outcome, processes would be interrupted in order to avoid errors and to prevent serious adverse events for patient health.

4.2 SECOND LEVEL APPLICATION STEP

Processes were re-engineered, and a PDA/Tunnel reader based RFId system was included in the study. Blood donors are recognized by healthcare ID card optical reading and they have a Tag-embedded ID wristband or a RFId Donation card which stores their personal data. All assets (blood bags, pilot test tubes) have an RFId tag which stores donor's personal data. Data cross match tests would be performed between wristband (or Donation card) and pilot test tube and empty blood bag tags before blood donation stage. If test returned a negative outcome, processes would be interrupted in order to avoid errors and serious adverse events for patient health. To Be model also includes a simultaneous asset reading through a Tunnel Reader during "Whole-Blood Check in" macro-process, and blood components disposal and storage PDA-aided processes.

4.3 TIMING AND METHODS ANALYSIS

Blood Transfusion Centre (BTC) productivity has been analyzed, focusing on both blood inventory management and Transfusion Loop processes.
A time and methods analysis has been performed for each activity, global and unit cycle times were measured, differentiating each kind of involved operator.

4.4 EXPECTED RESULTS

Process reengineering and RFId technology application expected results are very important:

- Patient and blood assets identification errors impact reduction.
- "Transfusion Loop" Blood Asset full tracking
- Process traceability and checking during each activity: PDA downloaded data (timetables, logins etc.) would be available to BTC and Operative Units authorized personnel.
- Interdepartmental communication enhancement.
- Post-transfusion viral transmission due to reduction of blood bags handling human errors impact.
- Blood supply inventory data base real time up-to-date development.
- Paper register use reduction or disposal.
- Personnel safety enhancement, thanks to PDA-aided procedures.
- Cycle times reduction. Personnel have more time to take care of patients, and this leads to a service quality enhancement.

The two study steps implementation would allow complete asset tracking and the whole blood chain processes checking. RFId system is not invasive for patients and no additional skill is required to BTC personnel. The studied RFID-based solution is also a flexible ICT system and could be an optimal solution to other health logistic processes.

5 REENGINERED PROCESS FMECA

A blood chain reengineered processes FMECA was necessary in order to assess Return on Safety (ROS) obtained through the use of RFID-enabled procedures. This analysis aimed to evaluate process effectiveness before the experimentation step (ex-ante).
The following are the main critical activities for each macro process, and their major failure modes.
"Clinical data typing into digital request form" and "Paper request form labeling" are "Blood components request" Macro-process activities with the highest RPI value (RPI=36).
"Whole Blood Check in" macro-process have two different critical activities. The first one, is related to listing of suitable units by physician personnel during "Validation" process: Physician personnel must enjoy clinical decision-making wide power, while Computing infrastructures may only have a control and directing role within physician decisional steps, and they may point out unconventional

and suspected choices through warning messages. Nevertheless physician's clinical experience nowadays is not replaceable by any computer algorithm, so human error is not completely erasable. This is the most critical stage (RPI=54), it has an high severity factor (S=9) while a low detection factor (R=3) due to warning message introduction possibility. The second one is related to "Blood Components Separation" process. The main failure mode is the non sterile-air inlet into blood bags. This even could be given by the operator during whole blood separation, and it becomes a dangerous event if it is not properly reported. This event increases the likelihood of severe adverse events for patient,[13] e.g. septic shock (RPI=48).

"Blood transfusion" is the most critical activity and transfusion of a not properly kept blood component is the main failure mode (RPI=72). Guidelines impose strict temperature limits during handling and analysis stages and this parameter is nowadays verified through a blood bag stamp that changes colour in case of prolonged exposure to high temperature, and through a visual quality check. Moreover operators eventually report that blood units could have exceeded time limits outside of blood banks through paper documents filling. Transfusion of a damaged blood component could have serious effects on patients, so a blood temperature monitoring system project is a clear need.

The accidental non-sterile air inlet inside whole-blood bag was pointed out also within "blood donation" process (RPI=48) [13] so several quality control need was confirmed.

"Final blood unit Allocation Confirmation or Revocation" and "Automatic Clinical Testing" are the "Blood request check-in & Blood component Allocation" macro-process critical activities. The first one is a computer-enabled activity, nevertheless human error, due to physician personnel essential decision task (RPI=54), is not erasable. As for the second one (RPI=50), preventive maintenance and supply level periodical check is strictly recommended. Automatic Clinical Test system reliability is a significant item for patient safety. FMECA also confirmed current procedures requirements regarding AB0 clinical tests: it must be performed both manually (by O.U. personnel) and automatically (through Automatic Test systems), so that outcomes can be compared.

"Blood Unit delivery to an incorrect O.U. auxiliary staff member" is the main failure mode within "Blood Component Check-out" stage; however this error is detected by RFId system before blood transfusion, so it could only bring to a process time delay (RPI=20).

Reengineered-processes FMECA RPI data, were classified through ABC charts, which pointed out 14 critical activities.

These activities are potentially affected by several kinds of error. Human errors in manual operations are still the most important (n=7). Particularly clinical activities (including patient treatment, manual testing etc.) are fewer (n=2), than other general activities (writing, material handling etc.) (n=5). Some criticalities regarded activities for which blood component quality check could fail (n=4). Other error modes concern blood bags selection stages in "Blood Validation" and "Blood Component Allocation" processes due to the physician essential decision task (n=2), and automatic clinical analysis system reliability (n=1).

Within reengineered processes FMECA, main error modes were considered for each analyzed activity. In addition to human errors, any communication difficult, any missing or misplaced supplies chance and any equipment problem were considered [12]. Particularly data reading, writing, matching, automatically performed by RFId system, were considered as equipment problems potentially affected activities, although they are carried out individually and in ideal conditions.

Nonetheless bar-charts and ABC-charts data graphical analysis clearly pointed out a critical failure modes number reduction and an important RPI value decrease.

5 KEY PERFORMANCE INDICATORS

Key Performance Indicators (KPI) were designed in order to improve results analysis and to point out quantitatively process performance variation within As Is – To Be transition. KPI design is a very important study step and it is based on the company management goals. Most important process parameters are chosen and constantly measured, then they are processed in order to obtain KPI. They are usually used for online performance monitoring and their trend analysis allows to evaluate or to forecast economic and productivity status, and to study strategic changes in order to maintain or to achieve goals.

Within this study KPI are used in order to evaluate "ex ante" clinical risk reduction in Blood Transfusion Chain. Processes and activities cycle times, their amount, their failure modes amount, and their RPI values were the measured parameters of each macro-process. Three indicator types were designed:

Average RPI: Nonzero RPI Arithmetic Average calculated within the n activities of each macro-process.

$$AverageRPI = \frac{\sum_{i=1}^{n} RPI_i}{n} \tag{2}$$

Number of Activities: number of activities which form a macro-process.

Peak RPI: Maximum RPI value within the macro-process.

Cycle Times: Sum of activity Cycle Times calculated for each macro-process.

As-Is cycle time were derived from time and methods analysis, while To-Be cycle times were estimated by analysing To-Be model flow charts and activity forms.

Key Performance Indicators values of both "As Is" and "To Be" models were computed, and their increase or decrease were expresses in percentage.

5.1 OUTCOMES DISCUSSION

Study results are displayed in Table 1.

Most important result was pointed out for "Blood Component Request" Macro-process. RFId-enabled process, allowed two goals achievement: average (-73.2%) and peak (-75%) RPI severe reduction, supported by activity number reduction (-31.2%) and an appreciable cycle time expected reduction (-13.3%). Operative procedures have been made both safer and more streamlined, so that a cycle time reduction is predictable.

As for "Whole Blood Check-in" macro-process, average and peak RPI severe reduction (respectively -77.3% and -62.5%) was obtained while no appreciable activities count variations were observed (+4.3%). Thanks to the RFID Tunnel Reader multiple reading possibility, a severe cycle time reduction is expected within this process step (-66.7%).

On the contrary, severe clinical risk reduction within Donation critical activity was obtained through the activity number doubling. This result cannot be considered disappointing because the analysis step [4] pointed out the procedure integrations and additional automatic checks needs. The activity amount goes from 8 to 16, remaining at a medium level, and expected cycle time variation is held down (+9.1%) so this 100% increase is largely justified.

As for "Blood Transfusion" critical macro-process, results were quite satisfactory: RPI reduction (-67.4% average RPI and -55.6% peak RPI) was obtained through a necessary activity weak integration (activity amount goes from 10 to 13) and cycle time expected variation is +0.8%).

"Blood components allocation" macro-processes outcomes were less appreciable due to the weak changes imposed by RFId-enabled processes. Nevertheless fair improvements were pointed out (about -25% average and peak RPI reduction, -33% number of activities reduction).

RFId technology introduction and RFId-enabled process design was positively evaluated. The whole Blood Chain activity amount do not varies considerably from As-is to To-be models (-3.8%): procedures integration and streamlining are balanced, so that expected global cycle times variation is slightly favourable (-0.8%). Clinical risk reduction is appreciable in every Blood chain process. Total Average RPI reduction is 67.6% while total peak RPI reduction is 60.2%. Achievement of the Healthcare Facility strategic goal through the RFId system project is expected.

Considering FMECA-derived RPI as a random variable, both AS-IS and TO-BE RPI Normal distribution curves were plotted. The mean and variance values, and the variation range reduction were graphically pointed out (Figure 1).

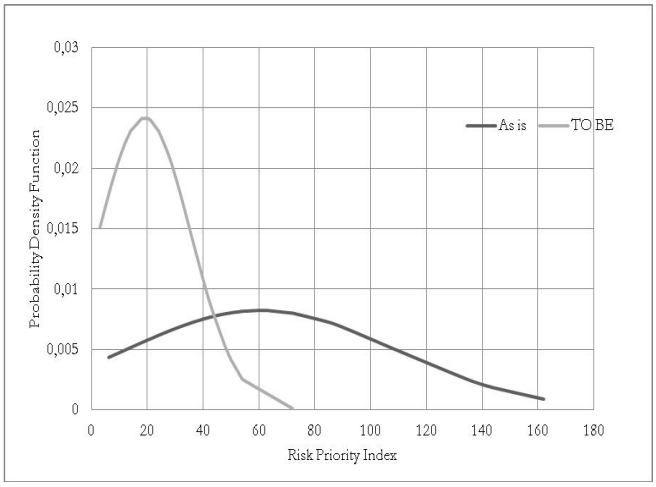

Figure 1 Probability density function of As-is and To-be models.

Table I - KPI variation within AS-IS and TO-BE models

Macro Process	Average RPI [%]	Number of activities [%]	Peak RPI [%]	Cycle Time [%]
Blood Component Request	-73.2	-31.2	-75.0	-13.3
Blood Transfusion	-67.4	+30.0	-55.6	+0.8
Blood Donation	-81.8	+100.0	-70.4	+9.1
Whole Blood check-in	-77.3	+4.3	-62.5	-66.7
Blood Component assignation	-26.4	-33.3	-25.0	-2.3
Blood components check-out	-63.7	+50.0	-33.3	+6.3
Total	-67.6	-3.8	-60.2	-0.8

CONCLUSIONS

A process reverse engineering was performed in order to identify and map the whole Blood Chain.
Through a FMECA, potentially error affected activities were founded and failure modes were classified by a risk priority index (RPI) which included detection possibility, severity and frequency factors.
Criticalities were processed through a new operative procedures definition based on the use of RFId system.
UHF and HF technology (passive tags, PDA and Tunnel readers) pros and cons were evaluated, and a cost- benefits analysis, nowadays in progress, resulted necessary in order to perform a final technology choice.
The TO-BE model, was validated through a reengineered-process FMECA and through Key Performance Indicators (KPI) evaluation, which confirmed a clinical risk reduction within Blood Transfusion Chain. Most important results regarded Blood components request macro-processes, particularly the main benefits were caused by PDA-aided cross match tests.
RFId-enabled processes FMECA also pointed out several important criticalities which have to be processed by the management staff. The most important one, is related to cold chain failure: biological damaged, due to high temperature, blood component transfusion. This issue opens up to a study improvement i.e. RFID semi active tags using to improve the performance of the cold chain. Manual-performed quality checks within several Blood Chain tasks are very important; they are by-passable only by using an appropriate system for blood temperature history measurement and storage during pre-transfusion handling stages. RFId semi-active tags could be integrated with temperature sensors in order to allow both periodic temperature measurement and data storage for a long time range, so that blood component storage and handling conditions always would be checked.
Due to the RFID platform flexibility, it can be used in order to control other logistic processes, for instance to improve processes characterized by activities and error modes comparable to transfusion processes (for instance drugs management, bone marrow transplant, chemotherapy drugs management), in order to achieve economic and safety improvements. The RFId platform use extension would also contribute to a global Pay Back Period decrease for AOB hospital.

REFERENCES

[1] Ahrens N., Pruss A., Kiesewetter H., et al., Failure of bedside ABO testing is still the most common cause of incorrect blood transfusion in the Barcode era. *Transfusion and Apheresis Science*, No.33, pp. 25-29, 2005.

[2] De Sanctis Lucentini E., Marconi M., Bevilacqua L., et al., Risk Management in Sanità. Il problema degli errori. *Ministero della Salute Commissione tecnica sul rischio clinico*, Roma, 2004. http://www.salute.gov.it/imgs/C_17_pubblicazioni_583_allegato.pdf (accessed 10 February 2012).

[3] Goodnough L.T., Risks of blood transfusion. *Crit Care Med*, No. 31, pp. S678–S686, 2003.

[4] Orrù P.F., Borelli G., Pilloni M.T., et al., RFID System Project for Enhancing Blood Supply Chain Safety and Blood Transfusion Center Productivity. *Proc. of Apms International Conference Advances in Production Management Systems*, Cernobbio (Italy), 2010.

[5] Borelli G., Pilloni M.T., Orrù P.F., et al., Riduction of clinical risk in blood transfusion center with an RFId system. *Proc. of The International Workshop on Applied Modelling & Simulation*, pp. 218-223, 2010.

[6] Marx D.A., Slonim A.D., et al., Assessing patient safety risk before the injury occurs: an introduction to socio technical probabilistic risk modelling in health care. *Quality and Safety in Health Care*; No. 12(Suppl. II), pp. ii33–ii38, 2003.

[7] Talone P., Russo G., *RFID Tecnologie e Applicazioni*, 1st edition, Fondazione Ugo Bordoni, 2006.

[8] Davis R., Geiger B., Gutierrez A., et al., Absence of acute adverse in-vitro effects on AS-1 RBCs and whole blood–derived platelets following prolonged exposure to 13.56 MHz radio energy. *Journal of Blood Services Management*, No. 50, pp. 1596-1603, 2010

[9] Hohberger C., Davis R., Briggs L., Gutierrez A., Veeramani D., Holcombe J., Applying radio-frequency identification (RFID) technology in transfusion Medicine. *Biologicals*, 2011, Pubblished online first: 18 February 2011 doi:10.1016 /j.biologicals.2011.10.008

[10] Hammer M., Champy J., *Reengineering the corporation: a manifesto for business revolution*. New York: Harper Business, 1993.

[11] Galgano A., Qualità totale. *Il metodo scientifico nella gestione aziendale*. Milano: Guerini e Associati 2008.

[12] Chiozza M.L., Ponzetti C., FMEA: A Model for reducing medical errors. *Clinica Chimica Acta*, No. 404, pp. 75-78, 2009.

[13] Giusti G., Isacchi G., Zinno F., *Trattato di medicina legale e scienze affini.* Cedam, 2009.

ISSN 1590-8844
International Journal of Mechanics and Control, Vol. 16, No. 01, 2015

AN APPLICATION OF LARM CLUTCHED ARM FOR ASSISTING DISABLED PEOPLE

Cristian Copilusi* Marco Ceccarelli**

* Department of Applied Mechanics. Faculty of Mechanics. University of Craiova. Romania

** LARM Laboratory of Robotics and Mechatronics. Department of Civil and Mechanical Engineering
University of Cassino and South Latium. Italy

ABSTRACT

This paper addresses attention to an application of LARM Clutched Arm for feeding process aiding disabled people. The research core is focused on experimental kinematic analysis of the robotic arm with high-speed video analysis equipment for validating its functionality. Originally the arm was designed for humanoid robots, but the reported results demonstrate that this arm can be also used in service human food feeding applications.

Keywords: Service robots, Robotic arms, Clutched systems, Assistive Food feeding robots, Experimental kinematics.

1 INTRODUCTION

Several solutions have been developed for helping disabled people to walk, to feed, to carry objects or to perform different tasks. These solutions are based on robotic systems or mechanical devices that are specifically designed for types of tasks.

In the particular case for human feeding process, there are several robotic systems already available as outlined in [1-9]. The meal assistance robot My Spoon (in Fig. 1a) is characterized by a manipulator arm with 5-DOF and an end-effector that is controlled by a joystick, with a spoon/fork of 1-DOF [1]. The assisting robotic system Handy 1 (in Fig. 1b) has a 5-DOF robotic arm that is installed on a non-powered wheeled platform to assist in very specific activities of daily life such as eating, drinking, and make-up application. During the eating application a scanning system of lights has been included into its tray section which helps the user to select food from any part of the dish [5].

Contact author: Cristian Copilusi[1], Marco Ceccarelli[2]

[1] Calea Bucuresti, 113 – 200512 Craiova, Romania.
Email: cristache03@yahoo.co.uk
[2] Via G. Di Biasio, 43 – 03043 Cassino, Italy.
Email: ceccarelli@unicas.it

Another example of an assistive robotic system is Neater Eater [3], which has two versions: a manual one and an automatic one. It consists of 2-DOF arm with a dish, as shown in Fig 1c. The manually controlled Neater Eater comes with a handle with damping mechanism which absorbs tremor. The electric programmable device can be controlled by using switches, in light-touch finger or head switches and foot switches.

The Meal Buddy in Fig 1d [4] has a three-DOF robotic arm and three bowls that can be mounted on a board using magnets.

The Winsford feeder robot in Fig. 1e, [5] is a mechanical system with a pusher, which moves the food onto the spoon, and a pivoting arm which raise the spoon. The height of the feeder can be adjusted with a command by a switch. In the case of the system Fig. 1f [7], the food is placed in three bowls, which rotate until the desired food is located under the spoon. The spoon dips into the bowl, scoops up the food, and presents a rounded spoonful of food very near the lips of the user. The user must lean forward slightly and remove the food from the spoon. Other assistive robots for feeding applications are described in [8] to [10].

In general these systems use a large number of actuators and the command and control unit cannot be

easily accessible to a disabled person. Considering human feeding robots or mechanical devices developed for this purpose, one can note that most of them cannot be readapted in order to fulfil multiple or combined tasks such as grasping objects and feeding process or writing and feeding process.

By taking the above considerations into account, this design has been aimed to readapt a clutched arm that was specifically designed for humanoid robots, to the case of feeding process. This clutched arm has been used for research purposes at LARM laboratory [11-16]. The functions of this arm is reported in [11] with some numerical examples and test results, while its functioning for humanoid robot's arm are described experiment tests in [12]. In [13] ADAMS simulations are reported for single motion of arm, and the simulations for combined motions of LARM clutched arm are reported in [14]. The design, capability and experimental validation of this arm are described in detail mainly in [15]. In [16] the characteristics and functionality of arm are described for different applications as industrial robot's movement, an assisting movement and pick and place of the objects.

This paper is organized as follows. In the first section the existing solutions that are designed for disabled human feeding process are shortly presented. A prototype of LARM Clutched Arm is described from a general viewpoint in the second section. Based on the desired task and by considering the existing prototype several adjustments are presented in the experimental setup on third section of the paper.

Tests for assisting the disabled people on feeding process were performed by setting up different functionality modes. The obtained results are comparable with the ones acquired in case a feeding process by a healthy human subject as reported in section four.

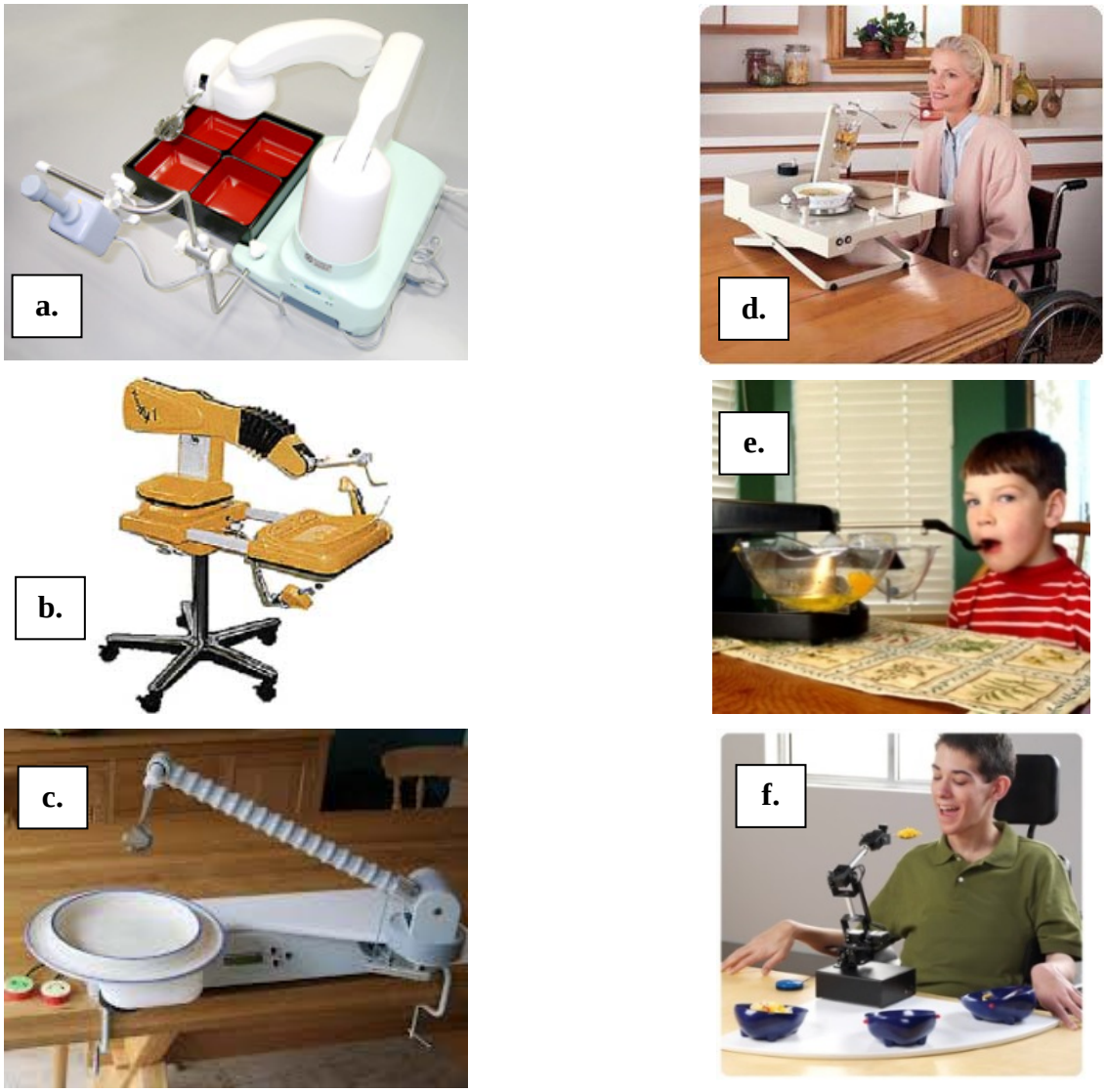

Figure 1 Examples of assistive feeding robots [1]-[9]; a) My Spoon, b) Handy 1, c) Neater Eater, d) Meal Buddy, e) Winsford feeder, f) Mealtime Partner Dining System.

2 LARM CLUTCHED ARM

LARM clutched arm [11-13] is a robotic arm with single actuator from which the motion is transmitted to joints with the help of gears and electromagnetic clutches. These components make possible the arm's movement in a 3D space by using only one electric motor. The design with the motor in the shoulder has been conceived to have most of the weight far from arm links that can be in contact with human users. This is for safety purposes with light weight design for low-inertia impacts.

Because of a single actuator, LARM clutched arm can be controlled fairly easily also by no expert users. Furthermore this arm is characterized by light weight structure, which ensures safety when a collision occurs between the robotic arm and a human. The single actuator implies a low cost design as compared with respect to other traditional robotic arms. Other aspect of this arm is that the motor works only when there is a movement of arm and there is no energy consumption when arm stops with energy saving. The size of all components are designed to give it an anthropomorphic aspect with specific cover.

The arm has a parallelogram-based mechanism for the limb part which makes to drive the upper arm and forearm from the shoulder. The main idea is to use a proper clutch system to obtain three sub-motions from the source motion of a single motor as shown in Fig. 2, [14].

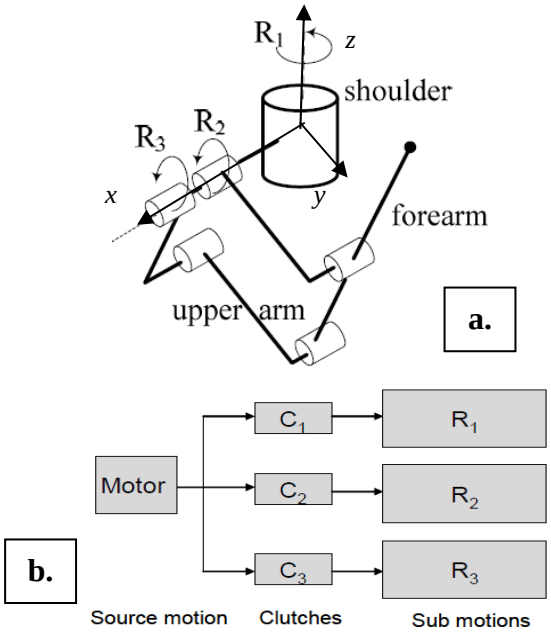

Figure 2 The design model of LARM clutched arm [14]; a) a kinematic scheme, b) an actuator scheme.

The shoulder is the main powered component of entire arm, because the motion for arm's functioning is given by it. The shoulder part gives output for three rotations R1 to R3. Rotation axes R1 and R2 are orthogonal to each other, while the axes for R2 and R3 are coaxial. Gearing systems are used to construct the transmitting lines for the required rotations. The entire structure is made up of light aluminium alloys which gives the light weight property.

In Fig. 3a the mechanical design of the shoulder is shown in which the z axis is orthogonal to R2 and R3 axes, while Fig. 3b shows a CAD model of the shoulder. The output shaft for R2 and R3 is a double cylindrical shaft, within which a full cylinder outputs the R2 rotation. Coaxial to this shaft there is a hollow cylindrical shaft which outputs the R3 rotation.

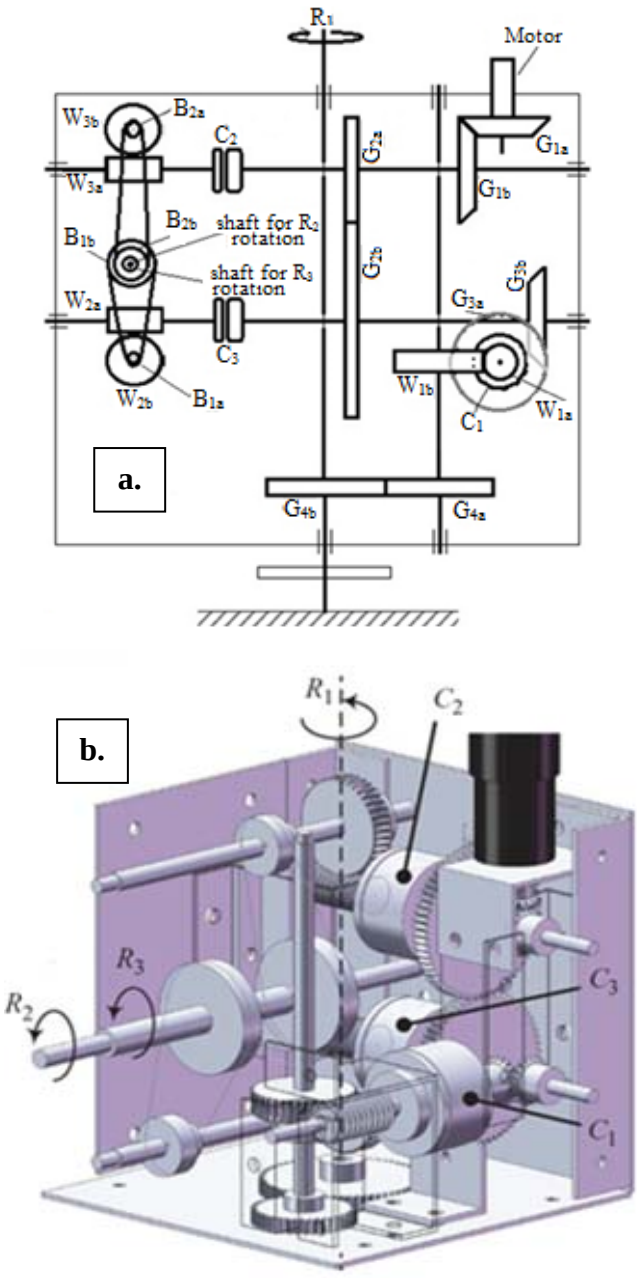

Figure 3 The mechanical shoulder design of LARM clutched arm; a) a kinematic scheme, b) a CAD model.

As referring to Fig. 3 (a), the components of the design can be identified in:
- $B_{ia/b}$ (i=1,2) represents belt wheels;
- W_{ia} and W_{ib} (i=1,2) represent the worm and the worm wheel respectively;
- C_i (i=1-3) are electromagnetic clutches assembled along the rotation axis;
- $G_{2a/b}$ represent cylindrical gear;
- $G_{1a/b}$ is the main conic gear;
- $G_{3a/b}$ is the secondary conic gear.

Fig. 4 shows a photo of the shoulder prototype of LARM clutched arm at LARM in Cassino. This figure shows how the gears and three electromagnetic clutches that are marked as C1, C2 and C3 are combined in the shoulder for the three rotations. The motion of joints can be transmitted or stopped by changing the state of clutches. With the three clutches there are eight possible modes of different combination of operation state, as summarized in Table I where 0 means the clutch is deactivated and 1 means the clutch is activated.

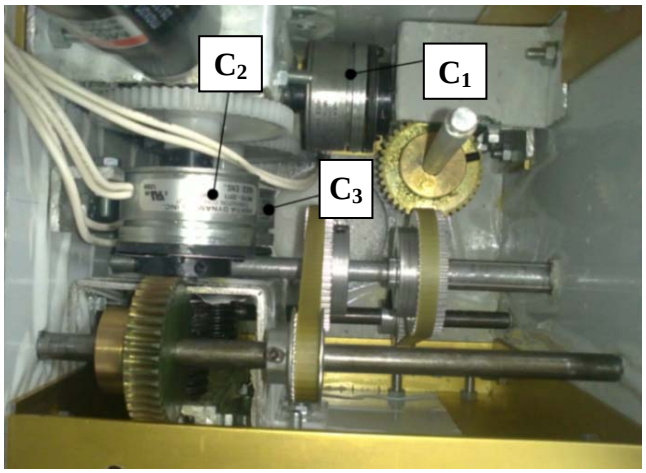

Figure 4 Mechanical design of the shoulder prototype of LARM clutched arm.

Table I - The operation modes for LARM clutched arm as function of clutches activation

Operation mode	Rotation	C_1	C_2	C_3
OP0	0	0	0	0
OP1	R1	1	0	0
OP2	R2	0	1	0
OP3	R3	0	0	1
OP4	R1 and R2	1	1	0
OP5	R1 and R3	1	0	1
OP6	R2 and R3	0	1	1
OP7	R1, R2 and R3	1	1	1

In Table 1 OP0 is a stationary mode, i.e. there is no rotation during this operation mode; while OP1 to OP3 are single operation modes, during which there is only one rotation at a time. OP4 to OP7 are multi-rotational operation modes, since during these operation modes there are more than one rotation simultaneously.
Figure 5 shows a photo of the prototype of LARM clutched arm at LARM in Cassino in a lab setup for tests. This arm can be attached to a wheel chair to help disabled persons for assistive movements like for example in food feeding. In this case a spoon is attached perpendicularly to the forearm as an end part with the aim to perform the food feeding action.

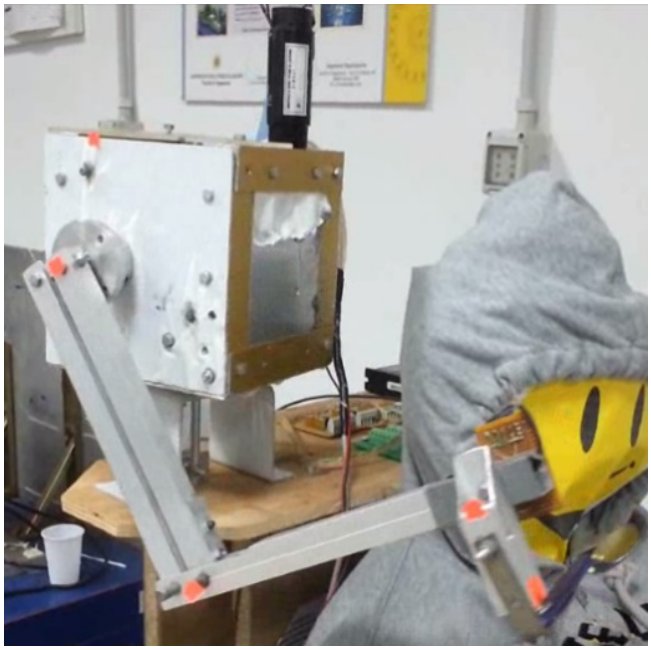

Figure 5 The prototype of LARM clutched arm in a lab setup for testing.

3 EXPERIMENTAL SETUP

Components of the prototype for lab tests are listed in Table II, and they are connected to each other as shown in the block diagram of Fig. 6.
A clamp handling the spoon with a three directional accelerometer is used as an end-effector. Further information on used components is given in the following.
In LARM clutched arm a 24V DC motor is used with information of motor speed and current given from a servo-amplifier. From the tests in [13] a maximum needed value of motor torque has been determined as 1.6Nm. Three equal 24V DC frictional electromagnetic clutches are used from Inertia Dynamics production with maximum transmissible torque of 1.7Nm. The control unit is composed of a PLC, a NI-PCI, and a servo amplifier as shown in the block diagram of Fig. 7, where C1, C2 and C3 represent the three clutches, respectively.

Table II - Components in the prototype of LARM clutched arm in Figures 4 and 5

Components	Characteristics
DC motor	70 watt, maximum speed 3000 (degrees/second)
Clutch	Maximum transmission torque (1.7Nm)
PLC	8 inputs and 4 outputs
PCI	6024E to communicate computer and periphery
Accelerometer	A three axis, measure range (±4g)
Worm	1 module, 20 (degrees) pressure angle, material: steel
Worm wheel	1 module, 40 teeth, material: brasses
Spur gear	1 module, 40/64 teeth, material: plastic
Bevel gear	1 module, 16 teeth, material: plastic
Belt wheel	32/60 teeth, material: aluminium

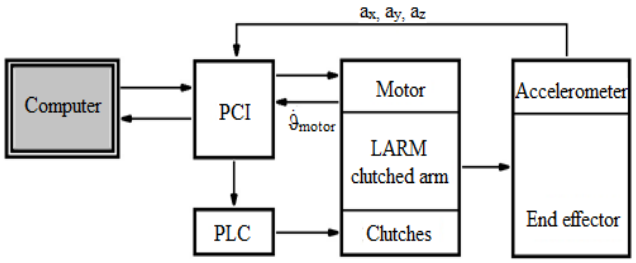

Figure 6 A block diagram for connection among components in lab layout in figure 5.

For a generic movement of LARM clutched arm, the CLANCONS program, elaborated in LabView, sends the signal to outer components with the help of PCI. This PCI sends a digital signal to an amplifier (with lines indicated as DIO), which regulates the current to pass in the PLC. The clutches state can be modified by changing the current value from PLC through a suitable command data [14]. The motor informations acquired by the servo-amplifier are analogical and they are sent to the PCI through ACH14 and ACH15. Comparing this information on motor's measured angular position with a prescribed value as in operation the program, an analogical signal created by the PID is sent to the servo-amplifier from PCI through DAC0OUT. The servo-amplifier gives current to the motor through commands for + motor and – motor as indicated in Fig. 7.

In order to control the arm operation, a GUI interface (Graphic User Interface) has been elaborated in LabView with the name CLACONS (CLutched Arm CONtrol System). It has two modes: Adjust mode and Control mode. The Adjust mode can be used to control the arm manually to reach on a desired position; while Control mode can be used for automatic function of arm. Through suitable programming during a controlled motion the system reads a text file in which the path is written for arm movement. For safety considerations, there is an emergency STOP button, which terminates the arm function leading the operation mode to OP0. Three virtual meters monitor the motor state while three LED lights indicate the state of three clutches, respectively. For arm's movement CLACONS sends a signal through the PCI to other components. The PCI sends a digital signal to an amplifier, which regulates the current that is given to the PLC. On the base of current value, PLC regulates the state of clutches by opening and closing the circuit through which the current passes to produce the electromagnetic field in the clutch. The servo amplifier receives a command signal from PCI, amplifies the signal and transmits electric current to the motor in order to produce a motion proportional to the command signal. An accelerometer as shown in Fig. 8 is attached at the end of the forearm to measure the acceleration of arm's end point along three directions.

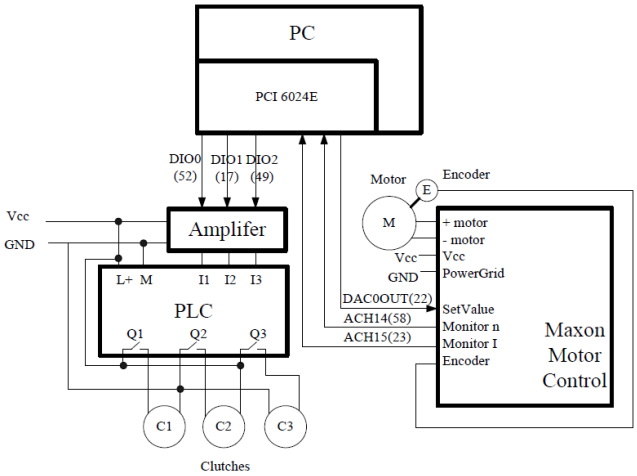

Figure 7 A block diagram of proposed control unit.

Figure 8 The accelerometer used at arm end point.

In order to compare the operation of food feeding achieved by the LARM clutched arm with a similar human operation, a video recording has been acquired through an ultra-high speed equipment CONTEMPLAS [17]. The CONTEMPLAS application layout is illustrated in Fig. 9 as was used for a motion analysis on a human subject and LARM clutched arm to study human upper limb motion

during feeding process. This equipment uses two ultra-high speed cameras which can track special markers with reflexive properties during motions. These markers are usually attached on joint centres of the interest mobile system by tracking and measuring certain characterization of a system motion. In our case, the mobile system it is firstly represented by the human upper limb and then by the LARM Clutched Arm. The equipment is capable to track automatically desired trajectories in real time or to analyze them after a video is recorded and stored in its computer host. The equipment is provided with software created by the CONTEMPLAS Company, and in our case this is the Templo Standard General Motion basic software.
The lab layout configuration is the following: TEMPLO Module, Ultra high speed cameras, C-Mount Objective, Tripod, Gigabit Ethernet ExpressCard, Gigabit Ethernet CAT6 cable, Charger, Special laptop, as summarized in Figs 9 and 10. The motion analysis processing is based on the scheme in Fig. 10.

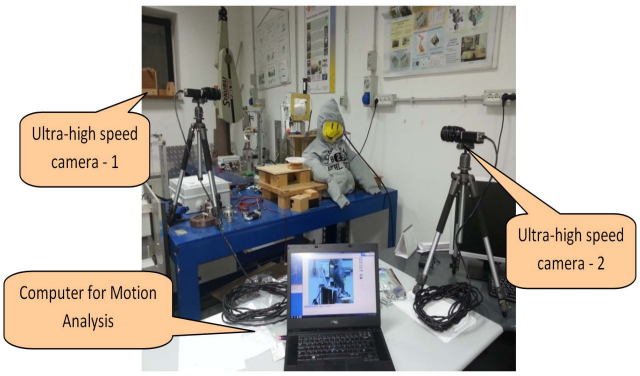

Figure 9 Lab layout of ultra-high speed video analysis equipment (CONTEMPLAS) for experimental tests.

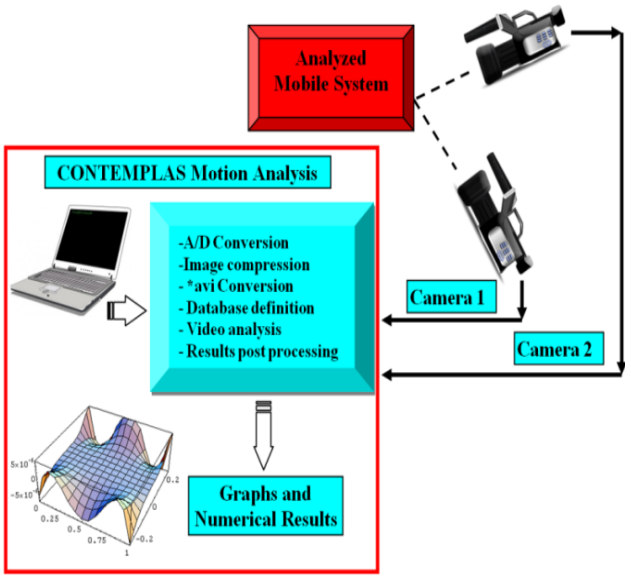

Figure 10 A processing scheme for video analysis by using CONTEMPLAS Motion Analysis Equipment as in figure 9.

4 TESTS FOR ASSISTING DISABLE PEOPLE

A lab layout has been settled at LARM in Cassino to perform tests, to check the feasibility and to characterize the performance characteristics of the proposed application with LARM clutched arm. By using combination of three clutches states, it is possible to obtain a desired movement for food feeding. In order to verify the functionality of the LARM clutched arm, a mannequin has been used as a disabled person and a macaroni food is used as the feeding food. The mannequin is located at the distance from arm which should be same as the distance between the arm and a disabled person sitting on a wheelchair. In Fig. 11 a photo sequence of arm's positions is reported during an experiment.

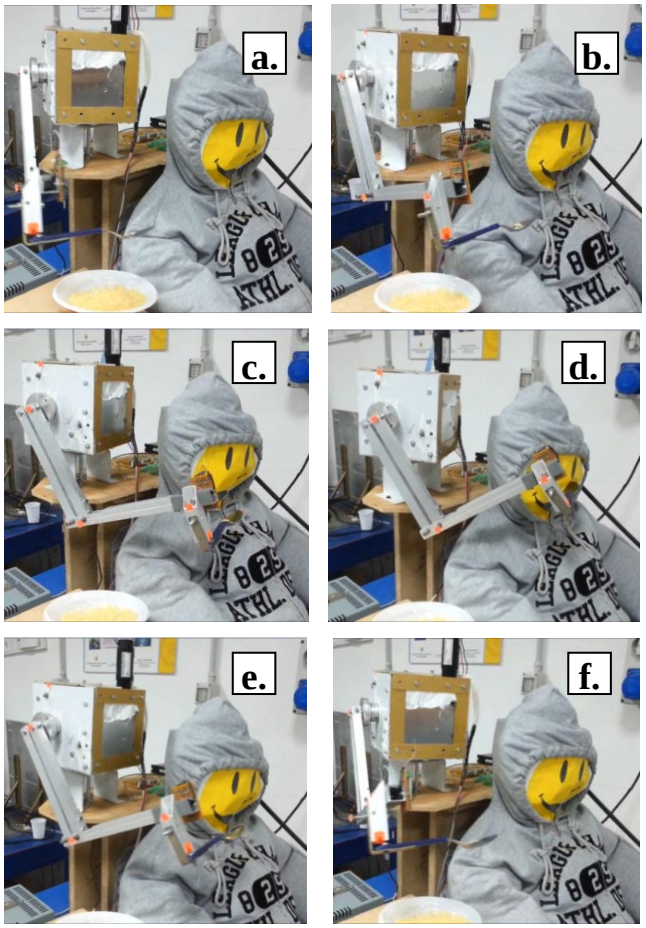

Figure 11 A photo sequence of arm's movement during an experiment at LARM.

The trajectory for the arm movement during the food feeding action is planned in joint space as in the plot of Fig. 12, where θ1 [degrees] is angle which characterizes the shoulder movement, while θ2 [degrees] and θ3 [degrees] are the angles characterizing the arm and forearm's movements, respectively.
At the beginning and returning movement of arm, there is a small time delay when there is no motion as due to the need

of time to load the food. The measured acceleration magnitude of arm's end point is plotted in Fig. 13. The acceleration components along the coordinate systems are shown in the plots on Figs 14, 15 and 16. These values of acceleration look very similar to the values of human arm's acceleration during a similar action of food feeding.

Referring to Figs. 12 and 13, the obtained 3D trajectory of the robotic arm through clutches combination can be explained as follows:

- the generated path between points 1 to 2 corresponds to the activation of clutch C3, Fig. 11a;
- next path between points 2 and 3 corresponds to the activated clutch C2;
- a combination of one pair of clutches, respectively C1 and C2 corresponds to the generated path from points 3 and 4, Fig. 11b;
- when the spoon is raised up, the clutch C3 is activated and a path is generated between points 4 and 5;
- another combination of a paired clutches, respectively C2 and C3 corresponds to the path between points 5 and 6, Fig. 11c;
- for path between points 6 and 7, clutches C1 and C3 are activated, Fig. 11d;
- during the path between points 7 to 8, the clutch C3 is activated and the spoon is situated near the mannequin mouth, Fig. 11e;
- after retracting the spoon from mannequin mouth, the path between points 8 and 9 is generated and it corresponds to the activation of the clutch C2.

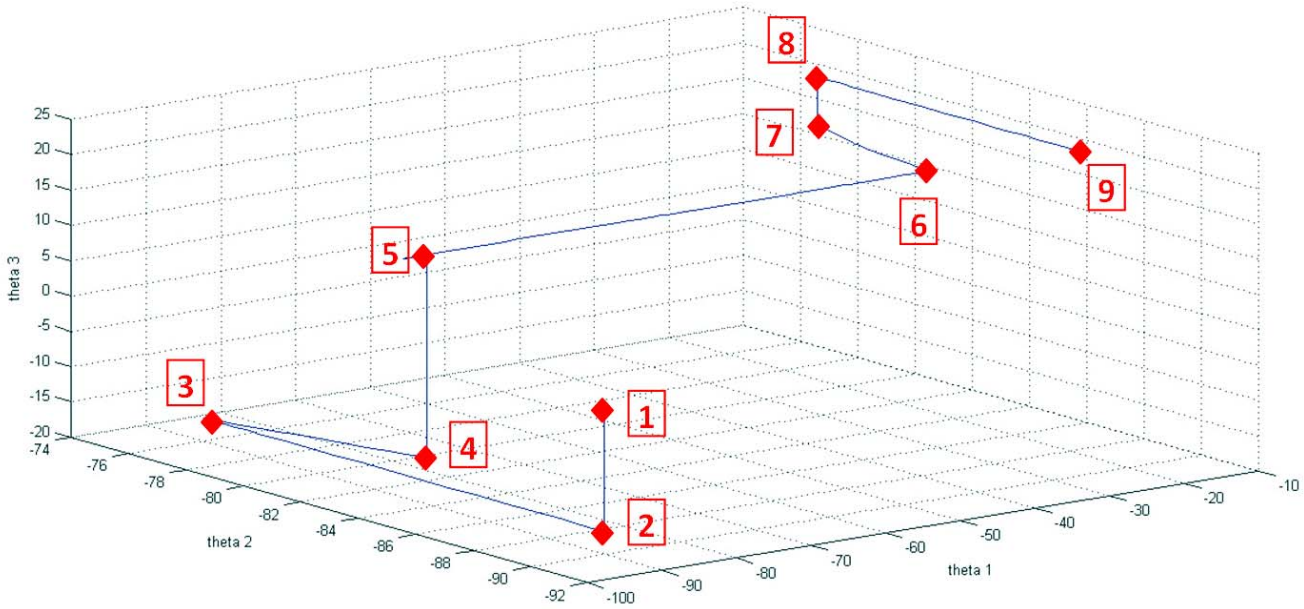

Figure 12 The chosen trajectory for arm's movement in the joint space.

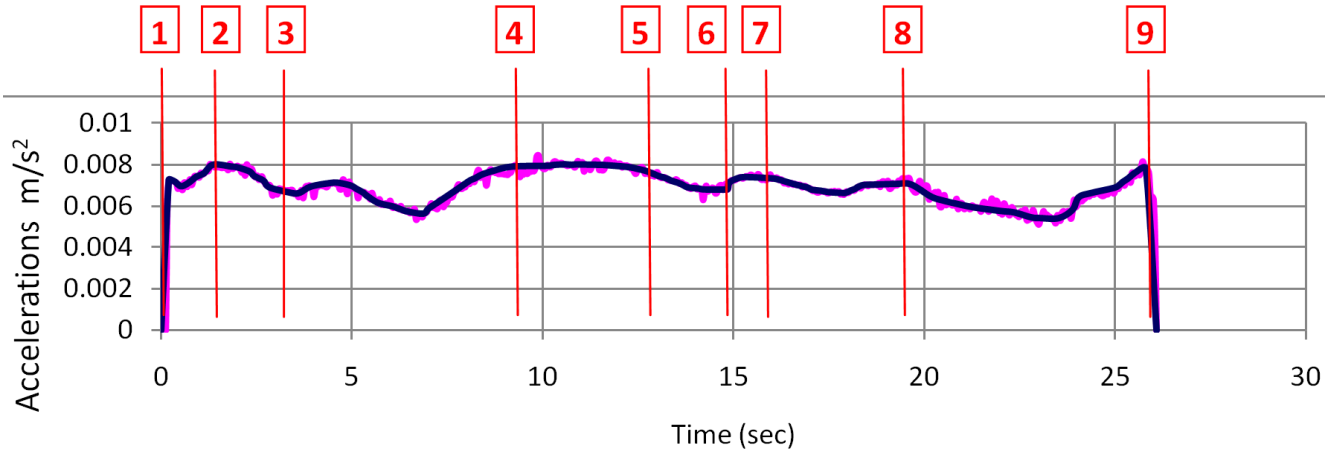

Figure 13 Acquired acceleration magnitude of LARM clutched arm end point during a test (Magenta line represents the acquired data, blue line represents the filtered data).

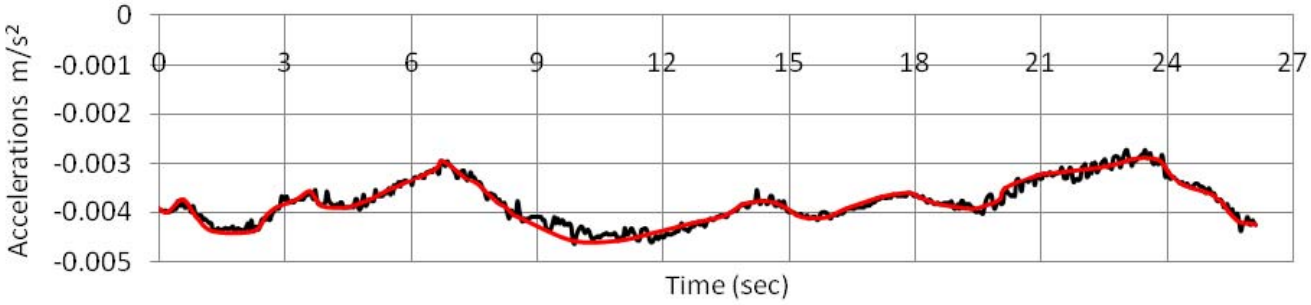

Figure 14 Acquired acceleration component in X direction of LARM clutched arm end point for test result in figure 13 (black line represents the acquired data, red line represents the filtered data).

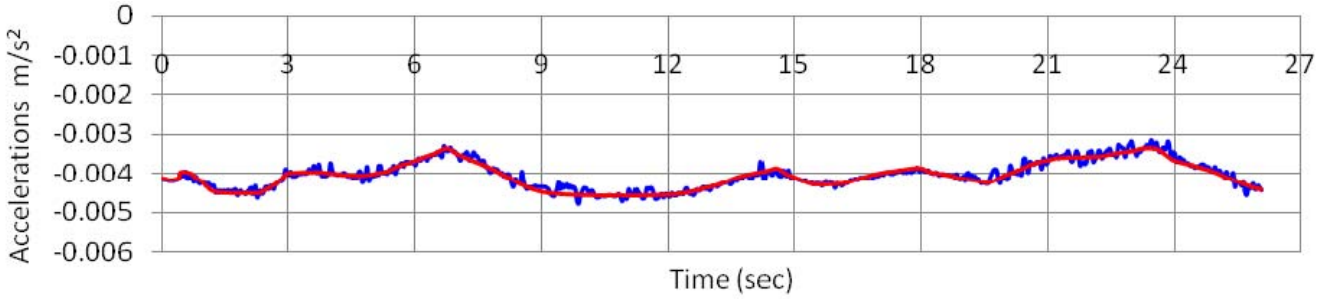

Figure 15 Acquired acceleration component in Y direction of LARM clutched arm end point for test result in figure 13 (Blue line represents the acquired data, red line represents the filtered data).

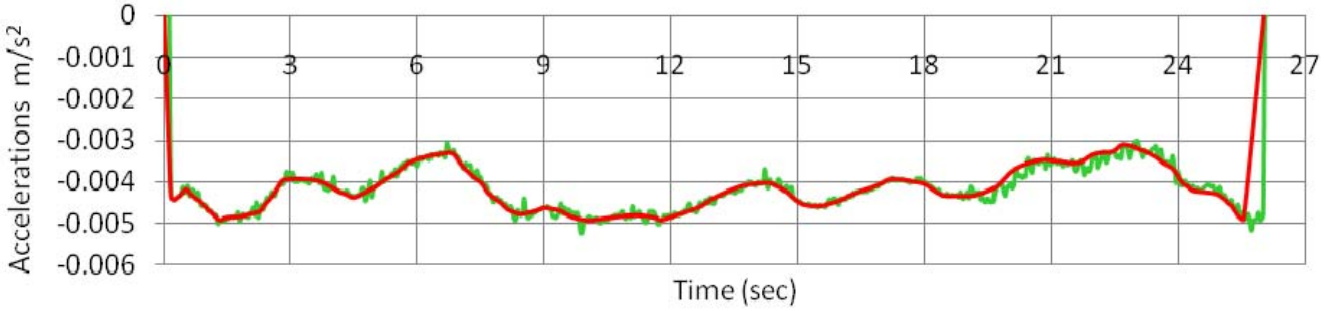

Figure 16 Acquired acceleration component in Z direction of LARM clutched arm end point for test results in figure 13 (green line represents the acquired data, red line represents the filtered data).

The video experimental analysis process has used special markers on shoulder, elbow and wrist joints. These markers are automatically tracked by the CONTEMPLAS equipment during a feeding process when a human performs a motion with a spoon. Moreover the trajectories can be used as a starting point for creating reference paths for a robotic system. First of all it is monitored the movement of a healthy person during the food feeding. After this it is monitored the LARM clutched arm during a similar motion. The experimental test conditions in this case were the same as the ones from the LARM clutched arm motion analysis. After this analysis a database was obtained and a comparative study was performed. The measured displacements are shown in Fig. 17 as obtained by analyzing the complete motion for food feeding action in both cases.

The time history variation of elbow position is almost the same in both cases. In human case the position variation has a value of 1m, and in the case of the LARM clutched arm reaches a value of 1.8 m. This larger value is due to the programmed path as in Fig. 12 and also to the plate position between mannequin position and LARM clutched arm.

For wrist position in Fig. 17b, the time history between human and robotic arm is different yet. But the obtained values are almost the same. The maximum measured displacement has a value of 2m in both cases.

The data provided by the accelerometer is useful to obtain displacement through numerical double integration. This was computed by a numerical elaboration by using the data in Fig. 13. The obtained values are shown in Fig. 18.

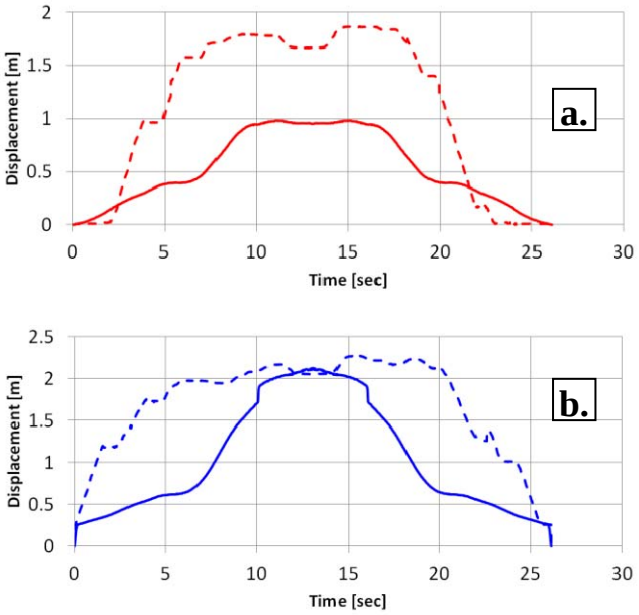

Figure 17 Results of experimental tests with a human subject and LARM Clutched Arm (Continuous line for human elbow, dotted line for LARM clutched arm); a) Elbow position, b) Wrist position.

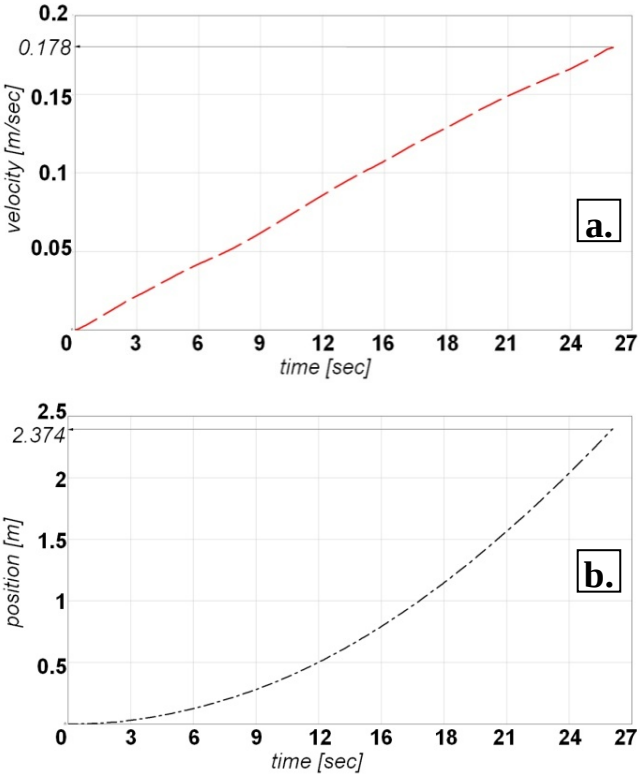

Figure 18 Wrist position numerical processing by acceleration's double integration from figure 13: a) Velocities variation; b) Position variation.

The acceleration during food feeding process is almost constant with values from 0.005 m/s^2 to 0.008 m/s^2. Thus, the velocities show a quasi-linear variation and the displacement curve looks with a quasi-quadratic shape, but with smooth evolution. The obtained displacement value is about 2 meters. In addition, joint motion has been evaluated by monitoring the shoulder and elbow joint in a human subject and LARM clutched arm for a test of Fig. 12. Results are shown in Figs. 19 and 20.

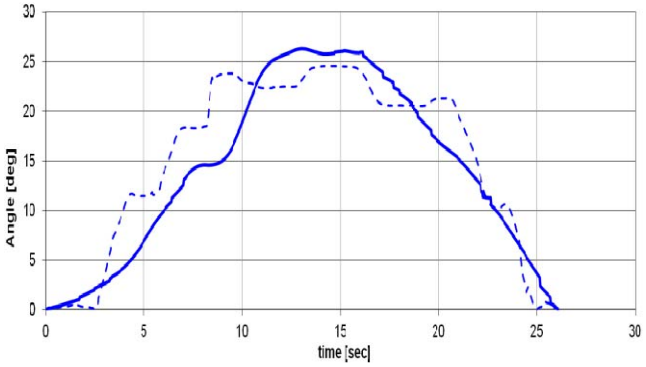

Figure 19. Measured shoulder angles of the human arm and LARM arm (Continuous line for human elbow, dotted line for LARM clutched arm).

The shoulder angular amplitude is from 0 to 26 degrees in case of a human subject, and in the case or LARM clutched arm this is from 0 to 24.95 degrees. In case of elbow joint the angular amplitude obtained in both cases are between 0 and 24 degrees as shown in Fig. 20.

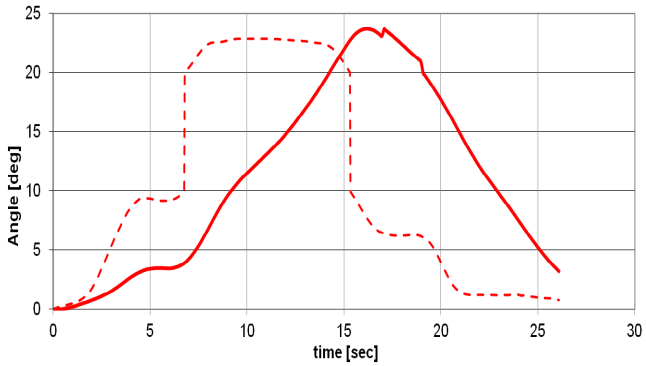

Figure 20. Measured elbow angles of the human arm and LARM arm (Continuous line for human elbow, dotted line for LARM clutched arm).

For the shoulder joint the time history is quite similar in the two arms, while the elbow joint shows difference that is very likely due to the intermittent motion due to clutch activation/deactivation. Nevertheless, it is to note that even in the joint angles, the motion looks enough smooth as to ensure a safe user-friendly action of the robot in the food feeding task.

5 CONCLUSIONS

In this paper, the characteristics and functioning of an anthropomorphic clutched arm built at LARM, in Cassino (Italy) are analyzed through an experimental experience for an application in assisting disable peoples for food feeding.

The robotic LARM clutched arm has only one actuator, from which the motion is transmitted to joints with the help of gears and electromagnetic clutches. Tests have proved the movement of this robotic arm as suitable for food feeding action, because it behaves like the human arm during the same action in terms of trajectory and acceleration.

In a near future, this arm can be modified in order to be adapted on a wheel chair and to assist disable persons. Also its functionality can be modified and can perform multiple tasks such as hand writing or carry on movable objects.

REFERENCES

[1] R. Soyama, S. Ishii, and A. Fukase. The Development of Meal-Assistance Robot My Spoon. *Proceeding of the 8th International Conference on Rehabilitation Robotics*. Daelon, Korea, pp.88-91, 2003.

[2] M. Topping. An Overview of the Development of Handy 1, a Rehabilitation Robot to Assist the Severely Disabled. *Journal of Intelligent and Robotic Systems. Kluwer Academic Publishers*. Vol. 34, pp. 253–263, 2002.

[3] NEATER. *User Manual Instructions*. [2013 – 11-15], http://www.neater.co.uk/brochures

[4] Hermann, R., Phalangas, A., Mahoney, R. & Alexander, M., Powered Feeding Devices: An Evaluation of Three Models. *Arch Phys Med Rehabilitation*. Vol. 80, pp.1237–1242, 1999.

[5] Topping, M. & Smith, J., The Development of HANDY 1, a Robotic System to Assist the Severely Disabled. *Proceedings of International Conference on Rehabilitation Robotics*. California, USA, pp.95-105, 1999.

[6] Kobayashi H. Development of Feeding Support System and its Quantitative Estimation. *Proceedings of the 2006 IEEE/RSJ International Conference on Intelligent Robots and Systems*. Beijing, China, pp.717-722, 2006.

[7] Guglielmelli, E.; Lauro, G.; Chiarugi, F.; Giachetti, G.; Perrella, Y.; Pisetta, A. & Scoglio, A., *Self-feeding Apparatus*. US Patent2009/0104004, 2009.

[8] Pourmohammadali, H.; Kofman, J. & Khajepour, A., *Design of a Multiple-user Intelligent Feeding Robot for Elderly and Disabled People*. Master Thesis, University of Waterloo, Ontario, Canada, 2007.

[9] W. K. Song and J. Kim. Novel Assistive Robot for Self-Feeding. *Robotic Systems - Applications, Control and Programming. InTech*, USA, pp.43-60, 2012.

[10] Song, W.-K.; Kim, J.; An, K.-O.; Lee, I.-H.; Song, W.-J. & Lee, B.-S. New Dual-Arm Assistive Robot for Self-Feeding. *Second International Symposium on Quality of Life Technology*. Las Vegas, USA, pp. 152-159, 2010.

[11] M. Ceccarelli, H. Gu. Trajectory planning for a 1-dof clutched robotic arm. *Robotica, Cambridge University Press*, Vol. 29, pp. 745-756, 2011.

[12] H. Gu, M. Ceccarelli, G. Carbone. Design and simulation of a 1-dof anthropomorphic clutched arm for humanoid robots. *International Journal of Humanoid Robotics*, Vol. 7, pp.157–182, 2010.

[13] Hao Gu and Marco Ceccarelli. A Multiobjective Optimal Path Planning for a 1-DOF Clutched ARM. *Mechanics Based Design of Structures and Machines*. Vol.40:1, pp.109-121, 2012.

[14] Copilusi C., M. Kaur, Ceccarelli M. Lab Experiences with LARM Clutched Arm for Assisting Disabled People. *New Trends in Mechanism and Machine Science Mechanisms and Machine Science* . Vol. 24, pp.603-611, 2012.

[15] Klippel S., Seeholzer T. *CONTEMPLAS, User Manual*. Kempten, Germany. 2013.

ISSN 1590-8844
International Journal of Mechanics and Control, Vol. 16, No. 01, 2015

THE EARLIER EXPERIENCES OF PHOTOGRAPHIC MEASUREMENTS IN RUSSIA

Andrei Vukolov, Olga Egorova

Bauman Moscow State Technical University, 2nd Baumanskaya Street, 5,
105005 Moscow, Russian Federation

ABSTRACT

Contactless measurement methods are widely used in industry and research. As we know, they passed more than one century of development, but the main principles remained constant. Photographic measurement methods are taking the very special place between others because of easy results treatment and precision control, low complexity and high integration level of the used equipment. This paper presents a path of evolution of early photographic measurements to the new perspectives of photogrammetric control in Russia. Alexey N. Krylov, the famous Russian scientist, was the pioneer who forced usage of photographic measurements for applied needs of Russian Navy. Additionally, he developed the new ship pitching measurement method that had become a precursor of the most modern sophisticated methods.

Keywords: contactless measurement, photographic method, A.N. Krylov, ship pitching, evolution of measurements

1 INTRODUCTION

The photographic contactless measurement methods in their evolution are all practically derived from very earlier experiences of well-known scientists E. Muybridge and E. Marey [13, 14, 23]. These researches were usually based on synchronic photography with time points. The object broke the time point wire bound to activate recording device (figure 1). From the beginning, they used the photographic contactless measurement methods to record a motion of animals. Further development of equipment and recordings treatment techniques led to appearance of more sophisticated methods such as strobelight photography [17] and photogrammetric treatment [2, 16]. However, before beginnings of 20th century the photographic contactless measurements were not presented in Russia. There were several researches known [20], but they described photography only as a technique of visualization for high-speed processes. Practically the first Russian scientist who began to use such methods as basis of precise experiment was Alexey Nikolaevich Krylov.

Contact author: Andrei Vukolov[1]

[1]Email: andrei.vukolov@gmail.com

1.1 ALEXEY N. KRYLOV: BRIEF BIOGRAPHY

Alexey Nikolaevich Krylov was born on the 15th of August, 1863, in Siberia. He worked in Compass Forge of Hydrographic Department from 1885 to 1887. Later Krylov continued his education in the Naval Academy where he also began to teach as a tutor of mathematics. As mathematician, he built a basis, inter alia, for photographic measurement and analysis of trajectories. However, as the experimentalist, Krylov developed several new methods of measurement and photographic ship pitching recording was the one of them.

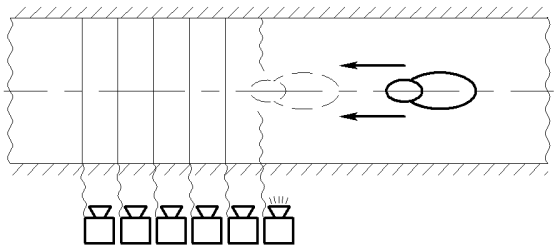

Figure 1. Synchronic photography with time points (Muybridge's schema) [13]

From February, 1902 to January, 1904 he was active in carrying investigations of survivability and insubmersibility of ironclad ships [11]. A research of artillery direction systems behaviour in case of pitching was a part of these investigations. In the era of supersized artillery, the correction of projectile trajectories was necessary. Especially, combination of factors (e.a. large shooting distance, necessity of synchronous measurement for large and small values, high perturbation velocity, and low temporal density of measurements) required to develop special principles of measurement. Krylov developed the new photographic method near 1904 – 1906.

2 PECULIARITIES AND REALIZATION OF PHOTOGRAPHIC PITCHING MEASUREMENT

As beginning, assigned development of idea and base theory to French engineer Huet [9] with reference to ”Mémorial du Génie Maritime”, 1874. Krylov forced to collect data about contactless measurement techniques from all around the world. Krylov also had visited Italy; there at he could learn theory of photography and photogrammetric methods [11]. Studies of photogrammetry helped him to produce several original measurement techniques in Russia, thus Krylov was an inventor in all cases. For example, he developed a photogrammetric technique of artillery shooting control and trace registration [8].

The method proposed by Krylov [19], turns practically the photo camera to analog oscilloscope with direct values conversion. As it is shown on figure 2, camera is installed on the ship with optical axis oriented perpendicular to lengthwise keel plane (rolling mode) or to lengthwise axis (plunging mode). The sighting point of a camera should be positioned to the skyline.

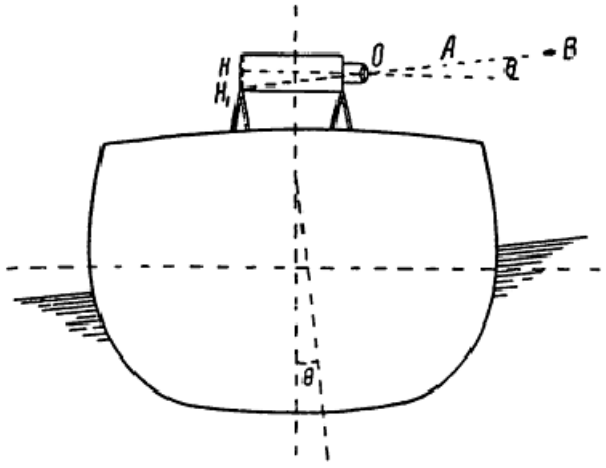

Figure 2. Installation of a camera

Resulting photograph registers the viewable (by brightness) boundary between sky and water. When pitch angle value is θ, then the boundaries on photograph become displaced by:

$$HH_1 = OH \cdot \tan(\theta) = f \cdot \tan(\theta) \quad (1)$$

where OH is a distance from refraction point to focal plane; f — focal length of the lens. Timebase for recording is obtained using following decision. There is the slot diaphragm near focal plane.

The paper tape coated with photosensitive material is being driven by the slit with known speed using clockwork. Resulting oscillogram looks like it is shown on figure 3.

Measurement kit includes a gearing set for the clockwork for different tape drive speed setting. Constrained by camera stand toughness, the described installation provides excellent angular resolution and precision on level of lens aberration amount.

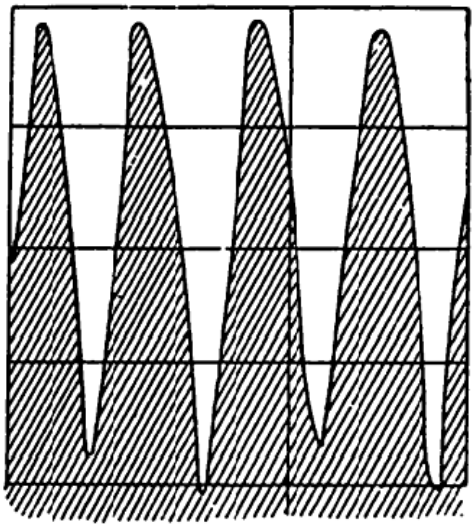

Figure 3. Oscillogram sample

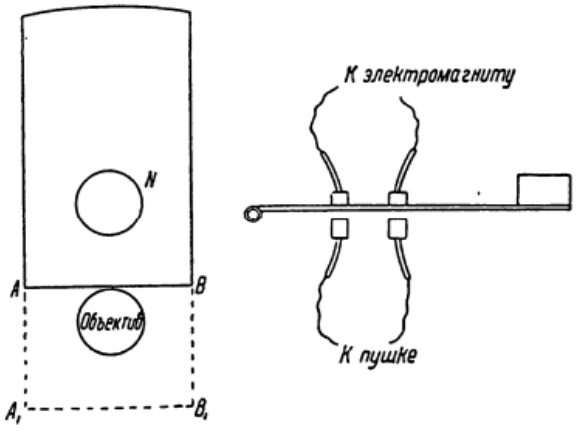

Figure 4. Shot marker (original facsimile)

Krylov developed the special camera for ship pitching recording. This camera, its drawings and full technical description aren’t preserved until present. It contained electromagnetic shot marker (figure 4), which connected to cannon shutter releasing button. Marker consists of shutter N, which is released when cannon fires by electric signal.

Shutter is driven by pre-pressurized spring and provide timings near 1/100 seconds. Releasing of the shutter was implemented by electromagnet which still working when cannon shutter releasing button is not pressed. The oscillogram with shot mark given on figure 5. The lens kit made it possible to vary the measurement scale within wide range. Parameters of the lenses were preserved until now [9] and they are presented in table 1.

The first proved document that contained a reference to practical application of the photographic ship pitching recording technique is ”Uraletz” gunboat workbook [5]. This document contains also the original oscillogram (145-mm negative photographic paper tape more than 5 meters length). Sample of an oscillogram is shown on figure 6.

Table I - Scaling parameters for different lenses.

Focal length, mm	***Ort length, mm***	***Pitching angle***	***Scale, mm/rad***
250 (Zeiss)	10	2°29’	230.72
350 (Zeiss)	10	1.63°	351.51
600 (DeRogée)	10	0.95°	603.11
900 (DeRogée)	10	0.64°	895.25

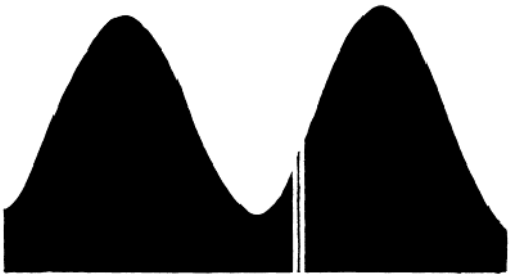

Figure 5. Oscillogram with shot mark

When scales were determined, the oscillogram was used to calculate deviations and influence of shots on pitching. There is unclassified document in Krylov’s personal archive, which contains table of deviations. The results obtained in 1907 were included into the scientific report [6] and unpublished work ”The Influence of Pitching to Shooting Accuracy”[7]. The experimental protocol contains impact points coordinates as it was marked on photograph, real coordinates of that points on field and standard deviations which are snapped to timings. Then using mathematical analysis [6] the pitching (rolling or pludging separately, if needed) component of ship motion could be extracted from protocol.

In described case of measurement Krylov was a pioneer in Russian Navy, and possibly, in Europe also. As a proof to this the Krylov’s memoir books [9, 11] could be used. At that level of the measurement devices development the photographic contactless technique of pitching recording was on the same level of precision with most progressive gyroscopic methods, as Krylov had written about later [10] and where he mentioned photographic technique as primary for calibration of equipment.

Figure 6. Pitching oscillogram

3 VERIFICATION

Main practical application of photographic ship pitching recording technique has been found in February, 1913 when carried out large research with Fram tanks. Tank system was being prepared to install on battle cruisers ”Izmail” and ”Kinburn” which are under construction that time, and it also being prepared to commit into project of ship family ”Gangut”. The test was performed [10] on steamship ”Meteor”. It was equipped with Fram tanks, and immediately before experiment it have been retrofitted with photogoniometers, gyroscopic pitching recorders designed by Fram and Petrovac, photographic oscilloscope designed by Krylov. Photographic chemicals and materials, laboratory equipment components for film treatment and fixation were also loaded aboard. In one of empty storerooms, the darkroom laboratory with semi-automatic film treatment was developed under guidance of professor N. A. Smirnov [11]. Photographic oscilloscopes and gyroscopic recorders were placed at point where pitching is most noticeable — on uppermost deck near wireless house. Krylov described the registration process [10]:

"A tank testing performs as following. The ship lay on course at odds wave. It was laying on that course for 10 minutes with dry tanks and then for 10 minutes with full tanks. Besides, the rolling pitch value was being recorded by all devices and moreover, pludging pitch was being recorded by Petrovac device and one of photographic devices.
After that the ship changed course by 45° e. a., to the right and again it was laying on that course for 10 minutes with dry tanks and then for 10 minutes with full tanks, and after change the course again on 45° to the right, and so on until the ship had laid on course at odds wave finally.
…
On evening of the same day all data was treated as follows:

1. *Records of roll pitching obtained with each device were copied*
2. *Records of pludge pitching obtained with Petrovac device and photographic device, also were copied*
3. *All roll pitching amplitudes obtained with gyroscopic devices were measured, and the most characteristic ones compared with photographic oscillograms to control precision of gyroscopic devices*
4. *Results of amplitude measurement for each course were collected into separate worksheet, and then average and maximal amplitudes* (figure 7) *are determined…"*

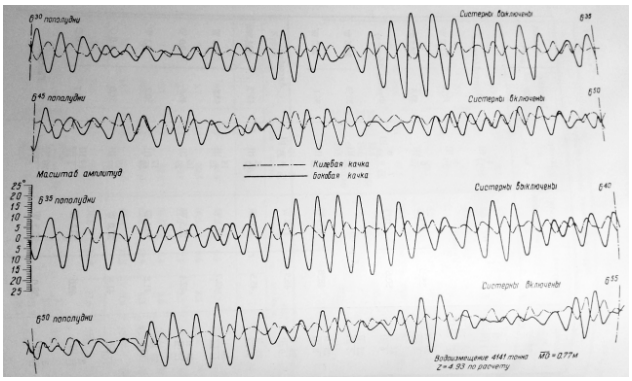

Figure 7. Oscillogram worksheet (original facsimile)

The resulting diagram (figure 8) contains polar distribution of pitching amplitudes with full and dry tanks. As it was shown that diagram was obtained and verified using photographic contactless pitching measurement. It could be used to calculate cycle of filling for Fram tanks.
Simplicity of photographic pitching recording technique in theory and realization brings it to leadership in terms of accuracy and reliability, further given that gyroscopic technology level was slightly low that time, in spite of highest standards of measurement devices design and production.

4 DEVELOPMENT OF CONTACTLESS METHODS

Other mentions of photographic non-invasive measurements in Krylov's memoirs located after 1917. As pointed in "Notes about Works of acad. A. N. Krylov" which are presented in USSR Academy of Science between 1918–1940, he returned in theme near 1920. It were mostly unfinished works dedicated to distant recording of artillery shell trajectory and explosion using photogoniometers. Subsequently before invention of digital photography the photographic contactless measurement techniques occupied in Russian science a narrow niche in sphere of sophisticated experiments on stationary equipment. From that times photographic equipment were integrated into measurement facility, e.a. bubble chamber or emulsion tracker. These applications are difficult to consider as contactless measurements.

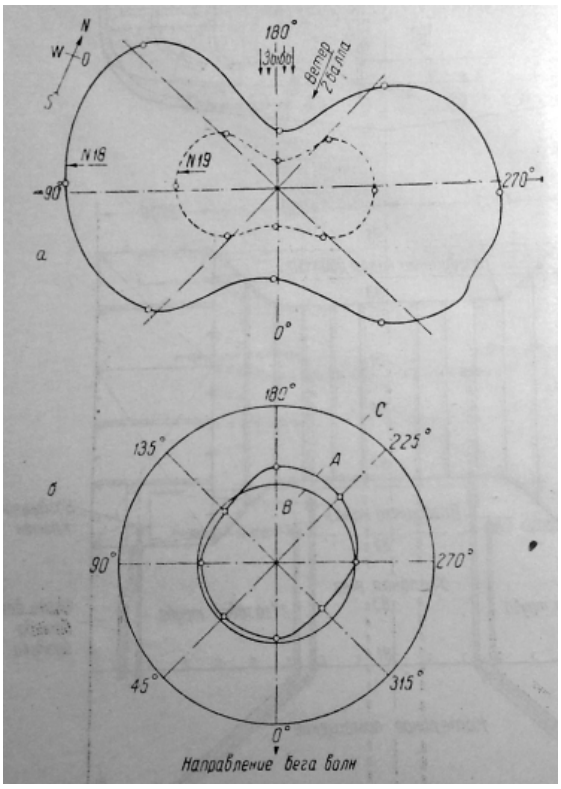

Figure 8. Angular pitching distribution diagram

Gambaryan, Sukhanov and Zacyorsky [15] used photographic measurement methods for animal motion registration. These experiments [24] were the extension of researches of Hildebrand [21, 22] about horse gaits. Just after 1970s perspectives of contactless measurements in Russia are obscured.
Development of digital photo equipment made it possible to use photogrammetry and direct measurements to determine geometry [16, 25]. These works explored error sources while usage of new cameras.
Very wide usage of contactless photographic measurements takes place in robotics [26]. Mathematical methods developed by Krylov built a basin for these researches, especially, in section of technical vision. Some new perspectives of photographic contactless measurements were discovered in accordance with development of digital

video sources [18]. Digital video allows recording of very large amount of data to recover errors. The similar process the strobelight photography also uses [17, 18].
In present, the photographic and photogrammetric contactless measurement methods are widely used in digital image processing and specific tasks, e.g. bullet-time application or 3D-photographic conversion [2].

CONCLUSIONS

New hardware systems and software products (figure 9) turn photographic equipment to universal optical measurement facility. This is correct through all process of contactless measurement evolution.

Krylov's works and early experiments built a basin for applicable techniques, which use a digital processing. From pioneers' works they returned as instruments of a high-tech data creation, art and computer science.
The methods that are based partially on Krylov's researches are widely used today in many areas: geophysics [27], robotics [26], geotechnic, large-area technical vision [28, 29], and biomedics [30].
According to development of new sophisticated methods of digital signal treatment, photographic contactless measurement methods have large perspectives of usage in wide range of areas such as robotics, architectural maintenance procedures, remote control of dangerous objects.

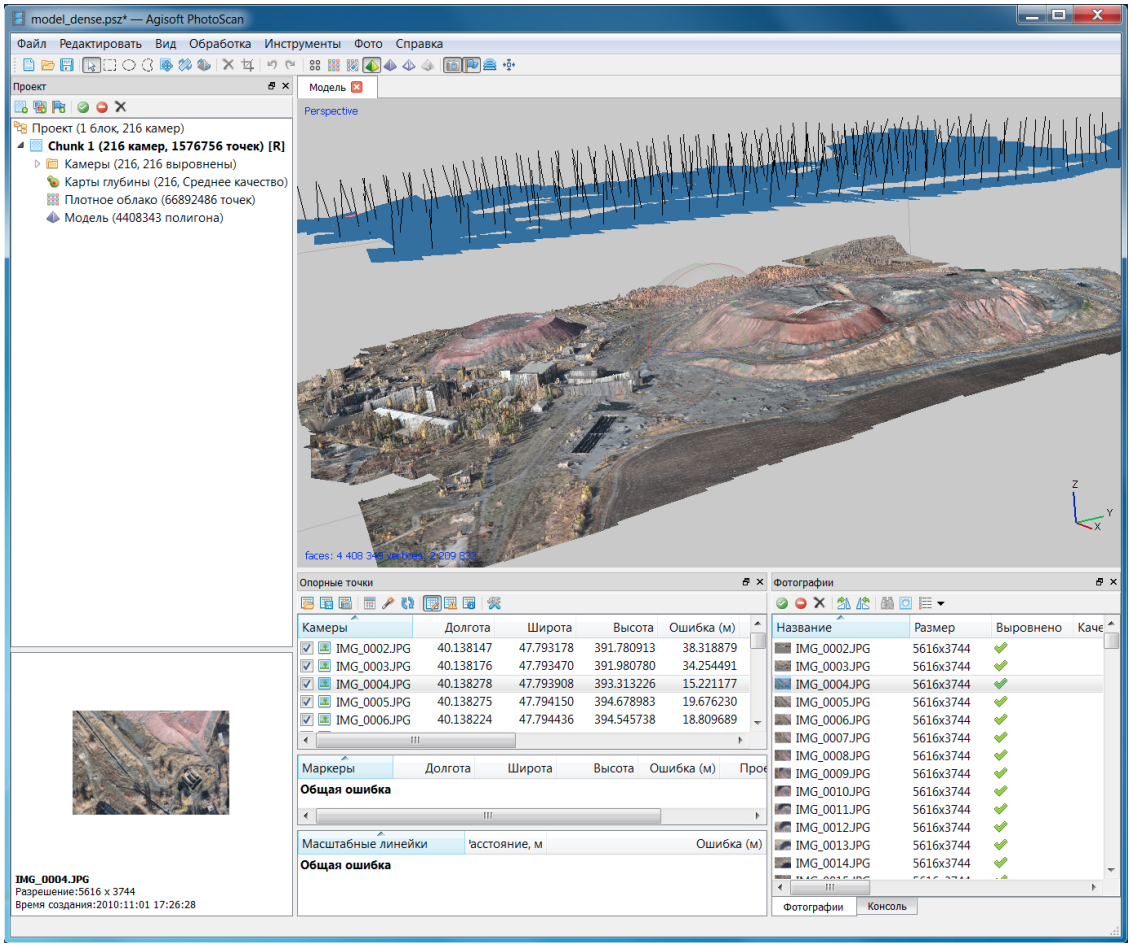

Figure 9. Software product, which uses photogrammetric contactless measurement method [2]

ACKNOWLEDGEMENTS

Authors send their thanks to the crew of St-Petersburg branch of Archive of the Russian Academy of Science.

REFERENCES

[1] The report about scientific works of A. N. Krylov An appendix to protocol of II session of Special Council. Official works (in Russian). // In *Protocols of Academy of Science Special Council*, chapter 29, c. 355, page 45. 1916.
[2] *Agisoft PhotoScan User Manual Standard Edition*, Version 1.0.0 // St. Petersburg, Agisoft LLC, 2013. http://www.agisoft.com/pdf/photoscan_1_0_en.pdf
[3] Krylov A. N. *About photographic recording of ship pitching. The Report for Marine Technical Committee.* Litography (in Russian) // In Fund 759, inv. 1, #98

(special request needed for actual seat allocation). St. Petersburg branch of Archive of Russian Academy of Science, 1906.

[4] Krylov A. N. *Memorandum to F. D. Remesnikov about the end of work upon installation of photographic pitching recording devices on "Uraletz" gunboat and about necessity of exchanging the artificial pitching by natural in swell at open space* (in Russian). In Fund 759, inv. 1, #98/2, pages 33–34. St. Petersburg branch of Archive of Russian Academy of Science, July 15 1907.

[5] Krylov A. N. *"Uraletz" workbook* (in Russian). In Fund 759, inv. 1, #98/5, pages 1–29. St. Petersburg branch of Archive of Russian Academy of Science, 26 September – 18 October 1907.

[6] Krylov A. N. *About experimental shootings on pitching from "Uraletz" gunboat in 1907. Report of colonel Krylov. With 4 appendices* (in Russian). In Fund 759, inv. 1, #98/1, pages 1–46. St. Petersburg branch of Archive of Russian Academy of Science, December 1908.

[7] Krylov A. N. *The influence of ship pitching to shooting accuracy* (in Russian). In Fund 759, inv. 1, #98/10, pages 27–28. St. Petersburg branch of Archive of Russian Academy of Science, 1908.

[8] Krylov A. N. *About usage of photogrammetric recording to shell trajectory determination* (in Russian). Uncompleted work. In Fund 759, inv. 1, #100, par. 1, 2, pages 1–3. St. Petersburg branch of Archive of Russian Academy of Science, 1920.

[9] Krylov A. N. Collected Works of acad. A. N. Krylov, volume XI. Ship pitching // *chapter "About Photographic Recording of Ship Pitching"* (in Russian), pages 261–264. USSR Academy of Science Publishing House, Moscow – Leningrad, 1951.

[10] Krylov A. N. Collected Works of acad. A. N. Krylov, volume XI. Ship pitching // chapter *"Testing of Fram tanks on Meteor steamship"* (in Russian), pages 273–285. USSR Academy of Science Publishing House, Moscow – Leningrad, 1951.

[11] Krylov A. N. *My Memories* (in Russian) Leningrad, "Sudostroenie", 1984

[12] Smirnov V. I. (editor). Handwritten Legacy of Academician Alexey Nikolaevich Krylov (in Russian) // In *Volume 23 of Works of USSR Academy of Science.* "Nauka". Leningrad branch, Leningrad, 1969.

[13] Miles W. R. *Muybridge animal pictures* // Science. 1929. Vol. 70, no. 1809. Pp. 216a–217.

[14] Geddes L. A. *Gaits of Horses: Marey's Studies* // Science. 1966. Vol. 151, no. 3707. Pp. 152a–152.

[15] Sukhanov V. B. *The Generalized System of Symmetric Locomotion of Terrestrial Vertebrates* (in Russian) // Leningrad, "Nauka", Leningrad branch, 1986.

[16] Golovin A., Vukolov A., Potapova A. Peculiarities of Flat Cam Measurement by Results of Digital Photo Shooting // *New Trends in Mechanism Science: Analysis and Design* / Ed. By D. Pisla, M. Ceccarelli, M. Husty, B. Corves. Springer, 2010. Pp. 269–276.

[17] Golovin A., Vukolov A., Umnov N. Horse Gait Exploration on Step Allure by Results of High Speed Strobelight Photography // *New Trends in Mechanism Science: Analysis and Design* / Ed. by D. Pisla, M. Ceccarelli, M. Husty, B. Corves. Springer, 2010. Pp. 361–368.

[18] Vukolov A., Kharitonov E. Kinematical Analysis of Mechanical Systems by Results of Digital Video Recording // *Proceedings of the 10th IFToMM International Symposium on Science of Mechanisms and Machines SYROM 2009* / Ed. by I. Visa. Springer, 2009. Pp. 457–464.

[19] Vukolov A., Golovin A. A.N. Krylov: The Pioneer of Photographic Non-invasive Measurement Methods in Russian Science // *New Trends in Mechanism and Machine Science* / ed. By P. Flores, F. Viadero, Springer, 2015, Pp. 903-911.

[20] A. Instantaneous Photographs of Flying Rifle Bullet (in Russian) // *Herald of Experimental Physics and Elementary Mathematics*. 1892, 150: 130-131.

[21] Hildebrand M. Motions of the running cheetah and horse // *Mammal*. 1959. 40: 481–495.

[22] Hildebrand M. How animals ran // *Scientific American*. 1960. 202(5): 148–157.

[23] Muybridge E. *Animal Locomotion* New York, 1957.

[24] Swanevelder A. G. An optical gait analysis system for horses // *Masters Abstracts International*. 1995. Vol. 33, 2: 5–81

[25] Yakushina E. Place Function Definition of the Cam Mechanism by the Digital Photography Method and Statistical Processing of Measurements Results // *Proceedings of Russian-Italian Students' Workshop "Problems in Robotics"*. Kursk, KSTU: 2008.

[26] Vorotnikov S. A. *Information devices of robotic systems* (in Russian). // M., Bauman Moscow State Technical University: 2005. ISBN 5-7038-2207-6

[27] Datcheva M., Meier J., Moser M. et al. Numerical modelling and inverse parameter estimation of the large-scale mass movement Gradenbach in Carinthia (Austria) // *Acta Geotechnica, vol. 8, #4, pp. 355-371*. Springer-Verlag, 2013. DOI 10.1007/s11440-013-0211-1

[28] Wasil B. A., Merchant, D.C., Del Vecchio, J. J., JR. Photogrammetric measurements of dynamic displacements // *Experimental Mechanics, vol. 5, #10, pp. 332-339*. Kluwer Academic Publishers, 1965. DOI 10.1007/BF02327536

[29] Chen, G., Li L., Lytton R., Zhang X. A photogrammetry-based method to measure total and local volume changes of unsaturated soils during triaxial testing // *Acta Geotechnica, 2014-08-26, pp. 1-28*. Springer Berlin Heidelberg, 2014. DOI 10.1007/s11440-014-0346-8

[30] Yang F., Yuan X. Human Movement Reconstruction from Video Shot by a Single Stationary Camera // *Annals of Biomedical Engineering, vol. 33, #5, pp. 674-684*. Kluwer Academic Publishers – Plenum Publishers, 2005. DOI 10.1007/s10439-005-1976-7

ISSN 1590-8844
International Journal of Mechanics and Control, Vol. 16, No. 01, 2015

CONTRIBUTION TO R.A.M.S ESTIMATION IN EARLY DESIGN PHASES OF UNMANNED AERIAL VEHICLES – UAVS

R. Fusaro S. Chiesa S. Cresto Aleina M. Fioriti

Politecnico di Torino, Mechanical and Aerospace Engineering Department

ABSTRACT

The aim of this work is to establish a methodology for assessments of Reliability, Safety and Maintenance features for future UAVs, to be integrated in complex Monitoring Systems, like SMAT System. This paper highlights the high level of complexity connected to this type of assessment. In particular, one of the principal sources of difficulties is the need of estimating RAMS characteristics for a product that is still not known in detailed, like it is usual for airplane in Conceptual Design phase. A further problem concerns the need of dealing with UAVs, i.e. aircraft with strong peculiarities and, due to the very recent development, poor historical data. By the way, referring to a methodology that has been previously developed for manned aircraft (by the research group the authors belong to), a new estimation process applicable to unmanned airplanes is here proposed. At the end, a comparison between the obtained results and few historical data is reported.

Keywords: Reliability, Safety, Maintenance, UAV, Conceptual Design

1 INTRODUCTION

Today, in the Aerospace field, the assessment of Reliability, Safety and Maintenance features of a new System has become a common practice since the earliest design phases [1] [2]. During these preliminary stages, the new System concept is defined, as well as its architecture and its relevant features (not at detailed level). This process is clearly depicted in Ref. [3]. The aforesaid requirements should be considered as guidelines since the very first design phases, even if the approach to Reliability, Safety and Maintenance could be affected by some additional difficulties, mainly due to the lack of definition of detailed features. This implies ad-hoc strategies to be implemented throughout the development of each single product. Moreover, this is a relevant aspect in case the designers face with Unmanned Aerial Systems (UAS), i.e. a System constituted by aircraft without human pilot on board, the so-called Unmanned Air Vehicle (UAV), and related ground infrastructures.

Contact author: Roberta Fusaro[1]

[1] Email roberta.fusaro@polito.it
Politecnico di Torino
Mechanical and Aerospace Engineering Department
Corso Duca degli Abruzzi, 24 - 10129 Torino, Italy

Among all the relevant aspects engineers should take into account, the peculiarity of a GCS-Ground Control Station and of all other support elements (better, the "system support") typical of all other kind of aircraft. Please note that, UASs are becoming more and more relevant, both from the technical and the industrial point of view. As far as the technical point of view is concerned, it can be useful to underline the advantages of UAVs. Indeed, the absence of human pilot allows eliminating many onerous devices, like cockpit and the necessity of defining aircraft shape to conjugate Pilot visibility requirements with aerodynamics, the furnishing or many other elements required to host and support human Pilot, like Environmental Control System, Voice Communications, Displays and Controls. Another more relevant feature is the possibility of avoiding all the constraints related with physiological aspects like time limitations, the lack of attention, tiredness and boredom, and, in general, all the risks that can affect a human life. Obviously, most relevant drawback is the need for a GCS able to perform a part of Human Pilot Tasks and of creating a sort of "Artificial Intelligence" on board. The level of complexity of this sort of intelligence strictly depends on the desired or required autonomy level for the considered UAS. Focusing on the above-mentioned advantages, the success of UAVs is clearly demonstrated by the very high number of models built and currently in-service or in-development phase, as well as the extremely wide spread range of performances, technical characteristics, sizes, architectural solutions, kinds of engines, etc.

Northrop Grumman RQ-4 Global Hawk

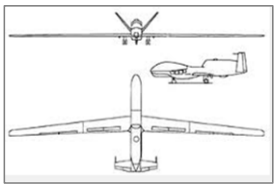


Role:Reconaissance, Surveillance, Monitoring
Lenght 15.40 m
Wing span 35.42 m
Wing Area 50,10 sqm
TOGW 12133 kg
Empty Weight 5100 kg
Power Plant 1 x T.Fan AE3007H - Thrust: 36.8 kN
Speed 640 km/h
Ceiling 19000 m
Range 25000 km

General Atomics MQ-9 Reaper

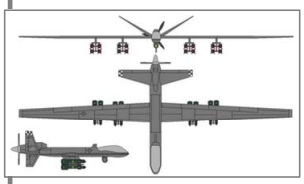


Role: Surveillance, Monitoring & Combat
Lenght 11.00 m
Wing span 20.00 m
Wing Area 20.80 sqm
TOGW 4760 kg
Empty Weight 2223 kg
Power Plant 1xT.Prop TP331-10T – Power: 712 kW
Speed max 480 km/h
Ceiling 15000 m
Endurance 14 – 28 hours

General Atomics RQ-1 Predator

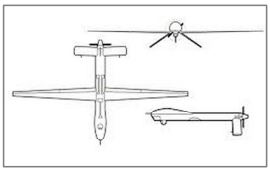


Role: Surveillance, Monitoring & Combat
Lenght 8.22 m
Wing span 14.80 m
Wing Area 11.50 sqm
TOGW 1000 kg
Empty Weight 512 kg
Power Plant 1x4-Piston ROTAX 912 - Power: 72 kW
Speed 218 km/h
Ceiling 7800 m
Endurance 24 hours

Northrop Grumman RQ-5 Hunter

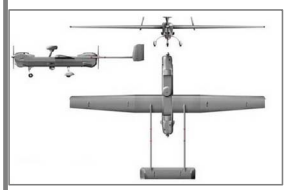


Role: Reconnaissance, Target acquisition
Lenght 7.00 m
Wing span 8.90 m
Wing Area 8,00 sqm (estimated)
TOGW 725 kg
Empty Weight 510 kg (estimated)
Power Plant 2 x 2 cylinder – Power:2 x48 kW
Speed 196 km/h
Ceiling 4570 m
Endurance 12 hours

AAI corporation RQ-2 Pioneer

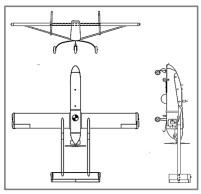


Role:Reconaissance, Surveillance, Monitoring
Lenght 4.00 m
Wing span 5.20 m
Wing Area 50,10 sqm
TOGW 205,00 kg
Empty Weight 155,00 kg (estimated)
Power Plant 1xUEL AR-741 (Wankel eng.) Power:28.3 kW
Speed (max) 200 km/h
Ceiling 4600 m
Endurance 5 hours (at 185 km distance)

Dassault (et alii) nEUROn

Role: Combat (experimental aircraft)
Lenght 9.20 m
Wing span 12.50 m
Wing Area 50,10 sqm
TOGW 6500 kg
Empty Weight 4900 kg
Power Plant 1 x R.R. Adour - Thrust: 40.8 kN
Speed 0.8 Mach
Ceiling 14000 m
Range ? km

Figure 1 Typical UAVs overview

Figure 1 shows typical UAVs models, ranging from a Take Off Gross Weight (TOGW) of more than 10,000 kg (the Northrop-Grumman Global Hawk, with turbofan engine), going from the General Atomics Reaper with turboprop, to the smaller UAVs with reciprocating engines and different roles. Concerning the typical UAV roles, the readers should notice that UAVs could range from the pure Combat task (and in this case they are called UCAV-Unmanned Combat Air Vehicle, of which a clear example is the experimental "nEUROn"), to a wide spread of Reconnaissance, Surveillance, Monitoring and Target Acquisition tasks. Obviously, the difference in roles implies variations in performance and size of the airplane. Even if combat tasks can be performed too (for example see in Fig. 1, the weapons of "MQ-9 Reaper"), UAVs designed for Reconnaissance, Surveillance, Monitoring and Target Acquisition tasks reveal a clear homogeneity. Furthermore, this last group of UAVs has real perspectives to be used in Civilian applications [4]. Thus, in this paper, the Authors will discuss only about this last kind of UAVs, focusing on the way to reach an acceptable capability in terms of Reliability, Availability, Maintainability, Safety (RAMS) assessment. Moreover this paper proposes a possible way to reach an enough high level in the definition of those related requirements since the earliest phases of a new UAV development.

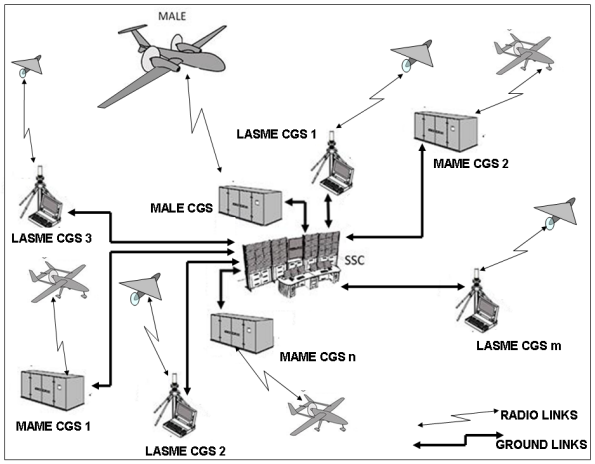

Figure 2 SMAT system configuration

The idea of in-depth studying these RAMS characteristics arose from the participation of the Authors to the Research Program SMAT – *Sistema di Monitoraggio Avanzato del Territorio* (Advanced Land Monitoring System). The Project has been proposed and funded by Regione Piemonte Government and Fondo Sociale Europeo. It hypothesized a Territory Monitoring System, whose configuration is schematically shown in Figure 2. It is based on several kinds of UAS with the aim of controlling and monitoring the entire Piedmont Region or an even wider territory. Indeed, the final target is to define a System able to be offered, in customized configurations, at a higher number of interested Users from all over the word. In Fig. 3 several possible scenarios are illustrated, showing different areas to be covered. In particular, the research focuses on a fleet of several UAVs belonging to different categories (MALE-Medium Altitude Long Endurance, MAME-Medium Altitude Medium Endurance, LASME-Low Altitude–Short/Medium Endurance and Mini and Micro UAVs) and operating from a certain number of possible bases located in Italy. Figure 2, depicts a possible integrated system able to exploit MALE, MAME and LASME. SMAT program has been intended as a way to support the ground operation in both critical, like fire and flood, and nominal situations, as traffic control or thematic mapping.

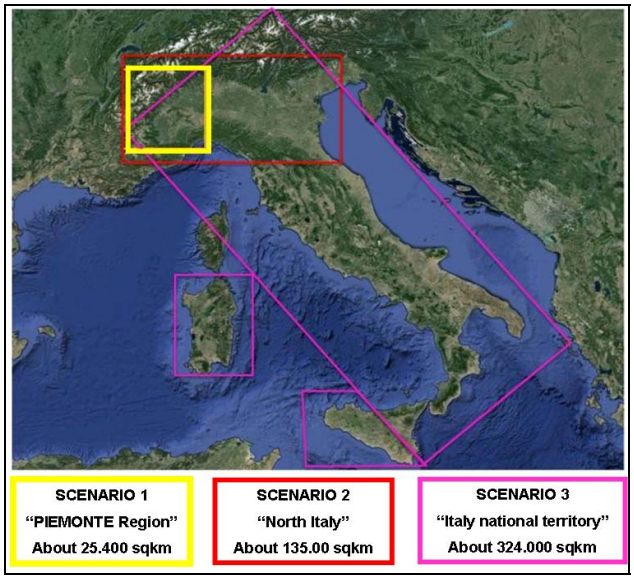

Figure 3 SMAT example of scenarios with different extension

2 RELIABILITY ASSESSMENT IN EARLY DESIGN PHASE

A system like the one proposed in SMAT project is a clear example of how it is necessary to acquire the capability of assessing reliability and all the other related characteristics, like safety and maintenance features of new aerial systems. Fig. 2 reveals how many constraints on the system efficiency can be related to Reliability and Maintenance features. The variety and the relevance of these constraints are schematically shown in Fig. 4. Moreover, this Figure allows the readers to understand the multiple influences on both the efficacy and on the costs of the system, highlighting the key role played for the success possibility of the System itself. In Fig. 4, maintenance features have been separated into two contributions: the one directly related to the product (i.e. Maintainability, Ref. [5]) and the ones concerning the Maintenance Organization, or, better, to the support system.

For all the above-mentioned reasons it seems to be clear that Reliability characteristics of Sub-Systems and their Maintenance features have to be kept under close control

during the development of System and the System Support definition. In particular, in case there would be the wish of integrating already existing UAS in a new Monitoring System, Reliability and Maintenance features of the under-investigation elements are known and it is possible to take them into account. However, it is clear that this is not the more convenient way to develop an optimal system. Indeed, in this case, the designers have to accept not only reliability and maintenance features but also performances and size of the basic components of the system. Conversely, if the system is completely conceived *ex novo*, the engineer should have the possibility of obtaining a really optimal system, perfectly adapted to the considered Scenarios and to all the already existing exploitable like bases infrastructures, maintenance organization characteristics, etc. In this case, reliability and maintenance, as well as all the other UAS characteristics must be defined as specification requirements the system's components must comply with. The relevance of this operation it is well known in case of UAS, in which there isn't a great amount of historical data. The problem is becoming even more difficult, as far as reliability and maintenance features are concerned, because these characteristics are strictly connected to the details of the design. These connections mainly depend on the relevance of these RAMS features in defining a system, in particular a complex and critical one [6], and on the consideration that more advanced system design methodologies [7], forcing us to take into account all relevant features of a new product since from the early Design phases [8]. To this purpose the authors developed a methodology for reliability, safety and maintenance features assessment in aeronautical Conceptual Design Phase [9], but the problematic to apply it to a kind of a quite peculiar airplane with a still short story and not so many historical data available are well kwown

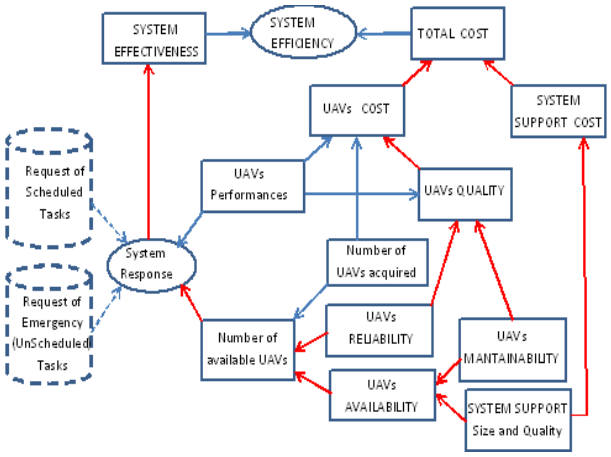

Figure 4 Influence of Reliability and Maintenance features on system efficiency

3 UAV RELIABILITY AND SAFETY ASSESSMENT AT CONCEPTUAL DESIGN LEVEL

In developing the aforesaid methodology for a preliminary estimation of Reliability, Safety and Maintenance features in the Conceptual design phase, the Authors had to face with the lack of detailed data, typical of these phases of the Design. Essentially, they try to solve the problem by using not only technical macro-features already known in early development phases, (such as the vehicle overall weight, and/or indicative main performances) but also compensating the lack of information by introducing qualitative concepts (such as the level of complexity, role, technological age, etc.). These concepts are based on known data of existing airplanes. These aircraft are clearly defined by the point of view of the Complexity level, of the Role, of the Technologies adopted and of the Innovation level. A first estimation attempt for the basic failure rate λ_b is reported n Eq. (1a) and it can be solved using statistical data.

$$\lambda_b = k \cdot \mathrm{MEW} \cdot \mathrm{IR} \cdot \mathrm{IC} \cdot \mathrm{IA} \qquad (1a)$$

where:
MEW = Manufacturer Empty Weight [t];
k = ratio between the failure rate and MEW for a Medium Civil Aircraft, usually equal to 1.8 (failures/1000h)/t;
IR = Index of Role;
IC = Complexity Coefficient;
IA = Technological Age Index.

Some indications are then suggested for the values of the qualitative parameters present in (1a), and this is made in Tables I, II and III, with the warning, already told, that methodology has been developed for Conceptual Design Level of "manned aircraft".

Table I - Index of Role suggestions

Role	IR
Fighter	16.60
Military Transport	2.10
Civil Transport	1

Table II - Complexity Coefficient suggestions

Complexity Level	Complexity Coefficient	Reference Aircraft
Low	0.8	S211
Middle	1.0	AMX
High	1.4	Tornado, Eurofighter EF 2000
Very High	1.6	F-22

Table III, reported from reference [9] shows how (1a) is able to give satisfactory estimation for many kind of manned aircraft, only utilizing few parameters that are easy to fix even in early design phases.

Table III - Technological Age Index suggestions

Technological Age	Age Coefficient	Reference Aircraft
2000	0.66	F-22
1990	1.0	Eurofighter EF 2000
1980	1.5	AMX
1970	2	Tornado
1960	2.5	F104S

Table IV [9] shows how the Eq. (1a) is able to give satisfactory estimations for many kinds of manned aircraft, only utilizing few parameters that are easy to fix also in the earliest design phases. Certainly, the problem becomes even more complex in the case of UAVs, not only for the poor base of historical data, but also for the peculiarities of this type of aircraft.

Table IV - Example of λ_b estimation for manned aircraft, Ref. [9]

Aircraft	k	IR	IC	IA	MEW (ton)	λ_b (failures/1000h)
Eurofighter EF 2000	1.8	16.6	1.4	1	9.6	402
TORNADO	1.8	16.6	1.4	2.0	13.8	1155
AMX	1.8	16.6	1.0	1.5	6	269
JAS 39 GRIPEN	18	16.6	1.4	1.2	6	301
C130	1.8	2.1	1.0	2.5	35	331
A400	1.8	2.1	1.0	0.7	45	119
C17	1.8	2.1	1.4	0.8	120	508
G222	1.8	2.1	1.0	2.0	15	113
A320	1.8	1.0	1.4	1	42	106
B747	1.8	1.0	1.4	2.0	170	857
ATR42	1.8	1.0	1.0	1.5	10	27

Indeed, as far as the "Role Index" is concerned, it is quite sure that UAVs for Monitoring and Surveillance are different both from Fighters and from transport aircraft, considering military and civil applications. However, UAVs with monitoring & surveillance roles canbe considered more similar to fighters, as far as on-board systems are concerned.

This can be justified noticing that they are extremely far from the features of aircraft hosting passengers and that there is the need of taking into account the additional complexity of ground station and the communication links between air and ground segment. By the way, it is also clear that, neglecting Unmanned Combat Air Vehicle (UCAV), the UAVs devoted to the reconnaissance, monitoring, target acquisition do not face with high "g" maneuvers and never utilize weapons and related systems, like Fighters do. Thus, the Authors hypothesize to define an Index Role, see Eq. (2), equal to the 50% of the one defined for fighters, even for present application, limiting the field of application to UAVs with civilian purposes.

$$IR_{UAV} = 8.30 \tag{2}$$

On the contrary it is possible to estimate the other coefficients required by Eq. (1a) applying a similar methodology. With reference to Table II and Figure 1, *ad-hoc* values have been proposed, in order to characterize a group of existing UAVs as it is shown in Table V.

Table V - UAV Example of parameters required for λ_b estimation

UAV	k	IR	IC	IA
Global Hawk	1.8	8.30	1.6	0.66
nEUROn	1.8	8.30	1.6	0.66
Predator RQ-1A	1.8	8.30	1	1
Reaper RQ-1B	1.8	8.30	1	0.8
Pioneer RQ-2B	1.8	8.30	0.6	1.3
Hunter RQ-5	1.8	8.30	1.4	1.3

But some considerations on the UAV peculiarity are certainly necessary and, to this purpose, the Ref. [10] constitutes an optimal data source. In particular, it reveals some strong differences between Fighters and UAVs. For example, in the methodology proposed in Ref. [9], a proportionality between the Basic Failure Rate (which is comprehensive of any kind of failure) and Safety Failure Rate (which takes into account only critical failures) is considered. This has been explicated in Eq. (3).

$$\lambda_s = \frac{\lambda_b}{LR} \tag{3}$$

In Eq. (3) LR is a sort of "role index" and it is different accounting for the several kinds of airplanes. Ref. [9], suggests a value of 10^4 for fighters and of 10^6 for civil transports. These values are related both to the different order of magnitude in the total life flown hours and to the different kind of legal position of a Military Pilot and of a Civilian Passenger, as well as the more stressed technical characteristics of Fighters. In the current assessment, complying with the previous hypothesis of considering UAVs similar to Fighters, the Eq. (3) could be rewritten as presented in Eq. (4a):

$$\lambda_s = \frac{\lambda_b}{10^4} \tag{4a}$$

Please note that this relationship can be useful as a verification with values of "Safety Failure Rates" that are quite strongly fixed (up to now, almost for Manned Aircraft!) due to certification reasons.

Putting aside this method, Unmanned Aerial Vehicles data have to be considered more similar to those to be included in a new System as, for example, SMAT. These data should refer to UAV with a yet considerable number of cumulated flight hours, in order to be relevant from the statistical point of view. In this case, aircraft in service among several U.S.A. Armed Forces Units were considered. These data are provided by Ref. [11] and Table VI summarizes the most relevant ones for our applications. This table provides several considerations. Considering the value of MEW for the selected UAVs, it can be observed that there is a trend to have higher Basic Failure Rates with the decreasing of weight (in particular if the Manufacturer Empty Weight is concerned). This effect is not considered in (1a) but it is clearly shown in Figure 5.

Table VI - UAV (currently operating) failure rates (Basic and Safety) comparison

UAV	MTBF [hours]	λ_b [failures/1000h]	λ_s [mishaps/105h]	$\frac{\lambda_s}{\lambda_b}$
Predator RQ-1A	32	31.25	43	$1.38/10^2$
Reaper RQ-1B	55	18	31	$1.7/10^2$
Pioneer RQ-2B	28.6	35	139	$4.0/10^2$
Hunter RQ-5	11.3	88.49	16	$1.6/10^3$

This fact can be explained noticing that, under a certain weight, there is an amplification effect for basic failure rate λ_b due to:

a) higher criticality of micro-components;
b) use of aeromodelling-derived technologies;
c) difficulties in assembly due to reduced size;
d) criticalities due to high density in terms of number of components in a reduced volume;
e) anomalies in aerodynamic behavior due to unusually low Reynolds Number values.

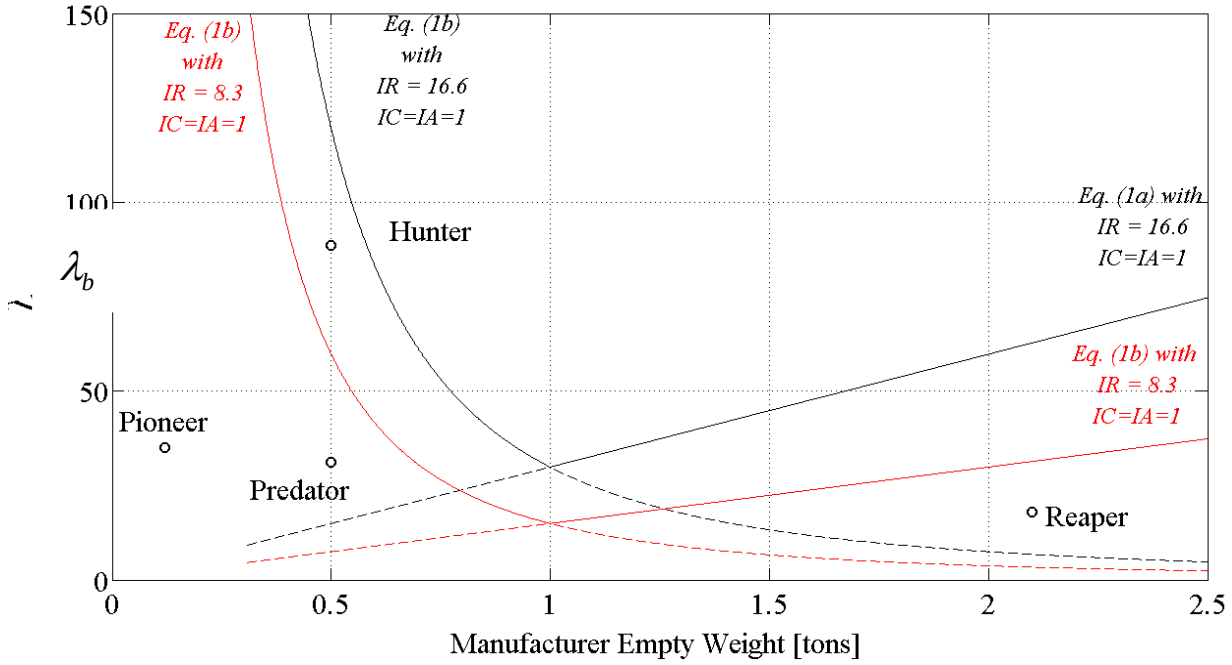

Figure 5 Relationship between λ_b and MEW

Such effect can be modeled by substituting the (1a), for Failure Rate λ_b estimation, only for small UAVs, as follows:

$$\begin{cases} \lambda_b = k \cdot \text{MEW} \cdot \text{IR} \cdot \text{IC} \cdot \text{IA} & \text{for MEW} > 1 \quad (1a) \\ \lambda_b = k \cdot (1/MEW)^2 \cdot \text{IR} \cdot \text{IC} \cdot \text{IA} & \text{for MEW} \le 1 \quad (1b) \end{cases}$$

The (1b) can replace the (1a) in the range of MEW between 0.1 to 1 [tons], while the (1a) maintains its validity for MEW>1 [ton], as it is shown in Figure 6 by the red curve, obtained from (1b) and (1a) in the aforesaid ranges of MEW values, with IR=8.3 and IA=IC=1.

By introducing, in Table VII a comparison between typical UAVs and typical Fighter Aircraft (as an example, three of the most relevant U.S. Fighters have been considered), "Basic Failure Rate" λ_b seems to be, for UAVs, almost an order of magnitude lower than the Fighters, as shown in the aforesaid Table. This can easily be explained with the generally lower weight (for at least an order of magnitude) for UAVs with respect to the Fighters. Furthermore, it confirms the assumption made for the Index Role.

Conversely, the Mishap Rate of UAVs appears to be at least one order of magnitude higher than the Fighter's one (data reported about λ_s for both UAVs and Fighters are taken from reference [10]). Trying to explain these facts, please note that the safety failure rate, λ_s [Mishaps/hour], seems to be highly variable among all vehicles, Manned or Unmanned (probably with lower, thus better, values for more "mature" vehicles). By the way it is clear that the majority of the considered fighters are compliant with the ratio $\lambda_s/\lambda_b=10^{-4}$, expressed by (4a), whereas, as for UAVs, it is highly necessary to reduce λ_s of 1 or 2 orders of magnitude. In particular, this would became a stringent requirement if it will be necessary to operate on civil field or on highly populated territories, as it is clearly requested for SMAT. For such applications, a target value of λ_s equal to $1 \cdot 10^{-5}$ can be expected, taking as reference Table 8, referring to [11], currently one of the main documents for Safety-related issues. The las column of Table 8 reports the system loss cumulative probabilitiy requirements. This can be assimilated to a mishaps rate not necessary meaning catastrophic events. This value could be further reducedbtaking into account population density, exposition area for vehicle crash, the probability that effects of mishap could be "mitigated", etc…

4 FAILURE RATE AND SAFETY FAILURE RATE PROPOSED FOR SMAT's UAVs

As already said, the UAV in use in SMAT program belongs to three categories: MALE (Figure 6 and Table IX), MAME (Figure 7 and Table X) and LASME (Figure 8 and Table XI). In the following figures and tables the main features of the considered UAV are reported. Starting from the indications provided from AER P2 [11], Table VII suggests that the Safety Failure Rate is the first value to be fixed. This is due to its involvement with an Authorities Approval for operations in Civil Area that is clearly *condicio sine qua non* for the realization of SMAT. Table XII, for three UAVs that will be integrated in SMAT, a proposal of Safety Failure Rate has been formulated. Please note that the rule AER P2 covers only military vehicles and UAVs with a weight larger than 150 kg and created without scientific purpose or for research. For the other vehicles, national rules are allowed. In Italy recently a Rule called "*Regolamento per APR con peso<150 kg*", Ref. [12], has been recently issued by ENAC (Ente Nazionale Aviazione Civile – Italian Authority for Civil Aviation). Given that it is still under discussion the technical Specifications of SMAT's UAVs, it is clear that LASME UAV (also intended as "Light" UAV) could be subjected to different Rules for its definition. Thus, in the following considerations, the attention will focus on MALE and MAME. From the above seen data reporting UAS servicing among USA Military Forces, it can be clearly seen that values of λ_s, for UAVs features, appear worse (or better too high, with values almost between $1/10^3$ and $1/10^4$) and so, not compliant with, for example, the AER P2 regulations.

This is a consequence of the fact that the ratio λ_s/λ_b for UAVs in service appears to be higher than the one which was thought to be assumed by Fighters (please, remember the (4a), i.e. $\lambda_s/\lambda_b=10^{-4}$).

Nevertheless, assuming an improvement of an order of magnitude on λ_s (that appears mandatory for safety reasons) the ratio expressed in (4b) could be adopted, maintaining the current basic reliability values for the components:

$$\lambda_s = \frac{\lambda_b}{10^3} \quad (4b)$$

Table VII - Comparison Basic Failure Rate vs. Safety Failure Rate for Fighters and UAVs

Fighter	λ_b [failures/1000h]	λ_s [mishaps/10^5h]	UAV	λ_b [failures/1000h]	λ_s [mishaps/10^5h]
AV-8	807	10.7	Reaper RQ-1B	18	31
F-16	299	3.35	Pioneer RQ-2B	35	139
F-18	427	3.2	Hunter RQ-5	88,49	16

Table VIII - Cumulated probabilities of failures (Rule AER P2)

Vehicle	Airplane Class	Catastrophic event probability	System loss cumulative probability
Military UAV	(S7) Ultra-light UAV, 20<TOW<150 kg	Catastrophic $\leq 10^{-6}$	System Loss $\leq 5 \cdot 10^{-5}$
	(S8) Light UAV, 150<TOW<500 kg	Catastrophic $\leq 10^{-6}$	System Loss $\leq 3 \cdot 10^{-5}$
	(S9) Medium UAV, 500<TOW<2700 kg	Catastrophic 10^{-6}	System Loss $\leq 10^{-5}$
	(S10) Heavy UAV, TOW>2700 kg	Catastrophic 10^{-7}	System Loss $\leq 1\text{-}5 \cdot 10^{-6}$

Table IX - Hypothesized Safety Failure Rate of SMAT UAVs

UAV (SMAT)	Weight [kg]	λ_s [mishaps/10^5h]
MALE	4000	$5 \cdot 10^{-6}$
MAME	500	$3 \cdot 10^{-5}$
LASME	150	$3 \cdot 10^{-5}$

This means to adopt an $LR_{UAV}=10^3$. Thus, starting from an order of magnitude of Basic failure rate lower than the one of the Fighters, UAVs have (also taking into account an improvement compared to current situation) λ_s of at least an order of magnitude higher of the Fighters one, the following considerations can be done:

a) There is no crew on board;
b) The fact of having no crew on board reduces the resources to deal with critical situations and emergencies (in other terms, a critical situation has less probabilities to be carried out successfully).

According to these considerations, it is worthwhile to use the methodology proposed in reference [1], adopting an IR=8.3 (as well the 50% of the one of the Fighters) and the other differences already explained for the ratio λ_s/λ_b of UAV in service and for the Role Index, that can be defined LR_{UAV} and that is, as already seen, equal to 10^3.
Nevertheless, to make SMAT UAVs, the "future" vehicles with a strict need of certifications to operate in Civil Field, even on highly populated areas, the Role Index used for Fighters, $LR=10^4$ should be considered valid.
The application of the methodology with the choice of the various factors is reported in the following Table XIII for:

a) UAVs for which real data are available (used for comparison);
b) UAVs included in SMAT system.

Values reported in bold font in the previous table, could be therefore indicative of requirements in terms of λ_s/λ_b for the three UAS of SMAT system.

Table X - Failure rates estimated for existing and future UAVs

UAV	k	IR	IC	IA	MEW [t]	Relation. utilized	λ_b [fail/1000h] estimated	λ_b [fail/1000h] known
Predator RQ-1A	1.8	8.3	1.0	1.0	0.5	(1b)	21.13	31.25
Reaper RQ-1B	1.8	8.3	1.0	0.8	2.1	(1a)	25.09	18.00 (25 at specification)
Pioneer RQ-2B	1.8	8.3	0.6	1.3	0.12	(1b)	33.64	35.00
Hunter RQ-5	1.8	8.3	1.4	1.3	0.5	(1b)	38.45	88.49
MALE for SMAT	1.8	8.3	1.1	0.6	2.4	(1a)	23.66	-
MAME for SMAT	1.8	8.3	0.8	0.8	0.3	(1b)	17.45	-
LASME for SMAT	1.8	8.3	0.5	0.7	0.12	(1b)	15.10	-

Table XI - Safety failure rate estimation with Role Index

UAV	λ_s [mishaps/h]
MALE (SMAT)	λ_s = 23.66 10^{-3} 1/LR = 2.4 10^{-6}
MAME (SMAT)	λ_s = 17.45 10^{-3} 1/LR = 1.8 10^{-6}
LASME (SMAT)	λ_s = 15.10 10^{-3} 1/LR = 1.5 10^{-6}

Applying the Role Index LR=10^4 (typical of "Fighters") to the above mentioned values, according to what was previously defined, the Safety Failure Rates reported in the following Table XI can be considered as consistent for the three UAVs considered for SMAT. These values, as it can be easily verified, are fully in agreement with the previously mentioned prescription of AER P2 [11]. These values of λ_s for the three UASs of SMAT system are not in conflict with the need of certification for operations in civil areas, even if highly populated. Moreover, accordingly to the previously explained reasons, are coherent with the estimated values for Basic Failure Rates. By the way, in more long times, another order of magnitude reduction of these λ_s values has to be considered. Obviously, in the same time, the corresponding λ_b values will be confirmed.

5 MISSION RELIABILITY ESTIMATION

This selection deals with the Mission Reliability estimation, that is the probability to successfully complete the mission that each UAS must perform. It can be assumed that the "Mission Failure Rate" (λ_m), that is the failure rate due to failures that cause the abort of a mission, has an intermediate value between those of Basic and Safety Failure Rates, such as:

$$\lambda_b > \lambda_m > \lambda_s \tag{5}$$

Logically, it can be assumed that λ_m has a value with an order of magnitude intermediate between those of λ_b and λ_s, because, luckily, not all the basic failures lead to abort the mission and not all the unsuccessful mission, lead to the loss of the vehicle. This assumption is true for fighters, while for UAVs this value must be considered in a slightly different way, Ref. [10]. Indeed, for UAVs it can be considered, in a more precautionary way, that λ_m has a value closer to λ_b, therefore rather high, mainly due to the already explained reasons of higher λ_s values and due to the fact that having no crew on board leads to an unlikely success when solving anomalies.

As a consequence, in a first approximation, for the three UAVs of the SMAT system, λ_m can be assumed as in Table XII.

As verification, the mission reliability for the three SMAT's UAVs was estimated such as:

$$R = \mathrm{e}^{-\lambda_m \cdot t_m} \tag{6}$$

Table XII - Mission failure rates estimation for SMAT UAVs

UAV	λ_m
MALE	λ_m=2.4 10-3
MAME	λ_m =1.8 10-3
LASME	λ_m=1.5 10-3

The results from (6) are reported in the following Table XVI, considering λ_m from Table XV and different values of mission length (t_m), proper for each of the three platforms considered, according to the foreseen kinds of usage.

In the same Table XV the Reliability values from reference [10] are also reported for the USA Armed Forces UAS already considered. The good concordance with calculated and real values, confirms the methodology validity and in particular the mission reliability values calculated (always in the Table XV) also for the SMAT's UAVs.

Please note that mission reliability values can be quite different, due to the t_m values dispersion, in particular for USA Armed Forces UAS, for which, in the reference, only R_m values have been reported.

Table XIII - Reliability estimate for SMAT UAVs and comparison with USA Armed Forces UASs

UAV		λ_m	t_m [hours]	R_m
SMAT	MALE for SMAT	2.4 10^{-3}	30	1.0
	MAME for SMAT	1.8 10^{-3}	10	0.8
	LASME for SMAT	1.5 10^{-3}	5	1.3
USAF	Predator RQ-1A	/	/	1.3
	Reaper RQ-1B	/	/	0.6
	Pioneer RQ-2B	/	/	0.8
	Hunter RQ-5	/	/	0.7

6 MAINTENANCE MAN HOURS/FLIGHT HOURS ESTIMATION

Complementary, it is also necessary to estimate how many efforts will be necessary to support the operations of future UAVs. This estimation could be done both from the point of view of entity of "Down Time" (i.e. the amount of time for which the System could not operate as it is under Maintenance or waiting for that) and the contribution of Maintenance to the Life Cycle Cost. A very good index for these purposes seems to be the "Maintenance Man Hours / Flight Hours" (MMH/FH). By hypothesizing the number of Maintainers that at the same time will work on the System, it is possible to deduce the "Down Time" and, then, the "System Availability" [9]. Based on Maintenance Man Hours an estimation of Maintenance cost can be derived. Based on such considerations, using the methodology for Reliability, Safety and Maintenance features assessment in aeronautical Conceptual Design Phase, already applied to the UAV as to Reliability (Basic and Mission) and Safety [9], an estimation strategy for MMH/FH has been developed for the Airplane Conceptual Design Phase, and it is based on the relationship:

$$MMH/FH = IRM \cdot CDTM \cdot IC \cdot IA \cdot MEW^{0.25} \quad (7)$$

where:

- MEW [tons], IC and IA are the same already utilized for the (1a) and (1b);
- IRM is an "Index Role for Maintenance", defined in Table 14;
- CDTM is a coefficient, taking into account how much the RAMS Techniques, in particular the ones influencing maintenance, have been considered in design phase; suggestions for the values are given in Table XVIII.

The following Table, reporting data from reference [9] shows how the (7) is able to give satisfactory estimation of MMH/FH for many kinds of manned aircraft, only utilizing few parameters that is easy to fix even in early design phases; please note that in such a Table all values utilized to calculate MMH/FH are reported as well as the calculated values that are compared with known ones, showing a very good realism of the estimations. So it was decided to apply also this part of Methodology to UAVs, in particular to the three models considered in this paper for the integration in SMAT System. Please note the following considerations:

Table XIV - Role Index of Maintenance Values for different kind of Aircraft

"Index Role" for Maintenance"	Fighters	Military Transport Vehicles	Civil Transport Vehicles
IRM	IRM=4.4	IRM=3.0	IRM=1.5

Table XV - Role Index of Maintenance Values for different kind of Aircraft

Influence level of maintenance in the design	Maintenance nearly not considered in the design	Early attempts to consider maintenance in the design	RAMS disciplines considered as design requirements	Testability and integrated logistic support considered since early design phases
CDTM Coefficient of influence of maintenance in the design	2.1	1.5	1.2	1.0

Table XVI - MMH/FH estimate examples for manned aircraft, Ref. [9]

Aircraft	IRM	CDTM	IA	IC	MEW [t]	MMH/FH, (calculated)	MMH/FH (known value)	Source Data
TORNADO	4.50	1.10	2.00	1.40	13.80	26.71	24.30	-
AMX	4.50	1.00	1.50	1.00	6.00	10.56	11.02	-
Eurofighter EF2000	4.50	0.90	1.00	1.40	9.60	9.98	9.67	-
SCALT	4.50	0.80	0.90	1.20	4.20	5.57	-	DIASP
F104	4.50	1.50	2.50	1.00	8.00	28.38	27.70	-
FIAT G91	4.50	2.10	3.00	0.60	3.50	23.27	25.50	-
C130	3.00	1.10	2.50	1.00	35.00	20.07	19.60	-
G222	3.00	1.10	2.00	1.00	15.00	12.99	-	-
ATR42	1.50	1.00	1.50	1.00	10.00	4.00	3.64	ATR
A320	1.50	1.00	1.00	1.50	42.00	5.73	-	-
B747	1.50	1.00	2.00	1.40	170.00	15.17	14.50	Roskam

On the basis of some considerations previously made, about the λ_b estimate, the Index of Role for Maintenance adopted for UAVs is the same of Fighters, i.e. IRM=4.4, as the similarity aspects have been considered prevalent.
Please note that a judgment on MMH/FH estimate will be, at the moment, only qualitative, as in reference [9] data the MMH/FH for UAVs of USA Armed Forces are not reported apart the Availability values. Unlikely Availability is a concept that requests more parameters to be defined and it is not reported in Ref. [10], so the values given are only indicative.
The presence in Eq. (7) of a MEW=0.25, i.e. with an exponent <1, seems a good interpretation of the contraction caused by the lower values of MEW, thinking that an UAV with high empty weight will probably have more component and so more maintenance operations but an easier work for Maintainers. Conversely, a reduced empty weight will probably have a greater number of unrepairable components that have to be directly replaced, compensating the difficulties of work for the reduced dimensions and the trend to a greater defectiveness seen about λ_b estimation.
By the way, the application of (7), with all assumed values, is reported for the three SMAT UAVs in Table 20 and the results, at a first glance, seem consistent.

Table XVII - MMH/FH estimated for SMAT UAVs

UAV	MEW [t]	IC	IA	IRM	CDTM	MMH/FH
MALE for SMAT	2.40	1.1	0.6	4.4	0.8	2.9
MAME for SMAT	0.30	0,8	0.8	4.4	0.8	1.7.
LASME for SMAT	0.12	0.5	0.7	4.4	0.8	0.75

7 CONCLUSIONS

The previously defined methodology for estimation of Reliability, Safety and Maintenance features in Conceptual Design Phase, even if developed for manned aircraft, has been adapted to the case of Monitoring and Surveillance of UAVs in order to study their integration in a complex Monitoring System, like SMAT. In the study, the very few available data for existing UAVs have been utilized. In this way, an assessment methodology has been established and some first almost indicative values of wanted features have been defined and found applicable.

REFERENCES

[1] E. Antona, S. Chiesa, S. Corpino, N. Viola, "L'avamprogetto dei Velivoli" Atti dell'Accademia delle Scienze di Torino, 2009.
[2] S. Chiesa, M. Fioriti, N. Viola, "Methodology for an integrated definition of a System and its Subsystems: the Case-Study of an airplane and its subsystems" Chapter of the book: Systems Engineering - Practice and Theory, ISBN: 978-953-51-0322-6, INTECH, 2012.
[3] S. Chiesa, S. Corpino, N. Viola, M. Fioriti "Sulla previsione di Costi, Sicurezza, Affidabilità e Entità della Manutenzione in Avamprogetto" XIX Congresso Nazionale AIDAA, Forlì (FC), 17-21 September 2007.
[4] S. Chiesa, M. Fioriti "UAV Logistic Support definition" from: Handbook of Unmanned Aerial Vehicles, edited by Kimon P. Valvanis and George J. Vachtservanos, ISBN 978-90-481 -9706-4, SPRINGER ed., 2014.
[5] S. Chiesa, "La manutenzione nel progetto dei sistemi aeronautici", Logistica di Impresa, numero speciale, ESTE, Milano, Dicember 1988.
[6] D. Ala, S. Chiesa, P. Gianotti, P. Maggiore, "Reliability estimation in Aircraft Conceptual Design", 32nd Annual International Logistics Conference & Exhibition, Orlando, Florida, August 1997.
[7] S. Chiesa, D. Camatti, G. Luda Di Cortemiglia "Design to System Effectiveness Methodology: a trial application", 34th Annual International Logistics Conference & Exhibition, Las Vegas, NV-USA, 30 august – 3 September 1999.
[8] D. Camatti, S. Chiesa, S. Corpino, M. Pasquino, "Simple statistical model for failure rate and maintenance amount estimation applied to a new aircraft conceptual design", SOLE Congress, New Orleans, August 2000.
[9] S. Chiesa "Affidabilità, Sicurezza e Manutenzione nel Progetto dei Sistemi" Nuova edizione riveduta e ampliata ed. CLUT, Torino, January 2008.
[10] Document "Office of the Segretary of Defence – Unmanned Aerial Vehicle Study – February 2003".
[11] Italian Department of Defence Regulation, "Omologazione di Aeromobili Militari e Relativi Sistemi – Idoneità alla installazione AER.P-2".
[12] ENAC Regulation, "Remotely Piloted Aerial Vehicles", Edition N.1 dated 16 December 2013.

ISSN 1590-8844
International Journal of Mechanics and Control, Vol. 16, No. 01, 2015

PREDICTIVE CONTROL OF SPATIAL FLEXIBLE MECHANISMS

Erfan Shojaei Barjuei Alessandro Gasparetto

Department of Electric, Managerial and Mechanical Engineering, University of Udine, Italy

ABSTRACT

In this paper, position control and reduction of vibration of a 3D flexible L-shape mechanism has been achieved through the synthesis of a constrained Model Predictive Control (MPC). A finite element model, based on the equivalent rigid link system (ERLS) theory, is used in order to describe accurately the dynamic behaviour of the system. The model has been validated through the experimental tests. In order to apply the constrained MPC control on the mechanism, a linearized model which takes gravity force into account is derived as well as a Kalman state estimator. The effectiveness and robustness of the control system has been evaluated and discussed through several tests. Furthermore, the performance of the MPC control has been compared with the performance of classical industrial control (PID).

Keywords: predictive control, flexible-link mechanisms, vibration control

1 INTRODUCTION

Modelling, analysing and controlling of flexible mechanisms have been under investigations for about four decades. Moreover, the consequence of accurate modelling and controlling the phenomena of mechanical vibration in flexible mechanisms is designing and fabricating lighter robot manipulators, which is a very important factor of lower operation cost and as well as high operation speed. Several studies have been done in order to define and present a precise mathematical model for flexible multi-body systems. These studies have started with investigation on a single flexible-link mechanisms, after with consideration flexible multi-body mechanisms in a planer and finally flexible mechanisms in the spatial environment [1–5]. The most used and adopted methods for modelling the flexible mechanism includes the usage of discretization methods such as finite element method (FEM) with the purpose of presenting dynamics models using a finite number of elastic degree-of-freedom. Models of such a kind, providing a nodal representation of the mechanism, have been proposed. Some author have also proposed description of flexible mechanisms making use of modal coordinates in place of physical coordinates. [6–9]

Contact author: Alessandro Gasparetto[1]

[1] DIEGM, University of Udine
Via delle Scienze, 208 - 33100 Udine, Italy

The available literature on model-based control strategies for flexible-link mechanisms is often the result of application of modal dynamic models, and less frequently on finite element-based models. Comprehensive reviews of the large number of available works can be found in [5] and [10].

Either linear or nonlinear control schemes have been developed. Linear control schemes have been utilized mostly. Some notable examples are robust control by Caracciolo [11] and sliding mode control by Kurode [13]. Also several works have proposed the use of Model Predictive Control (MPC) as an effective and suitable solution to the problem of damping vibration in flexible link mechanisms and structure. An experimental validation of MPC as position and vibration control is available in [20]. The mechanism under consideration is a single-link, and control is achieved on a relatively slow sampling frequency. A good overview of the topic, with several applicative example, is available in [21]. Other kind of mechanisms have been investigated by Boscariol for five bar link mechanism in [12] and four bar link mechanism in [23].

Currently, to the best of authors' knowledge, there are no available works on the predictive control of spatial flexible-link mechanisms. It should be mentioned that the majority of works in this area are application to planar mechanisms, often moving in the horizontal plane, thus without taking into account gravity. The aim of this paper is also to provide a feasible solution that can deal with the nonlinearities imposed by the presence of gravity force.

In this paper model predictive control (MPC) with constrains is proposed to control the position and minimize the amplitude the mechanical vibration during the motion of a 3D flexible L-shape mechanism. There are some motivating reasons for choosing this controller: first, the prediction ability based on an internal model can be a very effective advantages in fast-dynamic systems. Then MPC is well applicable to MIMO plants, because the outputs are calculated by solving a minimization problem which can take in consideration of several variables. Another remarkable advantages of this control scheme is its competences to perform constrains on both control and controlled variables [14].

The linearized model which is used in the MPC controller scheme is based on equivalent rigid-link system (ERLS) theory which is developed and proposed by Vidoni in [15] . The spatial flexible L-shape mechanism is taken into consideration in this work as a test bench mechanism, while having a single degree of freedom and allows 3D motion and elastic displacement.

The paper is organized as follows: Section 2 briefly explains the mathematical model of flexible mechanism, which is valid for any spatial flexible multi-body system. The description of the reference mechanism is given in Section 3. Section 4 provides a description on the linearization procedure as well as the accuracy validation and designing procedure of Kalman state estimator. A brief description of synthesis of model predictive control is presented in the Section 5. In Section 6 simulation results obtained controlling the nonlinear system with the MPC controller have been discussed. An evaluation of robustness properties of the controller is provided by several tests in Section 7. In Section 8 the results of a comparison between the performance of proposed MPC controller and a classical PID controller are presented.

2 DYNAMICS MODEL OF A 3D FLEXIBLE MECHANISM

One of the most studied topics in flexible multi-body systems is dynamic modelling which is still an open issue to investigate. In comparison with rigid mechanisms, the elastic behaviour of flexible mechanism makes the mathematical formulation of the models, which influence and regulate the real physical behaviour of the system, quite complex.

The approach used here for modelling of the systems with large displacements and small elastic deformation is based on Equivalent Rigid Link System (ERLS) concepts which first was introduced for a planer mechanisms by Giovagnioni in [3], and then expanded to 3D environment by Vidoni in [15,22] which is briefly explained in this section .

One of the main advantages of the ERLS approach in is that the standard mechanisms definitions and concepts of 3D kinematics could be adopted to formulate and solve the ERLS dynamic model.

2.1 Kinematics

As shown in Figure 1, each flexible link of the mechanism can be divided into finite elements. Being {X, Y, Z} a constant

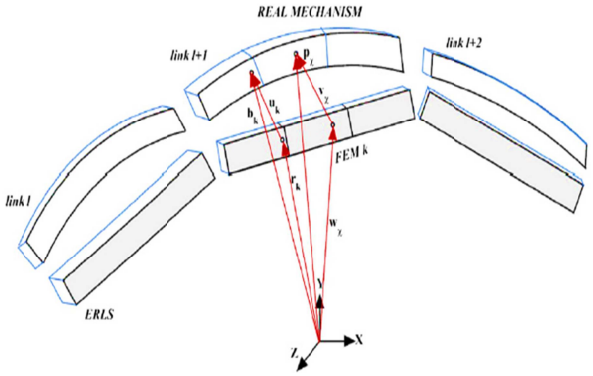

Figure 1 Kinematic definition of the ERLS

global reference frame, let us consider u_i and r_i as the vector of the nodal elastic displacements of the *i-th* finite element and the vector of nodal position and orientation for the *i-th* element of the ERLS, respectively. Moreover position vector of the generic point of the *i-th* element of the ERLS and its elastic displacement are w_i and v_i respectively. Hence, the absolute nodal position and orientation of the *i-th* finite element b_i with respect to the global reference frame is:

$$b_i = r_i + u_i \tag{1}$$

The absolute position p_i of generic point inside the *i*-th finite element is:

$$p_i = w_i + v_i \tag{2}$$

For each finite element $\{x_i, y_i, z_i\}$ is the local reference frame that follows the ERLS motion. Given this, it can be defined a block-diagonal global-to-local transformation matrix $T_i(q)$and a local-to-global transformation matrix $R_i(q)$ can be defined. Therefore it is possible to reform Equation 2 as follows:

$$p_i = w_i + R_i(q)N_i(x_i, y_i, z_i)T_i(q)u_i \tag{3}$$

Where $N_i(x_i,y_i,z_i)$ is the shape function matrix for the interpolation of the *i-th* finite element defined in local frame, and q is the vector of the generalized coordinates.

It can demonstrated that the expression for the virtual displacement δp_i in the constant reference frame is:

$$\delta p_i = R_i(q)N_i(x_i, y_i, z_i)T_i(q)\delta r_i \delta R_i(q)N_i(x_x, y_x, z_x)T_i(q)u_i + R_i(q)N_i(x_x, y_x, z_x)\delta T_i(q)u_i + R_i(q)N_i(x_x, y_x, z_x)T_i(q)\delta u_i \tag{4}$$

Twice differentiating Equation 3 leads to the expression of the acceleration of a generic point inside the *i-th* finite element as:

$$\ddot{p}_i = R_i(q)N_i(x_i,y_i,z_i)T_i(q)\ddot{r}_i + R_i(q)N_i(x_i,y_i,z_i)T_i(q)\ddot{u}_i + 2\left(\dot{R}_i(q)N_i(x_i,y_i,z_i)T_i(q) + R_i(q)N_i(x_i,y_i,z_i)\dot{T}_i(q)\right)\dot{u}_i + (\ddot{R}_i(q)N_i(x_i,y_i,z_i)T_i(q) + 2\dot{R}_i(q)N_i(x_i,y_i,z_i)\dot{T}_i(q) + R_i(q)N_i(x_i,y_i,z_i)\ddot{T}_i(q))u_i \quad (5)$$

If the kinematic entities of all the finite elements are gathered into one vector, differentiating Equation 1 with respect to time leads to:

$$db = du + dr \quad (6)$$

The configuration of the ERLS (as well as its velocity and acceleration) basically depends upon on the vector q of the free coordinates. This can be reformulated as:

$$dr = S(q)dq \quad (7)$$

S(q) is the matrix of the sensitivity coefficients for all the nodes. Finally, by substituting Equation 7 into Equation 6 the following equation in matrix form can be obtained:

$$db = \begin{bmatrix} I & S_{in} \\ 0 & S_0 \end{bmatrix}\begin{bmatrix} du_{in} \\ dq \end{bmatrix} \quad (8)$$

2.2 Dynamics

The dynamic equations of the system can be obtained by applying the principle of virtual works:

$$\delta W^{inertia} + \delta W^{elastic} + \delta W^{external} = 0 \quad (9)$$

which can also be written as:

$$\sum_i \delta u_i^T M_i(\ddot{r}_i + \ddot{u}_i) + 2\sum_i \delta u_i^T (M_{G1i} + M_{G2i})\,\dot{u}_i + \sum_i \delta u_i^T (M_{C1i} + 2M_{C2i} + M_{C3i})u_i + \sum_i \delta u_i^T K_i u_i = \sum_i \delta u_i f_{gi} + \delta u^T f \quad (10)$$

in which the mass matrix of the *i-th* element is:

$$\int_{vi} T_i^T N_i^T R_i^T R_i N_i T_i\, \rho_i dv = M_i \quad (11)$$

The stiffness matrix of the *i-th* element is:

$$\int_{vi} T_i^T B_i^T D_i B_i T_i dv = K_i \quad (12)$$

The vector of the equivalent nodal loads due to gravity is:

$$\int_{vi} T_i^T N_i^T R_i^T \,\mathrm{g}\, \rho_i dv = f_{gi} \quad (13)$$

The Coriolis terms are related to:

$$\int_{vi} T_i^T N_i^T R_i^T \dot{R}_i N_i T_i\, \rho_i dv = M_{G1i} \quad (14)$$

$$\int_{vi} T_i^T N_i^T R_i^T R_i N_i \dot{T}_i\, \rho_i dv = M_{G2i} \quad (15)$$

The centrifugal stiffness terms are:

$$\int_{vi} T_i^T N_i^T R_i^T \ddot{R}_i\, N_i T_i \rho_i dv = M_{C1i} \quad (16)$$

$$\int_{vi} T_i^T N_i^T R_i^T 2\dot{R}_i N_i \dot{T}_i\, \rho_k dv = 2M_{C2i} \quad (17)$$

$$\int_{vi} T_i^T N_i^T\, N_i \ddot{T}_i \rho_i dv = M_{C3i} \quad (18)$$

Being $\delta\emptyset_i$ the block-diagonal matrix which contains the virtual angular displacement and B_i the strain displacement matrix, the following equations holds:

$$\delta T_i^T = \delta\emptyset_i T_i^T \quad (19)$$

Since the virtual nodal elastic displacements δu and virtual displacement of the ERLS δr are independent from each other and taking into account the damping trough Rayleigh model using α and β damping constants, Equation 10 can be subdivided in two equations:

$$M(\ddot{r} + \ddot{u}) + 2(M_{G1} + M_{G2})\dot{u} + \alpha M\dot{u} + \beta K\dot{u} + (M_{C1} + 2M_{C2} + M_{C3})u + Ku = f_g + f \quad (20)$$

$$S^T M(\ddot{r} + \ddot{u}) + 2S^T(M_{G1} + M_{G2})\dot{u} + \alpha S^T M u + S^T(M_{C1} + 2M_{C2} + M_{C3})u = S^T(f_g + f) \quad (21)$$

Dynamic equations, after the substitution of the second order differential equations of the ERLS, can be grouped and rearranged in matrix from after discarding the equations for elastic degrees of freedom that have been zeroed:

$$\begin{bmatrix} M & MS \\ S^T M & S^T MS \end{bmatrix}\begin{bmatrix} \ddot{u} \\ \ddot{q} \end{bmatrix} = \begin{bmatrix} -2(M_{G1} + M_{G2}) - \alpha M - \beta K & -\dot{M}S & -(M_{C1} + 2M_{C2} + M_{C3}) - K \\ S^T(-2(M_{G1} + M_{G2}) - \alpha M) & -S^T M\dot{S} & -S^T(M_{C1} + 2M_{C2} + M_{C3}) \end{bmatrix}\begin{bmatrix} \dot{u} \\ \dot{q} \\ u \end{bmatrix} + \begin{bmatrix} M & I \\ S^T M & S^T \end{bmatrix}\begin{bmatrix} g \\ f \end{bmatrix} \quad (22)$$

Then, taking $x = [\dot{u}\ \dot{q}\ u\ q]$ as the augmented state vector, and rearranging the matrices, the system expressing the dynamics of the mechanism can be written also as:

$$\begin{bmatrix} M & MS & 0 & 0 \\ S^T M & S^T MS & 0 & 0 \\ 0 & 0 & I & 0 \\ 0 & 0 & 0 & I \end{bmatrix}\begin{bmatrix} \ddot{u} \\ \ddot{q} \\ \dot{u} \\ \dot{q} \end{bmatrix} = \begin{bmatrix} -2M_G - \alpha M - \beta K & -M\dot{S} & -(M_{C1} + 2M_{C2} + M_{C3}) - K & 0 \\ S^T(-2(M_{G1} + M_{G2}) - \alpha M) & -S^T M\dot{S} & -S^T(M_{C1} + 2M_{C2} + M_{C3}) & 0 \\ I & 0 & 0 & 0 \\ 0 & I & 0 & 0 \end{bmatrix}\begin{bmatrix} \dot{u} \\ \dot{q} \\ u \\ q \end{bmatrix} + \begin{bmatrix} M & I \\ S^T M & S^T \\ 0 & 0 \\ 0 & 0 \end{bmatrix}\begin{bmatrix} g \\ f \end{bmatrix} \quad (23)$$

The values of acceleration can be computed at each step by solving the Equation 22, while the values of velocities and of displacements can be obtained by an appropriate integration scheme (e.g. the Runge-Kutta algorithm) and, hence, the dynamic behaviour of the system can be simulated.

3 REFERENCE MECHANISM

The model presented in the previous section is valid for any spatial mechanism with any number of free coordinates. Hence, an L-shape mechanism is chosen as the basis of the simulation. The mechanism is made by two steel rods, connected by a rigid aluminium joint. The kinematics and dynamics characteristics of the reference mechanism are reported in Table I.

Figure 2 the mechanism built in the laboratory for the experimental validation of the model

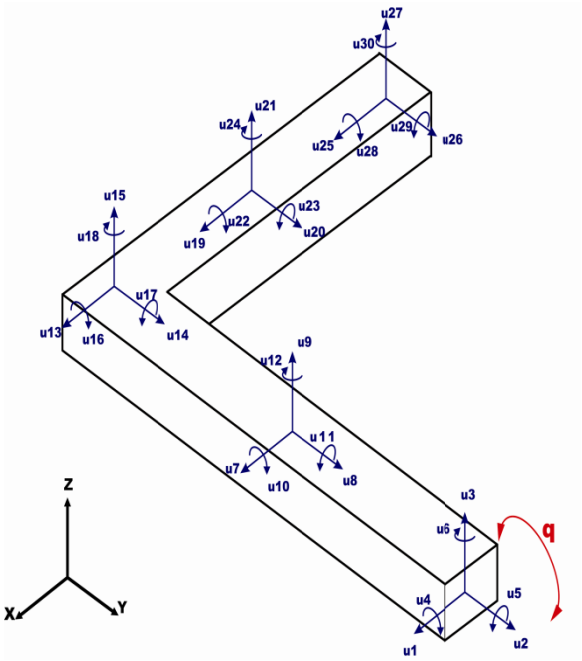

Figure 3 Elastic displacement in the L-shape mechanism

Each beam finite element in the spatial environment has 12 degrees of freedom. According to Figure 3, the mechanism has been discretized using 4 beam elements. After assembling them and considering the constraints imposed by the kinematic couplings and neglecting one of the nodal displacements in order to make the system solvable [15], the resulting flexible system is described by 24 nodal elastic displacements and one rigid degree of freedom.

Table I - Kinematics and dynamics characteristic of the reference mechanism

	Symbol	Value
Young's modulus	E	2×10^{11} [Pa]
Flexure inertia moment	J	11.102×10^{-10} [m^4]
Poisson's coefficient	v	0.33
Beam width	a	30×10^{-3} [m]
Beam thickness	b	10×10^{-3} [m]
Density	φ	2.7×10^{3} [Kg/m^3]
First link length	L_1	0.5 [m]
Second link length	L_2	0.5 [m]
Rayleigh damping constant	α	7×10^{-4} [s^{-1}]
	β	2.13×10^{-7} [s]

4 LINEAR STATE-SPACE DYNAMIC MODEL

In order to develop a state-space linear model, to be used as the prediction model for a linear MPC controller, a linearization procedure has been applied to the differential Equation 22 which is nonlinear due Coriolis term and to the effects of gravity. Gasparetto has presented linearization procedure that can be applied to planar mechanisms in [16]. A similar procedure is applied here, by extending it also to spatial mechanisms.
From the basics of linear system theory, a linear time-invariant (LTI) model in state space form can be written as:

$$\begin{cases} \dot{x}(t) = F_{lin}x(t) + G_{lin}v(t) \\ y(t) = H_{lin}x + D_{lin}v(t) \end{cases} \quad (24)$$

where $x(t)$, $y(t)$ and $v(t)$ represents the state vector, output vector and input vector respectively and F_{lin},G_{lin}, H_{lin} and D_{lin} are time-invariant matrices. Considering $x = [\dot{u}, \dot{q}, u, q]^T$ as the state vector, linearized state-space form of the dynamic model of Equation 23 can be reported as:

$$A_{lin}\dot{x} = B_{lin}x + C_{lin}\tau \quad (25)$$

Taking into account the equilibrium point x_e in the mechanism configuration and choosing $u = u_e$ under the system input $v = v_e$ in the proximity of the equilibrium point, the following equation can be considered:

$$\begin{cases} x(t) = x_e + \Delta x(t) \\ v(t) = v_e + \Delta v(t) \end{cases} \quad (26)$$

By substituting the above relations into Equation 23, the following relation can be found:

$$A_{lin}(x_e)\Delta\dot{x} = B_{lin}(x_e + \Delta x)(x_e + \Delta x) + C_{lin}(x_e + \Delta x)(v_e + \Delta x) \quad (27)$$

After some mathematical operations, the constant A_{lin} and B_{lin} matrices in Equation 24 can be evaluated as:

$$A_{lin} = \begin{bmatrix} M & MS & 0 & 0 \\ S^T M & S^T MS & 0 & 0 \\ 0 & 0 & I & 0 \\ 0 & 0 & 0 & I \end{bmatrix}_{x=x_e} \quad (28)$$

$$B_{lin} = \begin{bmatrix} -2M_G - \alpha M - \beta K & 0 & -K & B_{14} \\ S^T(-2M_G - \alpha M - \beta K) & 0 & 0 & B_{24} \\ I & 0 & 0 & 0 \\ 0 & I & 0 & 0 \end{bmatrix}_{x=x_e} \quad (29)$$

in which:

$$B_{14} = -\frac{\partial K}{\partial q}.\frac{K}{F_g} + \frac{\partial F_g}{\partial q} \quad (30)$$

$$B_{24} = \frac{\partial S^T}{\partial q}.F_g + S^T.\frac{\partial F_g}{\partial q} \quad (31)$$

where F_g represents the gravity force.

C_{lin} is unaltered by the linearization procedure since is composed of only zeroes and ones. Finally, the standard the state-space form of A_{lin}, B_{lin} and C_{lin} can be easily extracted:

$$\begin{cases} \Delta\dot{x} = F_{lin}\Delta x + G_{lin}\Delta v \\ y = H_{lin}x + D_{lin}v \end{cases} \quad (32)$$

where:

$$\begin{aligned} F_{lin} &= A_{lin}^{-1} B_{lin} \\ G_{lin} &= A_{lin}^{-1} C_{lin} \end{aligned} \quad (33)$$

4.1 Accuracy of the linearized Model

In this subsection, a simple comparison test in order to evaluate the extracted accuracy linearized model has been described. The mechanism, introduced in section 3, has been fed with 5 *Nm* torque impulse with 0.05 *sec* delay in the initial configuration of $q_0 = 90°$, i.e. starting from the vertical position; however, it should be mentioned that the test can be implemented to any mechanism configuration with similar results.

From the Figure 4 and 5 it can be inferred that linearized model has a very high level of precision as well as the rotation motion of q is considered. As can be seen from the Figure 4, the response of the linear and nonlinear models of q as the generalized coordinate is very close and similar to each other; however, the difference between them increases when moves away from the equilibrium point. Additionally, it can be inferred from Figure 5 that the error on q increases slowly as the error after 0.4 *s* is around 0.06%.

Figure 6 shows a comparison of the responses of nonlinear and linearized system impulsive on the subject of nodal displacements u_{11}. According to Figures 6, the difference between the linear and nonlinear modelling of u_{11} are negligible while the mechanism moves from the equilibrium configuration as far as u_{11} is concerned. Figures 7 shows the modelling error on u_{11}, which is very small at beginning of the motion and grows slowly during the mechanism manoeuvre.

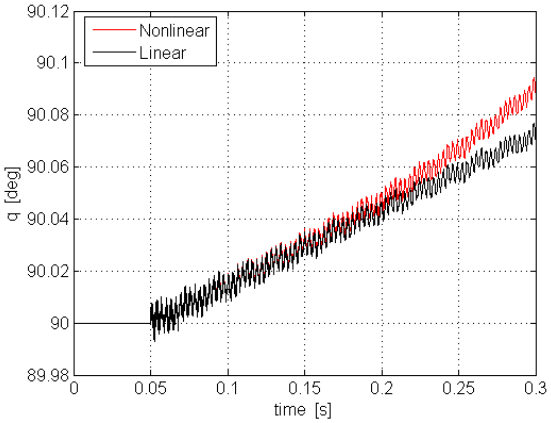

Figure 4 Comparison between linear and nonlinear impulsive response: angular position q

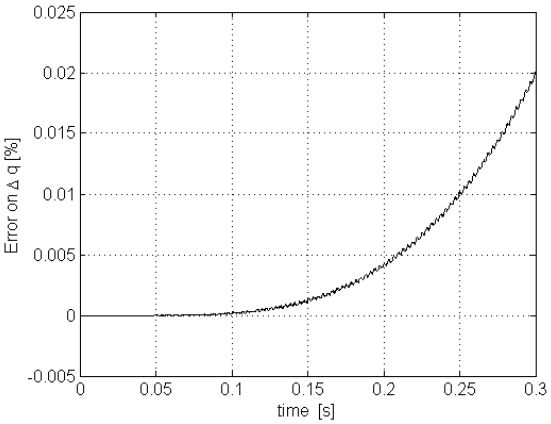

Figure 5 Comparison between linear and nonlinear impulsive response: percentage error on angular position q

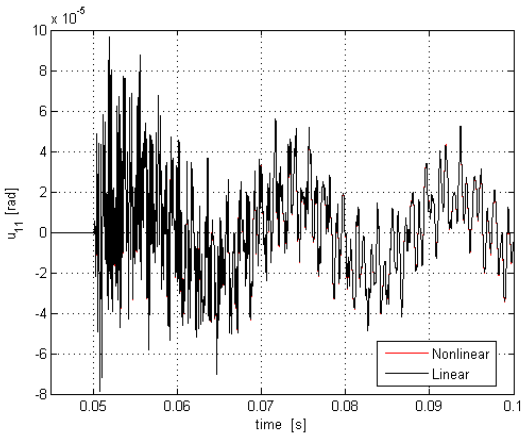

Figure 6 Comparison between linear and nonlinear impulsive response: elastic displacement u_{11}

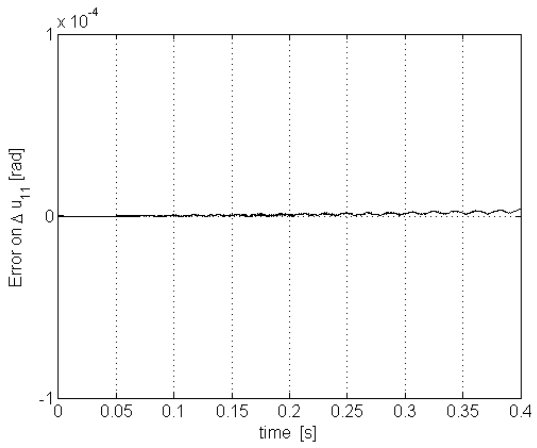

Figure 7 Comparison between linear and nonlinear impulsive response: error in radian on elastic displacement u_{11}

4.2 State Observer

Fundamentally, a state observer estimates the state variables by means of measuring a subset of the output and control variables in order to reconstruct the state of a system where the measurement is difficult or even impossible in some specific situations.

A brief explanation of the Kalman observer used in our system, is summarized here. For more details about methodology and designing refer to [17].

Basically an observer design depends upon on two basis, a linear time invariant dynamic model of the system and linear relation between the state variables and the sensed outputs. The dynamic of the overall system is described very briefly by the following system of equations:

$$\Delta\hat{\dot{x}} = F\Delta\hat{x} + G\,\Delta u + L(\Delta y - \Delta\hat{y}) \quad (34)$$

$$\hat{y} = H\Delta\hat{x} \quad (35)$$

$$\Delta z = -W\Delta\hat{x} \quad (36)$$

$$e = \Delta\hat{x} - \Delta x \quad (37)$$

where e and L are the vector of the errors of the state variable estimates ($\hat{x}$) and the time invariant gain matrix of the asymptotic Kalman estimator, respectively.

Additionally W is the time invariant gain vector of linear regulator and F and H matrices are used to assess the system observability as well. The control vector is shown by u while y and $\hat{y}$ present the real output signals and estimated ones respectively. G is a matrix which is related to the linearized model of the equilibrium configuration. However, it should be noticed that these equations only hold in the neighbourhood of an equilibrium configuration.

In order to evaluate our system observer, a similar test described in the previous subsection with the same input and configuration has been implemented. In this test knowledge about nodal displacement u_{19} and generalized coordinate q are available by the measurement in the purpose of estimating all states of the system.

From the Figure 8 and 9, it can be concluded that the Kalman observer has a good accuracy for estimating the generalized coordinate q as a one system state. Regarding the Figure 8, the impulsive response of nonlinear and observer are very similar; although, more far from the equilibrium point, more differences among the responses. Particularly, Figure 9 shows the error on q that is, after 0.4 *sec* the error between nonlinear and estimator is still so small and converge to zero.

Figure 10 illustrates the comparison between the impulsive respond of actual measurement of displacement u_{19} and estimated u_{19} by Kalman observer. As it can be seen from Figure 11 the difference is not so significant during the transient. Nevertheless they increase as the mechanism moves from the equilibrium configuration. In particular the difference on u_{19} between the nonlinear system and the observer are so small as long as the motion from the original position is kept.

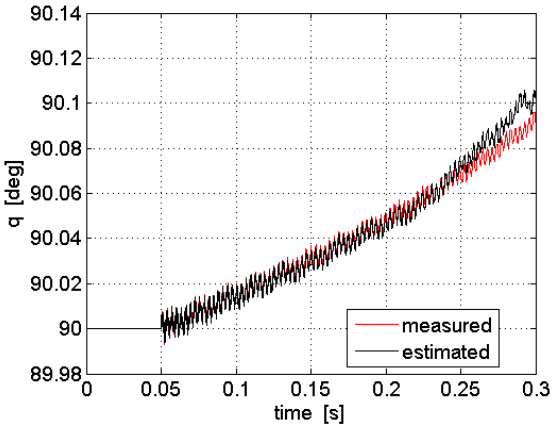

Figure 8 Comparison between measured and estimated angular position q

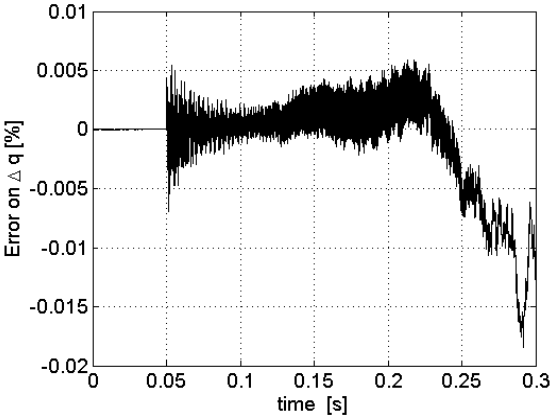

Figure 9 Percentage error on estimation of angular position q

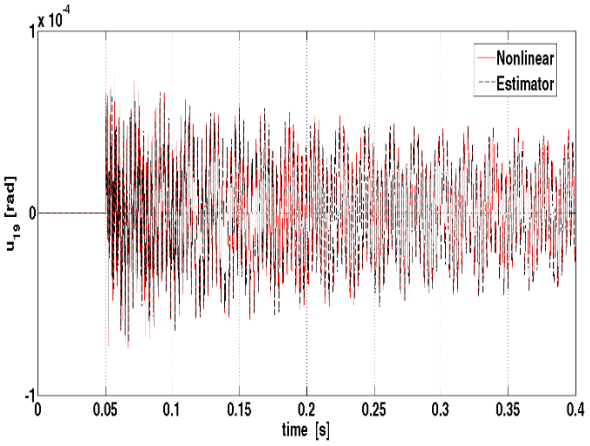

Figure 10 Comparison between response of impulsive response of nonlinear and estimated u_{19}

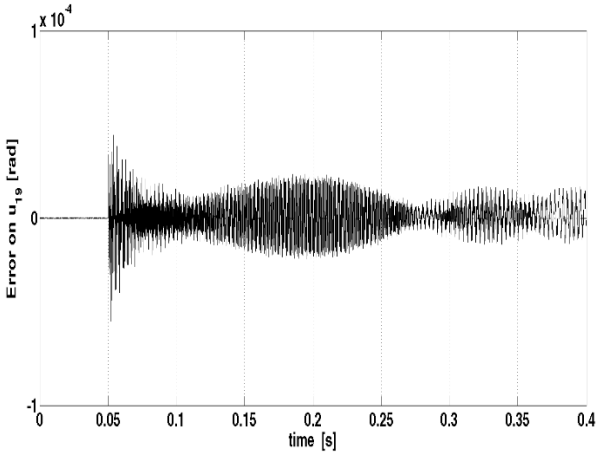

Figure 11 error in radian on estimation of elastic displacement u_{19}

5 MODEL PREDECTIVE CONTROL WITH CONSTRAINT

In this section a short introduction to constrained MPC is given. Model Predictive Control (MPC) is a class of computer control algorithms that is based on constructing controllers that are able to adjust the control action before a variation in the occurrence of the output set point. At each control interval the MPC algorithm attempts to optimize future plant performance by computing a sequence of future manipulated variable adjustment. An MPC algorithm can be tuned according to a cost function, constraints on controlled and control variables and to a model of the process to be controlled. For further reading on constrained MPC see [18].

5.1 Prediction and Control Horizons

Prediction horizon H_P is the number of samples over which a prediction of the plant outputs is evaluated at each iteration of the controller, while control horizon H_C is the number of samples over which the control variables can change their value.

As it can be seen in Figure 12, the MPC controller performs a prediction from current time step k to the future time step $k+H_p$. In the same figure it is shown that the control action can change only over the time interval $[k, k+H_c]$. The control action is chosen in order to minimize a given cost function. The first value of the optimal control sequence is actually fed to the plant, and the whole calculation is be repeated at subsequent control intervals. Prediction horizon is moving forward for every iteration in time and the MPC controller predicts the plant output again.

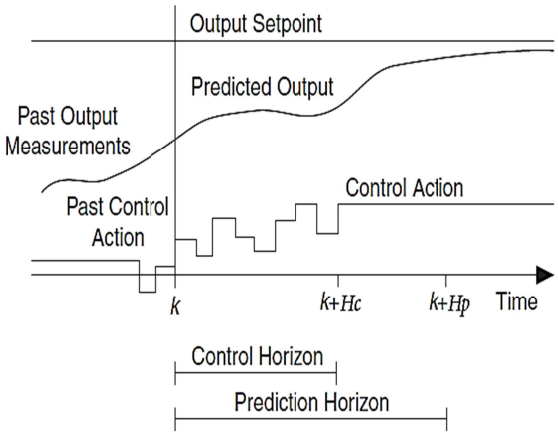

Figure 12 A discrete MPC controller scheme

5.2 Model Prediction and Cost Function

A discrete time state-space model is often used to provide predictive capability in MPC controller:

$$x_{k+1} = Ax_k + Bw_k \tag{38}$$

$$y_k = Cx_k + Dw_k \tag{39}$$

The MPC controller computes a sequence of the predicted a new control input vector in order to minimize a cost function. Often used cost function in MPC is the linear quadratic function:

$$J = \sum_{k=0}^{H_P}(\hat{y} - r)^T Q(\hat{y} - r) + \sum_{k=0}^{H_c} \Delta w^T R_1 \Delta w + \sum_{k=0}^{H_C} w^T R_2 w \tag{40}$$

in which $\hat{y}$, r, Δw, w are the predicted plant outputs, the reference signal for outputs, the change rate of control action and the control action, respectively. Q, R_1 and R_2 are the weighting matrices used to tune the control performance. Q is used to penalize the tracking error, while R_1 and R_2 are used to penalize the change rate and the absolute value of control action, respectively. In general, Equation 40 is used in MIMO systems (Multiple Input and Multiple Outputs) and also could be expanded to MISO systems (Multiple Input and Single Output) such as our case, a system with 50 inputs (states) and one output (torque).

Constrained MPC controller has ability to take into account constraints of physical systems in its future control performance calculations. The formulation used in this paper allows to define constraints as follows:

$$y_{min} \leq y \leq y_{max} \quad (41)$$

And inputs constrains can be defined as:

$$\Delta w_{min} \leq \Delta w \leq \Delta w_{max} \quad (42)$$
$$w_{min} \leq w \leq w_{max} \quad (43)$$

6 RESULT OF MODEL PREDICTIVE CONTROL WITH CONSTRAINT

In this section the results of several numerical tests are provided and discussed to show the capabilities of the MPC controller for position and vibration control of flexible mechanisms. The tuning of the MPC controller depends on weight on u_{19}, weight on q, sampling time (T_s), prediction horizon (H_p) and control horizon (H_c).
In practical applications, the values of T_s, H_p and H_c should be selected on the basis of the available computational resources. The computational cost of solving the optimization problem of each iteration of the controller depends on both H_p and H_c.
Generally speaking, longer H_c results in aggressive control action while longer H_p causes more damped response and more precise reference tracking [12].
The whole behaviour of the controller relies on a large set of variables. Constraints on actuation torque are chosen to comply with the physical limitations of the actuator. Other parameters can be tuned quite freely. In this case, constraints can be imposed on elastic displacement (u), angular position (q) and input torque (τ) as:

$$u_{k_{min}} \leq u_k \leq u_{k_{max}} \ , k = 1 \ldots 24 \quad (44)$$

$$q_{min} \leq q \leq q_{max} \quad (45)$$

$$\tau_{min} \leq \tau \leq \tau_{max} \quad (46)$$

It should be mentioned that in our system just the constraint on torque, which is $-8 \leq \tau \leq 8$ Nm, is active.
In the following the effects of choosing different values for tuning parameters of MPC controlled are discussed by means of numerical tests.

6.1 Effects of f_c on the Closed-loop System

Figure 13 and 14 demonstrate the response of angular position q and elastic displacement u_{12} with different sampling frequency. In all the tests reported in this work, the mechanisms performs a 30 degree of rotation in counter-clockwise direction starting from the horizontal position.
It can be seen from Figure 13 that the performance of the angular position response for both values of sampling frequency 100 Hz and 1kHz are very similar; however, it should be mentioned that the values of H_p and H_c are chosen 20 and 5 for f_c = 100 Hz and 200 and 50 for f_c=1kHz, respectively. The vibration amplitude for the system with f_c=100 Hz is bigger than the system with f_c=1 kHz during the transient as it is depicted in Figure 14 for elastic displacement u_{12}. The more effective vibration damping achieved by the 1 kHz control can be explained by taking into consideration the faster control has a sufficient bandwidth to take into account all the significant vibration modes of the flexible mechanism.

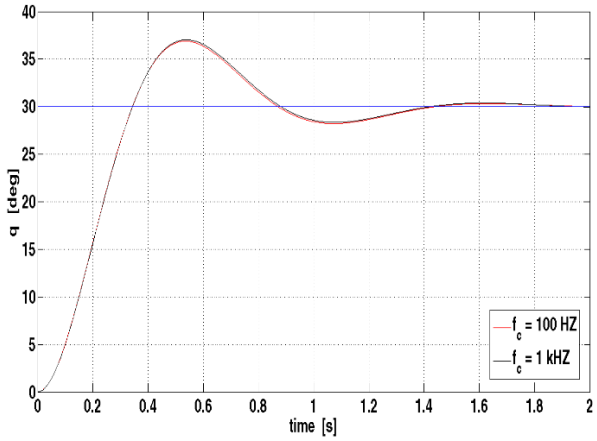

Figure 13 Response of the Angular position q at with different sampling frequency, 1 kHz and 100 kHz

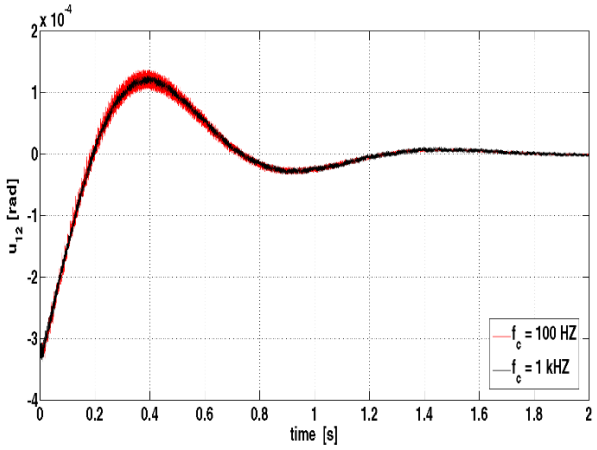

Figure 14 Effect analysis of different sampling frequency (f_c) on the elastic displacement u_{12}

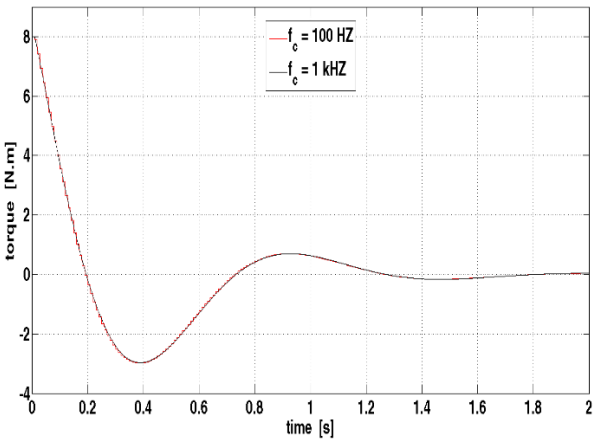

Figure 15 Applied torque to the mechanism

From the Figure 15 it can be inferred that applied torque by the control system is within the range defined by the constraint.

6.2 Effects of H_c and H_p on the Closed-loop System

In Figure 16 and 17 the effects of choosing different control horizon has been investigated. It can be inferred that tuning the H_c parameter has a limited effect on the response of the closed loop system. Consequently, H_c can be increased up to H_p but the performance of the controller will not be improved significantly. In most cases Hc should be kept quite small, since a longer control horizon increases the computational effort required to solve the minimization problem defined by Equations 38-40.

Regarding Figure 18 and 19, changing the value of the prediction horizon (H_p) has a significant effect on the performance of the controller. As it can be inferred from Figure 18, selecting bigger value for H_p causes more damped response for angular position q; conversely, smaller value for H_p result in more aggressive response. A similar consideration can be achieved by analysing the Figure 19, which reports the time evolution of elastic displacement u_{12}.

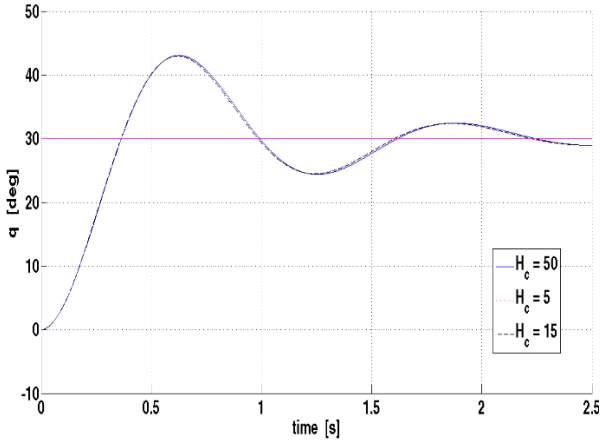

Figure 16 Effect analysis of different control horizon (H_c) on angular position q

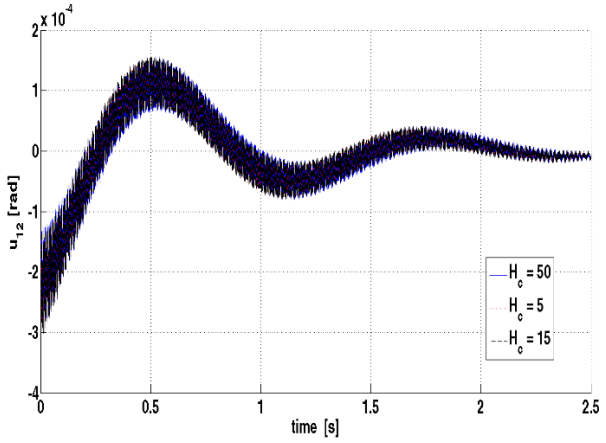

Figure 17 Effect analysis of different control horizon (H_c) on elastic displacement u_{12}

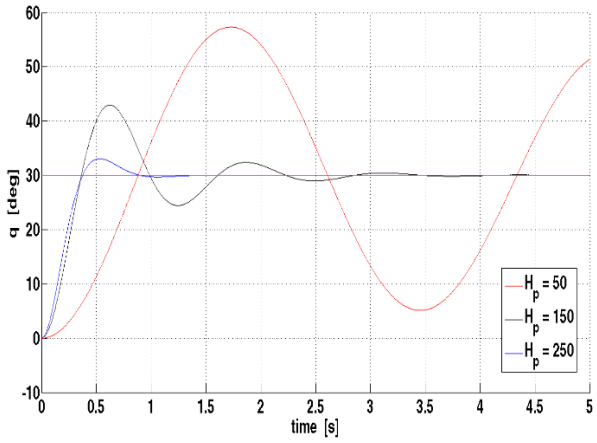

Figure 18 Effect analysis of different control horizon (H_p) on angular position q

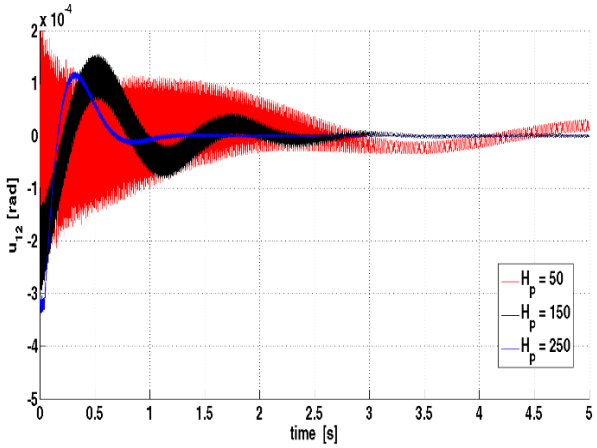

Figure 19 Effect analysis of different control horizon (H_p) on elastic displacement u_{12}

Again, higher values of the prediction horizon leads to a higher damping of vibrations.

Therefore we can conclude that the prediction horizon should be set as high as the computational resources allows it. Since the performance of the closed-loop system are less sensitive to the choice of the control horizon, H_c can be set to a low value to reduce the computational effort required to solve the optimization problem.

7 ROBUSTNESS

In this section the results of two tests which are implemented in order to evaluate robustness of the proposed control scheme are discussed.

Several simulations have been performed with applying the same control system on the nonlinear model with different parameters. The tests have been done with uncertainties of different sign (i.e. +20%, -20%) on the mechanism links lengths ($L=L_1+L_2$) and on the Young's elastic modulus E.

These tests that have been developed in order to evaluate the robustness properties of the proposed control scheme, using an approach already reported in other works such as [14,19].

In Figure 20 the effects of changing the mechanism length ($L=L_1+L_2$) of the mechanism have been shown. According to the Figure 20, the tolerance in the mechanism length does not bring the closed loop to instability. If the actual length of the links is 20% larger than the nominal value, the response of the system will be more damped. On the other hand, by decreasing by 20% the mechanism length, the overshoot of angular position q is increased with respect to the nominal case.

Thus it can be inferred that the developed controlled is quite robust to this kind of uncertainty, as far as angular position tracking is concerned. It can be seen in Figure 21 that also vibration damping is influenced by mismatches in mechanism length. If mechanism length is under-estimated, a more effective vibration damping can be achieved, since the overall response of the closed-loop system is slower.

According to Figure 22 and 23, changing the value of elastic modulus E of a $\pm$ 30% does not alter significantly the performance of the control scheme, thus the designed MPC controller is also robust respect to changes in the vibration models of the plant.

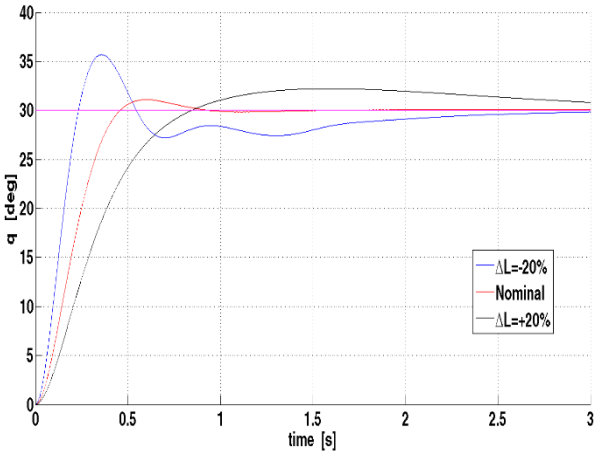

Figure 20 Robustness analysis of the change in the mechanisms links lengths ($L=L_1+L_2$) on angular position q

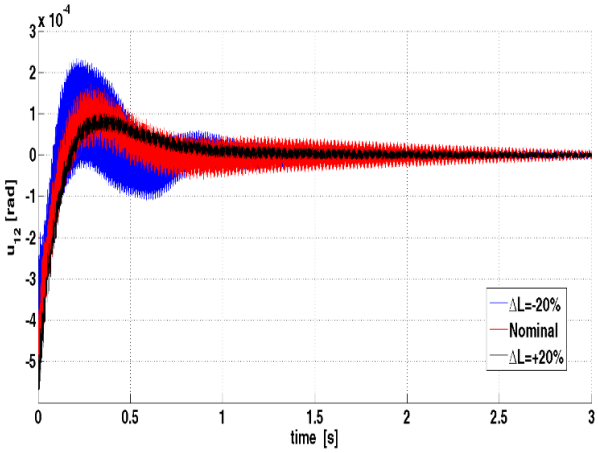

Figure 21 Robustness analysis of the change in the mechanisms links lengths ($L=L_1+L_2$) on elastic displacement u_{12}

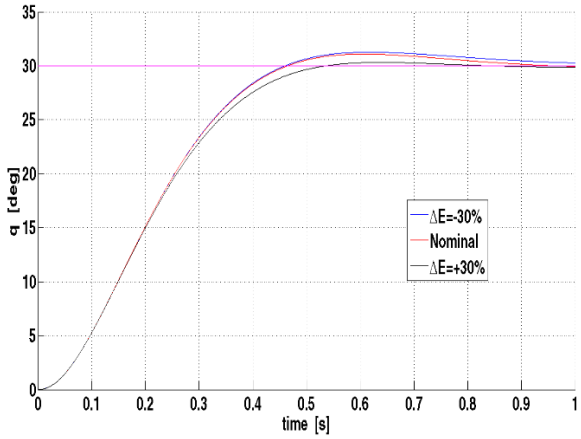

Figure 22 Robustness analysis of the change of elastic modulus E on angular position q

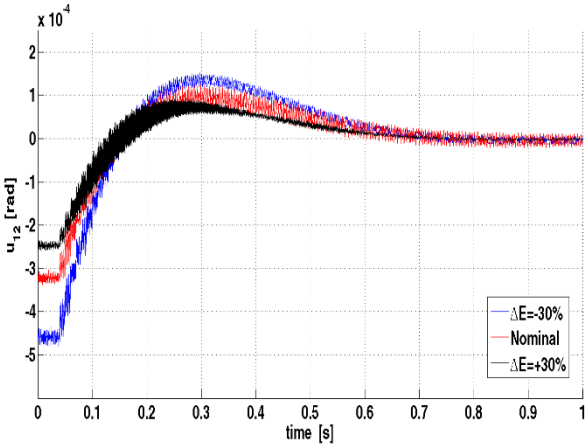

Figure 23 Robustness analysis of the change of elastic modulus E on elastic displacement u_{12}

8 MPC CONTROLLER VS. PID CONTROLLER

In this section a comparison between results of MPC and PID controller has been made and discussed. While PID controller are applied in single loop controllers, MPC controller are used for overall system. PID controllers support only a single input put system but MPC are applicable in multi input and multi output systems (MIMO system).

As is shown at Figure 24 PID controller follow the target reference with high speed and low error but with remarkable overshoot ($\cong$ 35%). The tuning of the PID control has been chosen to provide for a similar rise time. Moreover, it can be inferred from the Figure 25 that the amplitude of elastic displacement u_{12} is significantly larger if a simple PID controller is used.

It can be therefore inferred that in this case MPC control outperforms PID, which is currently the most widely used control technology in industrial applications.

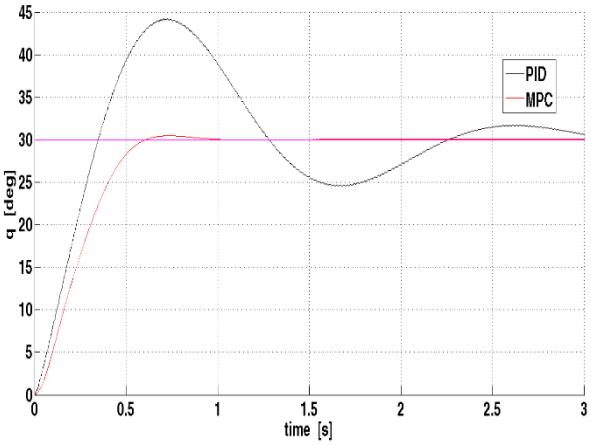

Figure 24 Response of the closed loop system with PID and MPC controller on angular position q

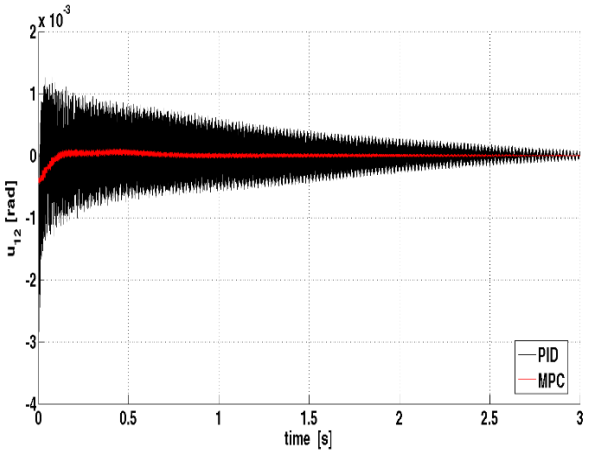

Figure 25 Response of the closed loop system with PID and MPC controller on elastic displacement u_{12}

CONCLUSION

In this work, a model predictive control with constrains for a 3D L-shape mechanism has been designed and tested. The dynamic behaviour of the flexible mechanism is described by means of a high accurate finite element method, based on the equivalent rigid link system (ERLS) theory and accounting for geometric nonlinearities and gravity force. In order to develop the constrained MPC controller the dynamic model of the mechanism is linearized; accordingly, a Kalman state observer has been developed as well. The proposed control scheme allows to minimize a performance index which takes into consideration both the amplitude of vibrations and the angular position of the mechanism. Meanwhile two tests on different perturbed plants has been implemented in order to analyse the robustness performance of the proposed control scheme. Finally a comparison between performance of the standard PID controller and MPC controller performance has been done and the results show that MPC controller not only is very effective for both reference position tracking and vibration suppression but also represent a high level of robustness to uncertainties on the plant.

REFERENCES

[1] R. Schwertassek, S. Dombrowski, and O. Wallrapp, "Modal Representation of Stress in Flexible Multibody Simulation," Nonlinear Dyn., vol. 20, no. 4, pp. 381–399, 1999.

[2] O. A. Bauchau, "Flexible Multibody Dynamics," Springer, 2011.

[3] M. Giovagnoni, "A Numerical and Experimental Analysis of a Chain of Flexible Bodies," J. Dyn. Syst. Meas. Control, vol. 116, no. 1, pp. 73–80, Mar. 1994.

[4] A. Shabana, "Flexible Multibody Dynamics: Review of Past and Recent Developments," Multibody Syst. Dyn., vol. 1, no. 2, pp. 189–222, 1997.

[5] O. Tokhi and A. K. M. Azad, Flexible Robot Manipulators: Modelling, Simulation and Control. Institution of Engineering and Technology, 2008.

[6] S. K. Dwivedy and P. Eberhard, "Dynamic analysis of flexible manipulators, a literature review," Mech. Mach. Theory, vol. 41, no. 7, pp. 749–777, Jul. 2006.

[7] S. S. Ge, T. H. Lee, and G. Zhu, "A nonlinear feedback controller for a single-link flexible manipulator based on a finite element model.," J. F. Robot., vol. 14, no. 3, pp. 165–178, 1997.

[8] P. Kalra and A. M. Sharan, "Accurate modelling of flexible manipulators using finite element analysis," Mech. Mach. Theory, vol. 26, no. 3, pp. 299–313, 1991.

[9] J. M. Martins, Z. Mohamed, M. O. Tokhi, J. Sa da Costa, and M. A. Botto, "Approaches for dynamic modelling of flexible manipulator systems," Control Theory and Applications, IEE Proceedings -, vol. 150, no. 4. pp. 401–411, 2003.

[10] M. Benosman and G. Le Vey, "Control of flexible manipulators: A survey," Robotica, vol. 22, no. 05, pp. 533–545, 2004.

[11] R. Caracciolo, D. Richiedei, A. Trevisani, and V. Zanotto, "Robust mixed-norm position and vibration control of flexible link mechanisms," Mechatronics, vol. 15, no. 7, pp. 767–791, Sep. 2005.

[12] P. Boscariol and V. Zanotto, "Design of a controller for trajectory tracking for compliant mechanisms with effective vibration suppression," Robotica, vol. 30, no. 01, pp. 15–29, 2012.

[13] S. Kurode and P. Dixit, "Control of tip position of flexible link manipulator using sliding modes," in 2nd Int. Conference on Advances on control and optimization of dynamical systems (ACODS 12) IISC Banglore, India, 2012.

[14] P. Boscariol, A. Gasparetto, and V. Zanotto, "Model Predictive Control of a Flexible Links Mechanism," J. Intell. Robot. Syst., vol. 58, no. 2, pp. 125–147, 2010.

[15] R. Vidoni, A. Gasparetto, and M. Giovagnoni, "Design and implementation of an ERLS-based 3-D dynamic formulation for flexible-link robots," Robot.

Comput. Integr. Manuf., vol. 29, no. 2, pp. 273–282, Apr. 2013.

[16] A. Gasparetto, “Accurate Modelling of a Flexible-Link Planer Mechanism by Means of a Linearized Model in The State-space Form for Design of a Vibration Controller,” J. Sound Vib., vol. 240, no. 2, pp. 241–262, Feb. 2001.

[17] R. Caracciolo, D. Richiedei, and A. Trevisani, “Design and experimental validation of piecewise-linear state observers for flexible link mechanisms,” Meccanica, vol. 41, no. 6, pp. 623–637, 2006.

[18] J. M. Maciejowski, Predictive Control: With Constraints. Prentice Hall, 2002.

[19] N. O. Ghahramani and F. Towhidkhah, “Constrained incremental predictive controller design for a flexible joint robot,” ISA Trans., vol. 48, no. 3, pp. 321–326, Jul. 2009.

[20] Bossi, L., et al. "Multivariable predictive control for vibrating structures: An application." Control Engineering Practice 19.10 (2011): 1087-1098.

[21] Takács, Gergely, and Boris Rohaľ-Ilkiv. Model Predictive Vibration Control: Efficient Constrained MPC Vibration Control for Lightly Damped Mechanical Structures. Springer, 2012.

[22] Boscariol, Paolo, et al. "On the modeling of flexible-link robots: First experimental validation of an ERLS-FEM dynamic model." Mechatronics (ICM), 2013 IEEE International Conference on. IEEE, 2013.

[23] P. Boscariol, A. Gasparetto, and V. Zanotto, “Active Position and Vibration Control of a Flexible Links Mechanism Using Model-Based Predictive Control,” J. Dyn. Syst. Meas. Control, vol. 132, no. 1, p. 14506, Dec. 2009.

ISSN 1590-8844
International Journal of Mechanics and Control, Vol. 16, No. 01, 2015

TEMPLATE FOR PREPARING PAPERS FOR PUBLISHING IN INTERNATIONAL JOURNAL OF MECHANICS AND CONTROL

Author1* Author2**

* affiliation Author1

** affiliation Author2

ABSTRACT

This is a brief guide to prepare papers in a better style for publishing in International Journal of Mechanics and Control (JoMaC). It gives details of the preferred style in a template format to ease paper presentation. The abstract must be able to indicate the principal authors' contribution to the argument containing the chosen method and the obtained results. (max 200 words)

Keywords: keywords list (max 5 words)

1 TITLE OF SECTION (E.G. INTRODUCTION)

This sample article is to show you how to prepare papers in a standard style for publishing in International Journal of Mechanics and Control.
It offers you a template for paper layout, and describes points you should notice before you submit your papers.

2 PREPARATION OF PAPERS

2.1 SUBMISSION OF PAPERS

The papers should be submitted in the form of an electronic document, either in Microsoft Word format (Word'97 version or earlier).
In addition to the electronic version a hardcopy of the complete paper including diagrams with annotations must be supplied. The final format of the papers will be A4 page size with a two column layout. The text will be Times New Roman font size 10.

Contact author: author1[1], author2[2]

[1]Address of author1.
[2]Address of author2 if different from author1's address
E-mail: author1@univ1.com , author2@univ2.com

2.2 DETAILS OF PAPER LAYOUT

2.2.1 Style of Writing

The language is English and with UK/European spelling. The papers should be written in the third person. Related work conducted elsewhere may be criticised but not the individuals conducting the work. The paper should be comprehensible both to specialists in the appropriate field and to those with a general understanding of the subject.
Company names or advertising, direct or indirect, is not permitted and product names will only be included at the discretion of the editor. Abbreviations should be spelt out in full the first time they appear and their abbreviated form included in brackets immediately after. Words used in a special context should appear in inverted single quotation mark the first time they appear. Papers are accepted also on the basis that they may be edited for style and language.

2.2.2 Paper length

Paper length is free, but should normally not exceed 10000 words and twenty illustrations.

2.2.3 Diagrams and figures

Figures and Tables will either be entered in one column or two columns and should be 80 mm or 160 mm wide respectively. A minimum line width of 1 point is required at actual size. Captions and annotations should be in 10 point with the first letter only capitalised *at actual size* (see Figure 1 and Table VII).

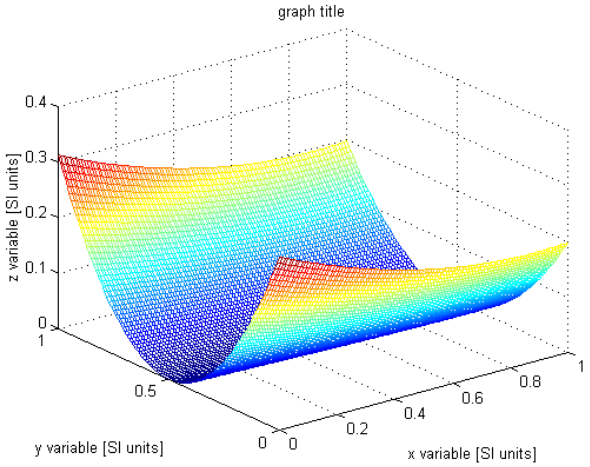

Figure 1 Simple chart.

Table VII - Experimental values

Robot Arm Velocity (rad/s)	Motor Torque (Nm)
0.123	10.123
1.456	20.234
2.789	30.345
3.012	40.456

2.2.4 Photographs and illustrations

Authors could wish to publish in full colour photographs and illustrations. Photographs and illustrations should be included in the electronic document and a copy of their original sent. Illustrations in full colour …

2.2.5 Equations

Each equation should occur on a new line with uniform spacing from adjacent text as indicated in this template. The equations, where they are referred to in the text, should be numbered sequentially and their identifier enclosed in parenthesis, right justified. The symbols, where referred to in the text, should be italicised.

- point 1
  - point 2
    - point 3

1. numbered point 1
   2. numbered point 2
      3. numbered point 3

$$W(d) = G(A_0, \sigma, d) = \frac{1}{T}\int_0^{+\infty} A_0 \cdot e^{-\frac{d^2}{2\sigma^2}} dt \qquad (1)$$

3 COPYRIGHT

Authors will be asked to sign a copyright transfer form prior to JoMaC publishing of their paper. Reproduction of any part of the publication is not allowed elsewhere without permission from JoMaC whose prior publication must be cited. The understanding is that they have been neither previously published nor submitted concurrently to any other publisher.

4 PEER REVIEW

Papers for publication in JoMaC will first undergo review by anonymous, impartial specialists in the appropriate field. Based on the comments of the referees the Editor will decide on acceptance, revision or rejection. The authors will be provided with copies of the reviewers' remarks to aid in revision and improvement where appropriate.

5 REFERENCES (DESCRIPTION)

The papers in the reference list must be cited in the text. In the text the citation should appear in square brackets [ ], as in, for example, "the red fox has been shown to jump the black cat [3] but not when...". In the Reference list the font should be Times New Roman with 10 point size. Author's first names should be terminated by a 'full stop'. The reference number should be enclosed in brackets.

The book titles should be in *italics*, followed by a 'full stop'. Proceedings or journal titles should be in *italics.* For instance:

REFERENCES (EXAMPLE)

[1] Smith J., Jones A.B. and Brown J., *The title of the book*. 1st edition, Publisher, 2001.

[2] Smith J., Jones A.B. and Brown J., The title of the paper. *Proc. of* C*onference Name*, where it took place, Vol. 1, paper number, pp. 1-11, 2001.

[3] Smith J., Jones A.B. and Brown J., The title of the paper. *Journal Name*, Vol. 1, No. 1, pp. 1-11, 2001.

[4] Smith J., Jones A.B. and Brown J., *Patent title*, U.S. Patent number, 2001.

International Journal of Mechanics and Control – JoMaC
Published by Levrotto&Bella
TRANSFER OF COPYRIGHT AGREEMENT

NOTE: Authors/copyright holders are asked to complete this form signing section A, B or C and mail it to the editor office with the manuscript or as soon afterwards as possible.	*Editor's office address:* Andrea Manuello Bertetto Elvio Bonisoli *Dept. of Mechanics* *Technical University – Politecnico di Torino* *C.so Duca degli Abruzzi, 24 – 10129 Torino – Italy* *e_mail: jomac@polito.it* *fax n.: +39.011.564.6999*

The article title:

By:_____

To be Published in ***International Journal of Mechanics and Control JoMaC***
Official legal Turin court registration Number 5320 (5 May 2000) - reg. Tribunale di Torino N. 5390 del 5 maggio 2000

A Copyright to the above article is hereby transferred to the JoMaC, effective upon acceptance for publication. However the following rights are reserved by the author(s)/copyright holder(s):
1. All proprietary rights other than copyright, such as patent rights;
2. The right to use, free or charge, all or part of this article in future works of their own, such as books and lectures;
3. The right to reproduce the article for their own purposes provided the copies are not offered for sale.

To be signed below by all authors or, if signed by only one author on behalf of all co-authors, the statement A2 below must be signed.

A1. All authors:

SIGNATURE_____DATE_____ SIGNATURE_____DATE_____

PRINTED NAME_____ PRINTED NAME_____

SIGNATURE_____DATE_____ SIGNATURE_____DATE_____

PRINTED NAME_____ PRINTED NAME_____

A2. One author on behalf of all co-authors:
"I represent and warrant that I am authorised to execute this transfer of copyright on behalf of all the authors of the article referred to above"

PRINTED NAME_____

SIGNATURE_____ TITLE_____ DATE_____

B. The above article was written as part of duties as an employee or otherwise as a work made for hire. As an authorised representative of the employer or other proprietor. I hereby transfer copyright to the above article to *International Journal of Mechanics and Control* effective upon publication. However, the following rights are reserved:
1. All proprietary rights other than copyright, such as patent rights;
2. The right to use, free or charge, all or part of this article in future works of their own, such as books and lectures;
3. The right to reproduce the article for their own purposes provided the copies are not offered for sale.

PRINTED NAME_____

SIGNATURE_____ TITLE_____ DATE_____

C. I certify that the above article has been written in the course of employment by the United States Government so that no copyright exists, or by the United Kingdom Government (Crown Copyright), thus there is no transfer of copyright.

PRINTED NAME_____

SIGNATURE_____ TITLE_____ DATE_____

CONTENTS – Special Issue for RAAD 2014

3 **Optimal Design of a New Spherical Parallel Manipulator Used as Master Device**

H. Saafi, M.A. Laribi, M. Arsicault, S. Zeghloul

11 **An Underactuated Mechanical Hand: Theoretical Studies and Prototyping**

V. Niola, F. Penta, C. Rossi, S. Savino

21 **Simulation and Construction of a MEMS CSFH Based Microgripper**

N.P. Belfiore, G.B. Broggiato, M. Verotti, M. Balucani, R. Crescenzi, A. Bagolini, P. Bellutti, M. Boscardin

31 **Conversion of Peaucellier–Lipkin Straight-Line Mechanism to Compact Compliant Device**

J. Hricko

39 **Separate Adjustment of Torque and Stiffness for Pneumatic Robot Actuators with Antagonistic Rotary Elastic Chambers**

D. Baiden, O. Ivlev

CONTENTS – Regular Issue

49 **Safety and Logistics Performance Evaluation of a RFID System in a Blood Transfusion Centre**

G. Borelli, P.F. Orrù, F. Zedda

57 **An Application of LARM Clutched Arm for Assisting Disabled People**

C. Copilusi, M. Ceccarelli

67 **The Earlier Experiences of Photographic Measurements in Russia**

A. Vukolov, O. Egorova

73 **Contribution to R.A.M.S Estimation in Early Design Phases of Unmanned Aerial Vehicles – UAVs**

R. Fusaro, S. Chiesa, S. Cresto Aleina, M. Fioriti

85 **Predictive Control of Spatial Flexible Mechanisms**

E.S. Barjuei, A.Gasparetto